Density Functional Theory Based Strategies for Tailoring the Magnetic and Morphological Properties of Surfaces

A Thesis
Submitted For the Degree of
Doctor of Philosophy
in the Faculty of Science

by

Sananda Biswas

Theoretical Sciences Unit
Jawaharlal Nehru Centre for Advanced Scientific Research
Bangalore – 560 064

JULY 2014

To my family

DECLARATION

I hereby declare that the matter embodied in the thesis entitled "**Density Functional Theory Based Strategies for Tailoring the Magnetic and Morphological Properties of Surfaces**" is the result of investigations carried out by me at the Theoretical Sciences Unit, Jawaharlal Nehru Centre for Advanced Scientific Research, Bangalore, India under the supervision of Prof. Shobhana Narasimhan and that it has not been submitted elsewhere for the award of any degree or diploma.

In keeping with the general practice in reporting scientific observations, due acknowledgement has been made whenever the work described is based on the findings of other investigators.

Sananda Biswas

CERTIFICATE

I hereby certify that the matter embodied in this thesis entitled "**Density Functional Theory Based Strategies for Tailoring the Magnetic and Morphological Properties of Surfaces**" has been carried out by Ms. Sananda Biswas at the Theoretical Sciences Unit, Jawaharlal Nehru Centre for Advanced Scientific Research, Bangalore, India under my supervision and that it has not been submitted elsewhere for the award of any degree or diploma.

Prof. Shobhana Narasimhan
(Research Supervisor)

Acknowledgment

First and foremost, I would like to thank my PhD supervisor, Prof. Shobhana Narasimhan, for her guidance and all scientific and non-scientific discussions. She has encouraged me to pursue research in the field that is of interest to me and has given me all the freedom for that. Among many things I have learnt from her are the finer details of preparing slides, delivering talks, writing papers, to name a few.

Next, I would like to thank my collaborators Prof. Stefan Blügel and Gustav Bihlmayer from Forschungszentrum, Jülich, Germany. I have gained a lot from the discussions we had during my visits in Jülich. I would also like to thank my other collaborators Dr. Sadanand Deshpande and Dr. Derren Dunn from IBM, and Prof. Krishnakumar Menon and Jayanta Das from Saha Institute of Nuclear Physics, India. I also thank B. Zimmermann, B. Schweflinghaus, Dr. Ph. Mavropoulos, Prof. S. Rosset, Prof. V. Repain, Dr. S. Mehendale, Prof. N. Spaldin, Prof. M. Weinert, Prof. T. Fischer, Prof. T. Saha Dasgupta, Prof. S. Scandolo for helpful discussions.

I would also like to acknowledge Prof. Umesh Waghmare, Prof. Swapan Pati, Dr. N. S. Vidyadhiraja, Dr. Subir Das, Prof. Vijay Shennoy, for all the things they have taught me through their courses. I thank Prof. Balasubramanian Sundaram for encouraging me to join TSU, JNCASR.

I would like to thank all my past and present labmates – Prasenjit, Jaita, Mighfar, Madhura, Brandon, Nisha, Kanchan, Vasudevan, Lakshmi, Bulumoni, Debarati, Sukanya, Debdipto, Rajdeep, Nurapati, Rajiv, Devina and Gaurav. A special thanks to Kanchan, Nisha, Rajdeep and Gaurav for helping me with the technical details to carry out some of the calculations which are included in this thesis.

Many friends had helped me directly or indirectly during my PhD – Adrija, Suman, Sujoy, Sourav, Aditi, Nipa, Sayan, Poulumi, Biswanath, Meera, Debashis, Abhijit, Jayeeta, Joydeep, Ranjeeta, Sayam, Sonia, Sumanta, Abhijit, Kaustuv, Sirisha, Supriyo, Kanchan, Pramod, Nikhil, Rounak, Arun, Varun, Sasmita, Sudipto, Anil, Vishwas, Shiladitya, Arun, Prakash, Nisha, Sharmila, Depashee, Pralok, Dibyo, Anirban, Somananda, Arkamita, Kaushik, Sudeshna, Pallavi, Jayashree, Kalpita, Ananthu, Anjali, Sarda, and Sona.

I would like to acknowledge funding from CSIR (for a research fellowship), IUPAP and DST.

I would like to acknowledge the computational facilities at TUE-CMS, JNCASR and Ershaad, Amit, Bharati and Vijay for the technical support. I would also like to acknowledge the computational facilities at Jülich Supercomputing centre, Forschungszentrum, Jülich, Germany and IBM, Fishkill, NY, USA.

I would like to thank all the administrative and academic staff at JNCASR, especially, Mr. Jayachandra, Dr. Princy, Ms. Sukanya, Ms. Jayamangala, Mr. Ramakrishna and the staff members of Dhanvantari, Dinning Hall, Hostel Gym, Hostel Office, and Hostel Mess. I would also thank all the stupreps.

Last but not the least, I would like to thank my family for showing irrational support and trust in me. It would not have been possible to write the thesis without having two special persons in my life: my sister Kitu and my loving husband, Soumitra.

List of Publications

Included in thesis

1. "Tuning patterning conditions by co-adsorption of gases: Br_2 and H_2 on Si(001)", Sananda Biswas, Sadanand V. Deshpande, Derren N. Dunn, and Shobhana Narasimhan, *J. Chem. Phys.* **139**, 184713 (2013).

2. "Origins of stability of surface alloys: a case study of the Mn-Au/Ru(0001) system", Sananda Biswas and Shobhana Narasimhan, (*Preprint*), 2014.

3. "Spin spirals in surface alloys on Ru(0001): A first-principles study", Sananda Biswas, Gustav Bihlmayer, Shobhana Narasimhan, and Stefan Blügel, ArXiv-1405.2152.

4. "*Ab initio* modelling of etching: conventional and supersaturation etching of Si(100) by Br_2 ", Sananda Biswas, Sadanand V. Deshpande, Derren N. Dunn, and Shobhana Narasimhan, (*Preprint*), 2014.

5. "Structure of two-dimensional c(2×2) antiferromagnetic Cr monolayer on Ag(100)", Jayanta Das, Sananda Biswas, Asish Kumar Kundu, Shobhana Naramsimhan, and Krishna Kumar Menon (*Preprint*), 2014.

Not included in thesis

- "Gas-sensing properties of defective- and transition-metal embedded graphene" Sananda Biswas and Shobhana Narasimhan, (*Manuscript under preparation*).

List of Abbreviations

$\hbar$	Planck's constant
μ_B	Bohr magneton
e	Charge of free electron
m_e	Mass of free electron
M_I	Mass of nucleus
$Z_I e$	Charge of nucleus
Å	Angstrom
a.u.	Atomic Unit
ABD	Alternating Buckled Dimers
AFM	Antiferromagnetic
AIAT	*Ab Initio* Atomistic Thermodynamics
ARPES	Angle-resolved Photoemission Spectroscopy
BZ	Brillouin Zone
CI-NEB	Climbing Image Nudged Elastic Band
CM	Constrained Minimization
DFT	Density Functional Theory
DM	Dzyaloshinskii-Moriya
dRAM	dynamic Random Access Memory
ECN	Effective Coordination Number
eV	electron Volt
FLAPW	Full-potential Linearized Augmented Plane-wave
FM	Ferromagnetic

GGA	Generalized Gradient Approximation
GMR	Giant Magnetoresistance
hcp	hexagonal close packed
IBZ	Irreducible Brillouin Zone
K	Kelvin
KS	Kohn-Sham
LDA	Local Density Approximation
LEED	Low-energy Electron Diffraction
LSDA	Local Spin Density Approximation
MEP	Minimum Energy Path
meV	mili electron Volt
ML	Monolayer
MT	Muffin-tin
NEB	Nudged Elastic Band
NM	Non-magnetic
nm	nanometer
NN	Nearest Neighbor
NNN	Next Nearest Neighbor
PAESD	Phonon-activated electron stimulated desorption
PES	Potential Energy Surface
PP	Pseudopotential
Ry	Rydberg
SC	Self-consistent
SO	Spin-orbit
SSE	Supersaturation Etching
STM	Scanning Tunneling Microscopy
TMR	Tunnel Magnetoresistance
TPD	Temperature Programmed Desorption
XC	Exchange-correlation
ZPE	Zero-point Energy

List of Figures

List of Tables

Contents

A Magnetic Properties of Surfaces

Chapter 1

Introduction

For the last few decades materials science has been the at the frontier of technological development. Today's computer age requires the development of efficient and "smart" materials to gain faster and quicker control over data processing and probing. This drive is further fueled by the demand for developing novel materials that permit ever-increasing storage density. The broad aim of this thesis is to understand and tailor the physics and chemistry of technologically important materials using first principles methods, particularly in the areas of information storage and semiconductor electronics. In this context, we have tried to develop strategies to (1) control the magnetic properties of metal surfaces to obtain new magnetic ordering, and (2) tune the chemical properties of semiconductor surfaces to obtain new surface morphologies. While magnetic metal surfaces are potential candidates for spintronics applications, semiconductor surfaces are already used for electronics applications, e.g., for the fabrication of integrated circuit chips.

In this thesis, we have primarily used density functional theory (DFT) to study the ground state properties of systems. Such properties include the relative stability of different phases, formation energy, surface stress, magnetic anisotropy energy, adsorption and co-adsorption energies, energy barriers, etc. Moreover, the results from DFT are used as inputs in order to calculate (a) the activation barriers for the minimum energy path for a (complex) chemical reaction using the nudged elastic band (NEB) method, and (b) the

Gibbs free energy of a system at finite temperature and pressure using the *ab initio* atomistic thermodynamics (AIAT) method. These methods are briefly discussed in Chapter 2.

The work in the thesis is divided into two parts: Part A deals with the magnetic properties of surfaces (Chapters 3, 4, and 5), while Part B deals with the chemical properties of surfaces (Chapters 6 and 7).

The motivation behind Part A of the thesis is provided by the desire to make materials for magnetic and spintronics devices. The search for such materials has been given a boost by the discovery of the giant magnetoresistance (GMR) [1, 2] and tunnel magnetoresistance (TMR) [3] effects, and the subsequent commercialization of GMR and TMR by IBM through the application as magnetic read heads of computer hard drives (where magnetization pointing up and down corresponds to '1' and '0' bits, respectively). In such memory devices, thin films of magnetic materials can be used as (high-speed) read/write heads. Devices made of such materials can have non-volatile memory by retaining the state of the memory cell when the power is turned off, in contrast to the volatile memory in a standard dynamic random access memory (dRAM) device. In addition, such memory devices require negligible power-consumption. Generally, magnetic thin films are composed of one or more magnetic elements and show enhanced properties compared to their bulk counterparts, due to the broken (crystal) symmetry and reduced coordination at the surface. As a result of this, hybridization between the orbitals of the surface atoms is decreased, leading to band narrowing. By the Stoner criterion [4], this can lead to a greater tendency toward band splitting (to majority and minority bands) and thus an increase in magnetic moments. Moreover, these magnetic thin films generally exhibit large magnetic anisotropy energy. This makes them good candidates for applications in non-volatile magnetic memory devices. Also, in these systems, the Dzyaloshinskii-Moriyainteraction [5, 6] can sometimes give rise to exotic noncollinear magnetic structures, which can possibly be used in applications such as magnetic motors and magnetic switching devices [7, 8]. Both the magnetic anisotropy energy and the Dzyaloshinskii-Moriya interaction arise due to spin-orbit coupling, which couples the spin and lattice degrees of freedom. In this thesis,

we have theoretically predicted the stability of a new magnetic thin film system, and shown that at least one phase in this system is a good candidate to exhibit a spin spiral state. We also obtain insight into the factors governing the atomic and magnetic structure of such alloys. We give below a brief summary of each Chapter of Part A.

In Chapter 3 of this thesis, we study the electronic and magnetic properties of a thin film consisting of a monolayer of Cr on Ag(100). We find that the Cr atoms want to go to sub-surface when placed on Ag(100), in order to reduce the surface energy of the system. By comparing the energetics of different magnetic configurations, we find that the Ag/Cr/Ag(100) system wants to have antiferromagnetic ordering. The magnetic moments on Cr atoms, however, reduce by only 3% on going from the surface to the sub-surface layer. Further, we observe that new surface states appear due to Cr deposition on Ag(100). The calculated band structure is in excellent agreement with data from experimental angle-resolved photoemission spectroscopy (ARPES).

In Chapter 4, we investigate the structural and magnetic properties of surface alloys of Mn-Au on Ru(0001). By comparing the nonmagnetic and (ferro) magnetic cases, we find that magnetism increases the miscibility of the surface alloys. Three possible driving forces for the structural stability are considered: (i) band energy, (ii) magnetic energy and (iii) elastic energy. We find that the most favored atomic structures can be simply explained by invoking the effective coordination number (ECN). In the nonmagnetic case, the lowest-energy structures have high ECN, which lowers the band energy. In contrast, when magnetism is turned on, the lowest-energy structures have low ECN, since this maximizes magnetic moments and thus lowers the magnetic energy. The elastic energy is also shown to be reduced in the case of ferromagnetic surface alloys compared to their non-magnetic counterparts; this result can be explained by the magneto-volume effect, which reduces the surface stress significantly.

In Chapter 5, we extend our study to noncollinear magnetic states, and compute the magnetic ground state of two surface alloys: $FeAu_2$/Ru(0001) and $MnAu_2$/Ru(0001). For both systems, we find that the lowest-energy magnetic configuration corresponds to a

left-rotating spin spiral, in which the sense of rotation is determined by the Dzyaloshinskii-Moriya interaction. These spirals are lower in energy than the ferromagnetic configuration by 3–4 meV per nm^2. The primary reason for the stability of the spin spiral in $FeAu_2$/Ru(0001) is found to be the asymmetric exchange interaction (Dzyaloshinskii-Moriya interaction), whereas the spin spiral in $MnAu_2$/Ru(0001) is stabilized mostly by symmetric exchange interactions. We also find that $FeAu_2$/Ru(0001) has a significantly high magnetic anisotropy energy, of the order 1 meV per Fe atom. By comparing with the corresponding freestanding alloy monolayers, we find that the presence of the Ru substrate plays a significant role in determining the magnetic properties of the surface alloy systems.

The motivation for Part B of the thesis is provided by the microfabrication of semiconductor devices. With the continual drive to miniaturize electronic components, it has become necessary to have the ability to carve out fine features on semiconductor surfaces. At present, this is done using mainly a gas mixture containing a halogen as the etchant, and the desired morphology is obtained using a mask [9,10]. An alternative way of etching at small length scales could be by initially patterning the surfaces by directed self-assembly of molecules [11], which then etch the substrate in the required pattern. In this thesis we explore ways through which such patterning can be achieved easily; we also study the chemical processes that take place during etching, in order to gain an atomistic understanding. We give below a brief summary of each Chapter of Part B.

Chapter 6 deals with developing strategies to tune patterning conditions by co-adsorption of gases. Earlier work had shown that it is possible to pattern the Si(100) surface by depositing Br_2; however, the patterns of interest can only be obtained at very low pressures and in a very narrow range of the phase diagram. In this chapter we explore whether it is possible to extend the domain of stability of such patterns, and/or obtain additional patterns, by co-adsorbing Br_2 with H_2. We have obtained co-adsorption energies and the surface phase diagram as a function of the chemical potentials and partial pressures of the two gases. To do this, we have used density functional theory calculations in combination with *ab initio* atomistic thermodynamics. Over large ranges of bromine and hydrogen chemical potentials, the favored configuration is found to be either one with only Br atoms

adsorbed on the surface, at full coverage, in a (3×2) pattern, or a fully H-covered surface in a (2×1) structure. However, we also find new patterns due to co-adsorption, as well as regions of the phase diagram where there are configurations with either only Br atoms, or Br and H atoms, arranged in a two-atom-wide zigzag pattern with a (4×2) surface unit cell. Most interestingly, we find that by co-adsorbing with H_2, we bring this pattern into a region of the phase diagram corresponding to pressures that are significantly higher than those where it is observed with Br_2 alone. We also derive a simple equation explaining why the pattern moves to higher partial pressures upon co-adsorption.

In order to gain an atomistic picture of etching, in Chapter 7 we have studied the process by which atoms are removed from the Si(100) surface by Br_2, via the formation of $SiBr_2$. We have considered two different etching conditions depending on the coverage of molecular bromine (θ_{Br}): (a) conventional etching (at $\theta_{Br} \leq 1$) and (b) supersaturation etching (at $\theta_{Br} > 1$). For both these cases, etching of Si(100) is found to occur via a complex sequence of reactions, featuring one or more intermediate precursors. The barriers for these reactions are calculated either by the nudged elastic band or by the constrained minimization methods. Comparing the effective activation barriers for Br_2 with the corresponding values for Cl_2 (obtained in an earlier study) at both etch conditions, we find that Br_2 is a better etchant than Cl_2, i.e., many of the barriers are lower in the Br_2 case than in the Cl_2 case. This is primarily due to the fact that the Si-Br bond is much weaker than the Si-Cl bond. Most importantly, we observe that the effective etch barrier for supersaturation etching is lower compared to the effective barrier for conventional etching. This counter-intuitive result is explained by the large steric interactions of the Br atoms.

The main findings of the thesis are summarized in Chapter 8, and an outlook for future directions of research is presented.

The thesis also contains three appendices. In Appendix A, the relaxed configurations obtained for the Mn-Au/Ru(0001) surface alloys in Chapter 4 (41 nonmagnetic configurations and 41 magnetic configurations) are shown pictorially. In Appendix B, we discuss the applicability of the (magnetic) force theorem while calculating energies of the spin spirals of surface alloys on Ru(0001). In Appendix C (presented on a CD-ROM) we present

animated movies displaying the etching processes dealt with in Chapter 7.

Chapter 2

Methodology

2.1 Introduction

The underlying theoretical framework used in this thesis is based on density functional theory (DFT). DFT is a powerful method for the calculation of ground state properties, e.g., the total energy and various related observables of a N-electron system. Among different approaches of DFT, two techniques are used in the thesis: (i) a method that makes use of plane-wave (PW) basis sets in conjunction with pseudopotentials (PPs) (ii) the full-potential linearized augmented plane-wave (FLAPW) method. Both these approaches are discussed briefly in this chapter. The results from DFT calculations are used as inputs for two other methods: (i) the *ab initio* atomistic thermodynamics method (AIAT) and (ii) the nudged elastic band (NEB) method. Brief descriptions of both these methods are also included here. While the AIAT method combines DFT with thermodynamics so as to enable one to calculate the Gibbs free energy of a system, the NEB method is used to obtain the activation barrier for a reaction pathway connecting two stable geometries obtained using DFT.

2.2 Density Functional Theory (DFT)

The time-independent N-body Schrödinger equation is given by:

$$\Big(-\frac{\hbar^2}{2m_e}\sum_i \nabla_i^2 - \sum_I \frac{\hbar^2}{2M_I}\nabla_I^2 - \sum_{i,I}\frac{Z_I e^2}{|\mathbf{r}_i - \mathbf{R}_I|} + \frac{1}{2}\sum_{i\neq j}\frac{e^2}{|\mathbf{r}_i - \mathbf{r}_j|} + \frac{1}{2}\sum_{I\neq J}\frac{Z_I Z_J e^2}{|\mathbf{R}_I - \mathbf{R}_J|}\Big)\mathbf{\Phi}(\{\mathbf{R}\},\{\mathbf{r}\}) \tag{2.1}$$

$$= E_{\text{tot}}\ \mathbf{\Phi}(\{\mathbf{R}\},\{\mathbf{r}\}),$$

where m_e and e represent the mass and charge, respectively, of a free electron; M_I and $Z_I e$ denote the mass and the charge, respectively, of a nucleus I; $\mathbf{r}_i$ and $\mathbf{R}_I$ are the position of the i^{th} electron and I^{th} nucleus, respectively; and $\hbar$ is Planck's constant divided by 2π. The first two terms of Eq. (2.1) represent the kinetic energy of the electrons and nuclei, respectively, while the last three terms denote the Coulomb interactions between electrons and nuclei [also called the external potential, $V_{ext}(\mathbf{r})$], electrons and electrons, and nuclei and nuclei, respectively. The wavefunction $\mathbf{\Phi}(\{\mathbf{R}\},\{\mathbf{r}\})$ is given by:

$$\mathbf{\Phi}(\{\mathbf{R}\},\{\mathbf{r}\}) = \mathbf{\Theta}(\{\mathbf{R}\})\ \mathbf{\Psi}(\mathbf{r}_1,\mathbf{r}_2,\ldots,\mathbf{r}_N), \tag{2.2}$$

here, $\mathbf{\Theta}$ and $\mathbf{\Psi}$ represent the nuclear wavefunction and an (antisymmetric) N-electron wavefunction, respectively. E_{tot} is the energy eigenvalue of the Hamiltonian given in Eq. (2.1).

Being much lighter than the nuclei, the electrons move much faster than the nuclei. Due to this, the motion of the nuclei [the second term on the left-hand-side of Eq. (2.1)] can be ignored when calculating the ground state electronic structures. This is called the Born-Oppenheimer (adiabatic) approximation [12]. Applying this approximation, the electronic wavefunction can be solved for fixed positions of the nuclei. Even with this approximation, solving Eq. (2.1) becomes a computationally daunting task and "exact" numerical solutions are only feasible for small systems (small N values).

To overcome this problem, the density functional theory (DFT) method maps the N-body interacting problem onto an effective non-interacting single-body problem. In doing so, DFT reduces the complexity of the problem drastically, as the basic variable is no longer $\mathbf{\Psi}$ with $3N$ variables [see Eq. (2.2)], but the corresponding electron density $n(\mathbf{r})$ with only

three variables [see Eq. (2.5) below]. The theoretical breakthrough of the DFT formalism is based on the Hohenberg-Kohn theorems and the subsequent Kohn-Sham formalism.

2.2.1 Hohenberg-Kohn theorems

Hohenberg and Kohn [13] were the first to formulate DFT as an "exact theory of many-body systems". They showed that the density $n(\mathbf{r})$ contains the same information about the N-body system as does the wavefunction $\mathbf{\Psi}$, where $\mathbf{\Psi}$ is the ground state wavefunction of the system. The relationship between the density and the ground state properties of the system is given in terms of two theorems [14]:

- Theorem 1 – "For any system of interacting particles in an external potential $V_{ext}(\mathbf{r})$, the potential $V_{ext}(\mathbf{r})$ is determined uniquely, except for a constant, by the ground state particle density $n_0(\mathbf{r})$."

- Theorem 2 – "*A universal functional* for the energy $E[n]$ in terms of the density $n(\mathbf{r})$ can be defined, valid for any external potential $V_{ext}(\mathbf{r})$. For any particular $V_{ext}(\mathbf{r})$, the exact ground state energy of the system is the global minimum value of this functional, and the density $n(\mathbf{r})$ that minimizes the functional is the exact ground state density $n_0(\mathbf{r})$."

Mathematically, this means that for every potential $V_{ext}(\mathbf{r})$ there exists a functional $E[n]$:

$$E[n] \geq E[n]_{n=n_0} \text{ and } E[n]_{n=n_0} = \left(F[n] + \int \mathrm{d}\mathbf{r} V_{ext}(\mathbf{r}) n(\mathbf{r}) \right)_{n=n_0}, \tag{2.3}$$

where $F[n]$ is the universal functional of the ground state density n_0. The remarkable consequence of these theorems is that in principle, it is possible to obtain all the ground state observables without determining $\mathbf{\Psi}$ explicitly.

2.2.2 Kohn-Sham equations

Hohenberg and Kohn provided an existence proof of DFT, note however that the energy functional $E[n]$ is unknown to us. In practice, applications of DFT became feasible with

the formulation of the Kohn-Sham (KS) equations [15]. The KS equations map an interacting many-body system onto a system with non-interacting electrons which experience an effective potential V_{eff} due to all the other electrons. This is done by introducing an auxiliary wavefunction Ψ^{KS}, which satisfies the following equation:

$$\Psi^{\mathrm{KS}}(\mathbf{r}_1, \mathbf{r}_2, \ldots, \mathbf{r}_N) = \frac{1}{\sqrt{N!}} \det\left(\psi_\nu(\mathbf{r}_{\nu'})\right)_{\nu,\nu'} \quad \text{with} \quad \int \mathrm{d}\mathbf{r}\ \psi_{\nu'}(\mathbf{r})^\dagger \psi_\nu(\mathbf{r}) = \delta_{\nu,\nu'}, \tag{2.4}$$

where ν and ν' are the band indices. $\{\psi_\nu(\mathbf{r})\}$ is the set of auxiliary single-electron wavefunctions and $\delta_{\nu,\nu'}$ is Kronecker delta. The electronic charge density $n(\mathbf{r})$ can be defined as:

$$n(\mathbf{r}) = \sum_{\nu(occ)} \psi_\nu(\mathbf{r})^\dagger \psi_\nu(\mathbf{r}), \tag{2.5}$$

where the sum is over all occupied states.

Now if we denote the energy contributions coming from the last term on the left-hand-side of Eq. (2.1) as E_{Ewald}, and the contributions coming from the rest of the terms as E, such that $E_{\mathrm{tot}} = E + E_{\mathrm{Ewald}}$, then from the Hohenberg-Kohn theorem one can write:

$$F[n] = E_{kin}[n] + E_H[n] + E_{\widetilde{xc}}[n], \tag{2.6}$$

$$\text{thus,}\ \ E[n] = E_{kin}[n] + E_{ext}[n] + E_H[n] + E_{\widetilde{xc}}[n], \tag{2.7}$$

where E_{kin} is the kinetic energy of the interacting system, such that $E_{kin} = T_s[n] = \sum_{\mathrm{i}} \left\langle \mathbf{\Psi} \right| -\frac{\hbar^2}{2m_e}\nabla_i^2 \left| \mathbf{\Psi} \right\rangle$. E_{ext}, E_H and $E_{\widetilde{xc}}$ are the energies corresponding to the external potential (V_{ext}), the Hartree potential (V_H) and the exchange correlation potential (V_{xc}), respectively. V_H and V_{xc} are given by:

$$V_H(\mathbf{r}) = e^2 \int \frac{n(\mathbf{r}')}{|\mathbf{r} - \mathbf{r}'|}\ \mathrm{d}\mathbf{r}', \tag{2.8}$$

and

$$V_{xc}(\mathbf{r}) = \frac{\delta E_{\widetilde{xc}}[n(\mathbf{r})]}{\delta n(\mathbf{r})}, \tag{2.9}$$

where $E_{\widetilde{xc}}$ is the energy due to the exchange-correlation interaction. Eq. (2.7) can be rewritten as:

$$E[n] = T_s[n] + \int \mathrm{d}\mathbf{r} V_{ext}(\mathbf{r}) n(\mathbf{r}) + \frac{e^2}{2} \int \mathrm{d}\mathbf{r}\ \mathrm{d}\mathbf{r}'\ \frac{n(\mathbf{r}) n(\mathbf{r}')}{|\mathbf{r} - \mathbf{r}'|} + E_{\widetilde{xc}}[n]. \tag{2.10}$$

Within the KS approach the first term on the right hand side of Eq. (2.10) (i.e., the kinetic energy) can be written as:

$$E_{kin}[n] = T_s[n] \simeq T_0[n] + E^{(1)}_{kin}[n], \tag{2.11}$$

where $T_0[n] = \sum_{\mathrm{i}} \left\langle \Psi_{\mathrm{KS}} | - \frac{\hbar^2}{2m_e} \nabla_i^2 | \Psi_{\mathrm{KS}} \right\rangle$ is the kinetic energy of the non-interacting system and $E^{(1)}_{kin}[n]$ is a correction term and can be approximated by a simple expression. Then $E_{\widetilde{xc}}[n]$ can be written as:

$$E_{\widetilde{xc}}[n] = E_{xc}[n] - E^{(1)}_{kin}[n] = E_{xc}[n] - \left(E_{kin}[n] - T_0[n]\right). \tag{2.12}$$

Thus, Eq. (2.10) can be rewritten as:

$$E[n] = T_0[n] + \int \mathrm{d}\mathbf{r}\ V_{ext}(\mathbf{r}) n(\mathbf{r}) + \frac{e^2}{2} \int \mathrm{d}\mathbf{r}\ \mathrm{d}\mathbf{r}'\ \frac{n(\mathbf{r}) n(\mathbf{r}')}{|\mathbf{r} - \mathbf{r}'|} + E_{xc}[n, \mathbf{m}]. \tag{2.13}$$

The KS equations can now be written as:

$$\left[\frac{-\hbar^2}{2m_e} \nabla_i^2 + V_{eff}(\mathbf{r})\right] \psi_\nu(\mathbf{r}) = \epsilon_\nu \psi_\nu(\mathbf{r}), \tag{2.14}$$

where ϵ_ν are the single-electron eigenvalues of the KS equations and $V_{eff}(\mathbf{r}) = V_{ext}(\mathbf{r}) + V_H(\mathbf{r}) + V_{xc}(\mathbf{r})$. The ground state energy of the system of N-electrons with ions at positions R_I can be obtained by solving Eq. (2.14). However, the exact form of the functional $E_{xc}[n]$

is unknown. Below in Section (2.2.5), we describe ways to approximate this functional.

2.2.3 Spin-polarized Kohn-Sham equations

The formalism described above does not include effects arising from the magnetic interactions in a solid. In order to do so, it is necessary to include the magnetization density $\mathbf{m}(\mathbf{r})$ along with the electron density $n(\mathbf{r})$ [16]. Then the generalized form of the KS equations becomes:

$$\left[\frac{-\hbar^2}{2m_e}\nabla_i^2 + V_{eff}(\mathbf{r}) + \boldsymbol{\sigma}\cdot\mathbf{B}_{eff}(\mathbf{r})\right]\psi_\nu(\mathbf{r}) = \epsilon_\nu\psi_\nu(\mathbf{r}), \tag{2.15}$$

where $\boldsymbol{\sigma} = (\sigma_x, \sigma_y, \sigma_z)$ are the Pauli spin-matrices. V_{eff} is the sum of V_{ext}, V_H, and V_{xc}, while $\mathbf{B}_{eff}$ is the effective magnetic field consisting of two terms:

$$\mathbf{B}_{eff}(\mathbf{r}) = \mathbf{B}_{xc}(\mathbf{r}) + \mathbf{B}_{ext}(\mathbf{r}), \quad \text{where } \mathbf{B}_{xc}(\mathbf{r}) = \frac{\delta E_{xc}[n(\mathbf{r}), \mathbf{m}(\mathbf{r})]}{\delta \mathbf{m}(\mathbf{r})}, \tag{2.16}$$

and $\mathbf{B}_{ext}(\mathbf{r})$ is the external magnetic field (if present). Similar to the charge density $n(\mathbf{r})$ [see Eq. (2.5)], a magnetization density $\mathbf{m}(\mathbf{r})$ can be defined in terms of single-particle Kohn-Sham wavefunctions:

$$\mathbf{m}(\mathbf{r}) = \sum_{\nu(occ)} \psi_\nu(\mathbf{r})^\dagger \boldsymbol{\sigma} \psi_\nu(\mathbf{r}). \tag{2.17}$$

The total electronic energy in this case can be written as

$$E[n, \mathbf{m}] = 2T_0[n] + \int \mathrm{d}\mathbf{r}\; V_{ext}(\mathbf{r})n(\mathbf{r}) + \frac{e^2}{2}\int \mathrm{d}\mathbf{r}\;\mathrm{d}\mathbf{r}'\;\frac{n(\mathbf{r})n(\mathbf{r}')}{|\mathbf{r}-\mathbf{r}'|} + E_{xc}[n, \mathbf{m}]. \tag{2.18}$$

For collinear magnetic cases, e.g., for ferromagnetic and antiferromagnetic systems, Eq. (2.15) can be represented as a diagonal Hamiltonian when ψ_ν is expressed as two-component spinors, one each for spin-up and spin-down electrons:

$$\psi_\nu(\mathbf{r}) = \begin{pmatrix} \psi_\nu^{(1)}(\mathbf{r}) \\ \psi_\nu^{(2)}(\mathbf{r}) \end{pmatrix}. \tag{2.19}$$

Such a representation leads to two independent KS equations, as the spin-up and spin-down problems can be decoupled, since the Hamiltonian becomes diagonal in spin space. In this case, the total energy and all the other related observables become functionals of both the electron density $n(\mathbf{r})$ and the magnitude of the magnetization density $|\mathbf{m}(\mathbf{r})|$, or equivalently in terms of spin-up $[n_\uparrow(\mathbf{r})]$ and spin-down $[n_\downarrow(\mathbf{r})]$ densities as:

$$n(\mathbf{r}) = n_\uparrow(\mathbf{r}) + n_\downarrow(\mathbf{r}) \quad \text{and} \quad |\mathbf{m}(\mathbf{r})| = n_\uparrow(\mathbf{r}) - n_\downarrow(\mathbf{r}). \tag{2.20}$$

Another equivalent way to include magnetic interactions into the DFT formalism is via the density matrix approach. The advantage of using this approach is that both collinear and noncollinear magnetism can be taken into account. Note that the spin-up and spin-down problems cannot be solved separately in the case of noncollinear magnetism. The energy functional of a general magnetic system can then be expressed in terms of the density matrix $\boldsymbol{\rho}$,

$$\boldsymbol{\rho} = \frac{1}{2}\left(n\mathbf{I}_2 + \boldsymbol{\sigma}\cdot\mathbf{m}\right) = \frac{1}{2}\begin{pmatrix} n+m_z & m_x - im_y \\ m_x - im_y & n - m_z, \end{pmatrix} \tag{2.21}$$

or equivalently,

$$\rho_{\alpha\beta}(\mathbf{r}) = \frac{1}{2}\left(n(\mathbf{r})\delta_{\alpha\beta} + \mathbf{m}\cdot\boldsymbol{\sigma}_{\alpha\beta}\right) = \sum_{\nu(occ)} \psi_\nu^{(\alpha)*}\,\psi_\nu^{(\beta)}, \quad \text{where} \quad \alpha,\beta \in 1,2, \tag{2.22}$$

and $\mathbf{I}_2$ is the 2×2 identity matrix. In this case the effective potential $\mathbf{V}$ can also be written as:

$$\mathbf{V} = V_{eff}\mathbf{I}_2 + \mu_B\boldsymbol{\sigma}\cdot\mathbf{B}_{eff}. \tag{2.23}$$

In the case of a collinear calculation, the direction of $\mathbf{B}_{eff}$ can be chosen to be along the

z-axis for numerical simplicity.

2.2.4 Relativistic Kohn-Sham equation

To take into account the relativistic effects of the electrons it is necessary to solve the Dirac equation instead of the Schrödinger equation. Staring from the Dirac equation, a relativistic density functional theory is developed [17]. The relativistic Kohn-Sham equation is given by:

$$\left(c\alpha \cdot \mathbf{p} + \beta m_e c^2 + V_{eff}(\mathbf{r}) + \mathbf{B}_{xc} \cdot \boldsymbol{\sigma}\right) \psi_\nu(\mathbf{r}) = E_\nu \psi_\nu(\mathbf{r}), \tag{2.24}$$

where c is the velocity of light, $\mathbf{p}$ is the momentum operator, $E_\nu = \epsilon_\nu + m_e c^2$ is the sum of the eigenvalue and the rest mass energy, and α and β are 4×4 matrices given by:

$$\alpha = \begin{pmatrix} 0 & \boldsymbol{\sigma} \\ \boldsymbol{\sigma} & 0 \end{pmatrix} \tag{2.25}$$

and

$$\beta = \begin{pmatrix} \mathbf{I}_2 & 0 \\ 0 & -\mathbf{I}_2 \end{pmatrix}. \tag{2.26}$$

ψ_ν is the 4-component vector:

$$\psi_\nu(\mathbf{r}) = \begin{pmatrix} \varphi_\nu^\uparrow(\mathbf{r}) \\ \varphi_\nu^\downarrow(\mathbf{r}) \\ \chi_\nu^\uparrow(\mathbf{r}) \\ \chi_\nu^\downarrow(\mathbf{r}) \end{pmatrix}. \tag{2.27}$$

where $\uparrow$ and $\downarrow$ denote the spin-up and spin-down electrons, respectively, and φ_ν and χ_ν are large and small components of the wavefuntion, respectively.

The Hamiltonian in Eq. (2.24) can be rewritten as the sum of three terms: the Hamiltonian of the spin-polarized KS equations H_{SP}, the contributions coming from spin-orbit

interaction H_{SO} and the contribution coming from the relativistic terms other than the spin-orbit (mass-velocity, Darwin, and non-hermitian) H_1. In the scalar relativistic approximation H_{SO} is neglected. This is particularly useful in the case of the collinear magnetic structures with spin-quantization axis parallel to the z-axis, since the scalar relativistic Hamiltonian $H_{SP} + H_1$ becomes block-diagonal.

2.2.5 Exchange-correlation functionals

The first approximation that goes into DFT is the approximation for the exchange-correlation (XC) functional. The simplest one is the local density approximation (LDA), where the XC functional is given by [18]:

$$E_{xc}^{\mathrm{LDA}}[n(\mathbf{r})] = \int n(\mathbf{r})\ f_{xc}\left(n(\mathbf{r})\right)\ \mathrm{d}\mathbf{r}, \tag{2.28}$$

where $f_{xc}(n(\mathbf{r}))$ is the exchange-correlation energy density of a homogeneous electron gas. It is important to note that f_{xc} is not a functional, but a function of $n(\mathbf{r})$. In this case the function f_{xc} depends locally upon the density. For magnetic systems, the LDA approach has been modified by taking into account the magnetization density $\mathbf{m}(\mathbf{r})$ along with the electron density $n(\mathbf{r})$. This modified approach is called the local spin density approximation (LSDA). The LSDA XC functional can be written as:

$$E_{xc}^{\mathrm{LSDA}}[n(\mathbf{r}), \mathbf{m}(\mathbf{r})] = \int n(\mathbf{r})\ f_{xc}\left(n(\mathbf{r}), |\mathbf{m}(\mathbf{r})|\right)\ \mathrm{d}\mathbf{r}, \tag{2.29}$$

As the function f_{xc} depends locally upon the densities at a point $\mathbf{r}$, it depends only on the magnitude of the magnetization density.

In order to deal with systems with (rapidly) spatially varying densities, improvements to the LDA have been suggested, which are called generalized gradient approximations (GGAs) [19, 20]. For collinear magnetization densities, this approximation has a form given by:

$$E_{xc}^{\mathrm{GGA}}[n(\mathbf{r}), \mathbf{m}(\mathbf{r})] = \int n(\mathbf{r}) f_{xc}\left(n(\mathbf{r}), |\nabla n(\mathbf{r})|, |\mathbf{m}(\mathbf{r})|, |\nabla \mathbf{m}(\mathbf{r})|\right) \mathrm{d}\mathbf{r}. \tag{2.30}$$

Note that putting $\mathbf{m}(\mathbf{r}) = 0$ in Eq. (2.30) one can obtain the E_{xc}^{GGA} for non-magnetic system.

These approximations have their own advantages and limitations. For instance, LDA and LSDA are known to overbind and hence results in smaller lattice constants for bulk materials, whereas GGA usually corrects this effect. However, the GGA is known to underbind which results in larger lattice constants. Some properties, such as magnetic moments, are often better estimated using the GGA.

2.2.6 Calculating the total energy

The total electronic energy is given by the functional given in Eq. (2.18). In terms of eigenvalues of the KS equations, this equation can be rewritten as:

$$\begin{aligned} E[n,\mathbf{m}] &= T_0[n,\mathbf{m}] + \int \mathrm{d}\mathbf{r}\ V_{ext}(\mathbf{r})n(\mathbf{r}) + \frac{e^2}{2}\int \mathrm{d}\mathbf{r}\ \mathrm{d}\mathbf{r}'\ \frac{n(\mathbf{r})n(\mathbf{r}')}{|\mathbf{r}-\mathbf{r}'|} + E_{xc}[n,\mathbf{m}], \\ &= \sum_{\nu=1}^{N}\epsilon_\nu - E_{dc}, \end{aligned} \tag{2.31}$$

where E_{dc} is called the double-counting term.

Finally the total energy E_{tot} [see Eq. (2.1)], which is used to extract the structural, magnetic, and chemical properties of a material, can be calculated as $E_{\mathrm{tot}} = E + E_{ewald}$, where E_{ewald} is the energy due to the Coulomb interaction between atomic nuclei.

2.2.7 Basis sets

Solving the KS equations become feasible in a periodic solid via expansion of the KS wavefunctions $\psi_{\mathbf{k},\nu}(\mathbf{r})$ in terms of a complete set of known functions:

$$\psi_{\mathbf{k},\nu}(\mathbf{r}) = \sum_i c^i_{\mathbf{k},\nu}\ \phi_i(\mathbf{k},\mathbf{r}), \tag{2.32}$$

where $\phi_i(\mathbf{k},\mathbf{r})$ are called the basis functions. $c^i_{\mathbf{k},\nu}$ are the expansion coefficients of the wavefunction and i represents the number of basis functions taken into account.

Such an expansion translates the eigenvalue problem of Eq. (2.15) to an algebraic eigenvalue problem of dimension i:

$$(H(\mathbf{k}) - \epsilon_{\mathbf{k}\nu}\ S(\mathbf{k}))\, c_{\mathbf{k},\nu} = 0 \quad \forall\ \mathbf{k} \in \mathrm{BZ}, \tag{2.33}$$

where BZ refers to the Brillouin zone. $H(\mathbf{k})$ and $S(\mathbf{k})$ are the Hamiltonian and overlap matrices, respectively, and they can be written as:

$$H(\mathbf{k}) = H^{n,n'}(\mathbf{k}) = \int_{\Omega} \phi_n^{\dagger}(\mathbf{k},\mathbf{r})\ H\ \phi_{n'}(\mathbf{k},\mathbf{r})\ \mathrm{d}\mathbf{r}, \tag{2.34}$$

and

$$S(\mathbf{k}) = S^{n,n'}(\mathbf{k}) = \int_{\Omega} \phi_n^{\dagger}(\mathbf{k},\mathbf{r})\ \phi_{n'}(\mathbf{k},\mathbf{r})\ \mathrm{d}\mathbf{r}, \tag{2.35}$$

where Ω is the volume of the unit cell. Both $H(\mathbf{k})$ and $S(\mathbf{k})$ are either Hermitian or real symmetric matrices, depending on the point symmetry of the crystal structure.

In this thesis, we have used two types of basis sets (1) plane-wave basis sets (in conjunction with pseudopotentials) and (2) linearized augmented plane-waves (LAPW) (in the full-potential linearized augmented plane-waves method). Below we briefly discuss these basis sets.

A. Plane-wave basis set

The wavefunction given in Eq. (2.32) can be expanded in terms of plane-waves such that:

$$\psi_{\mathbf{k},\nu} = \sum_{|\mathbf{k}+\mathbf{G}| \le K_{max}} c_{\mathbf{k}+\mathbf{G},\nu} \exp[i(\mathbf{k}+\mathbf{G})\cdot\mathbf{r}], \tag{2.36}$$

where $\mathbf{G}$ represents the reciprocal lattice vectors, $\mathbf{k}$ is a wavevector in the first Brillouin zone, and ν is the band index. For a periodic lattice the basis in Eq. (2.36) forms a finite and discrete basis set (restricted by the value of K_{max}) and such truncation is possible due to the fact that the Fourier component of the potential decreases fairly rapidly. The value of K_{max} can be chosen by specifying a maximum possible value of the kinetic energy E_{cut}

at each **k**, such that

$$\frac{\hbar^2}{2m_e}|\mathbf{k}+\mathbf{G}|^2 < E_{cut}, \tag{2.37}$$

This is similar to restricting oneself to only a certain number of **G** vectors at each **k** point. The error in energy $E_{\rm tot}$ arising from the truncation can be reduced by increasing the value of E_{cut}. In a simple estimation, the number of plane-waves (N_{pw}) related to E_{cut} at the zone-centre is given by:

$$N_{pw} = \frac{4\pi}{3\Omega_{\rm BZ}}(\sqrt{E_{cut}})^3, \tag{2.38}$$

where $\Omega_{\rm BZ}$ is the volume of the first Brillouin zone.

B. LAPW basis set

Here we describe the LAPW basis set. In the LAPW method, real space is divided into two regions: (i) spheres that are centered around each atom, called the muffin-tins (MTs) and (ii) the remaining regions in space, called the interstitial region [see Fig. 2.1]. These MTs are chosen such that two MT spheres do not overlap.

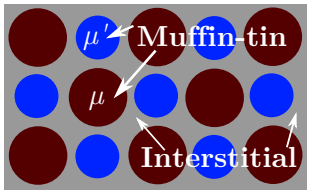

Figure 2.1: *Schematic diagram showing division of space in the LAPW method. Maroon and blue spheres represent the muffin-tins (MTs) of two types of atoms. The radii of the MT spheres for the two atoms are denoted as μ and μ', respectively. The gray region is called the interstitial region.*

For conceptual simplicity, one can work with a local coordinate frame for each MT sphere. Let us consider the μ^{th} MT sphere located at $\mathbf{R}^{(\mu)}$. An arbitrary vector **r** can be expressed in the local coordinate frame of the μ^{th} MT sphere (in spherical polar coordinates) by $\mathbf{r}-\mathbf{R}^{(\mu)} = r^{(\mu)}(sin\theta^{(\mu)}cos\varphi^{(\mu)}\hat{\mathbf{e}}_\mathbf{x} + cos\theta^{(\mu)}sin\varphi^{(\mu)}\hat{\mathbf{e}}_\mathbf{y} + cos\theta^{(\mu)}\hat{\mathbf{e}}_\mathbf{z})$. The LAPW basis function in the local frame of the MT sphere can be written as:

$$\phi_{\mathbf{G}}(\mathbf{k},\mathbf{r}) = \begin{cases} \exp[i(\mathbf{k}+\mathbf{G})\cdot\mathbf{r}] & \text{interstitial region} \\ \sum_{l,m} \mathrm{Y}_{l,m}(\theta^{(\mu)},\varphi^{(\mu)}) \left(A_{l,m}^{(\mu)}(\mathbf{k})\ u_l^{(\mu)}(r^{(\mu)}) + B_{l,m}^{(\mu)}(\mathbf{k})\ \dot{u}_l^{(\mu)}(r^{(\mu)}) \right) & \text{muffin-tin sphere } \mu, \end{cases} \tag{2.39}$$

where $\mathrm{Y}_{l,m}$ are the spherical harmonics. l and m are the orbital angular momentum quantum number and magnetic quantum number, respectively. u_l's are the regular solutions of the radial Schödinger equation:

$$\left(\frac{-\hbar^2}{2m_e}\frac{\partial^2}{\partial r^2} + \frac{-\hbar^2}{2m_e}\frac{l(l+1)}{r^2} + V(r) - \epsilon_l \right) r u_l(r) = 0. \tag{2.40}$$

$\dot{u}_l$ are the radial derivatives of u_l. ϵ_l are called the energy parameters. They are determined during the self-consistency cycle from the average band energies. It is generally sufficient to describe one value of $\epsilon_l^{(\mu)}$ for each pair of l and μ values. The coefficients $A_{l,m}^{(\mu)}$ and $B_{l,m}^{(\mu)}$ are determined from the continuity conditions of both u_l and $\dot{u}_l$ at the boundary of the μ^{th} MT sphere. Note that these basis truncations are not orthogonal and care has to be taken during diagonalization of the Hamiltonian. These basis sets are used in periodic crystals.

C. LAPW basis in slab geometry

For surfaces, one has to use a supercell so as to ensure negligible interactions between the two periodic images along one of the three axes. In order to describe a surface thus requires a very large supercell and a large number of basis functions. To avoid such scenarios an extension of the LAPW basis set is introduced in Ref. [21]. In such cases, the surface is simulated by a film/slab which is periodic and infinite along two directions, but finite along the third direction. This is done by introducing another region called the vacuum region, which is extended to infinity along the direction normal to the surface (see Fig. 2.2). The basis functions in those regions are constructed from a solution of the Schrödinger equation with aymptotically decaying potential.

The problem is solved by noting that the Bloch theorem holds only in two-dimensions. Let us consider a slab that is periodic in the x and y directions and truncated along the z direction (see Fig. 2.2). The unit cell (shown by blue) for this slab is extended to infinity

in the z direction due to the finite size of the slab in that direction. We can represent the in-plane components of a vector (along x and y) as "$\parallel$" and the out-of-plane component of a vector (along z) as "$\perp$". The interstitial region extends from $-D/2$ to $D/2$ along the z direction. For greater variational freedom, $k_\perp$ is defined not in terms of D, but in terms of $\widetilde{D}$, such that $k_\perp = \dfrac{2\pi M}{\widetilde{D}}$ with $\widetilde{D} > D$.

In this case the modified LAPW basis set can be written as:

$$\phi_{\mathbf{G}}(\mathbf{k},\mathbf{r}) = \begin{cases} \exp[i(\mathbf{k}_\parallel + \mathbf{G}_\parallel)\mathbf{r}_\parallel]\,\exp[ik_\perp z] & \text{interstitial region} \\ \displaystyle\sum_{l,m} \mathrm{Y}_{l,m}(\theta^{(\mu)},\varphi^{(\mu)})\left(A^{(\mu)}_{l,m}(\mathbf{k})\; u^{(\mu)}_l(r^{(\mu)}) + B^{(\mu)}_{l,m}(\mathbf{k})\; \dot{u}^{(\mu)}_l(r^{(\mu)})\right) & \text{muffin-tin sphere } \mu \\ \exp[i(\mathbf{k}_\parallel + \mathbf{G}_\parallel)\mathbf{r}_\parallel]\left(A^{(\eta)}_{vac}(\mathbf{k}_\parallel)\; u^{(\eta)}_{vac}(r_z) + B^{(\eta)}_{vac}(\mathbf{k}_\parallel)\; \dot{u}^{(\eta)}_{vac}(r_z)\right) & \text{vacuum region } \eta, \end{cases} \tag{2.41}$$

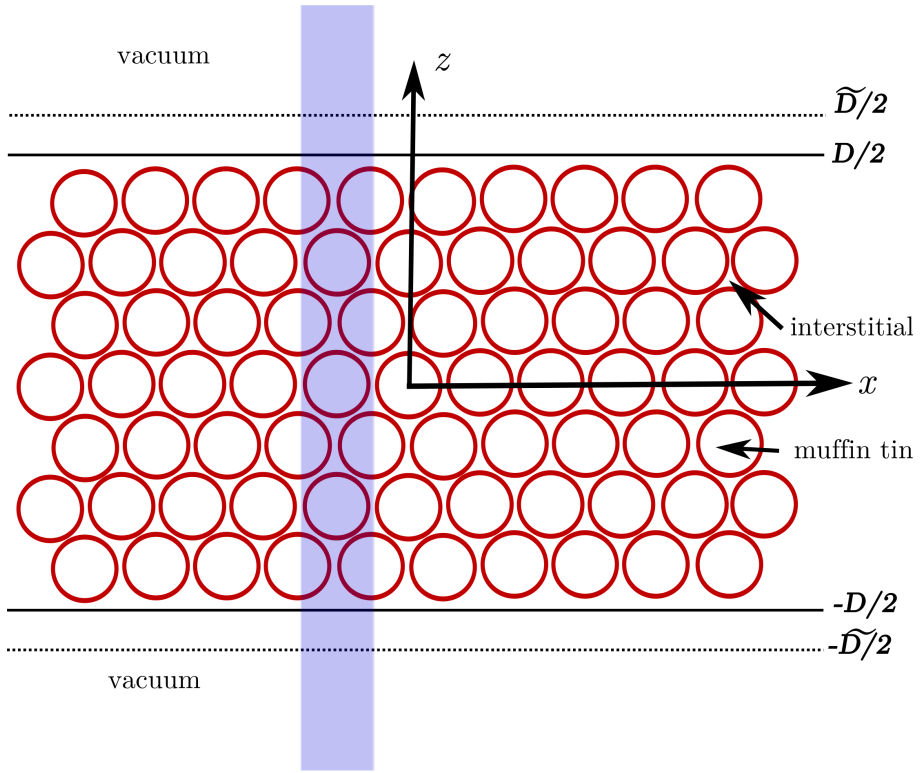

Figure 2.2: *Schematic diagram showing division of space in LAPW slab calculation. The slab is periodic in the x and y directions and truncated in the z direction. The unit cell, shown by blue, is periodic along x and y directions, whereas in the z-direction, it is extended to infinity. The interstitial region extends from $-D/2$ to $D/2$. For greater variational freedom, $\widetilde{D}$ is choosen greater than D such that $k_\perp = \dfrac{2\pi M}{\widetilde{D}}$, where M is an integer.*

2.2.8 Plane-wave and pseudopotentials method

The plane-wave basis functions are conceptually simple as well as have numerous numerical advantages. As the basis does not depend on the atomic positions (unlike localized basis sets), it is possible to calculate the charge density for different systems with the same degree of accuracy. In addition, being orthogonal and diagonal in momentum space, the plane-waves make the integration of the Poisson equation for the computation of the Hartree potential very simple. However, the fast oscillations of the valence wavefunctions near the nuclei requires a huge number of basis functions to accurately describe the properties of the system. The energies corresponding to the core electrons (i.e., the electrons residing very close to the nuclei) differ by orders of magnitude from the energies of the valence electrons. Being very tightly bound to the nuclei, the core electrons do not change their energy significantly while going from atoms to solid. However, such environmental changes are enough to change the energies of the valence electrons, significantly.

Thus one can simplify Eq. (2.15) by eliminating the degrees of freedom associated with the core electrons. This leads to a mapping of an all-electron frozen-core problem to an equivalent problem involving valence electrons only. Such a mapping enables us to replace the "true" nuclear potential with a "pseudopotential" such that (i) the lowest eigenvalues of $T+V_{ps}$ are equal to the all-electron eigenvalues of the valence electrons, where T and V_{ps} are the kinetic energy and the pseudopotential, respectively, (ii) the "pseudo" wavefunctions ϕ_l are nodeless and both ϕ_l and $\dfrac{\partial \phi_l}{\partial l}$ are differentiable, (iii) ϕ_l is identical with the all-electron wavefunction sufficiently far away from the nucleus, i.e., beyond a chosen core radius r_c. The pseudopotential which satisfies these conditions consists of two terms: an attractive Coulomb term and a short ranged repulsive term which invokes the orthogonality condition of the pseudo wavefunctions and the core wavefunctions.

Initially the construction of the pseudopotentials relied on the fact that the total integrated "pseudo charge-density" calculated from ϕ_l, and the corresponding all-electron charge density are equal inside the core radius. Such psedopotentials are called *norm-conserving pseupotentials*. Though such pseudopotentials are transferable (independent of the chemical environment of the atoms), for some elements a very large plane-wave cutoff

was required due to the highly peaked pseudo wavefunctions. In order to reduce the size of the basis set and to have smoother wavefunctions, D. Vanderbilt [22] proposed an alternative way to construct a pseudopotential and this is called the *ultrasoft psedopotential* formalism. By this approach one can obtain a smoother wavefunction and thus a smaller size of basis set, at the cost of producing an "augmented charge" to have an overall norm-conservation to take into account the valence charge density in the core region accurately.

There are several advantages of using pseudopotentials. When using a plane-wave basis set the size of the basis set reduces drastically, which leads to a reduction of the size of the Hamiltonian needed to be diagonalized to solve the KS equations. Moreover, the Coulomb singularity at the origin can be avoided by the construction of the psedupotential. However, one must take into account the non-linear core corrections [23] for elements where the core and the valence wavefunctions overlap considerably.

In this thesis we have performed calculations using this method in all the chapters except for Chapter 5. We have used the Quantum ESPRESSO package for all these calculations [24].

2.2.9 Full-potential linearized augmented plane-wave (FLAPW) method

Here, we describe an all-electron method for solving the KS equations called the full-potential linearized augmented plane-wave (FLAPW) method. The wavefunctions used in this method can be expanded in terms of a localized basis set which is dependent on the positions of the atoms (described in Section 2.2.7). This method is an improvement on the augmented plane-wave (APW) and linearized augmented plane-wave (LAPW) methods. In the APW and LAPW methods, the potential is approximated to be spherically symmetric inside the MT spheres and (in many implementations) the interstitial potential is set as a constant; such constructions of the potential are called shape-approximations. In the FLAPW method, the LAPW basis set is used by taking into account the full-potential and charge density, i.e., without considering any shape-approximations in the interstitial region and the muffin-tin regions.

Such a generalization is achieved by expanding the potential in similar fashion as the wavefunction:

$$V(\mathbf{r}) = \begin{cases} \sum_{\mathbf{G}} V_I^{\mathbf{G}} e^{i\mathbf{G}\cdot\mathbf{r}} & \text{interstitial region} \\ \sum_{l,m} V_{MT}^{(l,m)} \mathrm{Y}_{l,m}(\hat{\mathbf{r}}) & \text{muffin-tin sphere } \mu, \end{cases} \tag{2.42}$$

where $V_I^{\mathbf{G}} e^{i\mathbf{G}\cdot\mathbf{r}}$ is the warped interstitial potential. The potential $V_{MT}^{(l,m)} \mathrm{Y}_{l,m}(\hat{\mathbf{r}})$ takes care of both the spherical and non-spherical parts of the potential. Note that the APW/LAPW methods use a constant interstitial potential and a spherical potential inside the muffin-tins. This technique could not have been possible without a technique for obtaining the Coulomb potential for a general periodic charge density without shape-approximation [25].

This method is used in Chapter 5 of this thesis to perform calculations on spin spirals. We have used the FLAPW method as implemented in the FLEUR package [26].

2.2.10 Solving the Kohn-Sham equations self-consistently

Since the Hamiltonian in the KS equations depends on the density, which is what we need to determine, one needs to solve the KS equations self-consistently to obtain the ground state density, n_0.

In Fig. 2.3, we present a flow chart for solving the KS equations given in Eq. (2.15) self-consistently. Starting from initial guess densities $n(\mathbf{r})$ and $\mathbf{m}(\mathbf{r})$ (or equivalently $\rho_{\alpha\beta}$) for a periodic system with atomic charges $\{Z_i\}$ and atomic positions $\{\mathbf{R}_i\}$, the density-dependent potentials $V_H(\mathbf{r})$ and $V_{xc}(\mathbf{r})$ are calculated. Next, the eigenstates of the KS equations are obtained. The Bloch theorem is applied for periodic systems and the Brillouin zone is sampled by a finite mesh of wavevectors $\{\mathbf{k}\}$ (see Section 2.2.11). So, for each of these $\mathbf{k}$ points the equation

$$H\psi_{\mathbf{k},\nu} = \epsilon_{\mathbf{k},\nu}\psi_{\mathbf{k},\nu} \tag{2.43}$$

is solved in the subspace restricted by lattice-periodic functions. At the end of the self-consistent cycle, the output densities are obtained by summing over all the occupied states

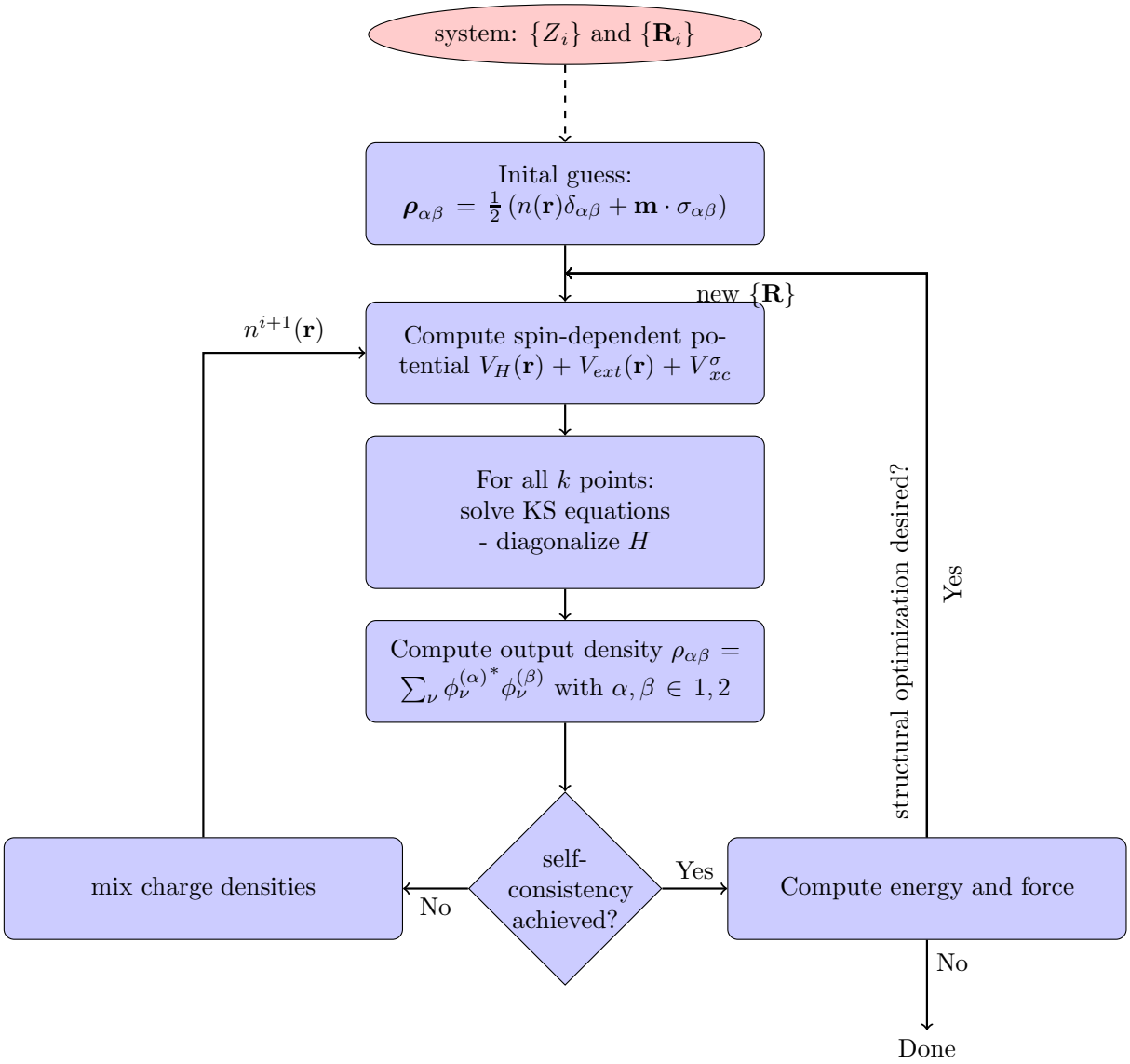

Figure 2.3: *Flow chart showing the self-consistency and geometric optimization loops for the iterative solution of the KS equations. i labels the iteration. Here σ can take values ± 1.*

at all **k** points. At this stage convergence of the total energy and/or density is checked. If convergence is not achieved, then a new charge density is calculated by mixing the newly obtained output charge density with the old input charge density. (Note that convergence is difficult to achieve if one uses only the newly obtained output densities.) Various mixing schemes can be utilized, e.g., simple linear mixing:

$$n_{in}^{i+1} = (1-\alpha)\; n_{in}^{i} + \alpha\; n_{out}^{i} \tag{2.44}$$

where α is the mixing parameter and i labels the iteration. The resultant density is again used for the calculation of the potentials and for solving the KS equations. This iterative cycle goes on until converged densities are obtained. Once self-consistency is achieved, one calculates the total energy $E_{\rm tot}$ (see Section 2.2.6).

2.2.11 k-point sampling and smearing technique

Fig. 2.3 shows that in order to obtain $\psi_{\mathbf{k},\nu}$ the KS equations are solved (iteratively) at each $\mathbf{k}$ point in the Brillouin zone. To calculate the electron density $n(\mathbf{r})$ and other related quantities, in general, integration of functions over all the $\mathbf{k}$ points in the Brillouin zone is required. Mostly these integrations are over the occupied states only. Such a quantity can be written as:

$$\frac{1}{\Omega_{\rm BZ}} \int_{\rm BZ} \sum_{\nu(occ)} g_\nu(\mathbf{k}) \quad d\mathbf{k}. \tag{2.45}$$

Numerically the integration in Eq. (2.45) is performed on a discrete mesh of $\mathbf{k}$ points in the Brillouin zone. Thus the integration gets replaced by a summation and there are several ways to perform this summation, e.g., using a Monkhorst-Pack mesh [27], special points [28,29] and the tetrahedron method [30,31]. In fact using symmetry one can further consider only those $\mathbf{k}$ points belong to the irreducible Brillouin zone (IBZ), where each $\mathbf{k}$ is assigned a weight $w(\mathbf{k})$. Thus Eq. (2.45) becomes:

$$\frac{1}{\Omega_{\rm BZ}} \sum_{\mathbf{k}\in{\rm IBZ}} \sum_{\nu(occ)} g_\nu(\mathbf{k}) w(\mathbf{k}) \quad d\mathbf{k}. \tag{2.46}$$

In order to obtain faster convergence, one can consider fewer $\mathbf{k}$ points by using the smearing technique, especially for metallic systems. DFT being a zero-temperature method, a sharp step function describes the occupation of electronic states below and above the Fermi energy. However, using a smearing technique, one can use a smoothly varying function for the occupation of states near the Fermi energy. Some of the existing techniques for doing theis are: Gaussian smearing [32], Methfessel-Paxton smearing [33] and Marzari-Vanderbilt smearing [34].

2.2.12 Calculation of the physical properties and some technical details

Once the self-consistent charge density n and total energy $E_{\rm tot}$ are calculated, one can extract various ground state properties of the system. Below we describe the procedures to calculate some such properties which are calculated in this thesis. In addition, we also discuss some of the technical issues when calculating the spin spirals.

A. Forces and the Hellmann-Feynman Theorem

In Fig. 2.3, we have also shown the flow chart for the structural optimization. Structural optimization involves the minimization of the forces acting on all or some of the atoms. In principle, these forces can be calculated using the Hellmann-Feynman theorem [35]. Thus, the force acting on the I^{th} ion can be given by:

$$
\begin{aligned}
\mathbf{F}_I &= -\frac{\partial \langle H(\mathbf{R})\rangle}{\partial \mathbf{R}_I}, \\
&= -\frac{\partial}{\partial \mathbf{R}_I}\langle \Psi|H(\mathbf{R})|\Psi\rangle\,, \\
&= -\left\langle \frac{\partial \Psi}{\partial \mathbf{R}_I}|H(\mathbf{R})|\Psi\right\rangle - \left\langle \Psi|\frac{\partial H(\mathbf{R})}{\partial \mathbf{R}_I}|\Psi\right\rangle - \left\langle \Psi|H(\mathbf{R})|\frac{\partial \Psi}{\partial \mathbf{R}_I}\right\rangle, \\
&= -\left\langle \Psi|\frac{\partial H(\mathbf{R})}{\partial \mathbf{R}_I}|\Psi\right\rangle - H\left[\left\langle \frac{\partial \Psi}{\partial \mathbf{R}_I}|\Psi\right\rangle + \left\langle \Psi|\frac{\partial \Psi}{\partial \mathbf{R}_I}\right\rangle\right] \qquad (2.47) \\
&= -\left\langle \Psi|\frac{\partial H(\mathbf{R})}{\partial \mathbf{R}_I}|\Psi\right\rangle - H\left[\frac{\partial}{\partial \mathbf{R}_I}\langle \Psi|\Psi\rangle\right] \qquad (2.48) \\
&= -\left\langle \Psi|\frac{\partial H(\mathbf{R})}{\partial \mathbf{R}_I}|\Psi\right\rangle, \quad \text{since} \quad \langle \Psi|\Psi\rangle = 1. \qquad (2.49)
\end{aligned}
$$

The Eq. (2.49) holds for orthogonal basis set such as plane-waves. In such situations, since Ψ does not depend on $\mathbf{R}$ explicitly, the derivative of Ψ with respect to $\mathbf{R}_I$ vanishes. The advantage of using the Hellmann-Feynman theorem is that to perform only a single-shot calculation (rather than multiple calculations) at a given geometry of the system.

For localized basis sets which are centered around the atoms (like the one used in FLAPW method), in addition to Hellmann-Feyman forces other terms are required to obtain forces that are tangential to the energy surface. Such additional forces are called

Pulay forces [36].

B. Calculation of Stress

To calculate the stress tensor σ, the derivative of the total energy (E) with respect to the strain (ϵ) can be calculated by making use of the Hellmann-Feynman theorem, such that [37]

$$\sigma_{\alpha,\beta} = -\frac{1}{\Omega_{\mathrm{BZ}}}\frac{\partial E_{\mathrm{tot}}}{\partial \epsilon_{\alpha,\beta}} = -\frac{1}{\Omega_{\mathrm{BZ}}}\langle\Psi|\frac{\partial H}{\partial \epsilon_{\alpha,\beta}}|\Psi\rangle, \tag{2.50}$$

where α and β are the Cartesian indices, and H and Ψ are the Hamiltonian and total wavefunction of the system, respectively. When using a plane-wave basis set, the converged value of stress generally is achieved at higher values of E_{cut} [see Eq. (2.37)] than those required for the convergence of the total energy.

C. Calculation of Magnetic Moments

The calculation of the total magnetic moment of a system is straightforward once the self-consistent charge densities $n_\uparrow$ and $n_\downarrow$ are obtained. The total magnetic moment m_{tot} is given by:

$$m_{\mathrm{tot}} = \int_{-\infty}^{E_F} (n_\uparrow(\mathbf{r}) - n_\downarrow(\mathbf{r}))\ \mathrm{d}\mathbf{r}, \tag{2.51}$$

where E_F is the Fermi energy of the system. Moreover, to obtain the contribution coming from each atom of the system one can employ different methods depending on the basis set used in a calculation. In the case of a plane-wave basis set, one can project the total wavefunction onto the atomic wavefunctions in order to obtain the atom-wise contributions to the magnetic moments. In the case of a LAPW basis set, the magnetic moment per atom can be calculated by obtaining the wavefunction inside the MT spheres of a given atom.

D. Spin-orbit Coupling

As mentioned in Section 2.2.4, one of the important consequences of a relativistic treatment is the spin-orbit coupling. The real space and the spin space get coupled via this interaction. The spin-orbit operator can be written as:

$$H_{SO} = \frac{1}{2m_e^2c^2}\boldsymbol{\sigma} \cdot (\nabla V_{eff}) \times \hat{\mathbf{p}}, \tag{2.52}$$

where $\hat{\mathbf{p}}$ is the momentum operator. Near the atomic core, V_{eff} can be approximated by its spherically symmetric average, i.e., $V_{eff}(\mathbf{r}) = V_{eff}(r)$. So, Eq. (2.52) can be written as:

$$H_{SO} \sim \frac{1}{2m_e^2c^2r}\boldsymbol{\sigma} \cdot (\frac{d}{dr}V_{eff})\mathbf{r} \times \hat{\mathbf{p}} = \frac{1}{2m_e^2c^2r}\boldsymbol{\sigma} \cdot (\frac{d}{dr}V_{eff})\hat{\mathbf{L}} = v(r)\boldsymbol{\sigma} \cdot \hat{\mathbf{L}}, \tag{2.53}$$

where $\hat{\mathbf{L}}$ is the angular momentum operator.

Note that in the FLAPW method used in this thesis, the spin-orbit interactions are only taken into account inside the MT spheres. This approximation is justified as the relativistic effects are only significant near the nucleus and diminish rapidly as one moves away from the nucleus.

E. Generalized Bloch Theorem

The Bloch theorem states that if an electron is moving in a potential which is periodic in space, then the wavefunction of the electron is given by,

$$\psi_{\mathbf{k},\nu}(\mathbf{r}) = e^{i\mathbf{k}\cdot\mathbf{r}}u_{\mathbf{k},\nu}(\mathbf{r}), \tag{2.54}$$

where $\psi_{\mathbf{k},\nu}(\mathbf{r})$ is the wavefunction of the electron with wavevector $\mathbf{k}$ and band index ν and $u_{\mathbf{k},\nu}(\mathbf{r})$ is a lattice periodic function such that $u_{\mathbf{k},\nu}(\mathbf{R}+\mathbf{r}) = \mathbf{u}_{\mathbf{k},\nu}(\mathbf{r})$, and $\mathbf{R}$ is a lattice vector. The Bloch theorem enables us to perform calculations for a periodic system within the chemical (primitive) unit cell.

When magnetization is taken into account the wavefunction $\psi_{\mathbf{k},\nu}(\mathbf{r})$ becomes a two-component spinor and the potential in that case is given by Eq. (2.23). In general, in the presence of spin-orbit coupling and dipolar interactions, the spin and spatial degrees of freedom couple, thus, the Bloch theorem no longer remains valid. However, when spin-orbit coupling is neglected, the spin space and spatial space are decoupled.

In the case of a homogeneous spin spiral [see Chapter 5], the magnetization on each atom remains the same while the relative orientation of the spins changes by a constant angle from atom to atom. This means, in the absence of spin-orbit coupling, all the atoms in a spin spiral are equivalent as they all have the same local environment. In principle, a large supercell is required to take into account such structures, although only commensurate structures can be addressed. However, the generalized Bloch theorem enables one to perform such calculations (both commensurate and incommensurate) within the chemical unit cell by defining a generalized translation which is a combination of a translation in real space and a rotation in spin-space. Below, we give a proof of the theorem [38].

Let us consider a spin spiral with anticlockwise rotation angle $\varphi = \mathbf{q}\cdot\mathbf{R}_n$, where $\mathbf{q}$ is the wavevector of the spin spiral and $\mathbf{R}_n$ is the position of the atom n. Then, the Hamiltonian $\mathcal{H}$ of the system satisfies the following relation,

$$\mathcal{H}(\mathbf{r}+\mathbf{R}_n) = \mathbf{U}(\varphi)\mathcal{H}(\mathbf{r})\mathbf{U}^{\dagger}(\varphi), \tag{2.55}$$

where $\mathbf{U}(\varphi)$ is an unitary rotation operator. Now, we can define a generalized translation $\mathcal{T}_n$ that combines a lattice translation and a spin rotation. Note that these translations ($\mathcal{T}_n$) do not belong to the usual space group but are members of the spin space group. Applying a generalized translation to $\mathcal{H}\psi$ yields

$$\begin{aligned}
\mathcal{T}_n\mathcal{H}(\mathbf{r})\psi(r) &= \mathbf{U}(-\varphi)\mathcal{H}(\mathbf{r}+\mathbf{R}_n)\mathbf{U}^{\dagger}(\varphi)\mathbf{U}(-\varphi)\psi(\mathbf{r}+\mathbf{R}_n), \\
&= \mathcal{H}(\mathbf{r})\mathbf{U}(-\varphi)\psi(\mathbf{r}+\mathbf{R}_n), \\
&= \mathcal{H}(\mathbf{r})\mathcal{T}_n\psi(\mathbf{r}).
\end{aligned} \tag{2.56}$$

So, the generalized translation commutes with the Hamiltonian. It can be shown that the generalized translation operators satisfy the following relation:

$$\mathcal{T}_n\mathcal{T}_m = \mathcal{T}_m\mathcal{T}_n = \mathcal{T}_{n+m}, \tag{2.57}$$

Thus, in a similar spirit to the proof of the Bloch theorem, it follows that the eigenstates can be chosen such that,

$$\mathcal{T}_n\psi(r) = \mathbf{U}(-\varphi)\psi(\mathbf{r}+\mathbf{R}_n) = e^{i\mathbf{k}\cdot\mathbf{R}_n}, \tag{2.58}$$

Eq. (2.58) can be equivalently written as:

$$\psi_{\mathbf{k},\nu}(\mathbf{r}) = e^{(i\sigma_z\mathbf{q}\cdot\mathbf{r}/2)}e^{i\mathbf{k}\cdot\mathbf{r}}.\begin{pmatrix} u^{\uparrow}_{\mathbf{k},\nu}(\mathbf{r}) \\ u^{\downarrow}_{\mathbf{k},\nu}(\mathbf{r}) \end{pmatrix}. \tag{2.59}$$

F. Local force theorem

Andersen's force theorem [39, 40] states that the difference in total energy due to a small perturbation can be calculated non-self-consistently from the self-consistent potential of the unperturbed Hamiltonian and can be given by the difference in the sum of the (Kohn-Sham) eigenvalues of the perturbed and unperturbed states. In the case of a magnetic system the theorem can be applied to calculate the energy difference between two structures with slightly different magnetization directions, e.g., to calculate the energy difference between spin spirals of different wavelengths, or the magnetic anisotropy energy. Let us explain this below:

Let us consider the KS equations for a Hamiltonian $\mathcal{H}$ such that

$$\mathcal{H}[n_0]\psi_{\nu,n_0} = \epsilon_{\nu,n_0}\psi_{\nu,n_0}, \tag{2.60}$$

where n_0 is the ground state density. If we perturb the system slightly, the resultant Hamiltonian can be written as $\mathcal{H}_1 = \mathcal{H} + \delta\mathcal{H}$, where $\delta\mathcal{H}$ is very small. In general some such perturbation would change the density of the system, such that $\mathcal{H}_1 = \mathcal{H}_1[n_1]$. By

using the force theorem one can write the difference in energy between the perturbed and the unperturbed system δE as the difference in the sum of eigenvalues of the occupied single-electron states (band energies) calculated with the unperturbed potential/density. Mathematically, one can write:

$$\delta E = \sum_{\nu} \epsilon^{FT}_{\nu,n_1} - \sum_{\nu} \epsilon_{\nu,n_0}, \tag{2.61}$$

where ϵ^{FT}_{ν,n_1} is the eigenvalue of the perturbed Hamiltonian, which has the same density as the unperturbed Hamiltonian, such that $\mathcal{H}_1[n_0]\psi_{\nu,n_1} = \epsilon^{FT}_{\nu,n_1}\psi_{\nu,n_1}$.

The local force theorem does not hold if the perturbation is too large, e.g., perturbation which changes the size or shape of the unit cell.

2.3 *Ab Initio* Atomistic Thermodynamics

The total energies obtained from *ab initio* DFT calculations correspond to properties of a system at zero temperature and pressure. If we want to go beyond this regime and want to study the behavior of the system at finite temperature T and pressure p, we can use the results obtained from DFT as inputs into a technique called *ab initio* atomistic thermodynamics. Below we describe this method briefly.

Using *ab initio* atomistic thermodynamics, it is possible to construct a thermodynamic free energy function in terms of environmental variables such as T and p. When T and p are kept fixed during a process, the relevant thermodynamic quantity of interest is the Gibbs free energy $G(T, p)$, which can be expressed in terms of the chemical potentials of the constituent atoms or molecules of the system. As an example, let us consider a semiconductor surface in contact with "realistic" gas-phase environments. Semiconductor surfaces often exhibit reconstruction due to rearrangement of the surface atoms (see Section 6.2). In the presence a of gas-phase environment, the surface may interact with the surrounding in order to saturate the dangling bonds on the surface. (This can be achieved in a molecular beam epitaxy growth by varying the partial pressure of the gases.) In such a reaction, the chemical potential μ measures the "rate of change" of G with respect to

the number of adsorbate atoms/molecules. Thus μ determines the tendency of a substance toward a reaction; with the tendency depending on the difference between values of the chemical potentials of reactants and products. This difference vanishes when the system is in thermodynamic equilibrium. When the system achieves thermodynamic equilibrium, a stable mixed phase can be obtained, where the gases are adsorbed on the surface. The resulting *surface* Gibbs free energy can be expressed as the sum of the contributions of electronic, translational, rotational, and vibrational degrees of freedom. For a surface, the translational and rotational free energies can be neglected, so the Gibbs free energy has only two major contributions, coming from electronic and vibrational degrees of freedom. This allows one to incorporate atomistic details, i.e., the information on the potential energy surface (PES), in the calculation of thermodynamic potential functions like the Gibbs free energy. The surface Gibbs free energy γ, of such a system with surface area S, can be defined as: [41, 42]

$$\gamma(T, \{p_i\}, \{N_i\}) = \frac{1}{S}\left[G_{\mathrm{m}}(T, \{p_i\}, \{N_i\}) - \sum_i \mu_i N_i\right], \tag{2.62}$$

where G_{m} is the total Gibbs free energy of the mixed system, which is the sum of the vibrational energy and the total energy E_{tot} of the mixed system. p_i, μ_i, and N_i are the partial pressure, chemical potential (of an atom/molecule) and the total number of atoms/molecules of species i, present in the system.

For a multi-component system, several gases may come in contact with the surface. In addition, the gas-phase reactions can change the environmental conditions for the surface. However, one can imagine a situation where the gas reservoirs are separately in thermal equilibrium with the surface, but not with each other. Such a case is called "constrained thermodynamics". This is valid when the gas-phase reaction between the gas reservoirs is prohibited or at least minimal. The system being very close to equilibrium, one can still invoke *ab initio* atomistic thermodynamics to obtain an idea about the probable phase space and to identify regions where kinetics may control the material properties.

We have employed this method in Chapter 6 in order to obtain the phase diagram of

the Si(100) surface due to co-adsorption of two gases, Br_2 and H_2. There we also have listed the limitations of using this method in the context of the co-adsorption.

2.4 Nudged Elastic Band

In order to obtain the energy barriers of a chemical reaction (see Chapter 7), we have used the nudged elastic band (NEB) method [43]. First-principles molecular dynamics (as formulated by Car and Parrinello in 1985) determines the kinetics and the equilibrium properties of a system that occur on time scales comparable with the characteristic time scale of the microscopic dynamics (some picoseconds). In such cases, the relevant kinetics is determined by the energy barriers that are low compared to the typical thermal fluctuations. When the energy barriers are larger than the thermal fluctuations, then the system spends more time within its stable states, so the transition (to overcomes the barrier) occurs only rarely. Such phenomena, named as "rare events", can no longer be studied by molecular dynamics and new numerical techniques to deal with such phenomena are called for.

The study of "rare events" in the context of a chemical reaction narrows down to the identification of a *transition state*. The transition state on going from reactants to products can be obtained by finding the saddle point in the PES that separates two minima corresponding to the stable states (reactants and products). However, finding the saddle point of a PES numerically is a challenging task. In the NEB method, a path connecting the reactants (often called the "initial" state) and the products (often called the "final" state) is considered to consist of a set of configurations (as a first guess, they are linearly interpolated between reactants and products) connected by springs of zero rest-length. These interpolated configurations are relaxed simultaneously to obtain the minimum energy path (MEP). The MEP is a path in the configuration space; along this path the components of the forces orthogonal to it are zero. This path is nothing but the reaction pathway for a chemical reaction. The MEP contains the saddle point, which is identified as the configuration having the highest energy along the path, and this configuration is called the

transition state. This saddle point divides the MEP q, into two branches which correspond to two steepest-descent trajectories away from the saddle point $q(s = s^*)$, s being the arbitrary reaction coordinate in the configuration space such that $s \in [0, 1]$. This condition can be written as:

$$\frac{\mathrm{d}q(s)}{\mathrm{d}s} = \begin{cases} \nabla V(q(s)) & \text{if } s < s^*, \\ -\nabla V(q(s)) & \text{if } s > s^*. \end{cases}$$

For steepest descent, the components of forces orthogonal to the MEP must be zero. Thus, if $\tau(s)$ represents the normalized tangent vector at any point of the MEP, then the expression for the orthogonal force can be written as:

$$\mathbf{F}(q)_{\perp}^{\text{true}} = \nabla V(q(s)) - (\nabla V(q(s)) \cdot \tau(s))\tau(s) = 0. \tag{2.63}$$

To solve Eq. (2.63), the reaction coordinate s is first made discretized and the MEP is represented on this discretized mesh. This discretized path $q(s)$, which was initially represented as a "chain of images", describes an elastic band. Note that an equivalent condition to Eq. (2.63) is also obtained for discrete s values.

Such a process avoids collapse of the images into the two stable minima due to the change in inter-image distances during the minimization process. Along with the "true" forces, the images also feel a "virtual" force due to the springs, $\mathbf{F}(q)^{\text{elastic}}$. However, due to the bending of the springs a component of $\mathbf{F}(q)^{\text{elastic}}$ can appear which is orthogonal to the path. A convergence problem arises due to this and this effect is called "corner cutting". In order to avoid such a situation, the elastic forces are projected along the tangent to the MEP:

$$\mathbf{F}(q_i)_{\parallel}^{\text{elastic}} = -\kappa\tau(s)((2q_i - q_{i+1} - q_{i-1}) \cdot \tau(s)), \tag{2.64}$$

where the index i represents a discrete point on the path, and κ is the spring constant. q_i is called the i^{th} image. This technique of projecting spring forces along the path is called "nudging" the elastic band. A solution is obtained when a chain of images satisfy Eq. (2.63)

in the presence of springs, where the evolution of each image found by the steepest-descent algorithm, with the forces acting on the image q_i at any time is given by:

$$\mathbf{F}(q_i) = \mathbf{F}(q_i)_{\perp}^{\text{true}} + \mathbf{F}(q_i)_{\parallel}^{\text{elastic}}. \tag{2.65}$$

The role of the "virtual" springs is to keep the images on a chain equispaced. The solution is converged to give an equal inter-image distances. The value of the elastic constant also does not matter as long as the projection is non-zero.

2.4.1 Climbing image NEB

The technique described above gives the MEP as a solution. However, the configuration corresponding to the transition state is not guaranteed. Henkelman, Uberuaga and Jónsson [44] developed a technique to obtain an image at the saddle point. This is the called climbing-image (CI) scheme as the image corresponding to maximum energy $[q(s^*)]$ is forced to move up-hill along the path tangent and down-hill along all the directions perpendicular to the path tangent. This is obtained by setting the force on this image as:

$$\begin{aligned} \mathbf{F}(q(s^*)) &= \mathbf{F}^{\text{total}}(q(s^*)) + \mathbf{F}(q(s^*))_{\parallel}^{\text{elastic}} \\ &= -\nabla V(q(s^*)) - k\tau(s^*)((2q_i - q_{i+1} - q_{i-1}) \cdot \tau(s^*)). \end{aligned} \tag{2.66}$$

The CI-NEB is a very useful method as it provides the activation energy barrier and the transition state coordinates, at the end of a path optimization.

Part A

Magnetic Properties of Surfaces

Chapter 3

Electronic and magnetic structure of thin films: Cr deposited on Ag(100)

3.1 Introduction

Monolayers of transition metals ($3d$, $4d$, $5d$) grown on noble metal substrates are good models to study two-dimensional magnetism. Since $3d$ orbitals are comparatively less localized than $4d$ and $5d$ orbitals, the $3d$ transition metals show itinerant magnetism. Among the $3d$ transition metals, the magnetic properties of Cr are very sensitive to the coordination number and symmetry of the crystal, as it has half-filled $3d$ bands. It has been shown that a monolayer of Cr on Cu(111) and on Au(111) has a 120° Néel structure [45,46], while Cr/Au(100) favors c(2×2) antiferromagnetic ordering [47]. In all these cases, the Cr atoms show very large magnetic moments due to negligible hybridization of Cr $3d$ bands with the coinage metal d bands. Using density functional theory, in this chapter we have studied the structural, magnetic and electronic properties of Cr deposited on Ag(100).

3.2 Previous Studies

When a metal A is deposited on another metal B, the stability of the combined system depends on the relative surface energy of the A and B surfaces. Cr having a larger surface energy (2400 mJ/m^2) compared to that of Ag (1250 mJ/m^2), formation of a monolayer of Cr on Ag(100) was expected to be unfavorable. In spite of this, in order to find a (metastable) system which exhibits two-dimensional magnetism, there have been several experimental and theoretical studies performed on Cr deposited on the Ag(100) surface addressing the following questions: (1) is it possible to grow a flat monolayer of Cr on Ag(100) at certain growth condition? (2) what is the magnetic configuration of the system when Cr deposited on the Ag(100)? The growth of Cr on Ag(100) had drawn huge attention due to the possibility of no intermixing at the interface, as there exists a large miscibility gap above the melting point in the phase-diagram of Cr-Ag alloys.

The early experiments [48] suggest that indeed no alloying takes place when Cr is deposited on Ag(100) at room temperature and epitaxial Cr can be grown on Ag(100) [49, 50]. However, films grown at this temperature do not form a perfect monolayer as a bilayer of Cr starts to form before completion of the first layer. Upon increasing Cr concentration, the simultaneous formation of different multilayers was observed. This type of growth is explained by the low mobility of adatoms at room temperature, favoring a growth mode described by random deposition models [51].

However, upon increasing the substrate temperature to 430–450 K, Krembel *et al.* showed that an ordered flat monolayer of Cr can be grown on Ag(100) [52–54]. They also showed that their LEED images exhibit a weak but distinct c(2×2) structure, which arises due to the exchange scattering of low-energy electrons from a structure having antiferromagnetic ordering [55]. The stability (of the metastable state) of flat Cr monolayer on Ag(100) was attributed to the presence of two-dimensional antiferromagnetic ordering. At the initial stages of growth, Cr was shown to form large two-dimensional islands with area proportional to the Cr coverage. Upon increasing the Cr coverage to ~ 1 ML, these islands were shown to cover the whole surface and thus, a flat monolayer of Cr was formed on the

surface. During growth, the Cr adatoms deposited in the second layer of the island quickly diffuse towards the edges of the two-dimensional island, where they stick, to sustain further growth of the flat monolayer. However, at high temperature ($>$ 500 K) Cr deposition of Ag(100) leads to agglomeration (formation of three-dimensional islands) of Cr atoms on Ag(100).

The formation of a c(2×2) antiferromagnetic Cr monolayer on Ag(100) is in agreement with the theoretical calculations of Blügel *et al.* [56, 57], where they have shown that the antiferromagnetic configuration is favored by $\sim$ 435 meV per Cr atom with respect to the ferromagnetic configuration. A very large magnetic moment of Cr was also reported ($\sim$ 3.8 μ_B) by these authors. However, the theoretically calculated band structure [58] and the experimental ARPES spectra did not seem to agree very well.

A confusion regarding the structure of Cr on Ag(100) arose when scanning tunneling microscopy (STM) experiments failed to observe a flat monolayer structure of Cr on Ag(100) [59]. Upon preparing a sample at 440 K, the authors of Ref. [59] showed that irregular two-dimensional islands of Cr on Ag(100) were formed. Further, their LEED images did not show any signature of a c(2×2) structure. Moreover, Lawler *et al.* [60] showed from their STM measurements that even though at low temperature the growth is characterized by multilayer formation, at high temperature an Ag overlayer starts to cover the Cr monolayers. This picture was supported by Steadman *et al.* [61] who showed that monolayer platelets of Cr get covered with Ag at high temperature. At 430 K, the Cr monolayer was also reported to intermix partly with the Ag overlayer. In an attempt to get rid of the confusion regarding the LEED structure, Hanf *et al.* [62] had repeated the experiment and were able to reproduce a weak c(2×2) signal. In addition, they suggested the existence of c(2×2) Cr domains and multilayer patches made of p(1×1) Ag islands on top of a mixed Cr-Ag phase.

In spite of all these studies, we believe that till date no conclusive study has been performed to determine the structural and magnetic properties of Cr deposited on the Ag(100) surface. The confusion arises due to (i) two groups reporting different LEED patterns and (2) no STM data having been obtained to support the existence of Cr monolayer

on Ag(100) surface. It is also surprising that no theoretical investigation seems to have carried out so as to obtain an understanding of the stability of the subsurface Cr monolayer on Ag(100). In order to develop a better understanding, we revisit the problem by performing both experiments (performed by our collaborators in the group of K. S. R. Menon) and theoretical calculations.

3.3 Experimental Motivation

Recently, low energy electron diffraction (LEED) and angle resolved photo emission spectroscopy (ARPES) experiments have been performed for Cr deposition on Ag(100), by

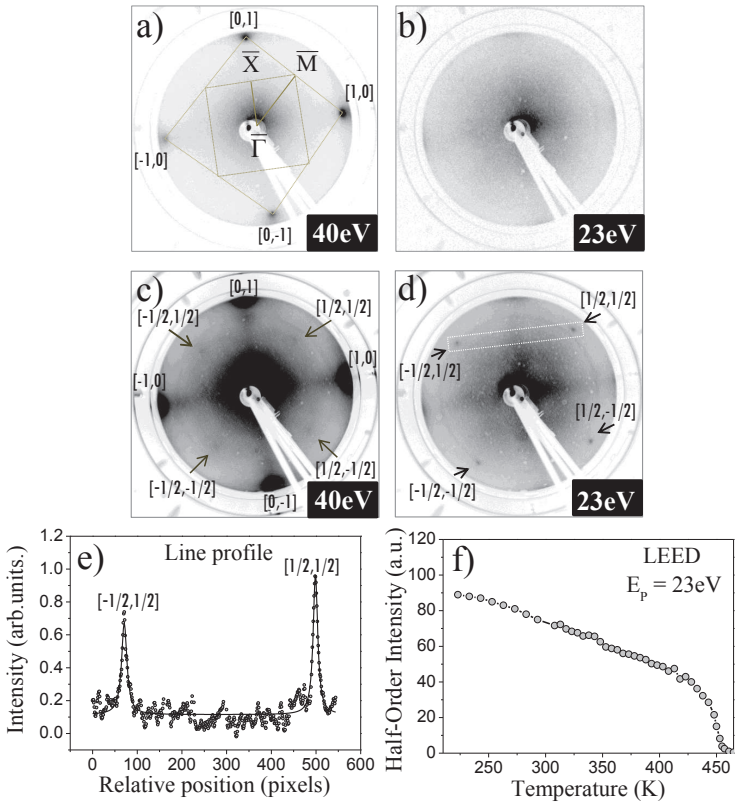

Figure 3.1: *(a)LEED images from Cr deposited on Ag(100) at room temperature for a primary electron energy E_p of 40 eV indicating sharp $p(1 \times 1)$ spots. The surface Brillouin zone and corresponding symmetry directions are marked. (b) LEED images for E_p = 23 eV at room temperature showing absence of half-order spots. (c) LEED image from Cr deposited on Ag(100) grown at 428 K (E_p = 40 eV) showing weak c(2×2) half-order spots along with integer-order spots. (d) For E_p = 23 eV, clear half-order spots are observed. A line profile along the half-order spots (-1/2, 1/2) and (1/2, 1/2) (boxed region) is shown in (e) for clarity. (f) Average intensity variation of the half-order spots at 23 eV (E_p) with sample temperature confirming the AFM order with a Nèel temperature T_N of ∼ 455 K. Images provided courtesy of K. S. R. Menon.*

our collaborators in the group of K. S. R. Menon [63]. At 428 K, the LEED images (see Fig. 3.1) are shown to consist of four half-order spots, presumably confirming a c(2×2) antiferromagnetic structure at low energies (23 eV). However, above the Néel temperature of Cr ($\sim$ 455 K), the intensity corresponding to these spots disappears [see Fig. 3.1(f)]; this confirms that the c(2×2) LEED structure is related to the magnetic properties of the Cr atoms. In addition, by varying the Cr concentration, they are able to show that the intensity of the half-order spots becomes maximum at 1.2 ML Cr thickness. By performing ARPES experiments for the Ag(100) surface both before and after the Cr deposition, they were able to show the appearance of new bands on the ARPES spectra after the Cr deposition. These results also suggest that a monolayer of Ag covers the flat monolayer of Cr at 428 K with some degree of Cr-Ag intermixing.

In this Chapter, by performing DFT calculations, we want to address the following questions: (1) does Cr stay on the surface or does it go subsurface? (2) what is the magnetic structure and how does it change with Cr position? (3) how does the electronic structure change on Cr deposition?

3.4 Calculation Details and Systems

All the calculations were performed using spin-polarized density functional theory (DFT) as implemented in the Quantum ESPRESSO code [24]. A plane-wave basis set was used to expand the electronic wavefunctions. The kinetic energy cutoffs for the wavefunctions were set to 40 Ry, while the cutoffs for the related charge densities were set to 400 Ry. Ultrasoft pseudopotentials [22] were used to describe the ion-electron interactions. A generalized gradient approximation with the Perdew-Burke-Ernzerhof form was used to approximate the exchange-correlation functional [20].

A 15 atomic layer thick slab of Ag(100) was used to model the surface of Ag(100). We have considered four different atomic configurations of the slab upon putting Cr monolayers on Ag(100) symmetrically (on both the top and bottom surfaces of the slab): (1) Cr/Ag(100), where each surface of Ag(100) had a Cr monlayer as an overlayer, (2)

1Ag/Cr/Ag(100), where each surface of Cr/Ag(100) system was covered by a monolayer of Ag, (3) 2Ag/Cr/Ag(100) with two Ag layers covering each surface of Cr/Ag(100), and (4) 3Ag/Cr/Ag(100), where each surface of Cr/Ag(100) was buried under three layers of Ag. In order to be able to compare the energies directly, for each of these cases we have considered a slab with 17 atomic layers. To minimize the interaction between the periodic images along the direction normal to the surface, a vacuum separation of 17.8 Å was used.

For geometric optimization the Broyden-Fletcher-Goldfarb-Shanno algorithm was used; all the atoms of the slab except the middle three layers were allowed to relax until the Hellman-Feynman force on these atoms was less than 0.001 Ry/a.u. along each Cartesian direction. For Brillouin zone sampling, Monkhorst-Pack grids [27] were used which were commensurate with an $(11 \times 11 \times 1)$ sampling for the 1×1 surface unit cell. The Marzari-Vanderbilt smearing technique [34] was used, for faster convergence, with smearing width set equal to 0.001 Ry.

For all the calculations, the in-plane lattice constant of the slab was kept fixed at the experimental lattice constant of Ag (= 4.09 Å). Before proceeding to perform calculations on Ag/Cr/Ag systems, we have calculated the band structure of Ag(100) (by taking a 21 monolayer thick Ag slab) along the high symmetry directions of the two-dimensional square Brillouin zone [see Fig. 3.2(a)]. Two surface states are found to appear in the bulk band gap in the vicinity of the $\overline{\mathrm{X}}$ point and are highlighted in blue color. These results are in good agreement with previous studies [64, 65].

Ag has a face-centered (fcc) crystal structure, while Cr crystallizes in the body-centered cubic (bcc) structure. The lattice constant of Cr is 2.88 Å. The in-plane Ag-Ag distance in Ag(100) is $(4.09/\sqrt{2} =)$ 2.89 Å [a 1×1 surface unit cell is shown in Fig. 3.3(a) by an orange square; note that this unit cell is rotated by 45° with respect to the fcc surface unit cell]. Due to the negligible mismatch between the surface lattice constants of Ag(100) and Cr(100), it is possible for the Cr monolayer to be pseudomorphic to Ag(100), i.e., the lattice constant of the Cr monolayer will be in registry with that of the Ag(100) surface.

For all the four systems described above, calculations are performed for both ferromagnetic (FM) and antiferromagnetic (AFM) configurations. The AFM configurations for all

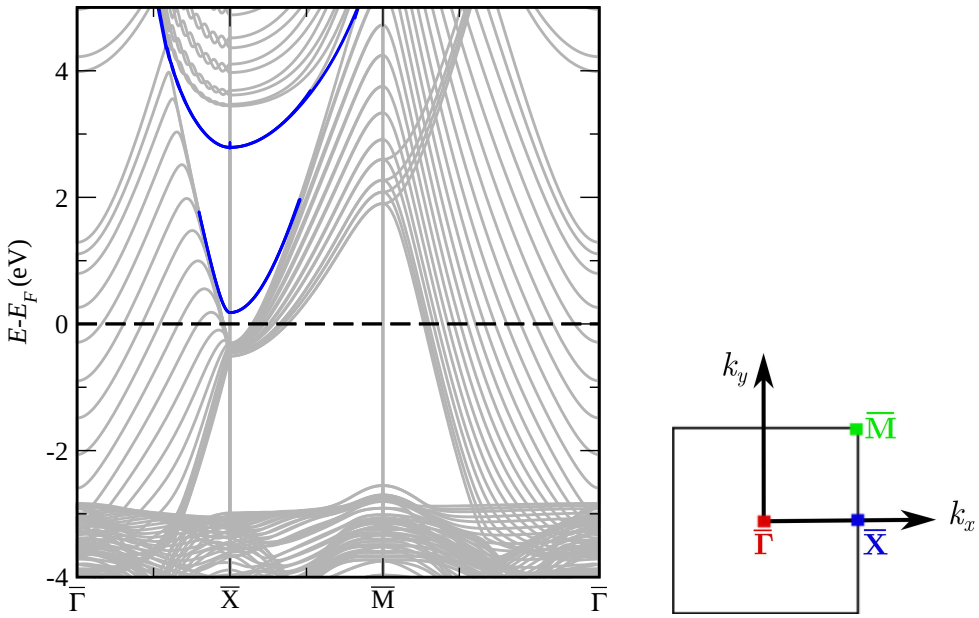

Figure 3.2: *(a) shows the calculated band structure. The surface states that appear in the bulk band-gap are highlighted in blue. (b) shows the high-symmetry points in the square Brillouin zone.*

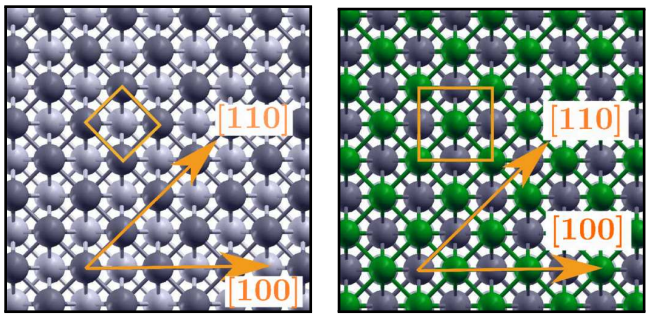

(a) Ag(100): 1×1 cell (b) Cr/Ag(100): $\sqrt{2} \times \sqrt{2}$ cell

Figure 3.3: *(a) and (b) show the top view of the atomic arrangements in the Ag(100) and Cr/Ag(100) systems. The green, dark gray, and light gray spheres represent the Cr, first substrate layer and second substrate layer Ag atoms, respectively. The primitive surface unit cells are indicated by solid orange lines.*

four systems are shown in Fig. 3.4, where the red arrows indicate the direction of spins. In order to directly and accurately compare the energetics of the FM and AFM configurations, as well as of different systems, we have performed all the calculations using a $\sqrt{2} \times \sqrt{2}$ surface unit cell [see Fig. 3.3(b)].

In order to compare our computed band structure with the experimental ARPES data,

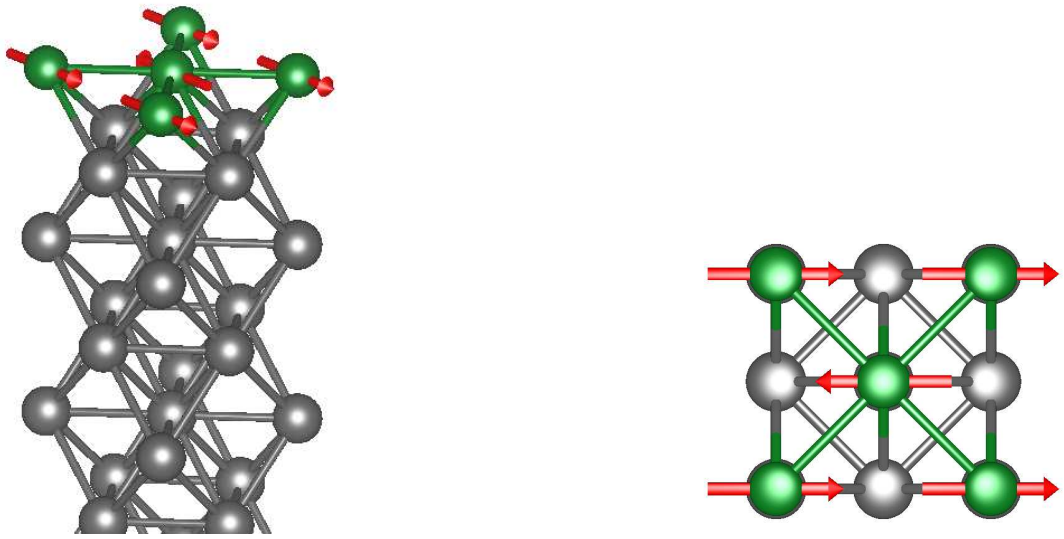

(a) Cr/Ag(100), side view (b) Cr/Ag(100), top view

Figure 3.4: *The side view (a) and the top view (b) of the atomic structure of Cr/Ag(100) in the antiferromagnetic configuration. The green and gray spheres represent the Cr and Ag atoms, respectively. The red arrows indicate the direction of the spins. Note that here we have shown the spins pointing in-plane; however, the out-of-plane directions of spins are also equivalent within the present calculation.*

one needs to employ a "band unfolding" scheme if the ground state of the system is antiferromagnetic, i.e., when the primitive (chemical) unit cell is not sufficient to describe the system and use of a supercell becomes mandatory. Below we describe the details of the method to unfold band structures of DFT supercell calculations with proper spectral weight. In addition, we also describe a procedure to obtain atom-wise-projection of the bands. Combining these two methods, one can obtain meaningful insights into the experimental ARPES data by performing DFT calculations.

3.4.1 Unfolding of band structure

Use of a supercell becomes indispensable in DFT calculations when the crystal symmetry changes, e.g., due to doping by impurities, lattice distortions, vacancies, or when the system exhibits a charge density wave, spin density wave, or orbital ordering. With the increase in the supercell size, the corresponding size of the Brillouin zone (BZ) decreases. Thus the first BZ of the primitive cell (PBZ) gets folded into the BZ of the supercell (SBZ). The

bands in the SBZ do no match with the experimental ARPES data due to the folding; thus, they are not very informative. So, the unfolding of the band structure corresponding to the supercell becomes essential. The theory behind the band unfolding methodology is given in Refs. [66–69]. Here, we only present a brief summary regarding the implementation in a DFT plane-wave basis set method.

In order to describe the method of unfolding, let us denote all the wave-vectors in the PBZ and SBZ as $\mathbf{k}$ and $\mathbf{K}$, respectively and the volumes of the PBZ and SBZ as Ω_{PBZ} and Ω_{SBZ}. For each $\mathbf{K}$ of the SBZ, there are $N_{\mathbf{G}}$ number of $\mathbf{G}^{\mathrm{SBZ}}$ vectors of the supercell that satisfy the following equation [70],

$$\mathbf{k}_i = \mathbf{K} + \mathbf{G}_i{}^{\mathrm{SBZ}} \quad \text{where} \quad i = 1 \ldots N_{\mathbf{G}}, \tag{3.1}$$

where $\mathbf{k}_i$ is any vector in the primitive BZ and $N_{\mathbf{G}} = \dfrac{\Omega_{\mathrm{PBZ}}}{\Omega_{\mathrm{SBZ}}}$.

Let us consider the single-particle Kohn-Sham states of the supercell $\psi^{\mathrm{SC}}_{\mathbf{K},m}$; these can be obtained by solving the KS equations self-consistently by performing calculations using supercell. When using a plane-wave basis, one can write:

$$|\psi^{\mathrm{SC}}_{\mathbf{K},m}\rangle = \sum_{\{\mathbf{G}^{\mathrm{SBZ}}\}} c_{\mathbf{K}-\mathbf{G}^{\mathrm{SBZ}},m} |\mathbf{K} - \mathbf{G}^{\mathrm{SBZ}}\rangle, \tag{3.2}$$

where m is a band index, $|\mathbf{K} - \mathbf{G}^{\mathrm{SBZ}}\rangle$ represents the plane-wave basis functions, and $c_{\mathbf{K}-\mathbf{G}^{\mathrm{SBZ}},m}$ are the plane-wave expansion coefficients. Similarly, the single-particle Kohn-Sham states of the primitive $\psi^{\mathrm{PC}}_{\mathbf{k},\nu}$ are written as:

$$|\psi^{\mathrm{PC}}_{\mathbf{k},\nu}\rangle = \sum_{\{\mathbf{G}^{\mathrm{PBZ}}\}} c_{\mathbf{k}-\mathbf{G}^{\mathrm{PBZ}},\nu} |\mathbf{k} - \mathbf{G}^{\mathrm{PBZ}}\rangle \tag{3.3}$$

where ν is the band index in the primitive cell. Note that the set of vectors $\{\mathbf{G}^{\mathrm{PBZ}}\}$ is only a subset of $\{\mathbf{G}^{\mathrm{SBZ}}\}$. Thus, Eq. (3.2) can be rewritten as:

$$|\psi^{\mathrm{SC}}_{\mathbf{K},m}\rangle = \sum_{\{\mathbf{G}^{\mathrm{PBZ}}\}} c_{\mathbf{k}-\mathbf{G}^{\mathrm{PBZ}},m} |\mathbf{K} - \mathbf{G}^{\mathrm{PBZ}}\rangle + \sum_{\{\mathbf{G}^{\mathrm{SBZ}} \neq \mathbf{G}^{\mathrm{PBZ}}\}} c_{\mathbf{K}-\mathbf{G}^{\mathrm{SBZ}},m} |\mathbf{k} - \mathbf{G}^{\mathrm{SBZ}}\rangle \tag{3.4}$$

Our aim is to obtain the $\{\mathbf{G}^{\mathrm{PBZ}}\}$ from the given set of $\{\mathbf{G}^{\mathrm{SBZ}}\}$. This can be obtained by employing a condition:

$$\mathbf{G}^{\mathrm{SBZ}} \cdot \mathbf{A} = 2\pi M \quad \forall\{\mathbf{G}^{\mathrm{SBZ}}\}, \tag{3.5}$$

where M is an integer and $\mathbf{A}$ is a lattice vector of the primitive unit cell. Eq. (3.5) gives non-zero contributions only for $\{\mathbf{G}^{\mathrm{PBZ}}\}$.

The probability of $|\psi^{\mathrm{SC}}_{\mathbf{K},m}\rangle$ having the same character as a primitive cell state with wave-vector $\mathbf{k}$ is given by the spectral weight $P_{\mathbf{K},m}(\mathbf{k})$. The spectral weight then can be obtained as [70]:

$$P_{\mathbf{K},m}(\mathbf{k}) = \sum_{\nu} \langle |\psi^{\mathrm{SC}}_{\mathbf{K},m} | \psi^{\mathrm{PC}}_{\mathbf{k},\nu} \rangle|^2. \tag{3.6}$$

As we are interested in obtaining the band structure in the PBZ, we can ignore the second term in Eq. (3.4). Then, from Eqs. (3.3) and (3.4) we can write

$$P_{\mathbf{K},m}(\mathbf{k}) = \sum_{\{\mathbf{G}^{\mathrm{PBZ}}\},\ \nu} |c_{\mathbf{K}-\mathbf{G}^{\mathrm{PBZ}},\nu}|^4. \tag{3.7}$$

As we will see below in Section 3. 5. 2, the spectral weight P is very useful to extract rich physics of the system, which is absent in the folded band structure.

3.4.2 Projected bands

To obtain the contributions coming from the atomic states to the bands, one can write $\psi^{\mathrm{SC}}_{\mathbf{K},m}$ as

$$\psi^{\mathrm{SC}}_{\mathbf{K},m} = \sum_{q} A_q \phi_q, \tag{3.8}$$

where $\{q\}$ is the set of good quantum numbers. ϕ_q is the atomic orbital of the state q and A_q's are the coefficients. The probability of the wavefunction $\psi^{\mathrm{SC}}_{\mathbf{K},m}$ having the same

character as a wavefunction ϕ_q is given by:

$$|\langle\phi_q|\psi_{\mathbf{K},m^{\mathrm{SC}}}\rangle|^2 = |A_q|^2 \tag{3.9}$$

Note that here we have assumed that all the calculations are performed in the supercell.

3.4.3 Unfolded projected bands

Now to obtain the contributions coming from the atomic states to the unfolded bands, one has to calculate the probability of the primitive cell wavefunction $\psi_{\mathbf{k},\nu^{\mathrm{PC}}}$ having the same character as a wavefunction ϕ_q. Thus, this projection can be written as:

$$|\langle\phi_q|\psi_{\mathbf{k},\nu^{\mathrm{PC}}}\rangle|^2 = |\langle\phi_q|\psi_{\mathbf{K},m^{\mathrm{SC}}}\rangle\langle\psi_{\mathbf{K},m^{\mathrm{SC}}}|\psi_{\mathbf{k},\nu^{\mathrm{PC}}}\rangle|^2 = |A_q|^2\ P_{\mathbf{K},\nu}(\mathbf{k}) \tag{3.10}$$

In section 3.5.2, we employ this method to obtain the band structure in order to compare with the experimental ARPES data.

3.5 Results

First, we examine the role of magnetic ordering in determining the relative stability of the four systems considered in this study. In this work, we have restricted ourselves to collinear magnetic ordering, i.e., ferromagnetic (FM) and antiferromagnetic (AFM) ordering. In Section (3.5.2), for the lowest energy system, we compare our results with experimental LEED images and ARPES data.

3.5.1 Stability and magnetic ordering

We have obtained the optimized geometries of all four systems considered here in both FM and AFM configurations. Table. 3.1 shows the tabulated values of the relative stability of different structures, with respect to the lowest energy structure (ΔE). We find that the most energetically favorable structure is 1Ag/Cr/Ag(100). This indicates that Cr prefers to be buried below one monolayer of Ag. Comparing the FM and AFM configurations

System	Results for magnetic structures			
	FM		AFM	
	ΔE (meV/Cr atom)	$m_{\mathrm{Cr}}^{\mathrm{FM}}$ (μ_B)	ΔE (meV/Cr atom)	$m_{\mathrm{Cr}}^{\mathrm{AFM}}$ (μ_B)
Cr/Ag(100)	850	4.70	476	4.42
1Ag/Cr/Ag(100)	437	4.13	0	4.30
2Ag/Cr/Ag(100)	498	4.86	4	4.22
3Ag/Cr/Ag(100)	501	4.87	49	4.26

Table 3.1: *Energetics of ferrromagnetic (FM) and antiferromagnetic (AFM) configurations of Cr on Ag(100) systems studied here. ΔE denotes the energy of a given configuration with respect to the lowest energy configuration, i.e., AFM configuration of 1Ag/Cr/Ag(100). m_{Cr} is the magnetic moment per Cr atom in a given system.*

for this structure, we find that 1Ag/Cr/Ag(100) favors AFM ordering over FM ordering. The AFM structures of 2Ag/Cr/Ag(100) and 3Ag/Cr/Ag(100) lie higher in energy than 1Ag/Cr/Ag(100) by only 4 meV/Cr atom and 49 meV/Cr atom, respectively. Interestingly, we find that for all the systems, the AFM structure lies lower in energy than the corresponding FM structure.

In Fig. 3.5 we have plotted d_{ij}'s, the interlayer distances between the i^{th} and j^{th} layers for all the systems studied here. As we have used a symmetric slab, we have only shown the interlayer distances up to d_{78}. For a given system, the interlayer distances are found to be independent of the magnetic configuration of the system. For all the systems, the interlayer distances are observed to be sensitive to the position of the Cr atoms in the slab, due to the interface effects.

In order to find out the reason behind the greater stability of the AFM configurations in comparison to the FM configurations, we have plotted the projected density of states (PDOS) per Cr atom in Fig. 3.6. Positive and negative values indicate the PDOS corresponding to the majority and minority spins, respectively. The red and blue curves represent the FM and AFM configurations, respectively. Two important features are observed when we compare the FM and AFM configurations of a given system: (i) the majority states for Cr atoms in the AFM configuration (shown by red dashed lines) near the Fermi energy (E_F) are narrower compared to the majority states of the Cr atoms in the FM configurations (shown by blue solid lines) and (ii) the center of the majority states

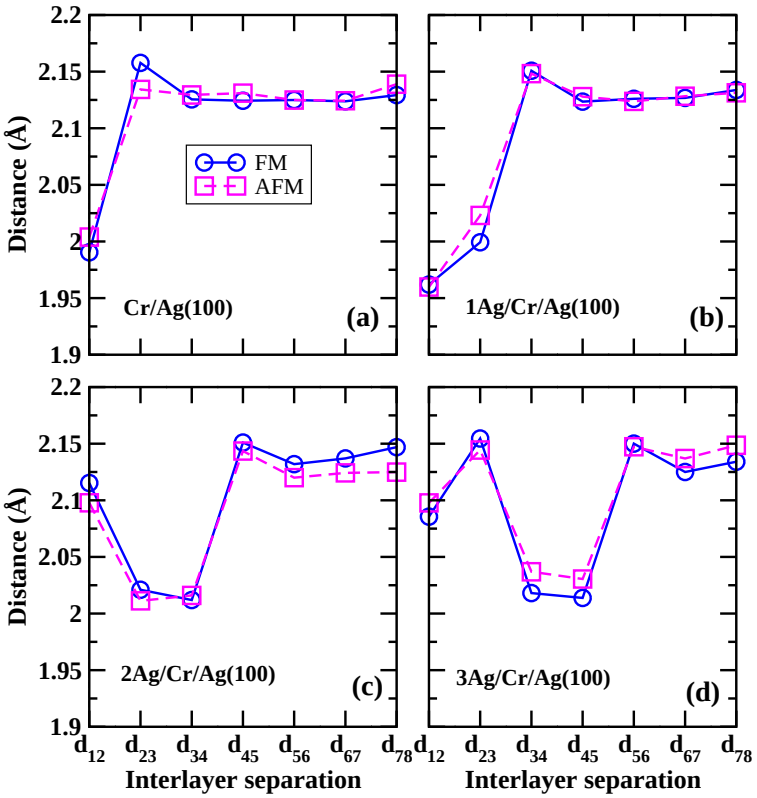

Figure 3.5: *The variation of interlayer distances for (a) Cr/Ag(100), (b) 1Ag/Cr/Ag(100), (c) 2Ag/Cr/Ag(100), and (d) 3Ag/Cr/Ag(100) in both the ferromagnetic (FM) [shown by blue circles] and the antiferromagnetic (AFM) [shown by pink squares] configurations.*

in the AFM configurations lie lower in energy than the corresponding states in the FM configuration. Both these facts indicate that the majority band-center of the Cr atoms in the AFM configurations lies lower in energy than the corresponding band-center in the FM configurations; this explains the lowering of energy in the AFM configurations compared to the FM configurations. As the minority states lie mostly above E_F in all the cases, their contribution is negligible in the energy lowering.

In Table. 3.1 we have also listed the magnetic moments per Cr atom (m_{Cr}) in all these structures. Intuitively, one might expect that m_{Cr} would decrease as the Cr monolayer goes deeper and deeper into the substrate due to larger and larger hybridization with Ag layers. Surprisingly, we find that m_{Cr} does not get reduced significantly as the Cr monolayer goes subsurface. By plotting the projected density of states (PDOS) of the Cr 3d orbitals and the Ag 4d orbitals (belonging to the Ag layers both above and below the Cr layer) in

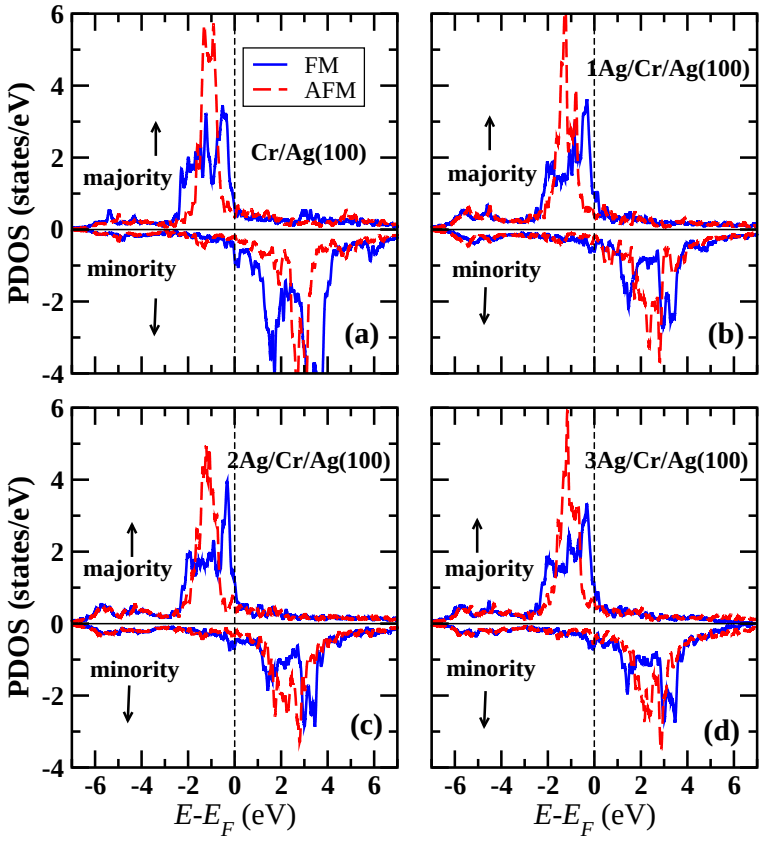

Figure 3.6: *The projected density of states (PDOS) of the Cr atoms in (a) Cr/Ag(100), (b) 1Ag/Cr/Ag(100), (c) 2Ag/Cr/Ag(100), and (d) 3Ag/Cr/Ag(100) for the ferromagnetic (FM) [shown by blue solid lines] and the antiferromagnetic (AFM) [shown by red dashed lines] configurations, respectively.*

the AFM configurations for all the systems (see Fig. 3.7), we find that below E_F, the $3d$ majority states of Cr (green curve) are well separated in energy from the $4d$ majority states of the nearest neighbor Ag atoms (gray filled curve). This indicates a weak hybridization between the $3d$ orbitals of Cr and the $4d$ orbitals of Ag. For this reason, Cr atoms are able to retain a large magnetic moment even for the 3Ag/Cr/Ag(100) system, the induced magnetic moments on the Ag atoms being negligible (0–0.03 μ_B). Note that the magnetic moments obtained by us are larger in magnitude than the values reported for Cr/Ag(100) by Blügel *et al.* [71]; however, the difference between the magnetic moment in the FM and the AFM cases are the same in our calculations and theirs.

Thus, we find that one monolayer of Cr wants to go to subsurface on Ag(100) and that the most stable structure is 1Ag/Cr/Ag(100). The Cr atoms prefer AFM ordering rather

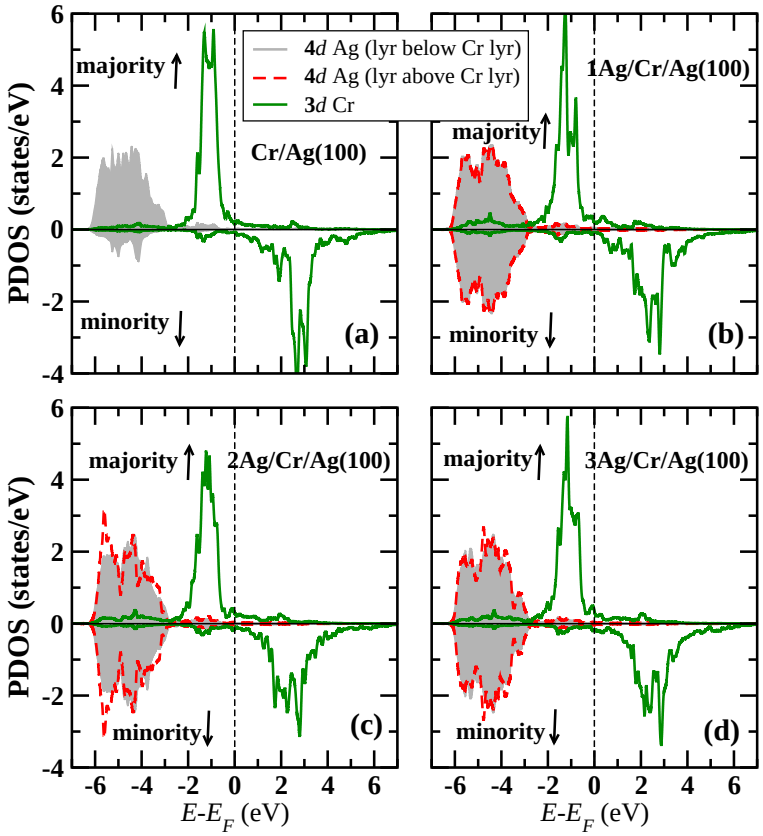

Figure 3.7: *The projected density of states (PDOS) of the Ag 4d states (shown by gray filled curve for the layer above the Cr monolayer and by red dashed lines for the layer below the Cr monolayers) and the Cr 3d states (shown by solid green lines) in the antiferromagnetic configuration of (a) Cr/Ag(100), (b) 1Ag/Cr/Ag(100), (c) 2Ag/Cr/Ag(100), and (d) 3Ag/Cr/Ag(100).*

than FM ordering. For this lowest energy configuration, below we compare our results with the experimental results obtained from LEED and ARPES data.

3.5.2 Comparison with experimental results

Let us first focus our attention on the experimentally obtained LEED images (see Fig. 3.1). The LEED images show both integral and half-integral spots upon deposition of Cr when the sample is grown at 428 K. The half-order spots originate from the antiferromagnetic exchange interaction of the low energy electrons [72,73]. From our calculation, we find that the lowest energy structure is the AFM 1Ag/Cr/Ag(100). Thus, the appearance of the half-integral spots can be attributed to the c(2×2) AFM configuration of 1Ag/Cr/Ag(100).

Next, we compare our calculated band structures with the ARPES data obtained for

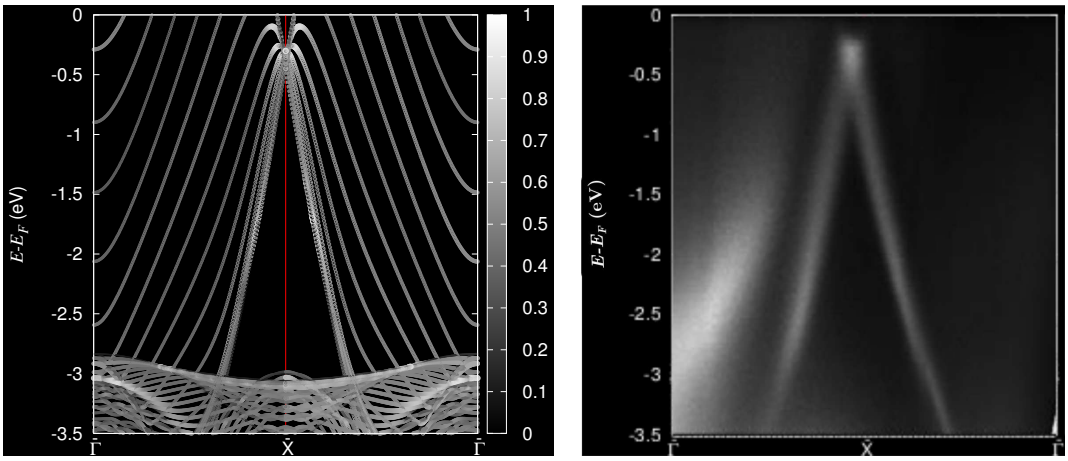

(a) Calculated band structure (b) ARPES data

Figure 3.8: *(a) shows the calculated band structure of bare Ag(100) along the high symmetry lines* $\overline{\Gamma}$-$\overline{\mathrm{X}}$-$\overline{\Gamma}$. *(b) shows the ARPES data along the same path for bare Ag(100). Experimental data provided courtesy of K. S. R. Menon.* E_F *denotes the Fermi energy. The gray scale in (a) represents the amount of projection.*

bare Ag(100) surface in Fig. 3.8 along the high-symmetry lines $\overline{\Gamma}$-$\overline{\mathrm{X}}$-$\overline{\Gamma}$. The band structure shown in Fig. 3.8(a) is projected on the first three surface layers of the Ag(100) slab (both top and bottom). The gray scale represents the amount of projection from the atoms of these layers; while "white" color represents the bands with highest projection, "black" color represents the bands with zero projection. Note that as we have used the (1×1) unit cell for this calculation, no unfolding was required. We find that the calculated band structure is in good agreement with the ARPES data obtained for bare Ag(100) surface.

In Fig. 3.9, we have plotted the calculated band structures, along with the second derivative of the experimental ARPES data obtained for AFM 1Ag/Cr/Ag(100). In this case, the unfolding of the band structure from the Brillouin zone of the $\sqrt{2} \times \sqrt{2}$ unit cell [shown by the dashed square and high symmetry points $\overline{\Gamma'}$, $\overline{\mathrm{X}'}$ and $\overline{\mathrm{M}'}$ in Fig. 3.9(b)] to the Brillouin zone of the primitive 1×1 cell [shown by the solid square and high symmetry points $\overline{\Gamma}$, $\overline{\mathrm{X}}$ and $\overline{\mathrm{M}}$ in Fig. 3.9(b)] cell was necessary as one cannot by any means define an antiferromagnetic configuration in the primitive chemical unit cell. Here, the color scale represents the amount of projection of the atomic states corresponding to the states of the top two layers of the slab, (i.e., the overlayer Ag atoms and the second layer Cr atoms) onto the unfolded bands [calculated using Eq. (3.10)]; while "red" color represents the

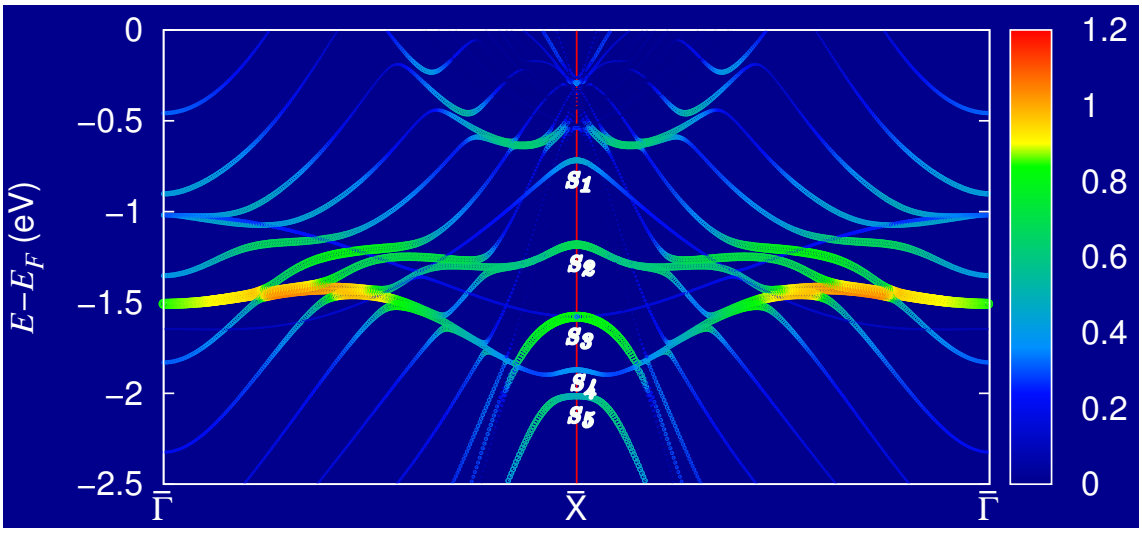

(a) Calculated band structure of AFM 1Ag/Cr/Ag(100)

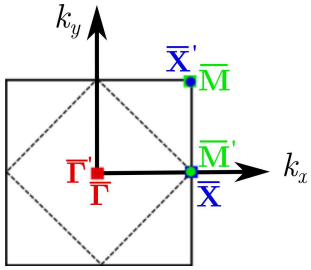

(b) Surface Brillouin zone

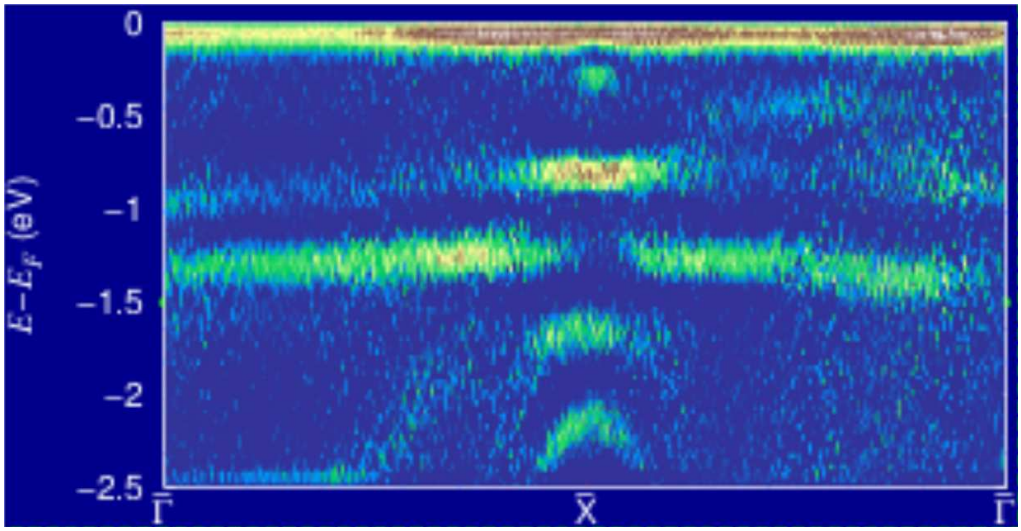

(c) Second derivative of ARPES data

Figure 3.9: *(a) shows the calculated band structure of antiferromagnetic 1Ag/Cr/Ag(100) along the high symmetry lines* $\overline{\Gamma}$-$\overline{X}$-$\overline{\Gamma}$*. The surface states at* $\overline{X}$ *are denoted by* S_1*,* S_2*,* S_3*,* S_4 *and* S_5*. (b) shows the surface Brillouin zone corresponding to the* 1×1 *cell (solid square and high symmetry points* $\overline{\Gamma}$*,* $\overline{X}$ *and* $\overline{M}$*) and* $\sqrt{2} \times \sqrt{2}$ *cell (dashed square and high symmetry points* $\overline{\Gamma}'$*,* $\overline{X}'$ *and* $\overline{M}'$*). (c) shows the second derivative of ARPES data along* $\overline{\Gamma}$-$\overline{X}$-$\overline{\Gamma}$ *for 1Ag/Cr/Ag(100). Experimental data provided courtesy of K. S. R. Menon.* E_F *denotes the Fermi energy. The color scale in (a) represents the amount of projection of the atomic states.*

bands with highest projection, "darkblue" color represents the bands with zero projection. The majority and minority bands are found to be degenerate in the entire energy range considered here. We find that the band structure gets modified significantly and additional surface states appear in the bulk band gap of Ag [compare Figs. 3.8(a) and 3.9(a)] due to the presence of Cr. We denote these surface states as S_1, S_2, S_3, S_4 and S_5, with band edges $E - E_F$ at -0.72 eV, -1.18 eV, -1.58 eV, -1.87 eV and -2.02 eV, respectively.

Comparing Figs. 3.9(a) 3.9(c), we find that the agreement with the calculated band structure of 1Ag/Cr/Ag(100) is very good, except for one state with band edge $E - E_F$ at ~ 0.8 eV, i.e., S_1. The intensity of S_1 appears to be very high in the experimental data; however, we do not observe such a high intensity for this state in the calculated band structure. Upon taking into account the projections from the Ag layers which are below the Cr layer, we did not observe any change in the intensity of S_1. In fact, we will see below that S_1 originates primarily from the Cr atoms. As the experimental results suggest that some degree of intermixing of Ag and Cr is possible; it may be that the high intensity of S_1 arises from Cr atoms in the surface layers, which are present due to the intermixing.

Next, we analyze the electronic properties of the surface states S_1–S_5 by using the projected density of states (PDOS), and charge density profiles. As these new surface states appear in the bulk band gap of Ag at the high symmetry point $\overline{\mathrm{X}}$, we have restricted ourselves to this high symmetry point, while analyzing the electronic properties. We find that for all the states at $\overline{\mathrm{X}}$, the contribution to the PDOS coming from the Cr layer is almost the same as the total contribution of that state. This confirms that the new surface states originate from the Cr layer. For both the majority and minority spins, we find that all the surface states are two-fold degenerate states, except for S_3, which is a 4-fold degenerate state. Only a few Cr 3d-orbitals are found to be responsible for the formation of these new surface states. This is clearly visible from the charge density profiles shown in Fig. 3.10 corresponding to the majority spins, with a isosurface value of 0.001 e/$(a.u.^3)$; for the minority spins, one can obtain similar charge density profiles by interchanging the states corresponding to the two Cr atoms in the $\sqrt{2} \times \sqrt{2}$ unit cell Cr1 and Cr2. We find that the state S_1 mainly originates from the Cr1 $3d_{x^2-y^2}$, the state S_2 mainly originates from the

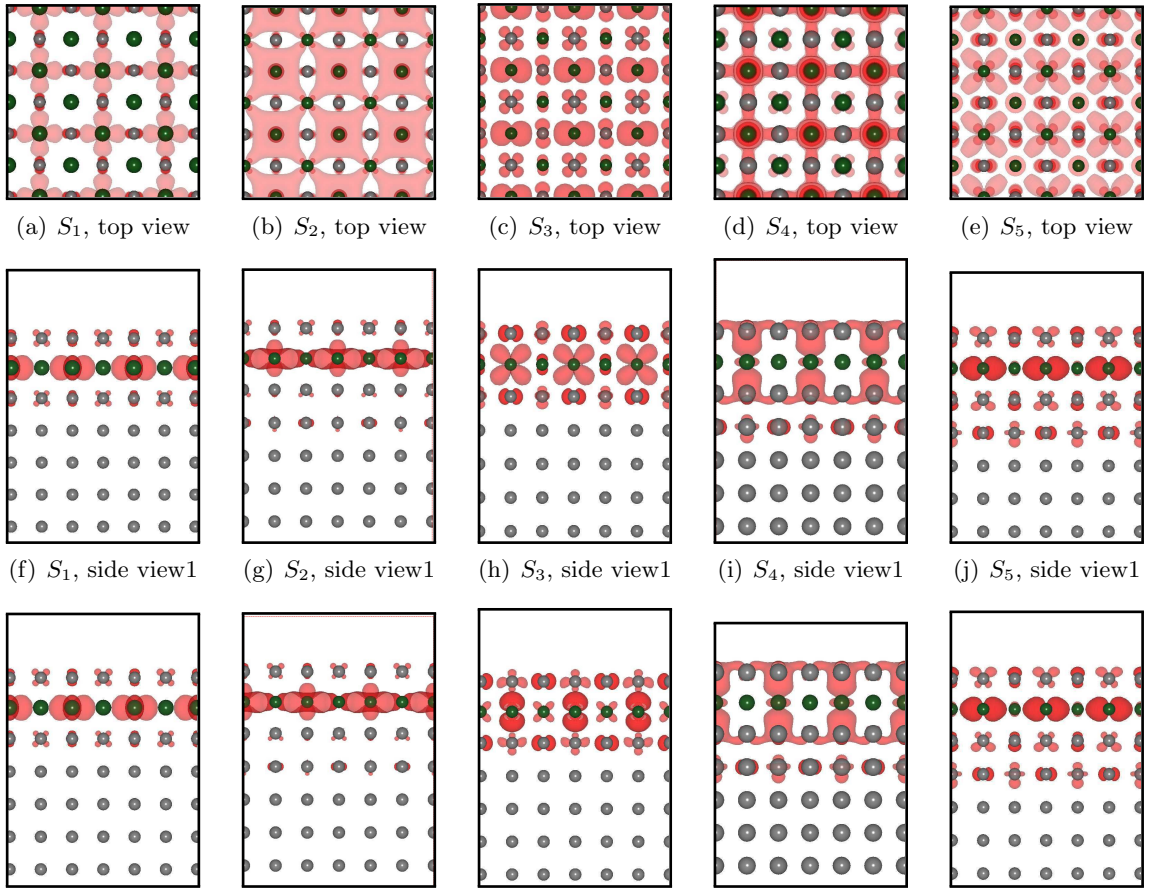

(a) S_1, top view (b) S_2, top view (c) S_3, top view (d) S_4, top view (e) S_5, top view

(f) S_1, side view1 (g) S_2, side view1 (h) S_3, side view1 (i) S_4, side view1 (j) S_5, side view1

(k) S_1, side view2 (l) S_2, side view2 (m) S_3, side view2 (n) S_4, side view2 (o) S_5, side view2

Figure 3.10: *The top and side views of charge density profiles (red) corresponding to the surface states for AFM 1Ag/Cr/Ag(100) system. The top view correspond to the x-y plane, while the side view1 and side view2 correspond to the y-z plane and x-z plane, respectively. The green and gray spheres represent the Cr and Ag atoms, respectively. The isosurface value (shown by red) for the charge density is 0.001 electron/a.u.*^{3}.

Cr1 $3d_{z^2}$ and Cr2 $3d_{xy}$, S_3 mainly originates from the Cr1 $3d_{yz}$, S_4 mainly originates from the Cr1 $3d_{z^2}$ and S_5 mainly originates from the Cr1 $3d_{xy}$. From Fig. 3.10, we also find that charge densities corresponding to these states decay as one moves from away from the Cr layer, both into the bulk and into the vacuum.

In order to find out how the charge densities of the surface states decay into the vacuum, we have plotted the planar average of the charge density for all the surface states in Fig. 3.11 for AFM 1Ag/Cr/Ag(100), as a function of distance along the z-direction. We find that except for S_3, all the surface states have a small peak just above the surface Ag layer, with a decaying behavior into the vacuum. The peaks corresponding to the S_4 and S_5 surface states are higher than the peaks corresponding to S_1 and S_2. At the position of the Cr layer, we find that the charge density is maximum for all the surface states; however, we find an exception for S_3. As S_3 mostly contains the $3d_{yz}$ state [as can be seen from Figs. 3.10(c), 3.10(h) and 3.10(m)], the planar average of charge density for this state has a peak both above and below the center of the Cr atoms on the second layer. We also clearly see evidence that all the surface states decay into the bulk beyond the fourth layer.

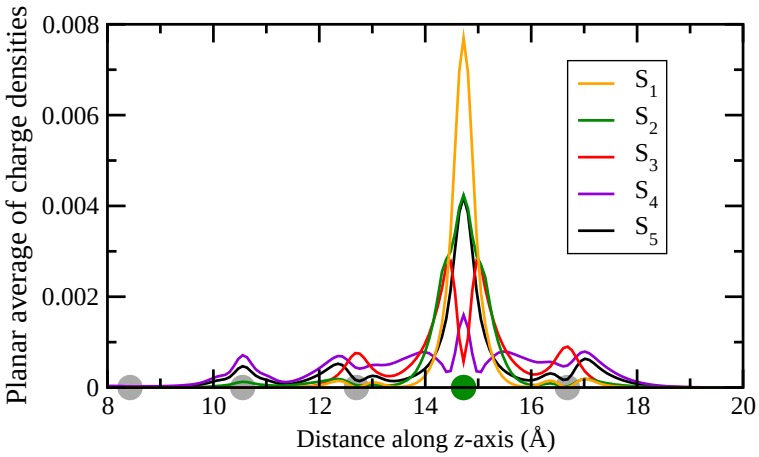

Figure 3.11: *Variation of the planar average of the charge density (corresponding to the charge density profile shown in Fig. 3.10) as a function of distance along the z-direction for all the surface states of the AFM 1Ag/Cr/Ag(100) for the majority spins. The gray and green filled circles represent the position of the Ag and Cr atoms of the slab along the z-direction.*

3.6 Summary

Using density functional theory, we have studied the structural, magnetic and electronic properties of Cr deposited Ag(100). We find that Cr wants to go subsurface on Ag(100). Considering different subsurface positions of the Cr monolayers, we find that the lowest energy structure is the one where the Cr monolayer is buried under one monolayer of Ag. Moreover, we find that in all the systems considered by us, Cr favors antiferromagnetic ordering. The $3d$–$4d$ hybridization between the Cr and Ag atoms is observed to be significantly small, even when the Cr monolayer is four layers deep into the substrate; this is why these systems attain large magnetic moments. Several surface states appear in the bulk band gap of Ag(100) due to Cr deposition. Our results are in excellent agreement with LEED images. By obtaining the projected unfolded bands of AFM 1Ag/Cr/Ag(100), and comparing with the projected band structure of Ag(100), we find that new surface states appear in the bulk band of Ag due to Cr deposition. By analyzing our results, we find that these new states arise purely from Cr $3d$ states. The calculated band structures of bare Ag(100), as well as of AFM 1Ag/Cr/Ag(100) are in very good agreement with the experimental ARPES data.

Chapter 4

Origins of stability of magnetic surface alloys: a case study of Mn_xAu_{1-x} on Ru(0001)

4.1 Introduction

In the previous chapter, we have studied the magnetic properties of an ultrathin film of A deposited on B, where A and B are magnetic and non-magnetic elements, respectively. In this chapter, we focus our attention on systems where two elements A and B are deposited on a non-magnetic substrate C. The resulting ultrathin films form surface alloys of the type, A-B/C, or more specifically, A_xB_{1-x}/C.

4.2 Surface Alloys

Bulk alloys are three-dimensional systems where two or more elements a form solid homogeneous mixture. Similarly, surface alloys are two-dimensional systems where two or more elements form an alloy restricted to the surface layer alone. These alloys display atomic level mixing. Initially, these materials were thought to be stabilized primarily by the relief of surface stress due to substrate-mediated strain interactions [74]; examples of

such systems of type A-B/C are monolayers of Cu-Ag and Pd-Au on Ru(0001) [75–77] and a monolayer of Pb-Sn on Rh(111) [78].

In the case of the surface alloy of A-B/B, Mn-Cu/Cu(001), Wuttig *et al.* showed that magnetism (arising from the Mn atoms) was the driving force for the stability of the alloy [79]. By performing DFT calculations, the authors showed that interdiffusion of the Mn atoms into the substrate Cu(001) was preferred over surface alloy formation, when magnetic interactions were switched off [79, 80].

It is important to note that surface alloys are different from alloy surfaces; the latter are formed due to the truncation of bulk alloys. Alloy surfaces may show different stoichiometry compared to their bulk counterparts. Surface alloys, on the other hand, are ultrathin layers on the surface which display alloying in the surface alone, i.e., not in the bulk.

4.3 Previous Studies

It is well known that Fe and Mn have different magnetic properties. The magnetic ordering in bulk Fe is ferromagnetic, while in bulk α-Mn the ordering is noncollinear antiferromagnetic [81]. While Fe and Au are bulk–immiscible, Mn and Au form bulk bimetallic alloys. These alloys exist in different stoichiometric ratios e.g., MnAu, Mn_2Au, $MnAu_2$, $MnAu_3$, $MnAu_4$, Mn_2Au_5, and Mn_3Au_5 [82–89]. Mostly these alloys show antiferromagnetic ordering of the spins on Mn atoms, with the exception of helimagnetic and ferromagnetic ordering for $MnAu_2$ [82, 89] and $MnAu_4$ [86], respectively.

A recent experimental and theoretical study by Mehendale *et al.* [90] showed that the Fe-Au/Ru(0001) system forms a long-range ordered bimetallic surface alloy, which gets stabilized by magnetism. On switching off the magnetism, the miscibility was dramatically decreased. The authors also showed that at every concentration the structure with the lowest energy was the one with the highest magnetic moment. This is particularly interesting as Fe and Au are bulk–immiscible. Interestingly, on going from Fe-Au/Ru(0001) to Fe-Au/Mo(110) [91], the results changed dramatically. The enthalpies of formation of surface alloys were reduced, and the tendency toward long-range ordering disappeared.

The reasons for this differing behavior were also traced back to magnetism: in particular, the fact that Ru atoms tend to get spin polarized parallel to Fe atoms, whereas Mo atoms get polarized antiparallel. In this work, we wish to explore the origins of the stability of ultra-thin surface alloys of Mn-Au on Ru(0001), using DFT calculations.

This class of magnetically stabilized surface alloys of type A-B/C, where the substrate C has an intermediate lattice constant between those of A and B, provides us the opportunity to investigate various mechanisms in operation and to obtain significant insights into the effect of the interplay between these mechanisms. This could be achieved by systematically trying out different combinations of materials. The understanding thus gained can then be leveraged to design surface alloys with desired properties. In this regard, it is important to note that in previous work [90–92], the following quantities had been varied, (i) magnetic moments on ferromagnetic A, (ii) size of non-magnetic B and (iii) substrate C. The results from the first two studies provide ways to gauge the relative importance of magnetic and chemical interactions, along with the stress-relief mechanism. On the other hand, the latter study underlines the importance of magnetism by comparing the properties of Fe-Au/Ru(0001) and Fe-Au/Mo(110). As the magnetic moments on the Fe and Ru atoms align parallel in Fe-Au/Ru(0001), while the moments on the Fe and Mo atoms align antiparallel to each other; these two systems behave completely differently (ΔH twice as large for the former as for the latter, and also, the former shows long-range ordering, but not the latter). Now, we want to explore what happens when we change the nature of magnetic interactions between A atoms by replacing Fe with Mn in Fe-Au/Ru(0001).

In this work, using DFT we will attempt to gauge the relative importance of three contributions to the alloy formation energy of Mn-Au/Ru(0001): the band energy, the magnetic energy, and the relief of surface stress. In contrast to many studies on alloys which make use of cluster expansions and attribute the stability of particular structures to dominant contributions from particular terms in the cluster expansion, here we will attempt to rationalize the appearance of certain favored structures using physical arguments.

4.4 Calculation Details and Systems

All the calculations were performed using spin-polarized DFT as implemented in the Quantum ESPRESSO package [24], which uses a plane-wave basis set. The plane-wave cutoffs for the expansion of the electronic wavefunctions and the related charge densities were set as 40 and 400 Ry, respectively. Ultrasoft pseudopotentials [22] were used to describe the ion-electron interactions, while the exchange-correlation functional was approximated by a generalized gradient approximation of the Perdew-Burke-Ernzerhof form [20]. To be able to separate out the effects of magnetism, we have performed both spin-polarized calculations and non-spin-polarized calculations (with spin-polarization suppressed).

To mimic the surface, we have used a slab geometry consisting of six atomic layers of Ru stacked in hexagonal closed packed (hcp) fashion along the [0001] direction, with a monolayer of Mn_xAu_{1-x} on the top surface, where x is the concentration of Mn. In order to minimize the interaction between periodic images along the direction normal to the surface, a vacuum separation of about 17.4 Å was used.

To obtain optimized structures, the Broyden-Fletcher-Goldfarb-Shanno algorithm was used; the atoms on the overlayer and the adjacent three substrate Ru layers were allowed to relax until the Hellmann-Feynman force on each atom of these layers was less than 0.001 Ry/a.u. along each Cartesian direction. The surface stress tensor was calculated using the Nielsen and Martin approach [37].

For Brillouin zone sampling, we have used Monkhorst-Pack k-point grids [27] commensurate with an (8×8) sampling for the (1×1) surface unit cell. To achieve faster convergence we have used the Marzari-Vanderbilt smearing technique [34] with smearing width equal to 0.01 Ry.

Use of these parameters leads to a Ru bulk lattice constant of 2.74 Å, which compares well with the experimental value of 2.70 Å [93]. For bulk Mn in the α-Mn structure, we have taken the nearest neighbor distances from Ref. [94].

For all our calculations we have allowed relaxation of the pseudomorphic single layer of Mn_xAu_{1-x} placed on the Ru(0001) substrate, as well as of single-component monolayers

of Mn on Ru(0001) or Au on Ru(0001); the slab with the overlayer is assumed to be in hcp stacking. As Ru is known to be a hard material, the diffusion of the overlayer atoms into the substrate is considered to be unlikely and is therefore not considered. For the alloy structures, different atomic arrangements of the overlayer atoms are taken into account by considering all possible periodic structures containing two, three, four, and five atoms per surface supercell, and several containing six atoms per surface supercell (see Appendix in Ref. [91] for the algorithm used to generate these). In this way, for Mn_xAu_{1-x}/Ru(0001), with x ($= 0.17, 0.2, 0.25, 0.33, 0.4, 0.5, 0.6, 0.67, 0.75, 0.8$ and 0.83), 41 different structures are obtained; these are shown in Appendix A to this thesis. Further, for each structure, calculations are performed for both non-magnetic (NM) and ferromagnetic (FM) configurations.

Our substrate is oriented such that the x- and y-axes correspond to the [1000] and [01$\bar{1}$0] directions, respectively, and the z-axis is [0001], which is perpendicular to the surface plane. We have divided all the structures, according to their structural similarities, into the following eight groups (see Appendix A):

(A) structures having a single-atom-wide stripe of Mn atoms, separated by Au atoms, along the x-axis,

(B) structures having a more-than-one-atom-wide stripe of Mn atoms along the x-axis,

(C) structures having a single zigzag stripe of Mn atoms along the y-axis,

(D) structures having a more-than-one-atom-wide zigzag stripe of Mn atoms along the y-axis,

(E) structures having isolated Mn atoms surrounded by Au atoms,

(F) structures having Mn dimers surrounded by Au atoms,

(G) a structure having a labyrinth-like pattern,

(H) structures with isolated Au atoms surrounded by Mn atoms.

4.5 Results

Here, we examine the energetics of alloy formation for surface alloys of the composition Mn_xAu_{1-x}/Ru(0001), with $0 \leq x \leq 1$. We wish to first verify whether mixed phases are favored over phase-segregated ones. Second, we wish to estimate the relative importance of three types of interactions that can promote the formation of surface alloys: (i) band energy, also sometimes referred to as cohesive interactions, (ii) magnetic interactions, (iii) elastic interactions, more specifically the relief of surface stress that arises from the mismatch in size between overlayer atoms and the substrate. Here, we restrict ourselves to the ferromagnetic (FM) and the non-magnetic (NM) configurations when examining these issues.

4.5.1 Optimized structures

We have obtained the optimized geometries of all the structures considered here of Mn_x-Au_{1-x}/Ru(0001), by performing non-spin-polarized and spin-polarized calculations for the NM and the FM configurations, respectively.

Considering the single-component monolayers, we find that for Au/Ru(0001), the first interlayer distance d_{o1}^{Au} (between the Au overlayer and the first Ru substrate layer) is expanded by 14% with respect to d_{bulk}^{Ru}, the bulk interlayer separation in Ru, whereas for Mn/Ru(0001), d_{o1}^{Mn} is contracted by 12% in the NM case, but by only 0.4% in the FM case. The expansion (contraction) is expected, since Au (Mn) atoms are larger (smaller) than Ru atoms. Note that d_{o1}^{Mn} increases by $\sim 13\%$ on going from the NM to FM configuration; it is well-known that spin-polarization increases the effective sizes of atoms.

In the case of the surface alloys, the overlayer is found to be considerably buckled, with the Mn atoms lying closer to the Ru substrate than the Au atoms. Since the overlayer is buckled, we cannot define a single interlayer distance, but can compute the value of d_{o1} for different atoms, by considering the difference in the z-coordinates of atoms in the overlayer and first substrate layer. For Mn atoms, we find 1.81 Å $\leq d_{o1} \leq$ 2.15 Å when considering NM configurations, and 2.14 Å $\leq d_{o1} \leq$ 2.21 Å when considering FM configurations. Once

again, we observe an enhancement of d_{o1}^{Mn} in the FM case due to the magneto-volume effect; we will come back to this point further below while discussing the effective coordination number.

We quantify the buckling of the alloy overlayer by $d_b \equiv d_{o1}^{Au} - d_{o1}^{Mn}$. We find that permitting spin polarization significantly reduces buckling: d_b ranges from 0.33 Å to 0.52 Å for NM configurations, but varies from 0.20 Å to 0.33 Å in the case of FM configurations. The buckling of the overlayer is of particular interest since it can significantly enhance the Dzyaloshinskii-Moriya interaction (see Chapter 5), which is an asymmetric exchange interaction between the magnetic atoms (Mn) acting via the non-magnetic atoms (either Au or Ru) [95].

4.5.2 Formation energy

In order to gauge the effect of magnetic interactions on Mn_xAu_{1-x}/Ru(0001), we have first computed the energy difference between the NM and the FM configurations, ΔE_{FM-NM}, for every structure considered by us [see Fig. 4.1(a)]. We find that $\Delta E_{FM-NM} < 0$ always, i.e., for all our structures, ferromagnetism is always favored over the non-magnetic configuration.

Two features of Fig. 4.1(a) are immediately striking and demand explanation: (i) $|\Delta E_{FM-NM}|$ increases with x, the relative concentration of Mn – this is to be expected because as the relative proportion of Mn atoms increases, so does the magnetic moment, and thus the energy lowering due to spin polarization, (ii) structures of a given type are clearly grouped together in this graph. Roughly speaking, the points seem to fall into three clusters (shown by brown dashed lines): one consisting of structures of types A, C, E, F and G (in all these structures, on average, a Mn atom has a rather large proportion of Au nearest-neighbors (NNs), and $|\Delta E_{FM-NM}|$ is found to be large), a second cluster consisting of structures of type B and D (in these, on average, a Mn atoms has a large proportion of Mn NNs and $|\Delta E_{FM-NM}|$ is found to be smaller) , and a third cluster consisting of structures of type H. While we could use hand-waving arguments, invoking the number of Mn NNs, to explain the clustering seen in this graph, we will instead postpone the discussion

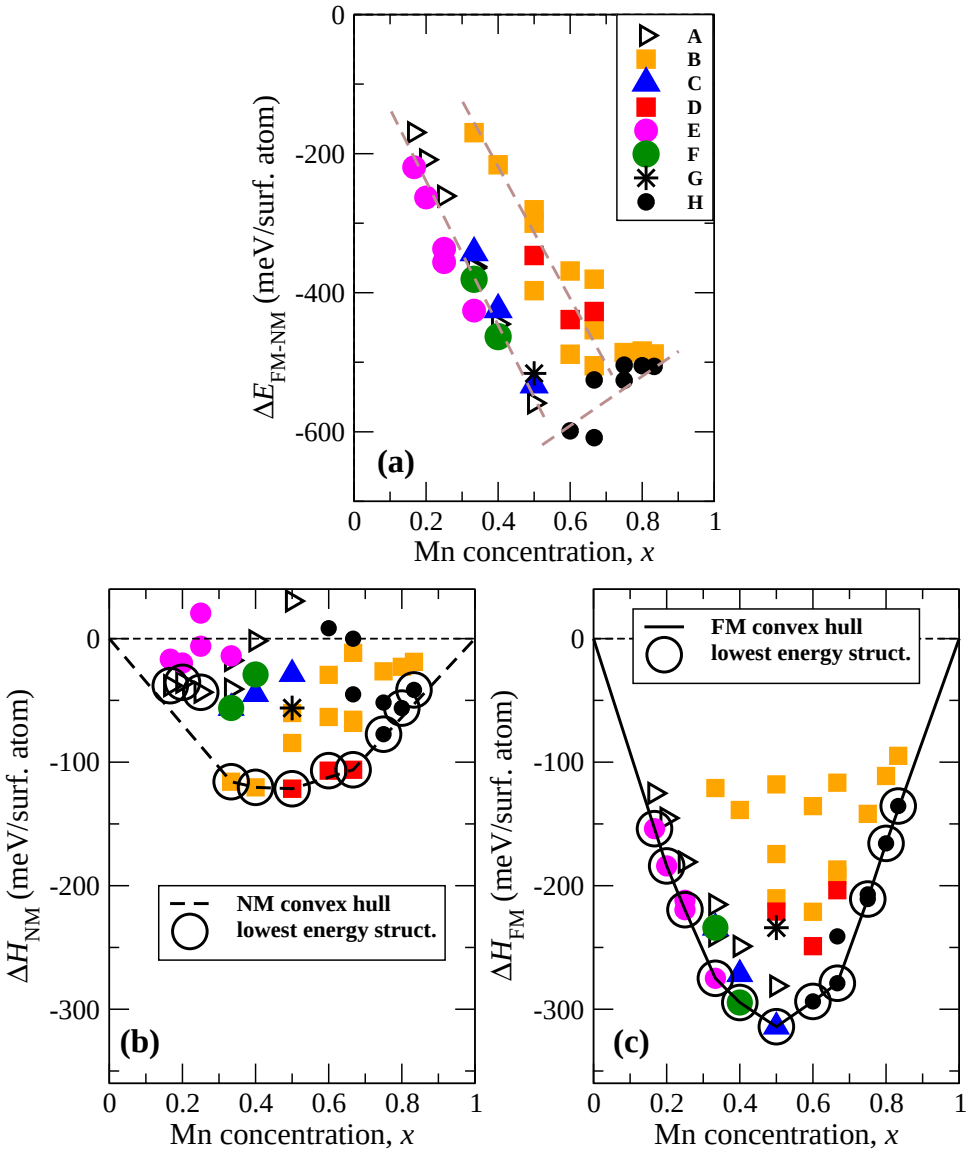

Figure 4.1: *Energetics of nonmagnetic (NM) and ferromagnetic (FM) phases of Mn_xAu_{1-x}/Ru(0001). (a) shows the energy difference $\Delta E_{\text{FM-NM}}$ between the FM and NM configurations for all the structures, and, (b) and (c) show the variation of formation energy ΔH as a function of x, for the NM and the FM configurations, respectively. The three brown dashed solid lines in (a) are guides to the eye, showing the clustering of types of structures. The black dashed and the solid lines in (b) and (c) indicate the NM and FM convex-hulls, respectively. The big black circles represent the lowest energy structures at each concentration, x. See the text for the description of the structures types A-H.*

until we can put it on a more quantitative footing by discussing the effective coordination number (ECN), coupled with our results for magnetic moments.

To find out whether Mn_xAu_{1-x} forms stable alloys on Ru(0001) or not, we have next

calculated the formation energy of the alloy with respect to phase-segregation to the single-component phases of Mn/Ru(0001) and Au/Ru(0001). The formation energy ΔH, is given by:

$$\Delta H \quad = E(\mathrm{Mn}_x\mathrm{Au}_{1-x}/\mathrm{Ru}) - xE(\mathrm{Mn/Ru}) - (1-x)E(\mathrm{Au/Ru}), \tag{4.1}$$

where $E(X)$ is the total energy of system X. A negative (positive) value of ΔH implies the formation of a stable (unstable) surface alloy. Note that to reduce errors arising from finite Brillouin zone sampling, the same supercell and k-point grid were always used when calculating the energies of all three systems in Eq. (4.1).

In Figs. 4.1(b) and 4.1(c), we have plotted the formation energy ΔH_{NM} and ΔH_{FM}, for all the structures in the NM and the FM configurations, respectively. It is interesting to note that: (i) in some cases ΔH_{NM} is positive, whereas ΔH_{FM} is always negative, (ii) $|\Delta H_{\mathrm{FM}}| \gg |\Delta H_{\mathrm{NM}}|$, and (iii) in general, the lowest energy structures differ in the NM and FM cases (except for a few phases at large x).

Findings (i) and (ii) show that, as has been found previously for the Fe-Au/Ru(0001) system [90, 91], here too magnetism contributes strongly to the miscibility of the surface alloys of $\mathrm{Mn}_x\mathrm{Au}_{1-x}$/Ru(0001).

At each x, a black circle indicates the structure having the lowest ΔH. In order to come to the conclusion in point (iii) above, we look at the black circles in Figs. 4.1(b) and 4.1(c), whereupon we see that in the NM configuration, these structures are of type A, B, D, and H, whereas in the FM configuration, they are of type C, E, F, and H. So, the structural preferences appear to be very different for the NM and the FM configurations, especially for $0 < x < 0.75$; only at a very high concentration of Mn (for $x \geq 0.75$), does the lowest energy structure in the NM and the FM configuration become the same (type H).

To determine which of these lowest energy structures of $\mathrm{Mn}_x\mathrm{Au}_{1-x}$/Ru(0001) are stable with respect to phase segregation, we have computed the NM and FM convex hulls [shown by the black dashed and the solid lines in Figs. 4.1(b) and Fig. 4.1(c), respectively]. Note

that out of the 41 structures considered by us, only four NM configurations and ten FM configurations lie on their respective convex hulls; the remaining configurations can be expected to phase-segregate to the two nearest phases lying on the convex hull.

In Figs. 4.2 and 4.3, we have shown the relaxed atomic geometries corresponding to the lowest energy NM and FM structure at each x [see large black circles in Fig. 4.1(b) and Fig. 4.1(c)]. Those structures that lie on the convex hull are indicated with a $\star$. Note that at $x = 0.83$ the lowest energy FM structure lies only 2.7 meV/surface atom above the tie line of the convex hull. As in the case of Fe-Au/Ru(0001) [91], we find that in the NM configuration, striped structures featuring alternating stripes of Mn and Au atoms are most favored (see Fig. 4.2). In contrast, in the FM configuration, for low x, phases with

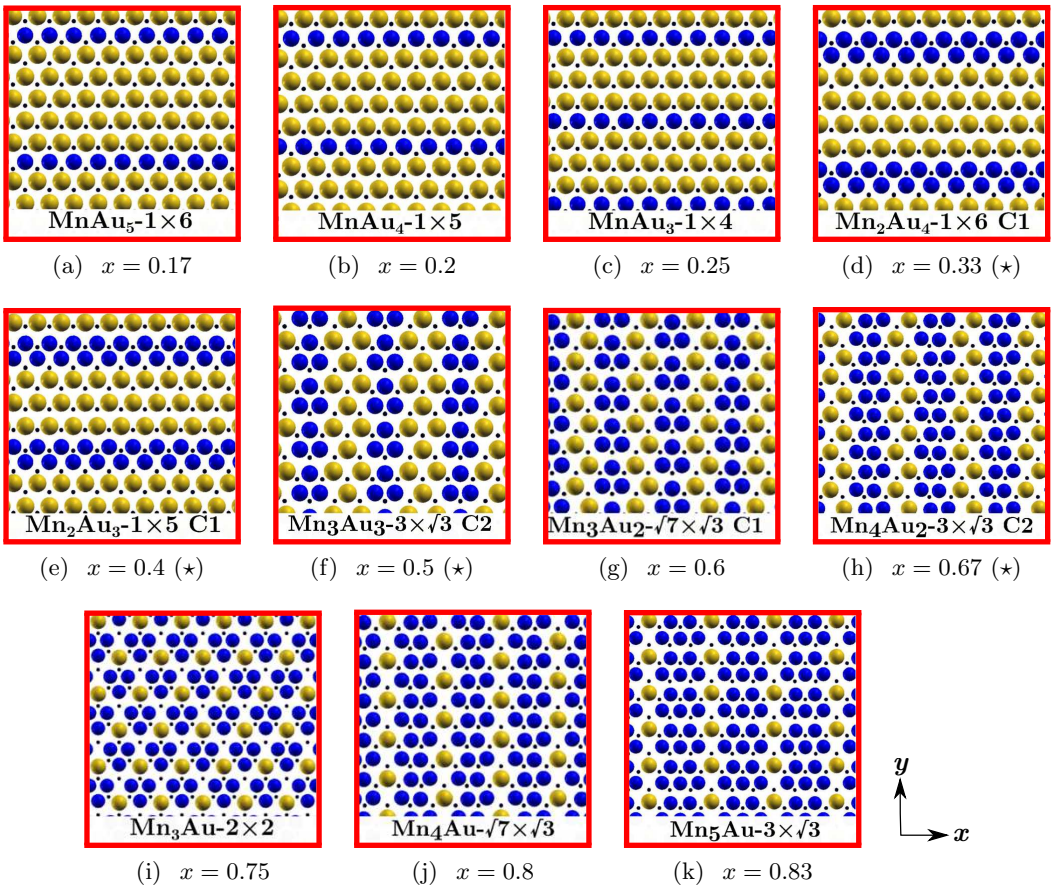

(a) $x = 0.17$ (b) $x = 0.2$ (c) $x = 0.25$ (d) $x = 0.33$ ($\star$)

(e) $x = 0.4$ ($\star$) (f) $x = 0.5$ ($\star$) (g) $x = 0.6$ (h) $x = 0.67$ ($\star$)

(i) $x = 0.75$ (j) $x = 0.8$ (k) $x = 0.83$

Figure 4.2: *The top views of the lowest energy structures of ΔH_{NM} vs. x curve of Mn_xAu_{1-x}/Ru(0001) [Fig. 4.1(b)] are shown above. The blue and the golden spheres represent the Mn and Au atoms, respectively, while the black dots represent the Ru atoms of the first substrate layer. The structures that fall on the NM convex-hull are indicated by a $\star$ mark.*

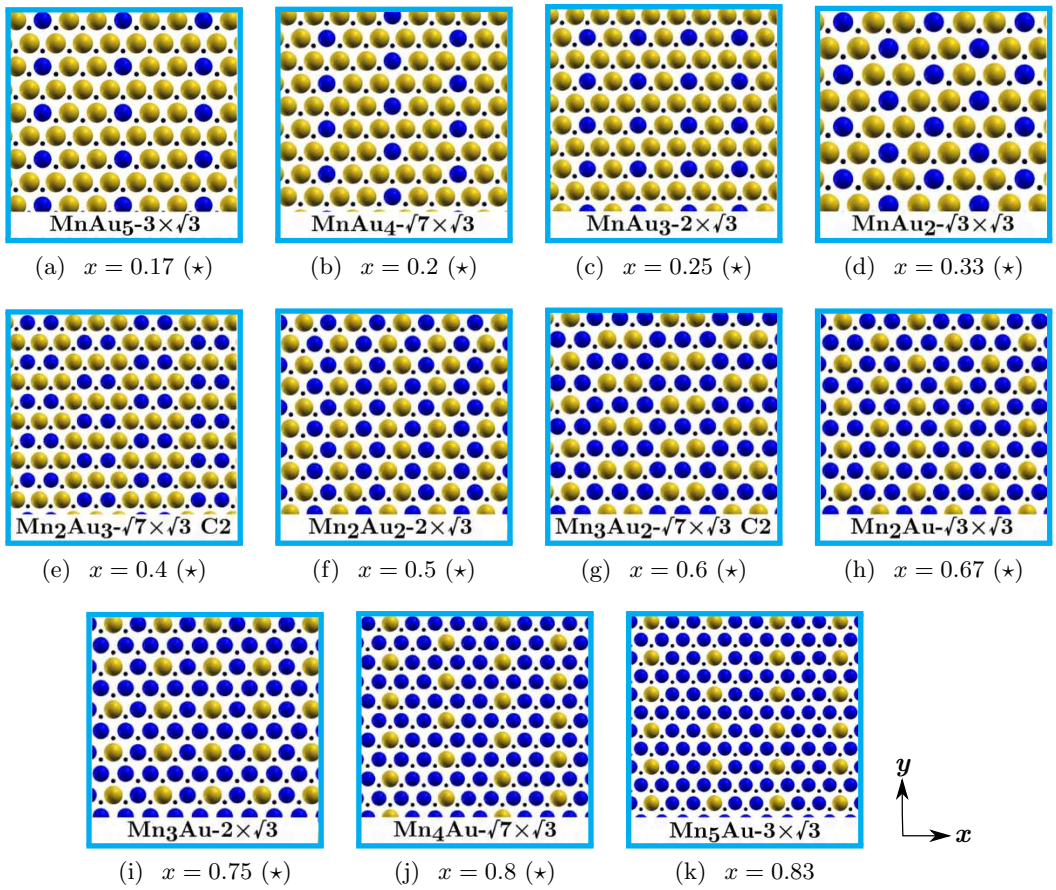

(a) $x = 0.17$ ($\star$) (b) $x = 0.2$ ($\star$) (c) $x = 0.25$ ($\star$) (d) $x = 0.33$ ($\star$)

(e) $x = 0.4$ ($\star$) (f) $x = 0.5$ ($\star$) (g) $x = 0.6$ ($\star$) (h) $x = 0.67$ ($\star$)

(i) $x = 0.75$ ($\star$) (j) $x = 0.8$ ($\star$) (k) $x = 0.83$

Figure 4.3: *The lowest energy structures of ΔH_{FM} vs. x curve of Mn_xAu_{1-x}/Ru(0001) [Fig. 4.1(c)] are shown above. The blue and the golden spheres represent the Mn and Au atoms, respectively, while the black dots represent the Ru atoms of the first substrate layer. The structures that fall on the FM convex-hull are indicated by a $\star$ mark.*

one or two isolated Mn or Au atoms become lower in energy than the striped phases.

4.5.3 Effective coordination number and the competition between band energy and magnetic energy

In this section, we wish to gain a physical understanding of why different kinds of structures are favored in the NM and FM situations, as well as the origins of the stability of the surface alloys. In order to do so, we need to examine the number of neighbors of each type that Mn atoms, in particular, have in different structures, and how far away they are. Simply counting the number of nearest neighbor atoms (of any type) would not suffice, yielding a nominal coordination number of nine for any surface atom on a hcp(0001) surface. Instead,

it is of considerable utility to define the effective coordination number of an Mn atom, given by [96]:

$$\mathrm{ECN(Mn)} = \frac{\sum_{i=1}^{M} \rho_{T_i}(|\mathbf{r}_i|)}{\sum_{j=1}^{N} \rho_{\mathrm{Mn}}^{\mathrm{bulk}}(|\mathbf{r}_j|)}, \tag{4.2}$$

where in the numerator, the sum is taken over all the neighboring atoms i, of type T_i, at a distance $|\mathbf{r}_i|$ from an Mn atom in the overlayer. In the denominator, the sum is taken over all the neighboring Mn atoms j, at a distance $|\mathbf{r}_j|$ from an Mn atom of bulk Mn. $\rho_T(|\mathbf{r}|)$ is the atomic charge density at a distance $|\mathbf{r}|$ from the nucleus of an isolated atom of type T, while M and N are the number of nearest neighbors of the Mn atom under consideration, in $\mathrm{Mn}_x\mathrm{Au}_{1-x}$/Ru(0001) and bulk Mn, respectively. In $\mathrm{Mn}_x\mathrm{Au}_{1-x}$/Ru(0001), an Mn atom can, in general, have three types of atoms as nearest neighbors, i.e., T can be any one of Mn, Au or Ru. When computing the denominator in Eq. (4.2), we have considered the α-Mn structure, which is the zero-temperature phase of bulk Mn. In those structures that contain more than one kind of symmetry-inequivalent Mn atom, we compute ECN(Mn) by taking an appropriately weighted average over the different kinds of Mn atoms. For notational convenience, in the rest of this manuscript, we will suppress the index "Mn" when discussing the effective coordination number, i.e., ECN $\equiv$ ECN(Mn).

The ECN reflects the ambient electron density at the site of an Mn atom, in the spirit of the embedded atom model or effective medium theory [97–99]. It decreases when bond lengths increase (e.g., when neighboring atoms are of larger size, or upon switching on exchange interactions) and/or when the number of nearest neighbors is reduced (e.g., on going from the bulk to the surface). It also reflects the type (Mn, Au or Ru) of neighbors.

The ECN provides an ideal tool for examining two of the principal interactions that compete in determining the stability of surface alloys, viz., the band energy E_b and magnetic energy E_m. When the ECN is large, hybridization is enhanced, and the bandwidth is increased. As a result, $E_b \equiv \int_{-\infty}^{E_F=0} \epsilon n(\epsilon)\, d\epsilon$ becomes large, where ϵ runs over the electronic energies, $n(\epsilon)$ is the electronic density of states, and E_F is the Fermi energy (set equal to

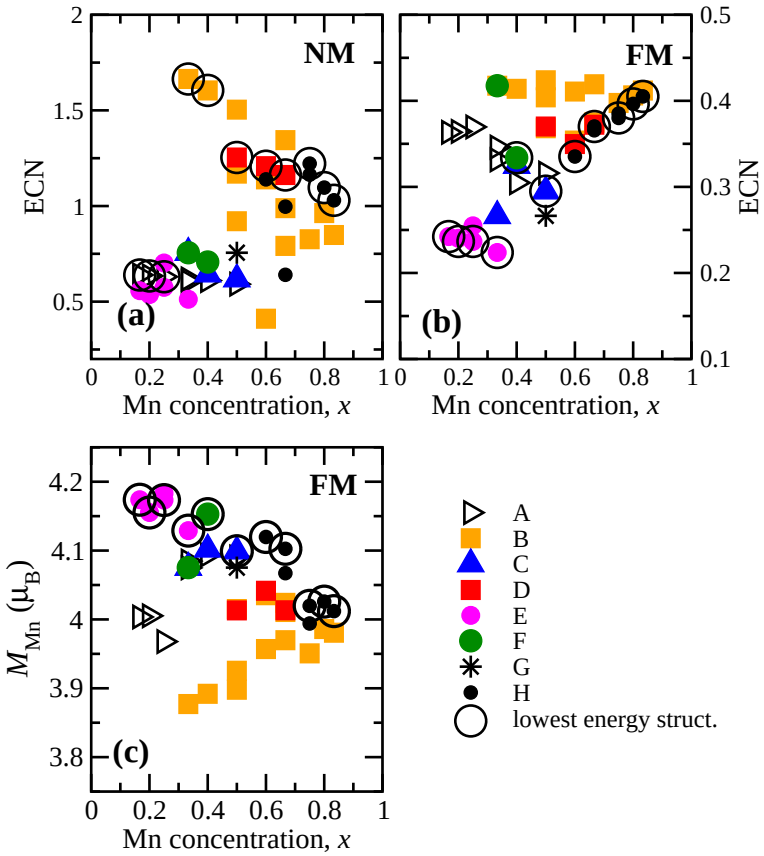

Figure 4.4: *The variation of ECN, the effective coordination number of the overlayer Mn atoms, as a function of Mn concentration x for (a) the nonmagnetic (NM) and (b) the ferromagnetic (FM) configurations of $Mn_xAu_{1-x}/Ru(0001)$. (c) shows the variation of the Mn magnetic moments M_{Mn}, as a function of x in the FM configuration. The points which lie on the NM and the FM convex hulls (in Fig. 4.1(b) and Fig. 4.1(c), respectively) are shown by large black circles. See text for description of structure types A-H. Note that the y-axis scale is different in (a) and (b).*

0). Note that with this definition, $E_b < 0$. Note also that a large ECN would imply a broad and low $n(\epsilon)$, and thus a low value of $n_{\rm NM}(E_F)$, the (non-magnetic) density of states at the Fermi energy. According to the Stoner model, this would disfavor ferromagnetism. In contrast, when the ECN is low, the bandwidth is decreased, and exactly the reverse arguments apply. Thus, in such a situation, E_b would be small and $E_m = -IM^2$ would tend to be large, where I is the Stoner parameter, and M is the magnetic moment.

Let us first consider the non-magnetic (NM) case. In such a situation, $E_m = 0$, and therefore E_b prevails. One should therefore observe a tendency for the structures with highest ECN to be favored always, in the NM case. In Fig. 4.4(a), we have plotted our results for ECN vs. Mn concentration x, for the NM configurations. The structure found

to have the lowest energy at each x has been circled in black. We find that for almost every x, our expectation is borne out: the most energetically favored NM structure also has the highest ECN. The only exceptions occur at $x = 0.5$ and $x = 0.67$, for each of which the structure that lies lowest in energy, while having a very high ECN, does not have the highest value of ECN among all the structures considered. In order to explain these two exceptions, we will (further below) examine the values of surface stress.

We recall that the phases that appeared in the NM convex hull featured more-than-one-atom-wide stripes of Mn atoms, running along either x or y. In these structures, Mn atoms have several Mn NNs. Also, an examination of Figs. 4.2(d)–4.2(f) and 4.2(h) will show that Mn-Mn distances are reduced considerably in such structures (resulting in a "clustering" of Mn atoms), compared to the Ru-Ru NN distance in the substrate. For these reasons, the ECN is significantly enhanced in these structures, and E_b (and therefore ΔH_{NM}) becomes large and negative.

One would normally expect the structures with isolated Mn atoms to have lower values of ECN compared to the striped structures. However, we find that in the NM case the structures of type A (single stripes of Mn atoms along x-axis) and E (isolated Mn atoms surrounded by Au atoms) have almost the same values of ECN. This is because increases/decreases in ECN due to neighbors in the surface plane are offset by decreases/increases in ECN due to longer/shorter bonds to substrate Ru atoms. For example, at $x = 0.25$, the (1×4) structure [see Fig. A1(c) in Appendix A] of type A has $d_{\mathrm{o1}}^{\mathrm{Mn}} = 1.94$ Å, while the (2×2) structure [see Fig. A.9(d) in Appendix A] of type E has $d_{\mathrm{o1}}^{\mathrm{Mn}} = 1.81$ Å.

We now examine how the scenario changes in the ferromagnetic (FM) case. In Fig. 4.4(b) we have shown how the ECN changes with x for the various structures considered by us, in the FM case. The very first thing we notice when comparing with Fig. 4.4(a), which plotted similar data for the NM case, is that the values of ECN have decreased [note that the y-axis scale is different in Figs. 4.4(a) and 4.4(b)]; this is because of the expansion of bond-lengths due to the magneto-volume effect. Second, we see that as for the NM case, striped structures tend to have larger values of ECN than structures that feature isolated atoms of one type surrounded by atoms of the other type. Third, and most importantly,

we see that the position of the black circles (denoting the structures with lowest energy at each concentration x) is completely reversed in the FM case, compared to the NM case. Whereas we had seen above that in the absence of magnetic interactions, structures with high ECN were favored, now it is clear that upon turning on magnetism, structures with low ECN are favored. At every single value of x, the structure with the lowest energy is also the one with the lowest ECN, with the exception of two values of x, where the lowest-energy structure has either the second-lowest ECN (at $x = 0.4$) or the third-lowest ECN (at $x = 0.5$). However, we note that in these cases, the difference in ECN between the low-lying structures is very small, and given the assumptions made in calculating the ECN (such as approximating the ambient electronic charge density as the sum of the atomic charge densities of NNs), we do not consider these differences to be significant.

As briefly discussed above, a low value of ECN will lead to a high (non-magnetic) density of states at E_F, and this in turn will, by the Stoner argument, lead to a high magnetic moment. Unambiguous evidence of the validity of this argument is provided by Fig. 4.4(c), where we have plotted M_{Mn}, the magnetic moment per Mn atom, as a function of Mn concentration x. We see a clear correlation between the effective coordination of Mn atoms, as plotted in Fig. 4.4(b), and their magnetic moment, as shown in Fig. 4.4(c). Crucially, we see that at every single value of x, the lowest energy structure also has the largest value of M_{Mn}. Similar behavior has also been observed previously in the case of the Fe-Au/Ru(0001) system [90], though there the supporting evidence in the form of the ECN was not established. The trend shown in Figs. 4.4(b) and 4.4(c) shows that the magnetic interactions E_m are dominating over the band energy E_b in the Mn-Au/Ru(0001) system, and provide a driving force for surface alloy formation. Additional evidence of this was already provided above by the fact that $|\Delta H|$ increased significantly on going from the NM to the FM case [see Figs. 4.1(b) and (c)].

One particular case that brings out the importance of the magneto-volume effect is the relative position of structures of type B (more-than-one-atom wide stripes of Mn, oriented along the x-axis; drawn as orange squares) and type H (isolated Au atoms surrounded by Mn atoms; drawn as black dots) in Figs. 4.4(a) and (b). When the atoms in the surface

layer do not move significantly away from the hcp hollow sites (as happens in the FM case), structures of type B and H have very similar values of ECN. However, in the NM case, for structures of type H, we notice that there is perceptible "clustering", so that groups of Mn atoms come much closer together [see, e.g., Figs. A.15(a)–(g) in Appendix A]. As a result, for such structures the value of ECN increases, and becomes larger than for structures of type B.

4.5.4 Role of surface stress

It has long been known that surface stress can play an important role in the formation of surface alloys, and indeed it was long believed that the relief of surface stress provided the main driving force for mixing at the surface [74]. We have computed the surface stress for all the systems considered in this study. Since we used asymmetric slabs, where the overlayer was deposited on only one side of the Ru(0001) substrate, this was done by subtracting out the surface stress due to the clean bottom surface. The sign convention used here is that positive/negative values of surface stress denote compressive/tensile stress.

The theoretically computed NN distances in bulk Mn, Au and Ru are 2.47, 2.96 and 2.68 Å, respectively. Thus (ignoring, temporarily, the fact that the effective size of a surface atom can be expected to be different from that of a bulk atom) one may expect that a monolayer of Au/Ru(0001) would be under compressive stress, but a monolayer of Mn/Ru(0001) would be under tensile stress. Indeed, upon carrying out the computations on Au/Ru(0001), we find that it is under compressive stress, with $\sigma_{xx} = \sigma_{yy} = 0.26$ eV/Å^2. In contrast, a NM monolayer of Mn/Ru(0001) is under tensile stress, with $\sigma_{xx} = \sigma_{yy} =$ -0.64 eV/Å^2. In the FM case, since the effective size of Mn atoms at the surface increases, this reduces the size mismatch between the substrate Ru atoms and the overlayer Mn atoms, and these numbers are shifted upward, with $\sigma_{xx} = \sigma_{yy} = 0.24$ eV/Å^2.

Since the two end-components have stress of opposite sign, this suggests that it should be favorable to form mixed phases of Mn and Au on the Ru(0001) substrate, thereby reducing the surface stress. In Fig. 4.5 we show how the diagonal components of the surface stress tensor vary with Mn concentration x, for the various structures considered

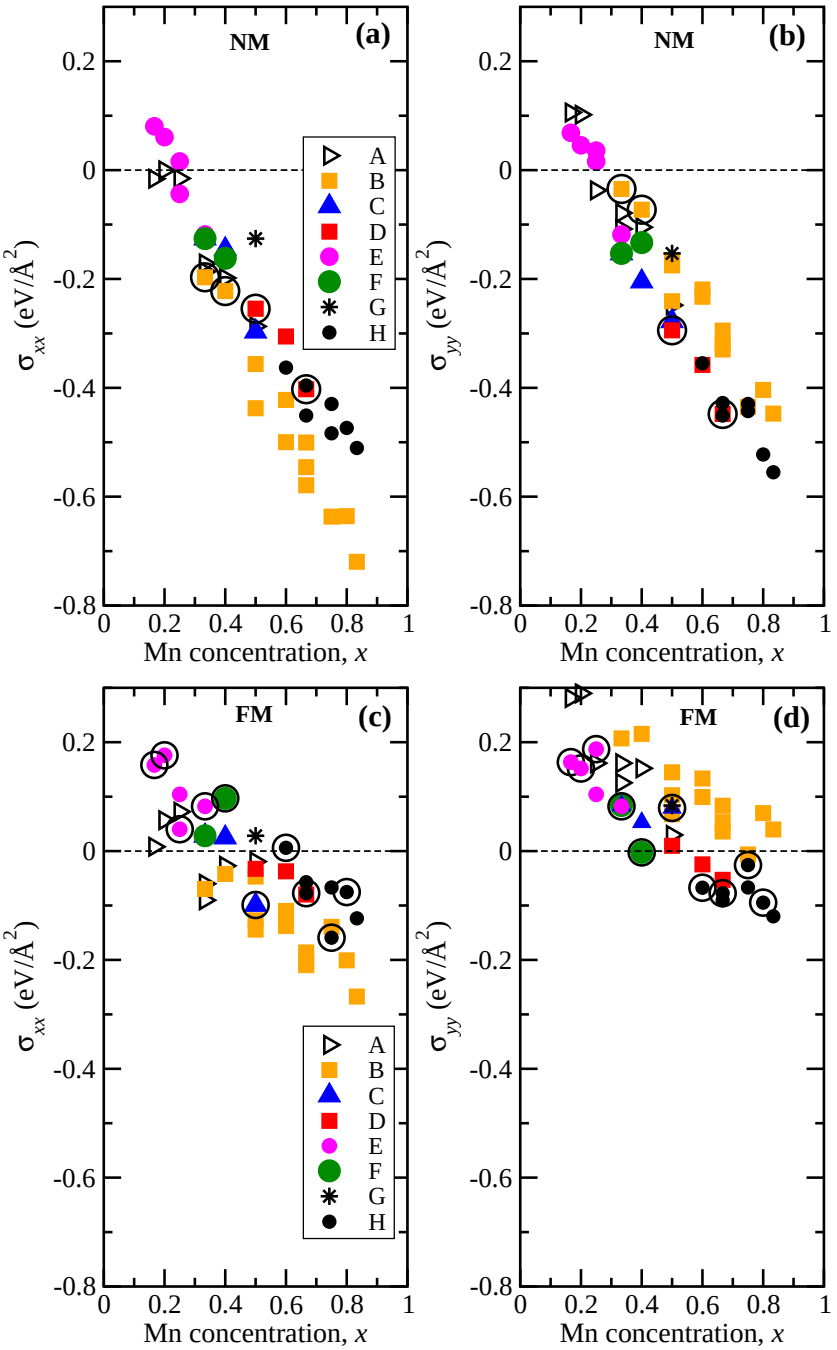

Figure 4.5: *Plot of xx-component and yy-component of the surface stress tensor σ of $Mn_xAu_{1-x}/Ru(0001)$ as a function of Mn concentration x in the NM [(a) and (b)] and the FM [(c) and (d)] configurations. The structures which lie on the NM and the FM convex hulls (in Fig. 4.1(b) and Fig. 4.1(c), respectively) are shown by large black circles.*

by us, for both NM and FM configurations. Note that in the NM case, the surface stress goes to zero for $x \sim 0.25$, whereas in the FM case, the surface stress goes to zero for $x \sim 0.5$.

Note also that the range of values of surface stress exhibited by the various structures in the FM case is much smaller than in the NM case, and the onset of ferromagnetism has also, in most cases, considerably reduced the magnitude of the surface stress.

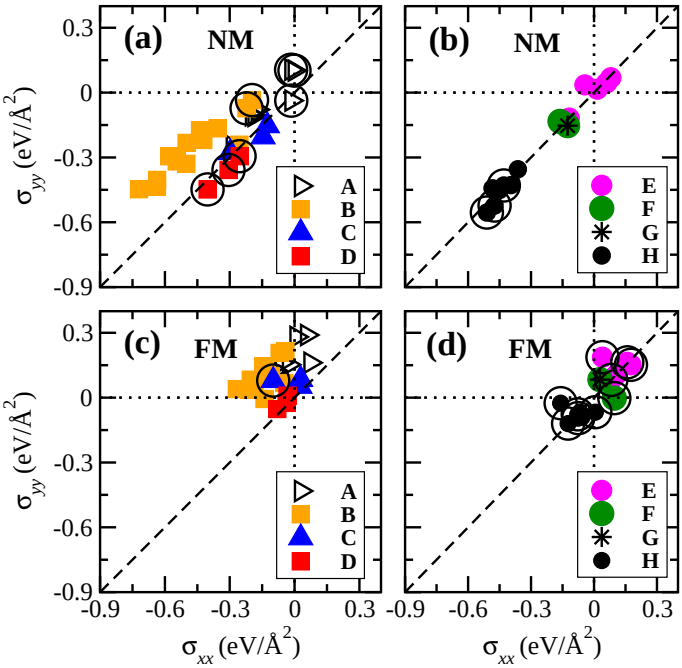

Figure 4.6: *Plot of xx-component vs. yy-component of the surface stress tensor σ of Mn_xAu_{1-x}/Ru(0001) in the NM [(a) and (b)] and the FM [(c) and (d)] configuration. The $\sigma_{xx} = \sigma_{yy}$ line is indicated by the dashed line. The structures which lie on the NM and the FM convex hulls (in Fig. 4.1(b) and Fig. 4.1(c), respectively) are shown by large black circles.*

Our results for surface stress clearly reflect the type of structure. In Figs. 4.6(a) and (b) we have plotted σ_{yy} vs. σ_{xx} for the NM case, for the striped structures and isotropic structures, respectively. We see in Fig. 4.6(a) that most of the points lie in the third quadrant, reflecting biaxial tensile stress. Moreover, those structures (types A and B) that consist of stripes running along the x direction, can only relieve stress along the y direction, and therefore have $|\sigma_{xx}| > |\sigma_{yy}|$. The reverse is true for structures (types C and D) with stripes running along the y direction, which therefore have $|\sigma_{yy}| > |\sigma_{xx}|$. For isotropic structures, as expected [see Fig. 4.6(b)] we have $\sigma_{yy} = \sigma_{xx}$.

We are now in a position to address the question of why we had two "exceptions", in the NM case, to the rule that for each Mn concentration x, the highest ECN corresponded to the lowest energy. The first exception occurred at $x = 0.5$, where the $(3\times\sqrt{3})$-C2 structure

of type D had the highest ECN, but the (1×4) structure of type B had the lowest energy. On examining Fig. 4.6(a), we see that the former structure has an anisotropic surface stress tensor, whereas the latter has a nearly isotropic surface stress tensor. We believe that this is the reason why the latter structure is favored over the former. Similarly, at $x = 0.67$, the (1×3) structure of type D has the highest ECN but an anisotropic surface stress tensor, whereas the $(3 \times \sqrt{3})$-C2 structure of type B has an almost isotropic surface stress tensor and the lowest energy. We note that there are other well-known cases, such as the herringbone reconstruction of Au(111) [100], where the ground state structure of a surface is driven by the tendency to make the surface stress more isotropic.

In Figs. 4.6(c) and 4.6(d) we have plotted σ_{yy} vs. σ_{xx} for the FM case, for striped and isotropic structures, respectively. As before, the lowest energy structures have been circled in black. Comparing with Figs. 4.6(a) and 4.6(b), we note many points corresponding to the striped structures along the x-axis have moved from the third quadrant to the second quadrant: the stress along the y-direction is now compressive, whereas in the absence of magnetism it was tensile, this is again because the effective size of Mn atoms has increased due to the presence of magnetism. More importantly, this increase in the effective size of Mn atoms has reduced the magnitude of surface stress considerably; the points in Figs. 4.6(c) and 4.6(d) lie much closer to the origin than do the points in Figs. 4.6(a) and (b). Thus for the Mn-Au/Ru(0001) system, magnetism promotes mixing in two ways: (i) since Mn atoms can increase their magnetic moments in the mixed structures, as compared to the phase-segregated phase, E_m favors the formation of surface alloys with high moments, (ii) the magneto-volume effect increases the relative size of Mn atoms and thus reduces the surface stress in mixed phases.

4.6 Summary

Using DFT calculations, we have shown that Mn_xAu_{1-x}/Ru(0001) forms stable surface alloys. The stability of the alloy has been examined in the light of the band energy, the magnetic energy and the stress-relief mechanism. We show that both the band energy

and the magnetic energy are related to the effective coordination number (ECN); while band energy increases as the ECN increases, the magnetic energy increases as the ECN decreases. We see very clearly that different structures are favored in the absence and presence of magnetism. In the non-magnetic case, at each composition, the structure with the highest ECN is favored. In a complete reversal, upon turning on ferromagnetic interactions, at each composition, the structure with the lowest ECN is favored. As the ECN is rather quick and easy to estimate, this provides a convenient rule of thumbs when trying to assemble possible structures that need to be considered when studying surface alloys. Our analysis show that stability of this alloy is primarily dominated by magnetism. Magnetism promotes mixing in Mn_xAu_{1-x}/Ru(0001) by increasing the magnetic moments in the alloy phases as compared to the phase-segregated phases and also by helping to reduce the surface stress in the alloy phases via the magneto-volume effect.

Though only ferromagnetic configurations are considered here, it is possible to have antiferromagnetic coupling between Mn atoms of Mn_xAu_{1-x}/Ru(0001). In the next chapter, we consider such antiferromagnetic ordering for one of the alloy composition: $MnAu_2$-/Ru(0001). In addition, we also consider the possibility of having a non-collinear magnetic structure for this system, such as spin spiral.

Chapter 5

Searching for spin spirals: surface alloys $FeAu_2$/Ru(0001) and $MnAu_2$/Ru(0001)

5.1 Introduction

The spin-orbit interaction in magnetic systems leads to the possibility of stabilizing exotic non-collinear magnetic structures, such as spin spirals induced by the Dzyaloshinskii-Moriya (DM) interaction [5, 6]. The recent emergence of the field of spintronics has led to additional interest in such systems. As an example, it has been suggested that the spin torque arising from the flow of a spin-polarized current through a system where the spins are arranged in a chiral fashion can lead to various phenomena such as the switching of magnetization, and microwave emission [7, 8]. The spin-orbit interaction can also lead to obtaining magnetic structures with significantly enhanced magnetic anisotropy energy (MAE) [101]. The MAE is defined as the energy barrier that has to be overcome to orient the magnetization oppositely, along the easy axis, by rotating it through a hard axis; for information storage applications, it is crucial that it should have a high value, so that stored data is not lost through thermal fluctuations. In this chapter, we use *ab initio* density functional theory to explore such issues for ultrathin surface alloys, created by the

co-deposition of two elements on a substrate. In particular, we obtain the magnetic ground states of two surface alloy systems: $FeAu_2$/Ru(0001) and $MnAu_2$/Ru(0001), by exploring the phase space of both collinear (ferromagnetic and antiferromagetic) and noncollinear magnetic structures of these alloys.

5.2 Spin Spirals

In a spin spiral, the moments on all magnetic atoms have approximately the same magnitude, but their direction rotates by a phase factor as one proceeds from one atom to the next, along the direction of propagation. Each spin spiral is characterized by a wavelength λ, where $\lambda = 2\pi/|\mathbf{q}|$, $\mathbf{q}$ being the wavevector. So, for a spin spiral with wavevector $\mathbf{q}$, the magnetic moment of a magnetic atom at position $\mathbf{R}$ is given by:

$$\mathbf{m}(\mathbf{R}) = m \begin{pmatrix} \sin\alpha \cos(\mathbf{q}\cdot\mathbf{R}) \\ \sin\alpha \sin(\mathbf{q}\cdot\mathbf{R}) \\ \cos\alpha \end{pmatrix}, \tag{5.1}$$

where m is the magnitude of the magnetic moment, and α is the cone angle of the spin spiral.

In order to describe a spin spiral, in addition to a wavevector $\mathbf{q}$, one must specify an axis about which the spins rotate. In helical spin spirals, this axis of rotation is parallel to $\mathbf{q}$, whereas in cycloidal spin spirals, it is perpendicular to $\mathbf{q}$. Symmetry arguments predict that, on an isotropic surface, cycloidal spin spirals will always be lower in energy than helical spin spirals [95,102]. In planar spin spirals, the spins are confined to a plane normal to the rotation-axis; the Dzyaloshinskii-Moriya interaction is expected to be largest in such a situation [5, 103]. Further, in homogeneous spin spirals, the relative angle between neighboring spins is always a constant, whereas for an inhomogeneous spin spiral, the relative angle between neighboring spins can vary. In this study, we restrict ourselves to considering only homogeneous, cycloidal, planar spin spirals.

5.3 Our Motivation

Only a few thin-film systems have been shown to display a spin spiral ground state: single and double layers of Mn on W(110) [104,105], a single monolayer of Mn on W(001) [102], a double monolayer of Fe on W(110) [106], and a PdFe bilayer on Ir(111) [107]. It is therefore appealing to see whether alloying can lead to more systems of this kind.

In this study, we focus on two supported surface alloy systems, $FeAu_2$/Ru(0001) and $MnAu_2$/Ru(0001). In order to better distinguish those effects that arise from the presence of the Ru substrate, we also consider two hypothetical systems, viz., a freestanding $FeAu_2$ monolayer, and a freestanding $MnAu_2$ monolayer, both maintained at a nearest-neighbor spacing equal to that in bulk Ru. Ru crystallizes in the hexagonal close packed (hcp) structure, and thus the Ru(0001) surface has a triangular lattice, which offers an ideal substrate to study magnetic frustration, that can lead to a variety of interesting magnetic structures. Fe and Mn are both magnetic elements, but while bulk Fe is ferromagnetic, bulk α-Mn is non-collinear antiferromagnetic at room temperature [81]. Moreover, while Fe and Au are bulk-immiscible, Mn and Au form bulk alloys, such as $MnAu_2$, which displays a helical arrangement of the spins on Mn atoms [82,89]. When a monolayer of Fe is deposited on Ru(0001), the resulting Fe/Ru(0001) system has a 120° Néel state [108]. In contrast, Mn/Ru(0001) displays a row-wise antiferromagnetic structure [109]. $FeAu_2$/Ru(0001) has been shown, both experimentally and theoretically [90], to have a pseudomorphic $(\sqrt{3}\times\sqrt{3})$ structure, with long-range-order. In this structure, the Fe atoms in the overlayer constitute a triangular superlattice, and every Fe atom is surrounded by six Au atoms [see Fig. 5.1(a)]. It has been shown, by density functional theory calculations, that this structure is stabilized primarily by magnetism rather than stress relief [90]. $MnAu_2$/Ru(0001) has a similar structure, with the Fe atoms replaced by Mn atoms. We have shown in Chapter 4 that this structure is also stable against phase-segregation. The presence of Au and Ru atoms is interesting for our purpose, since they are expected to enhance spin-orbit coupling, and thus increase both the DM interaction and the MAE.

The outline of this chapter is as follows. In Section 5.4, we describe the four systems on

which we have carried out our calculations. Next, in Section 5.5.1, we lay out the relevant formalism, describing separately each of the three main contributions to the total energy, viz., the symmetric exchange energy, the Dzyaloshinskii-Moriya energy, and the magnetic anisotropy energy. Next, in Section 5.5.2, we give the technical details of our calculations. Our results are presented in Section 5.6. Section 5.7 contains a discussion of our results. We present a summary in Section 5.8. In Appendix B to this thesis, we discuss issues related to the applicability of the force theorem.

5.4 Systems

As mentioned above, in order to clearly separate out the effects of the substrate, we perform calculations on XAu_2 layers (X = Fe or Mn), both with and without the Ru(0001) substrate. Thus, we have studied four systems: (A) freestanding $FeAu_2$ monolayer, (B) freestanding $MnAu_2$ monolayer, (C) $FeAu_2$/Ru(0001), and (D) $MnAu_2$/Ru(0001). Note that in all four cases, the in-plane nearest-neighbor spacing is fixed as equal to the experimental value for Ru(0001) = 2.70 Å [110].

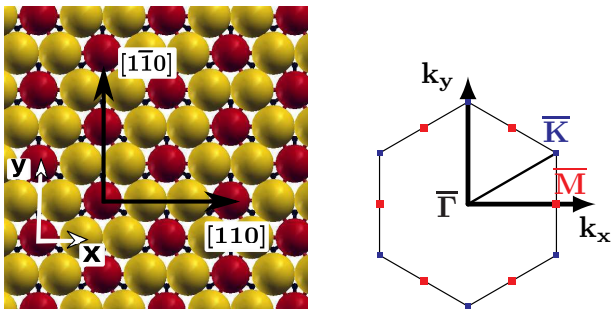

(a) (b)

Figure 5.1: *System geometry in real and reciprocal space: (a) shows the top view of the alloy monolayer, XAu_2, (X = Fe or Mn) on Ru(0001). The dark (red) and light (yellow) spheres represent X and Au atoms, respectively. The black dots indicate the topmost layer of the Ru atoms, for those systems in which the Ru substrate is present. (b) shows the corresponding hexagonal surface Brillouin zone and the high symmetry points $\overline{\Gamma}$, $\overline{M}$, and $\overline{K}$.*

Fig. 5.1(a) shows the top view of all four systems. The corresponding surface Brillouin zone, along with high symmetry points, is shown in Fig. 5.1(b). When computing spin spirals with wavevector $\mathbf{q}$, the $\overline{\Gamma}$ point (zone center) corresponds to the ferromagnetic

state, $\overline{\mathrm{K}}$ corresponds to a row-wise antiferromagnetic state, and $\overline{\mathrm{M}}$ corresponds to a 120° Néel state. Points in the interior of the Brillouin zone correspond to general spin spirals.

5.5 Method

5.5.1 Formalism

The total energy of a spin spiral of wavevector $\mathbf{q}$ is given by the sum of three terms:

$$E_{\mathrm{total}}(\mathbf{q}) = E_{\mathrm{SE}}(\mathbf{q}) + E_{\mathrm{DM}}(\mathbf{q}) + K_{\mathrm{avg}}. \tag{5.2}$$

In Eq. (5.2), the first term on the right-hand-side, E_{SE}, is the energy due to the symmetric exchange arising from the Heisenberg-type exchange interaction. The second term, E_{DM}, arises from the Dzyaloshinskii-Moriya interaction. The third term, K_{avg}, denotes the average value of the MAE over one wavelength λ of the spin spiral. In the absence of spin-orbit coupling, only the first of these three terms would be present (magnetic dipole-dipole interactions in low-dimensional systems generally being very weak). Note that though pseudo-dipolar exchange is also symmetric, here we only focus our attention on the Heisenberg-type symmetric exchange interactions. Throughout this chapter, the zero of energy is defined such that $E_{\mathrm{SE}}(\mathbf{q} = 0) = 0$. As $|\mathbf{q}| = 2\pi/\lambda$, we can also write Eq. (5.2) as a function of λ^{-1}. Below, we describe each of the terms contributing to the total energy in Eq. (5.2).

A. Symmetric Exchange Energy E_{SE}

If we consider a system consisting of spins $\{\mathbf{S}_i\}$, on lattice sites i, then one can write the contribution to the total energy from the symmetric Heisenberg exchange interaction as:

$$E_{\mathrm{SE}} = -\sum_{i<j} J_{ij}(\mathbf{S}_i \cdot \mathbf{S}_j), \tag{5.3}$$

where the sum runs over all pairs of distinct lattice sites i and j, and J_{ij} is the exchange coupling constant. Note that this interaction is symmetric with respect to the exchange

of spins between different lattice sites. If $J_{ij} > 0, \forall\{i,j\}$, the system has a ferromagnetic ordering; on the other, if $J_{ij} < 0$, for at least one $\{i,j\}$, the system has an antiferromagnetic ordering. However, a spin spiral state can be obtained when interactions beyond nearest neighbors become relevant. In addition to the 2-spin interactions (as in the Heisenberg model), higher order spin interactions can also give rise to noncollinear structures like spin spirals. The interaction involving four lattice sites $\{i,j,k,l\}$ can be expressed as:

$$H_{\text{4-spin}} = -K_{ijkl}\left[(\mathbf{S}_i \cdot \mathbf{S}_j)(\mathbf{S}_k \cdot \mathbf{S}_l) + (\mathbf{S}_i \cdot \mathbf{S}_l)(\mathbf{S}_j \cdot \mathbf{S}_k) + (\mathbf{S}_i \cdot \mathbf{S}_k)(\mathbf{S}_j \cdot \mathbf{S}_l)\right], \tag{5.4}$$

and

$$H_{\text{biquad.}} = -B_{ij}(\mathbf{S}_i \cdot \mathbf{S}_j)^2, \tag{5.5}$$

where K_{ijkl} and B_{ij} are the hopping intergrals for 4-spin and biquadratic interactions. The contribution to the total energy arising from $H_{\text{2-spin}} + H_{\text{4-spin}} + H_{\text{biquad.}}$ is denoted here as E_{SE}.

To calculate E_{SE} for a spin spiral with wavevector $\mathbf{q} \neq 0$ requires, in principle, the use of a supercell. This would hugely increase the computational time, especially for spin spirals of long wavelength. However, the use of supercells can be avoided by making use of the generalized Bloch theorem [111]; this permits one to carry out all calculations making use of the chemical unit cell.

There are two possible approaches for calculating E_{SE}. The quicker, but less accurate way, is to make use of Andersen's force theorem, also referred to as the magnetic force theorem or frozen force theorem [112]. This states that the change in energy due to the presence of a small perturbation can be calculated non-self-consistently from the eigenvalue sum, if the self-consistent solution of the unperturbed Hamiltonian is known. It is generally assumed that the force theorem can be applied for most small perturbations, and can be used, e.g., to calculate the energy difference δE_{SE} between two spin spirals of slightly different wavelengths, or the MAE.

The more time-consuming, but also more accurate, approach for calculating E_{SE} is to

perform fully self-consistent calculations. In this approach, the ground state electronic and magnetic densities (n_0, $\mathbf{m}_0$) are calculated self-consistently for each spin spiral, so as to yield a precise value for the energy difference δE_{SE} between two spin spirals of different wavelengths.

Given the wide use of the force theorem in calculations of magnetic structure, it would be of interest to obtain some insight into its domain of applicability, and to examine how accurate results obtained using it, are. For this reason, we have used both the force theorem and self-consistent approaches in this study, and present a comparison of results obtained using the two techniques.

B. Dzyaloshinskii-Moriya Energy E_{DM}

In an inversion-asymmetric system, such as a surface, not only the symmetric exchange interaction, but also the antisymmetric exchange (DM) interaction becomes important, and can play a crucial role in determining the magnetic ground state of the system [5, 6]. The energy due to the DM interaction can be written as:

$$E_{\mathrm{DM}} = \sum_{i<j} \mathbf{D}_{ij} \cdot (\mathbf{S}_i \times \mathbf{S}_j), \tag{5.6}$$

where $\mathbf{D}_{ij}$ is the DM vector, and the sum runs over distinct lattice sites $\{i, j\}$. It has been shown that depending on the symmetry of a system, some or all components of $\mathbf{D}$ may vanish [95]. The non-zero components of $\mathbf{D}$ can be obtained from performing spin spiral calculations with varying $\mathbf{q}$ along different crystallographic directions. For planar cycloidal spin spirals on a surface, such as those considered in this study, the component of $\mathbf{D}$ along $\mathbf{q}$ vanishes by symmetry. However, non-zero components of $\mathbf{D}$, which are orthogonal to $\mathbf{q}$, may exist. For example, if $\mathbf{q}$ lies along the x-axis ([110] direction), the non-zero components of $\mathbf{D}$ can be D_y and D_z, whereas, if $\mathbf{q}$ lies along the y-axis ([1$\bar{1}$0] direction), then the non-zero components can be D_x and D_z [see Fig. 5.1(a)]. Note that we find that the freestanding $FeAu_2$ and $MnAu_2$ monolayers remain completely flat, i.e., display no buckling, and thus, by symmetry, the DM interaction is absent for these systems.

To obtain $E_{\rm DM}$, one can solve the Dirac equation self-consistently. To do this one would, in principle, need to use large supercells, as the generalized Bloch theorem breaks down in the presence of spin-orbit coupling. However, to deal with this problem, a technique has been developed [113] to obtain $E_{\rm DM}$ within the chemical unit cell, treating the spin-orbit coupling as a small perturbation to first order. We have employed this method for calculating $E_{\rm DM}$.

C. Magnetic Anisotropy Energy K

The magnetic anisotropy energy (MAE) is the height of the energy barrier that has to be overcome to reverse the direction of the spin along the easy axis, and is given by:

$$K = E^{\text{hard-axis}} - E^{\text{easy-axis}}, \tag{5.7}$$

where $E^{\text{hard-axis}}$ and $E^{\text{easy-axis}}$ are the total energies of the system with magnetization along the hard-axis and the easy-axis, respectively, in the plane of rotation of the spins. The MAE (K) has two contributions, $K_{\rm SO}$ and $K_{\rm dip}$, arising from the spin-orbit (SO) coupling and the magnetic dipole-dipole interaction, respectively.

To calculate the value of $K_{\rm SO}$, one has to include the energy $E^{\rm SO}$ arising from SO coupling in Eq. (5.7). One can perform either self-consistent calculations or use the force theorem to obtain the value of $E^{\rm SO}$. We have used both methods and compared the results.

The value of $K_{\rm dip}$ is calculated by taking the difference between the magnetostatic energy $E^{\rm dip}$ along the hard-axis and the easy-axis obtained from the SO calculation. Note that the magnetostatic dipolar interaction by itself would always favor a situation where the spins lie in-plane. The $E^{\rm dip}$ of a magnetic dipole at position $\mathbf{R}_0$ with moment $\mathbf{M}_0$ due to the presence of other dipoles at position $\{\mathbf{R}_i\}_{i\neq 0}$ with moments $\{\mathbf{M}_i\}_{i\neq 0}$ is given by:

$$E^{\rm dip} = \frac{{\mu_B}^2}{2} \sum_{i\neq 0} \frac{(\mathbf{M}_i \cdot \mathbf{M}_0)\mathbf{R}_{i0}^2 - 3(\mathbf{R}_{i0} \cdot \mathbf{M}_i)(\mathbf{R}_{i0} \cdot \mathbf{M}_0)}{|\mathbf{R}_{i0}|^5} \quad \text{where} \quad \mathbf{R}_{i0} = \mathbf{R}_i - \mathbf{R}_0. \tag{5.8}$$

To obtain the total magnetostatic energy of the whole system along a magnetization direction, Eq. (5.8) has to be evaluated for each dipole. Note that in the case of a bulk system, E^{dip} depends on the macroscopic *shape* of the system (and gives rise to *shape anisotropy*); however, for magnetic thin-films, such as those considered in this study, E^{dip} depends only on the local orientation of the magnetic moments. This is because the sum in Eq. (5.8) converges only if the magnetic lattice is infinite in less than 3 dimensions.

5.5.2 Calculation details

We have used density functional theory (DFT) as implemented in the FLEUR code [26], which is based on the Full-potential Linearized Augmented Plane-wave (FLAPW) method [see Section 2.2.9]. Exchange-correlation interactions were treated using a generalized gradient approximation of the Perdew-Burke-Ernzerhof form [20]. The muffin-tin radii of Mn, Fe, Au and Ru were set equal to 2.56, 2.32, 2.42, and 2.32 a.u., respectively. The cutoff for the ℓ-value of the basis set consisting of spherical harmonics was fixed at 12, in order to expand the wavefunction inside the muffin-tins, while the ℓ-cutoff for the non-spherical part of the Hamiltonian was chosen to be 8. The plane-wave cutoff for the basis set used to expand the electronic wavefunction in the interstitial region was 3.6 a.u.$^{-1}$; this was increased to 4 a.u.$^{-1}$ when calculating the MAE, in order to achieve the increased accuracy necessary here. For the charge density and the exchange-correlation part of the potential, the plane-wave cutoffs were 12.3 a.u.$^{-1}$ and 10.3 a.u.$^{-1}$, respectively.

We have considered two collinear magnetic configurations: ferromagnetic (FM) and row-wise antiferromagnetic (AFM). For the freestanding $X\mathrm{Au}_2$ monolayer systems, the chemical (primitive) unit cell contains three atoms: one X atom and two Au atoms. All the calculations for the $X\mathrm{Au}_2$ alloy monolayers were carried out within this unit cell, except while performing collinear magnetic calculations for the antiferromagnetic (AFM) state. For these calculations a rectangular supercell, containing two X atoms and four Au atoms, was used. All the atoms were relaxed until the forces on each atom were less than 1 mHa/a.u. In both the FM and row-wise AFM configurations, we found that the freestanding FeAu_2 and MnAu_2 monolayers remained completely flat upon relaxation, i.e.,

no buckling was observed.

For the $X\mathrm{Au}_2$/Ru(0001) systems, the Ru(0001) substrate was modeled by a slab containing six atomic layers of Ru. For geometric optimization and MAE calculations, a symmetric slab was used, in which the alloy monolayer was placed on both sides of the slab. When optimizing geometries, the alloy layers and the first two Ru layers were allowed to relax, with the same force convergence criterion as used for the freestanding monolayers. To calculate E_{SE} and E_{DM} in an inversion-asymmetric environment, an asymmetric slab was used, in which the alloy monolayer was deposited on only the upper surface of the six-layer Ru slab.

We found that for $X\mathrm{Au}_2$/Ru(0001), the atoms on the overlayer buckled upon relaxation, in both FM and row-wise AFM configurations. Being larger, the Au atoms relax further away from the substrate, while the smaller X atoms remain closer to the substrate; the degree of buckling is quite significant. In order to quantify the degree of buckling, we computed $d_{\mathrm{b}} = d_{\mathrm{Au}} - d_X$, where d_{Au} and d_X are the z coordinates of the Au and X atoms, respectively. We found that for FeAu_2/Ru(0001), $d_{\mathrm{b}} = 0.38$ Å for both FM and AFM configurations, while for MnAu_2/Ru(0001), the values of d_{b} were 0.22 Å and 0.27 Å in the FM and row-wise AFM configurations, respectively. This buckling plays an important role in the DM interaction, as we will see further below.

The interlayer distance along the z-direction between the X atom and the first Ru layer is 2.12 Å for FeAu_2/Ru(0001) and 2.30 Å for MnAu_2/Ru(0001). The larger value in the latter case can be attributed to the presence of larger magnetic moments on Mn atoms than on Fe atoms (as shown in Table 5.1 below).

The different contributions to the total energy in Eq. (5.2) differ in magnitude, and thus require differing degrees of accuracy. For this reason, we have separately checked the convergence of each of these contributions, with respect to the density of Brillouin zone (k-point) sampling. In all cases, a smearing of width 0.001 Ha was used to improve the convergence, except for the calculation of MAE, where a smaller smearing width of 0.0001 Ha was used.

5.6 Results

We first perform collinear magnetic calculations; these are useful not only because they might correspond to the magnetic ground state, but because the relative energies of FM and AFM states help one to gauge the likelihood of obtaining non-collinear states such as spin spirals. We then go on to perform calculations on spin spirals with wavevectors $\mathbf{q}$ along high-symmetry directions of the Brillouin zone.

5.6.1 Collinear magnetic structures

We have considered two collinear magnetic configurations: (i) FM and (ii) row-wise AFM, for all four systems under study. These calculations were carried out using 132 $\mathbf{k}_{\parallel}$-points in the irreducible part of the surface Brillouin zone for $FeAu_2$/Ru(0001) and $MnAu_2$/Ru(0001), while for $FeAu_2$ and $MnAu_2$ monolayers 128 $\mathbf{k}_{\parallel}$-points were used in the irreducible Brillouin zone.

For the freestanding $FeAu_2$ monolayer, we find that the FM configuration is lower in energy than the AFM configuration, whereas for the freestanding $MnAu_2$ monolayer, the reverse is true. The energy difference between the two collinear magnetic structures considered, $\Delta E_{\mathrm{AFM-FM}}$, is 64 meV per Fe atom, for $FeAu_2$, and -70 meV per Mn atom, for $MnAu_2$. However, when deposited on the Ru(0001) substrate, the ferromagnetic state is lower in energy for both the Fe and Mn surface alloys; the value of $\Delta E_{\mathrm{AFM-FM}}$ is found to be 62 meV per Fe atom for $FeAu_2$/Ru(0001), and 19 meV per Mn atom for $MnAu_2$/Ru(0001). The fact that the stability of the magnetic structure switches from being row-wise AFM for the freestanding monolayer, to FM for the deposited monolayer, for $MnAu_2$, is already an indication that the presence of the Ru substrate can play an important role in determining the magnetic properties of the system.

In Table 5.1, we have listed the magnetic moments for the different types of atoms in the row-wise AFM (for $MnAu_2$ monolayers) and FM (for the other three systems) configurations. As expected, the magnetic moments of the Fe and Mn atoms are higher in the freestanding monolayers, where the atoms have a lower coordination than when they

Table 5.1: *The magnetic moments on the various atoms in the alloy layer, and the top two layers of the substrate (where present), for the collinear ground state of the four systems studied. Ru(1) and Ru(2) atoms lie in the first and second layer, respectively, of the Ru substrate. See the text for the description of Ru(2)-I and Ru(2)-II.*

Atom	Magnetic moments (μ_B)			
	$FeAu_2$/Ru	$FeAu_2$	$MnAu_2$/Ru	$MnAu_2$
Fe/Mn	2.88	3.2	3.75	$\pm$4.14
Au	0.02	0.04	0.02	$\pm$0.02
Ru(1)	0.00	–	-0.09	–
Ru(2)-I	-0.03	–	-0.02	–
Ru(2)-II	-0.11	–	-0.07	–

are deposited on the Ru substrate. We find that the magnetic moments on the Au atoms tend to be aligned parallel to the X atoms, implying a ferromagnetic interaction between them, whereas, in general, the magnetic moments on the Ru atoms in the substrate are aligned opposite to those of the X atoms. Note that there are two inequivalent types of Ru atoms in the second layer of the substrate, labeled as Ru(2)-I and Ru(2)-II; these are situated directly below X and Au atoms, respectively.

Note that the values of the magnetic moments for $MnAu_2$/Ru(0001) differ slightly from the values reported in Chapter 4. The discrepancy presumably arises from the different techniques used to calculate the magnetic moments: while a plane-wave pseudopotential method was used to calculate the values in Chapter 4, here we have used the FLAPW method. In the former method, individual atomic moments are obtained by projecting the system's wavefunctions onto the wavefunctions of isolated atoms, whereas in the latter, the atomic moments are calculated by integrating the spin-polarized charge densities inside the muffin-tin radius of a given atom.

In Fig. 5.2, we have plotted the local density of states (LDOS) for the FM $FeAu_2$/Ru-(0001) and $MnAu_2$/Ru(0001) as a function of $E - E_F$, where E_F is the Fermi energy of the system. In the upper panels [see Figs. 5.2(a) and 5.2(b)] the LDOS of the overlayer atoms shown; the solid lines represent the LDOS per X atom and the filled curves show the LDOS per Au atom. In the two lower panels [see Figs. 5.2(c) and 5.2(d)], the LDOS per Ru(1) atom (solid lines) and per bulk-like Ru atom (filled curve) are plotted. In both the systems, the LDOS per X atom shows large exchange splitting. On the other hand,

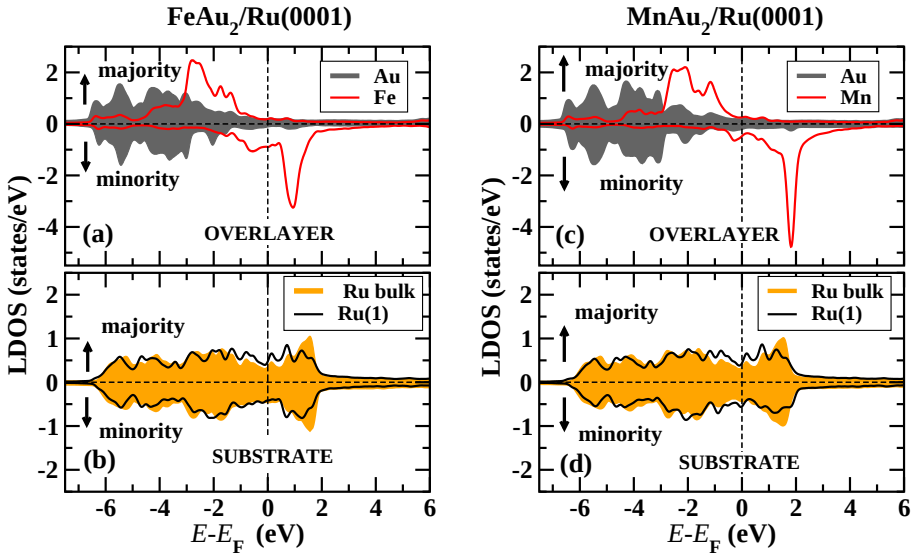

Figure 5.2: *The spin-polarized local density of states (LDOS) for ferromagnetic [(a) and (b)] $FeAu_2$/Ru(0001) and [(c) and (d)] $MnAu_2$/Ru(0001): The top two panels show the LDOS for the atoms constituting the overlayer, while the bottom two panels are for the substrate atoms. "Ru(1)" denotes Ru atoms in the topmost substrate layer, while "Ru-bulk" denotes atoms in the middle of the six-layer Ru substrate. The dashed vertical line indicate the position of the Fermi level E_F.*

the Au and Ru(1) show very small spin-polarization and thus these atoms have only very small magnetic moments (see Table 5.1).

5.6.2 Spin spiral calculations for $X\mathrm{Au}_2$/Ru(0001)

We now proceed to the question of primary interest for us, viz., whether the two supported systems, $FeAu_2$/Ru(0001) and $MnAu_2$/Ru(0001), exhibit a spin spiral ground state. While doing this, we have made use of the optimized geometry obtained for the collinear ferromagnetic state. In presenting these results, we have separated out each contribution to the energy [see Eq. (5.2)] of the spin spiral.

A. Results for Symmetric Exchange Energy E_{SE}

As mentioned earlier, we have obtained $E_{\mathrm{SE}}(\lambda^{-1})$ using two possible approaches, the force theorem (FT), and self-consistently (SC). Let us first consider the results obtained using the former approach. For this we have used a very dense $\mathbf{k}_{\parallel}$-point mesh containing 6400 points in the full Brillouin zone. Since we know that the FT approach should be valid

only for small perturbations, we perturb about a SC solution corresponding to the FM state (i.e., $\mathbf{q} = \mathbf{0}$), and restrict ourselves to regions of the Brillouin zone in the vicinity of the zone center. In particular, we consider $|\lambda^{-1}| \leq 0.32$ nm^{-1} along the [110] direction, and $|\lambda^{-1}| \leq 0.75$ nm^{-1} along $[1\bar{1}0]$. Our results are shown by the open circles in Fig. 5.3. [Note that as the relation $E_{\rm SE}(-\lambda^{-1}) = E_{\rm SE}(\lambda^{-1})$ holds for both systems, we have only shown the results for $\lambda^{-1} > 0$]. Interestingly, we find that for $MnAu_2$/Ru(0001), the graphs suggest that even with symmetric exchange interactions alone, a spin spiral state would be favored over the ferromagnetic state. However, for $FeAu_2$/Ru(0001), the ground state in this approximation remains the FM state.

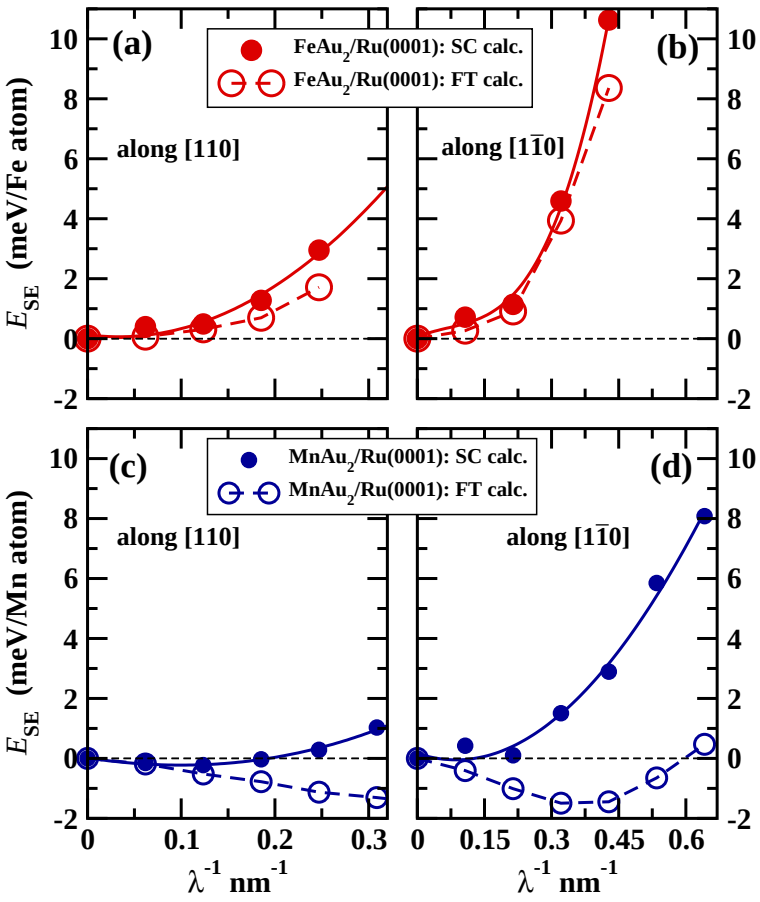

Figure 5.3: *Dispersion of symmetric exchange energy $E_{\rm SE}$ for small λ^{-1}, for [(a) and (b)] $FeAu_2$/Ru(0001) and [(c) and (d)] $MnAu_2$/Ru(0001), along high-symmetry directions in the surface Brillouin zone. The open circles are the results from the force theorem (FT) calculations. The filled circles are results from the self-consistent (SC) calculations and correspond to the zoomed-in regions of the top panel of Fig. 5.4.*

Next, we proceed to verify these FT results by performing more accurate SC calculations. For these, we have used 512 and 800 $\mathbf{k}_{\|}$-points when sampling the irreducible Brillouin zones for $FeAu_2$/Ru(0001) and $MnAu_2$/Ru(0001), respectively. These results are shown by the filled circles in Fig. 5.3. Somewhat surprisingly, the results obtained now are quite different, especially for $MnAu_2$/Ru(0001). The difference in energy between a spin spiral state and the FM state is now considerably reduced.

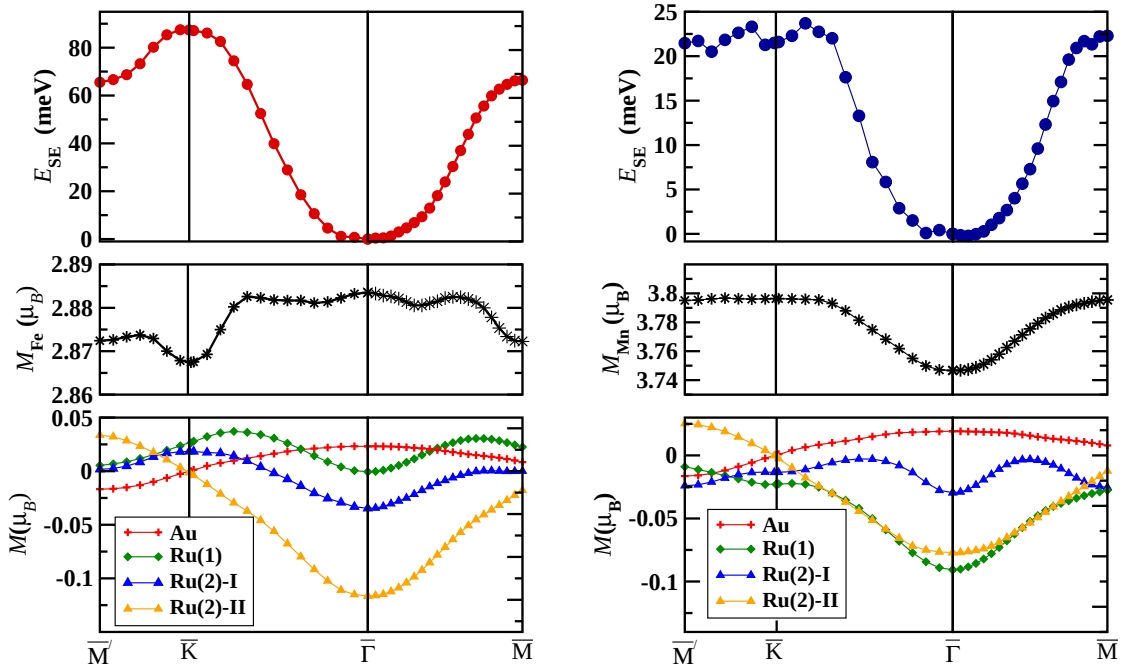

(a) **$FeAu_2$/Ru(0001)** (b) **$MnAu_2$/Ru(0001)**

Figure 5.4: *Results from SC calculations for variation of exchange energy E_{HE}, and magnetic moments M on the different atoms, along high symmetry directions of the surface Brillouin zone, for (a) $FeAu_2$/Ru(0001) and (b) $MnAu_2$/Ru(0001). E_{HE} is given in meV per X atom, and M is given in μ_B per atom. See the text for the convention used in labeling atoms.*

This suggests that results using the FT approach cannot always be trusted, and the force theorem must be used with considerable caution. This point is discussed further in the Appendix B to this thesis.

We now go on to use the SC approach to compute E_{SE} throughout the Brillouin zone, along high-symmetry directions. These results, along with results for the variation of magnetic moments, are shown in Fig. 5.4. In this figure, $\overline{\Gamma\mathrm{K}}$ and $\overline{\Gamma\mathrm{M}}$ lie within the first Brillouin zone, while $\overline{\mathrm{KM}'}$ belongs to the second Brillouin zone. On examining this figure,

we see that for $FeAu_2$/Ru(0001), the lowest value of E_{SE} is at the $\overline{\Gamma}$ point (see the top two panels of Fig. 5.4). In contrast, for $MnAu_2$/Ru(0001), the lowest value of E_{SE} corresponds to a spin spiral with $\lambda^{-1} = 0.12$ nm^{-1} along the $\overline{\Gamma M}$ direction. This is more evident from Fig. 5.3(c) (see the solid line and filled circles). Note however that: (i) the difference in E_{SE} between the FM state and the spin spiral state is small, and (ii) to obtain the final result for ground state magnetic structure, we have yet to add the other two contributions E_{DM} and K_{avg}, to E_{SE}.

The magnetic moments of the X atoms, M_X, (shown by the stars in the middle panel of Fig. 5.4) vary only slightly as $\mathbf{q}$ changes. The induced moments on the Au, Ru(2)-I and Ru(2)-II atoms can be either positive (ferromagnetically aligned) or negative (anti-ferromagnetically aligned), depending on the value of $\mathbf{q}$; however the magnitude of these induced moments is small.

B. Results for Dzyaloshinskii-Moriya Energy E_{DM}

We next calculate $E_{DM}(\lambda^{-1})$ for $FeAu_2$/Ru(0001) and $MnAu_2$/Ru(0001). For all the spin spirals considered by us, the relation $E_{DM}(-\lambda^{-1}) = -E_{DM}(\lambda^{-1})$ holds, where positive and negative values of λ^{-1} correspond to right-rotating and left-rotating spirals, respectively. We have obtained the different components of $\mathbf{D}$ by varying $\mathbf{q}$ along the [110] direction, with -0.25 nm^{-1} $< \lambda^{-1} <$ 0.25 nm^{-1}, and along the $[1\bar{1}0]$ direction with -0.42 nm^{-1} $< \lambda^{-1} <$ 0.42 nm^{-1}. The calculations were performed using 6400 $\mathbf{k}_{\parallel}$-points in the full surface Brillouin zone. Our results are presented in Fig. 5.5. For both $FeAu_2$/Ru(0001) and $MnAu_2$/Ru(0001), we have found that E_{DM} always favors left-rotating spirals, we have therefore shown only the negative λ^{-1} region in this figure.

Our results for $E_{DM}(\lambda^{-1})$ for $FeAu_2$/Ru(0001) and $MnAu_2$/Ru(0001) are shown by the open and filled squares, respectively, in Fig. 5.5. We find that the magnitude of E_{DM} is significantly larger for $FeAu_2$/Ru(0001) than it is for $MnAu_2$/Ru(0001) (the reason for this will be discussed below); note that this was however also true of the magnitude of E_{SE}, and that for negative λ^{-1} these two terms have opposite sign, leading in both cases to a similar compensation of energies. Further, $E_{DM}(\lambda^{-1})$ is found to be linear for $FeAu_2$/Ru(0001),

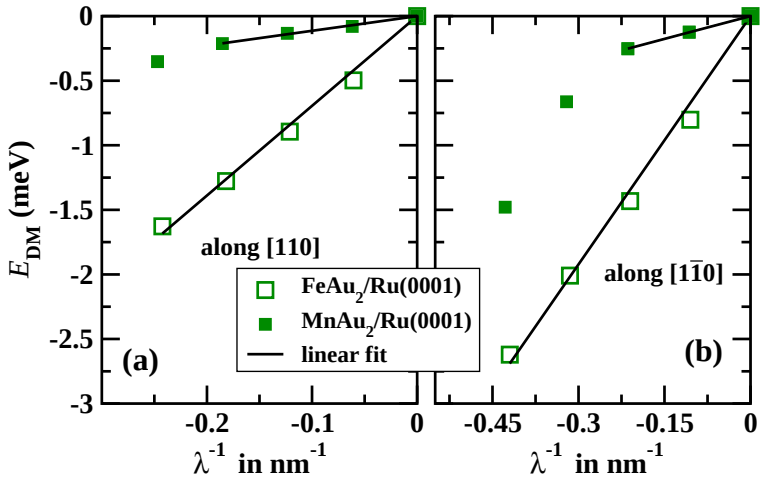

Figure 5.5: *E_{DM}, contribution from the Dzyaloshinskii-Moriya interaction, to the total energy along (a)* [110] *and (b)* [1$\bar{1}$0] *for $FeAu_2$/Ru(0001) and $MnAu_2$/Ru(0001).*

along both the [110] and [1$\bar{1}$0] directions, for the range of λ^{-1} considered here. However, we can see that this is clearly not true for $MnAu_2$/Ru(0001), where $E_{\mathrm{DM}}(\lambda^{-1})$ is found to deviate from linear behavior for $\lambda^{-1} \gtrsim -0.19$ nm^{-1}, along both directions. In the region where E_{DM} varies linearly with λ^{-1}, we fitted our data to straight lines (see the black lines in Fig. 5.5), so as to obtain the components of **D** along different directions. We obtain D_x and D_y by fitting along the [1$\bar{1}$0] and [110] directions, respectively; we find that the D_z component always vanishes. For $FeAu_2$/Ru(0001), we obtain the values of D_x and D_y to be 6.40 meV nm and 6.94 meV nm, respectively, whereas for $MnAu_2$/Ru(0001), the values of D_x and D_y are found to be 1.17 meV nm and 1.12 meV nm, respectively.

We have also extracted the contributions to **D** that arise from each kind of atom [113], focusing on the X, Au, Ru(1) and Ru(2) atoms, as the DM interaction is expected to be significant only near the surface. [Note that here, by the contribution of the Ru(2) atoms we mean the average contribution of the Ru(2)-I and the Ru(2)-II atoms.] These atom-wise contributions are depicted graphically in Fig. 5.6. It is interesting to note that for both $FeAu_2$/Ru(0001) and $MnAu_2$/Ru(0001), the largest (positive) contributions arise from the Au atoms. The contributions coming from the X atoms also always enhance **D**, but the magnitude is much smaller compared to those from the Au atoms. The Ru(1) and Ru(2) atoms have contributions reducing **D**, except for $MnAu_2$/Ru(0001), where Ru(1)

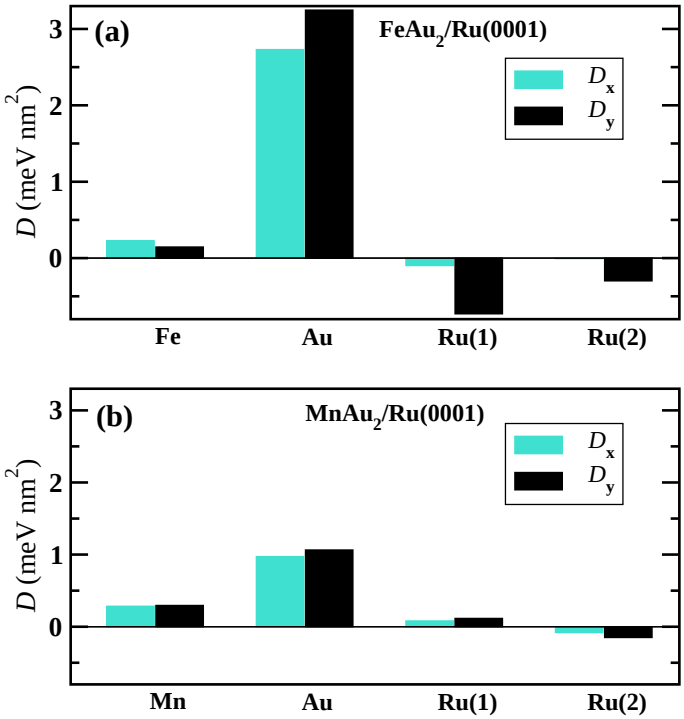

Figure 5.6: *Atom-wise contributions to non-zero components of* **D** *for (a) $FeAu_2$/Ru(0001) and (b) $MnAu_2$/Ru(0001). Along* [110] $D_y \neq 0 = D_x$, *while along* [1$\bar{1}$0] $D_x \neq 0 = D_y$. *X, Au and Ru(n) indicate the magnetic atom (Fe or Mn), Au atom and n-th layer Ru atoms, respectively, where n=1 and 2.*

contributes additively. There are two possible ways in which two magnetic atoms can interact through the DM mechanism, either directly, or involving a third, "non-magnetic" atom [114]. In our case, this third atom could be either Ru or Au. Our results suggest that it is this latter, three-site mechanism that is dominant in our case. The much larger contribution from Au atoms is in accordance with the large spin-orbit coupling in Au and the strong buckling of the overlayer. The larger buckling in $FeAu_2$/Ru(0001) than $MnAu_2$/Ru(0001) also leads to a stronger contribution to **D**.

C. Results for Magnetic Anisotropy Energy K

The third contribution to the energies of spin spirals on $FeAu_2$/Ru(0001) and $MnAu_2$/Ru-(0001) consists of the magnetic anisotropy energy K. For both these systems, we have calculated the energy barriers for a rotation of the magnetic moment in the xz and yz planes, which are given respectively by:

$$K^{110} = \quad E(\theta = \theta_1^{\text{hard}}, \varphi = 0) - E(\theta = \theta_1^{\text{easy}}, \varphi = 0), \tag{5.9}$$

$$K^{1\bar{1}0} = \quad E(\theta = \theta_2^{\text{hard}}, \varphi = \tfrac{\pi}{2}) - E(\theta = \theta_2^{\text{easy}}, \varphi = \tfrac{\pi}{2}), \tag{5.10}$$

where E is the energy, obtained including spin-orbit interactions, and the moments on the X atoms are constrained to point along the direction specified by the angles (θ, φ); the polar angle θ is measured from the surface normal and the azimuthal angle φ is measured from the x-axis [see Fig. 5.7]. The easy and hard axes for the two rotations are specified by the angles θ_i^{easy} and θ_i^{hard}. K has two contributions: K_{SO} and K_{dip}, which arise from spin-orbit interactions, and magnetic dipolar interactions, respectively.

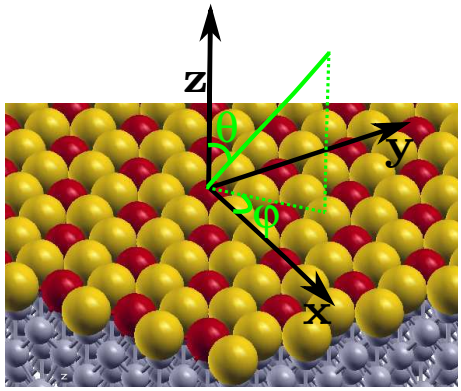

Figure 5.7: *The side view of the system XAu_2/Ru(000), where X = Fe or Mn, showing the polar and azimuthal angles θ and φ, respectively.*

Let us first consider K_{SO}, which can be calculated in two possible ways: either self-consistently (SC) or by using the force theorem (FT). To check the applicability of the FT for the calculation of the MAE of the systems considered here, we first compute as a test the quantity $K_{\text{test}} = E(\theta = \frac{\pi}{2}, \varphi = 0) - E(\theta = 0, \varphi = 0)$, using both approaches. The number of k-points required for a converged SC calculation is 256 in the full Brillouin zone, while 4096 k-points are needed for the FT calculations. For $FeAu_2$/Ru(0001), we obtain $K_{\text{test}} = 1.14$ and 0.93 meV per Fe atom, from the FT and SC approaches, respectively;

the corresponding values for $MnAu_2$/Ru(0001) are 0.18 meV and 0.19 meV per Mn atom. Based upon this, we conclude that results for K_{SO} using the two approaches are likely to agree to the desired degree of accuracy. Henceforth, we have used the FT to calculate all the values of K_{SO} reported in this section.

We now proceed to vary θ, keeping φ fixed at a constant value φ_c, which is equal to either 0 or $\frac{\pi}{2}$, when determining K_{SO} along the [110] and [1$\bar{1}$0] directions, respectively. We define

$$E_{\perp}(\theta, \varphi_c) = E^{SO}(\theta, \varphi_c) - E^{SO}(0, \varphi_c). \tag{5.11}$$

In Fig. 5.8(a), we have plotted our results for $E_{\perp}$ for $FeAu_2$/Ru(0001) and $MnAu_2$/Ru(0001), with $\varphi_c = 0$. The results for the two systems are quite different. For $FeAu_2$/Ru(0001), the highest value of $E_{\perp}$ occurs for $\theta = 0$, and the lowest value for $\theta = \frac{\pi}{2}$, whereas for $MnAu_2$/Ru(0001), the angles corresponding to the highest and lowest values of $E_{\perp}$ are reversed. This suggests that (assuming that the contribution from dipolar interactions is small; this remains to be verified below) the position of the hard and easy axes is interchanged in the two systems studied here. It is also interesting to note that K_{SO} is significantly higher for $FeAu_2$/Ru(0001) than for $MnAu_2$/Ru(0001).

We have also shown, in Fig. 5.8(b), how the orbital moment per X atom changes as θ is varied. One observes a sinusoidal variation, though the amplitude of variation is small. We find that, for both systems, the highest and lowest values of orbital moment occur when the magnetization is along the hard-axis and the easy-axis, respectively. Note that this contradicts the prediction of Bruno [115]. The prediction is based on the assumption that the majority and minority d-bands are well separated by the exchange interaction; though this is true for the X atoms, for the Ru atoms this assumption does not hold true.

Next, we consider K_{dip}, which arises from the magnetostatic interaction between the magnetic moments. We find that the contributions to K from dipolar interactions are significantly smaller than those from the spin-orbit interaction, especially for $FeAu_2$/Ru(0001); for this reason the easy axis is determined by the spin-orbit interaction. Our results for

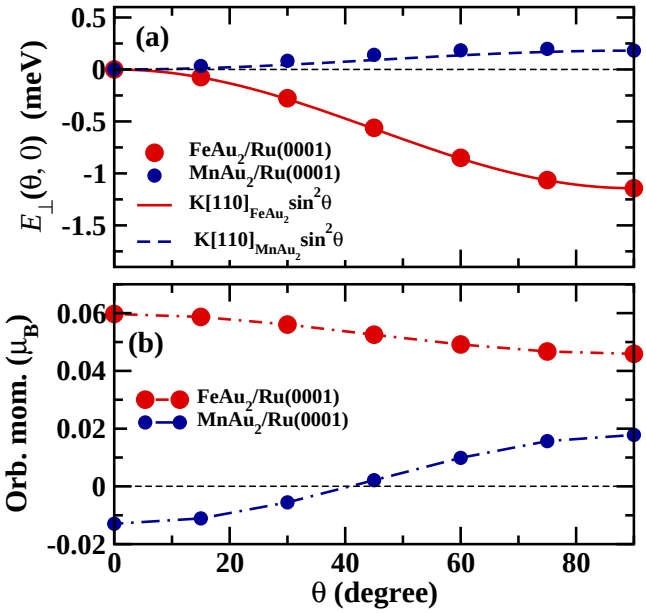

Figure 5.8: *The variation of (a) $E_\perp(\theta, \varphi_c = 0)$ and (b) orbital moment of the X atom as a function of the polar angle θ for $FeAu_2$/Ru(0001) and $MnAu_2$/Ru(0001). The easy axis lies along the direction of minimum $E_\perp(\theta, \varphi_c = 0)$.*

$K_{\rm dip}$ are listed in the fourth column of Table 5.2. As dipolar interactions always favor an in-plane axis for ferromagnetic configurations, the negative sign of $K_{\rm dip}$ in Table 5.2 for $MnAu_2$/Ru(0001) indicates that the easy axis of the system is out-of-plane.

Finally, the total value of K is obtained by adding $K_{\rm SO}$ and $K_{\rm dip}$ (see the last column in Table 5.2). We also obtain $K_{\rm avg}$, the average value of K in the (110) and (1$\bar{1}$0) planes [see Eq. (5.2)]; in all the cases studied here, $K_{\rm avg} = \int_0^\pi K sin^2\theta {\rm d}\theta = K/2$. We find that the easy axis lies in-plane for $FeAu_2$/Ru(0001), but out-of-plane for $MnAu_2$/Ru(0001).

Table 5.2: *Results for magnetic anisotropy energy K, along with $K_{\rm SO}$ and $K_{\rm dip}$, the contribution due to spin-orbit coupling and magnetic dipole-dipole interaction, respectively, along two high-symmetry directions, for XAu_2/Ru(0001).*

X	direction	$K_{\rm SO}$	$K_{\rm dip}$	K
		(meV per X atom)		
Fe	[110]	1.14	0.04	1.18
	[1$\bar{1}$0]	1.18	0.04	1.22
Mn	[110]	0.18	−0.06	0.12
	[1$\bar{1}$0]	0.14	−0.06	0.08

D. Results for E_{total}

Having obtained the values of E_{SE}, E_{DM} and K_{avg}, we are now finally in a position to calculate the total energy E_{total} for $FeAu_2$/Ru(0001) and $MnAu_2$/Ru(0001). In Fig. 5.9, the values of E_{SE} and E_{DM} are shown by (red) filled circles and (green) open squares, and the value of K_{avg} is shown by (blue) thick dashed lines. The final values E_{total}, obtained by adding these three terms, are shown by the stars and the solid black curves fit to them.

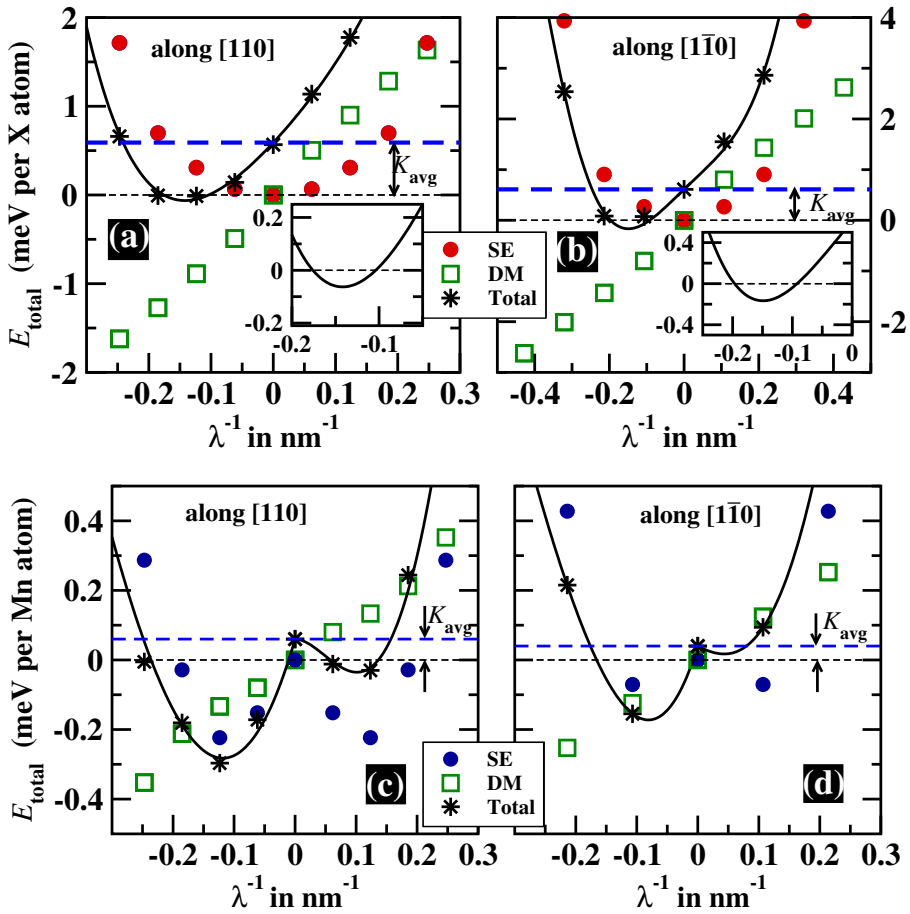

Figure 5.9: *Variation of total energy (E_{total}) as a function of λ^{-1} for [(a) and (b)] $FeAu_2$/Ru(0001) and [(c) and (d)] $MnAu_2$/Ru(0001) along* [110] *and* [1$\bar{1}$0]. *The insets in (a) and (b) are zoomed in areas using the same scale as in (c) and (d).*

For $FeAu_2$/Ru(0001), we find that along the [110] direction, the most energetically favorable state is a left-rotating spin spiral with $\lambda^{-1} = -0.14$ nm^{-1}, this is lower in energy than the FM state by 0.06 meV per Fe atom [see Fig. 5.9(a)]. Along [1$\bar{1}$0], a spin spiral

of $\lambda^{-1} = -0.15$ nm^{-1} becomes lower in energy than the FM state by 0.17 meV per Fe atom [see Fig. 5.9(b)]. Thus the latter spin spiral, with a wavelength of 6.7 nm, is the lowest-energy magnetic ground state for $FeAu_2$/Ru(0001). However, it is only very slightly lower in energy than the FM state.

Similarly, the two lower panels of Fig. 5.9 show the various contributions to the energies of spin spirals on $MnAu_2$/Ru(0001). We see that a left-rotating spin spiral with $\lambda^{-1} = -0.12$ nm^{-1} along [110] is lower in energy than the FM state by 0.28 meV per Mn atom, while a left-rotating spin spiral with $\lambda^{-1} = -0.08$ nm^{-1} along $[1\bar{1}0]$ is lower in energy than the FM state by 0.17 meV per Mn atom. Of these, the former, with a wavelength of 8.5 nm, is the magnetic ground state.

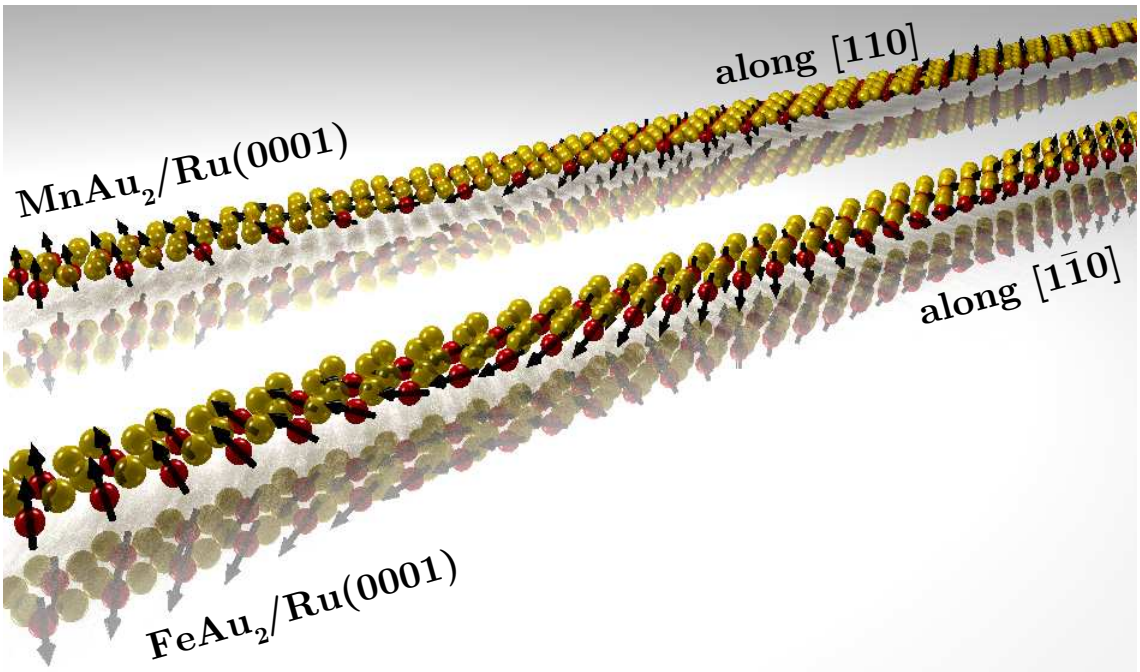

Figure 5.10: *The left-rotating spin spirals of $FeAu_2$/Ru(0001) and $MnAu_2$/Ru(0001) surface alloys. The red and yellow spheres indicate the X (X = Fe or Mn) and Au atoms, respectively. The Ru surface is shown as a reflecting mirror. The black arrows on the X atoms represent the direction of the magnetic moments.*

In Fig. 5.10 we show the left-rotating spin spirals of $FeAu_2$/Ru(0001) and $MnAu_2$/Ru-(0001).

5.6.3 Comparison with freestanding alloy monolayers of $X\mathrm{Au}_2$

In order to gauge what effect the Ru substrate has, we now repeat the previous calculations, but for freestanding $X\mathrm{Au}_2$ alloy monolayer systems, i.e., in the absence of the Ru substrate. As before, we present separately the contributions to the total energy from each term in Eq. (5.2).

A. Results for Symmetric Exchange Energy E_{SE}

We have calculated E_{SE} for freestanding FeAu_2 and MnAu_2 monolayers. From the already presented calculations on collinear magnetic structures (see Section 5.6.1 above), we have seen that both FeAu_2 and MnAu_2 freestanding monolayers remain flat upon relaxation, i.e., no buckling is observed. We now restrict ourselves to calculating E_{SE} self-consistently (SC) for flat freestanding monolayers (see also Appendix B to this thesis). For this, we have used 78 k-points in the irreducible Brillouin zone.

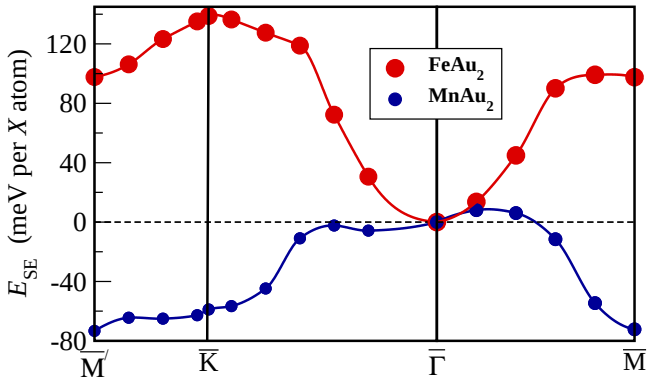

Figure 5.11: *Energy dispersion E_{SE} for freestanding monolayers of $FeAu_2$ [shown by gray (red) dots] and $MnAu_2$ [shown by dark (blue) dots]. The ground state magnetic structure for $FeAu_2$ is ferromagnetic (minimum at $\overline{\Gamma}$), whereas that for $MnAu_2$ is row-wise antiferromagnetic (minimum at $\overline{\mathrm{M}}$).*

Fig. 5.11 shows our results for E_{SE} along high-symmetry directions of the Brillouin zone for both FeAu_2 and MnAu_2 freestanding monolayers. We find that the lowest E_{SE} states are FM for FeAu_2 – see the large red dots – and row-wise AFM for MnAu_2 – see the small blue dots. Thus, for the freestanding alloy monolayers, we find that the collinear magnetic states are lower in energy than the spin spiral states. Note that for flat monolayers, E_{DM} is identically zero. So, upon going from freestanding alloy monolayers to surface alloys on

Ru(0001), the magnetic ground state changes from FM to a spin spiral state in the case of $FeAu_2$/Ru(0001), while for $MnAu_2$/Ru(0001), the ground state changes from a row-wise AFM state to a spin spiral state.

B. Results for Dzyaloshinskii-Moriya Energy E_{DM}

Though the freestanding $X\mathrm{Au}_2$ monolayers do not show any buckling, in order to be able to compare the asymmetric exchange coupling between the X and Au atoms with and without the substrate, we have obtained the value of $\mathbf{D}$ as a function of the buckling parameter d_{b} of the freestanding monolayers of $X\mathrm{Au}_2$. We have taken d_{b} to be 0.5, 1.0 and 1.5 Å. Further, in order to better enable a comparison with the corresponding systems on the Ru substrate, we have also considered d_{b} to be 0.38 Å (for the $FeAu_2$ monolayer) and 0.22 Å (for the $MnAu_2$ monolayer); these values correspond to the values of d_{b} for the overlayer in the $X\mathrm{Au}_2$/Ru(0001) systems.

In Fig. 5.12, we have plotted our results for D_x and D_y, as a function of the buckling parameter d_{b}, for freestanding $FeAu_2$ and $MnAu_2$ monolayers; the component D_z vanishes in all the cases considered here. For purposes of comparison, the values of D_x and D_y for the corresponding $X\mathrm{Au}_2$/Ru(0001) systems are shown by dashed and dotted lines, respectively. We find that for $FeAu_2$ monolayers, the values of both D_x and D_y at $d_{\mathrm{b}} = 0.38$ Å are much smaller than the corresponding values for $FeAu_2$/Ru(0001). In contrast, for $MnAu_2$ monolayers, the values of D_x and D_y at $d_{\mathrm{b}} = 0.22$ Å are similar to the values for $MnAu_2$/Ru(0001). It is therefore difficult to reach any general conclusions about the effect of the Ru substrate; it is apparently system-dependent, since the magnetic interactions between the Fe and Ru atoms differ from those between the Mn and Ru atoms. We also observe that for the alloy monolayers, the values of D_x and D_y can differ a lot, whereas the values are almost the same for the $X\mathrm{Au}_2$/Ru(0001) systems.

For $FeAu_2$/Ru(0001) the largest values of D_x and D_y occur for $d_{\mathrm{b}} = 0.5$ Å, while for $MnAu_2$/Ru(0001), we find that the values are the largest at $d_{\mathrm{b}} = 1.0$ Å. We observe that two competing effects determine the magnitude of $\mathbf{D}$: (i) a geometrical effect that enhances its value with increasing buckling and (ii) the influence of the distance between X and Au,

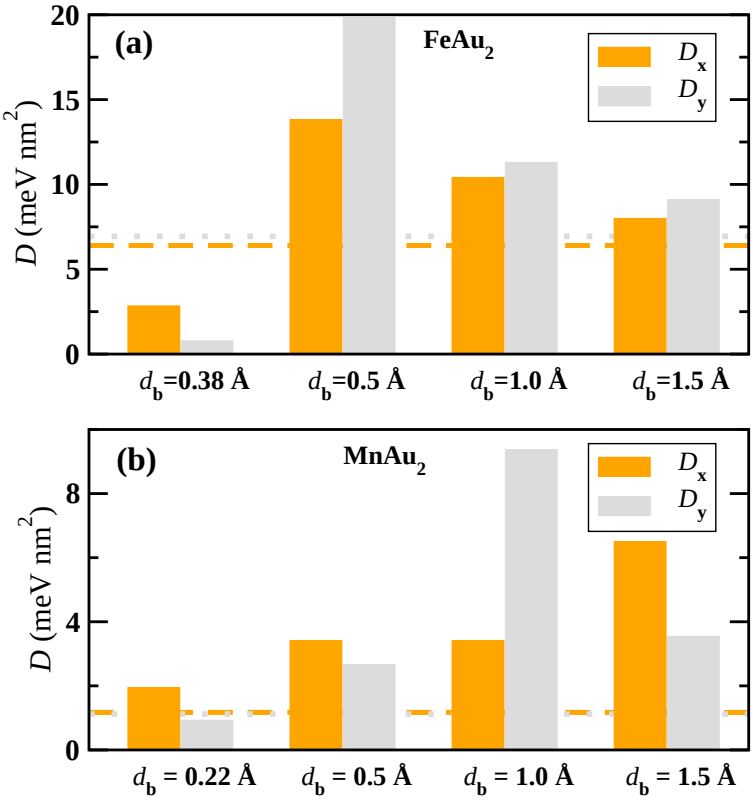

Figure 5.12: *The variation of D_x and D_y as a function of overlayer buckling d_b for freestanding monolayers of (a) $FeAu_2$ and (b) $MnAu_2$. Along* [110] $D_y \neq 0 = D_x$, *while along* [1$\bar{1}$0] $D_x \neq 0 = D_y$. *The dashed and dotted lines correspond to the values of D_x and D_y, respectively, in the case of $FeAu_2$/Ru(0001) and $MnAu_2$/Ru(0001). Note that the y-axis scale is different in (a) and (b).*

that decreases **D** if the X-Au distance is too large. This is in line with the model of Levy and Fert [114] for the DM interaction.

C. Results for Magnetic Anisotropy Energy K

We have calculated the value of the magnetic anisotropy energy K for freestanding monolayers of $X\mathrm{Au}_2$. Test calculations show that results obtained using the FT and SC methods are comparable. We therefore continue to calculate K_{SO} by using the FT. The calculations are performed using 4096 and 6400 $\mathbf{k}_{\parallel}$-points in the Brillouin zone of the FeAu_2 and MnAu_2 monolayers, respectively.

In Fig. 5.13(a), we have plotted our results for $E_{\perp}(\theta, \varphi_c = 0)$ vs. θ. The small red dots and large blue dots show the results for freestanding FeAu_2 and MnAu_2 monolayers, respectively. We have fitted $E_{\perp}$ to $\sin^2\theta$ (solid line). The positions of the minimum and

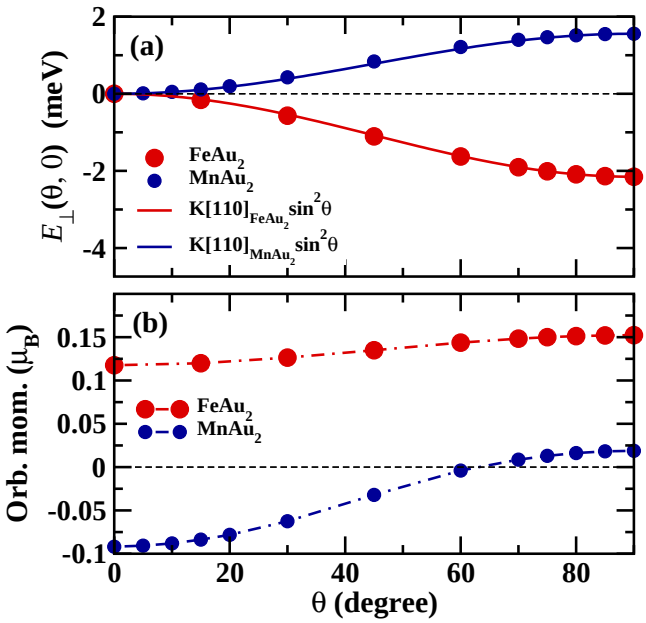

Figure 5.13: *The variation of (a) $E_\perp(\theta, \varphi_c = 0)$ and (b) orbital moment of the X atom as a function of the polar angle θ for $FeAu_2$ and $MnAu_2$ freestanding monolayers. The easy axis lies along the direction of minimum $E_\perp(\theta, \varphi_c = 0)$.*

maximum values of $E_\perp$ are seen to be the same as in the presence of the Ru(0001) substrate, and are again opposite for the two different X. However, the values of $K_{\rm SO}$ are found to have become significantly larger in the absence of the Ru substrate (see Table 5.3).

From Fig. 5.13(b), we see that the value of the orbital moment per X atom is the highest along the easy-axis for the freestanding monolayers of $FeAu_2$ and $MnAu_2$. This behavior differs from the trend seen in the XAu_2/Ru(0001) systems, though it is consistent with the prediction of Bruno [115]. The values of orbital moments are larger for the freestanding monolayers than the corresponding values on the deposited monolayers. This quenching of the orbital moments is an effect of the crystal field of the substrate.

Table 5.3: *Values of $K_{\rm SO}$ and $K_{\rm dip}$, the contributions to MAE due to spin-orbit coupling and dipole-dipole interaction, respectively, for freestanding XAu_2 monolayers. μ_z and μ_x are the orbital moments when magnetization points along z- and x-axis, respectively.*

X	$K_{\rm SO}$	$K_{\rm dip}$	μ_z	μ_x
	(meV per X atom)		(μ_B)	
Fe	2.1	0.05	0.12	0.15
Mn	1.8	−0.08	−0.09	0.02

We find that the value of $K_{\rm SO}$ does not differ appreciably in the [110] and [1$\bar{1}$0] directions; it is 2.1 meV per Fe atom for the $FeAu_2$ monolayer, and 1.8 meV per Mn atom for the $MnAu_2$ monolayers. Note that the direction of the easy axis differs in the two cases, for the former it is in-plane, while for the latter it is out-of-plane.

Next, we have obtained the values of $K_{\rm dip}$ for the freestanding alloy monolayers of XAu_2; once again we do not find an appreciable difference between our results for the [110] and [1$\bar{1}$0] directions. For $FeAu_2$ monolayers the value of $K_{\rm dip}$ is 0.05 meV per Fe atom, compared to the value of 0.04 meV per Fe atom for $FeAu_2$/Ru(0001) (see Table 5.2). The values of $K_{\rm dip}$ for $MnAu_2$ and $MnAu_2$/Ru(0001) are -0.08 and -0.06 meV per Mn atom, respectively (again, the negative sign implies out-of-plane easy axis). The slightly higher values of $K_{\rm dip}$ for the freestanding monolayers arise from the higher values of the magnetic moments.

5.7 Discussion

5.7.1 Relative contributions of different terms to $E_{\rm total}$

It is interesting to note that the primary reason for obtaining the spin spiral ground states is different for $FeAu_2$/Ru(0001) and $MnAu_2$/Ru(0001). By examining Fig. 5.9, we see that for $FeAu_2$/Ru(0001), it is the DM interaction that is chiefly responsible for stabilizing the spin spiral ground state over the FM state. In contrast, for $MnAu_2$/Ru(0001) the predominant role is played by the symmetric exchange interaction. One reason why the DM interaction is stronger in the case of $FeAu_2$/Ru(0001) is the larger value of the buckling parameter $d_{\rm b}$ in this system. From comparison with the unsupported alloys it can be seen that, in addition, the chemical nature of the magnetic element and its modification by the Ru substrate by bonding (charge transfer) also have an important influence on the strength of this interaction. The propensity of symmetric exchange to favor spin spirals is indicated by a small value of $\Delta E_{\rm AFM-FM}$; we have already seen above that this quantity is smaller for $MnAu_2$/Ru(0001) than $FeAu_2$/Ru(0001).

5.7.2 Role of Au

It was mentioned earlier that Fe/Ru(0001) shows a 120° Néel structure [108] and Mn/Ru(0001) shows a row-wise AFM structure [109]. In this study, we see that the magnetic interaction changes in these systems, due to the presence of Au in the overlayer, and the systems are driven toward a spin spiral ground state in $FeAu_2$/Ru(0001) and $MnAu_2$/Ru(0001), due to complex magnetic interactions. From Section (5.6.3B), we also see that due to the large spin-orbit coupling constant of Au atoms, the DM interaction mainly acts via these atoms, rather than the Ru atoms. On the other hand, it is the Ru substrate that makes the Au contribution very different in the Fe and Mn systems. The large additive contribution of the Au atoms toward the DM parameter thus helps to lower the energy of a spin spiral compared to the FM state, especially in the case of $FeAu_2$/Ru(0001).

5.8 Summary

In summary, we have performed *ab initio* density functional theory calculations to obtain the magnetic ground states of two surface alloys: $FeAu_2$/Ru(0001) and $MnAu_2$/Ru(0001). By considering both collinear and non-collinear magnetic structures, we have found that the magnetic ground state for both systems corresponds to a left-rotating spin spiral. For the Fe system the spiral propagates along the [110] direction with a period of 6.7 nm, while in the Mn alloy it is along $[1\bar{1}0]$ and has a period of 8.5 nm. In the former case, the spin spiral is stabilized by the Dzyaloshinskii-Moriya interaction, whereas in the latter case it is primarily stabilized by the symmetric exchange interaction. These results show that magnetic surface alloys constitute a new class of systems that can be explored for the existence of spin spirals. However, in the two particular systems considered in this work, the spin spiral states are only slightly lower in energy than the ferromagnetic state, by 0.17 and 0.28 meV per Fe and Mn atom, respectively.

We have seen that the strength of the DM interactions is very sensitive to the buckling of the overlayer. Of the two surface alloy systems considered in this study, $FeAu_2$/Ru(0001) has a buckling that is almost twice as large as that observed in $MnAu_2$/Ru(0001), and the

values of D_x and D_y are larger by a factor of ∼6–7. For a monolayer on a substrate, the buckling is fixed, being determined by the size mismatch between the overlayer and substrate atoms. However, when one considers surface alloys of the type AB/C, as in this study, one has more parameters to play with, since the buckling depends not only on the size difference between the overlayer atoms and the substrate, but also on the size difference between the two overlayer constituents A and B. One therefore has the ability to tune the buckling, and thus the strength of the DM interaction, over a wider range; this can be made use of as a way of further stabilizing spin spirals.

We also find that $FeAu_2$/Ru(0001) has a significantly high magnetic anisotropy energy, of the order of 1 meV per Fe atom, with an in-plane easy-axis. On the other hand, $MnAu_2$/Ru(0001) has a magnetic anisotropy energy that is smaller by an order of magnitude, and an out-of-plane easy axis. Upon comparing these values of the MAE with those obtained for the corresponding freestanding monolayers, we find that for both the systems, the presence of the substrate does not alter the direction of the easy-axis, but reduces the magnitude of the MAE considerably.

By comparing with the corresponding freestanding alloy monolayers, we find that the presence of the Ru substrate plays a crucial role in determining the magnetic properties of the surface alloy systems and Au atoms in the overlayer promote chirality in these systems.

Our results underline the need for considerable caution when applying the magnetic force theorem in calculations of magnetic structures, when small energy scales are involved.

Most importantly, we wish to underline that our work shows that bimetallic magnetic surface alloy systems of the type AB/C, such as those studied here, allow one to play with and tune the Dzyaloshinskii-Moriya interaction, thus allowing one to access novel magnetic structures such as spin spirals. Such surface alloys, which contain a heavy atom in the topmost layer, give one a way to tune the DM interaction via the structure, in contrast to A/B thin-film systems. This leads to the possibility of manipulating the spin spiral via electric fields or adsorbates.

Part B

Morphological Properties of Surfaces

Chapter 6

Tuning patterning conditions by co-adsorption: Br_2 and H_2 on Si(100)[1]

6.1 Introduction

In this chapter, we have attempted to develop a strategy to tune surface morphology by patterning using molecular self-assembly. Atomic-scale patterning of semiconductor surfaces can have important applications in the microfabrication of integrated circuits [117–120]. Patterned surfaces can also be used as templates for overlayer growth and controlling liquid crystal orientations. The existing techniques that are used to form ordered patterns on semiconductor surfaces [121] are scanning tunneling microscopy (STM), electron beam lithography, focused ion beams and reactive ion etching [122–124]. Though STM can provide fine control over atomic-scale features [125,126], for very large-scale manufacturing, it becomes ineffective and impractical. In contrast, while the other three techniques can be used in industrial applications, fine control over the surface morphology at the atomic length-scale has yet to be achieved.

For the efficient design of an electronic device, uniform generation of features is required.

[1]This work has been published in Ref. [116]

This can be achieved by directed self assembly, and this approach is being actively pursued in the electronics industry today. At present, there are several strategies being employed, but the basic idea is to form guiding patterns via conventional immersion lithography, and then use self-assembling systems to form regular patterns. These regular patterns are then etched using reactive ion etch processes; halogen chemistries are usually used for silicon and metal etches. It would be ideal if these two steps, of patterning and etching, could somehow be combined, e.g., if the patterning could be achieved by the self-assembly of halogen molecules on a semiconductor surface. Motivated in part by such considerations, in this chapter, we have focused our attention on the patterning due to co-adsorption of Br_2 and H_2 on the Si(100) surface.

6.2 Surface Reconstructions of Si(100)

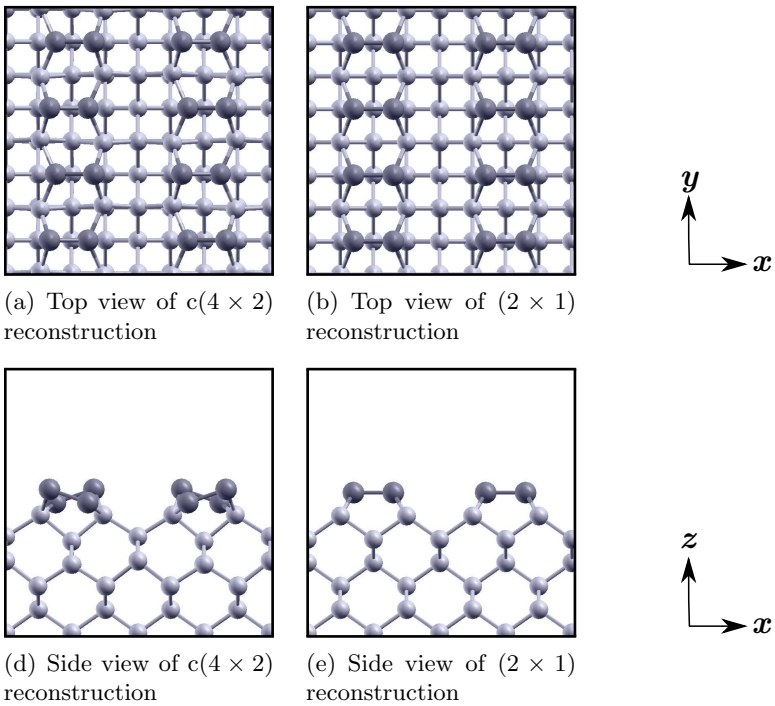

(a) Top view of c(4 × 2) reconstruction

(b) Top view of (2 × 1) reconstruction

(d) Side view of c(4 × 2) reconstruction

(e) Side view of (2 × 1) reconstruction

Figure 6.1: *The atomic arrangement of Si(100) surfaces for c(*4×2*) and* (2×1) *reconstructions. (a) and (b) show the top views, and (c) and (d) show the side views of the surface reconstructions. The Si atoms in the topmost layer, and the remaining Si atoms, are represented by dark gray and light gray spheres, respectively.*

Being a cheap yet high-quality material, silicon is the most widely used material in the

semiconductor industry. Si surfaces are known to show various reconstructions due to the rearrangement of surface atoms. For example, Si(100) exhibits either a (2×1) reconstruction (at high temperatures) or a c(4×2) reconstruction (at low temperatures) [127], Si(110) exhibits a (16×2) reconstruction [128], and Si(111) shows a very complicated 7×7 reconstruction [129]. Among these, Si(100) is characterized by the presence of a relatively simple reconstruction, consisting of rows of dimers forming a ladder-like structure (in all the figures in this chapter, we assume that the dimers, i.e., the rungs of the ladder, are oriented parallel to the x-axis). The formation of these dimers saturates one of the dangling bonds of the surface Si atoms, leaving one unsaturated dangling bond per atom. These dangling bonds are chemically active sites for adsorption. The dimerization on Si(100) leads to an asymmetric c(4×2) geometry at low temperature due to alternate buckling of nearest neighbor dimers, both along the dimer row (along the y-axis), and the direction perpendicular to the dimer row (along the x-axis) [see Fig. 6.1]. At high temperatures, STM images show an apparently symmetric (2×1) reconstruction due to a flip-flop mechanism of the dimers [130].

6.3 Previous Studies

Halogens are known to produce interesting patterns when deposited on the Si(100) surface [117, 131, 132]. Except for fluorine [133, 134], all the halogens form ordered structures on Si(100). As the atomic radius increases from chlorine to iodine, the size of the adsorbate halogen atoms gradually becomes larger than that of the underlying Si atoms. This results in steric interactions between the adsorbate atoms, which play a significant role in generating patterns for bromine and iodine adsorbates. Being small in size, hydrogen does not show such steric interactions when it is deposited on the Si(100) surface. However, we will show in this chapter that the presence of hydrogen can still play a crucial role, helping to generate new patterns and extend other patterns into a region of phase space that is more easily achievable experimentally. We note that hydrogen molecules are used for etching along with halogens [10].

There has been a previous density functional theory (DFT) study of the patterning of the Si(100) surface by bromine alone [118]. In this work, the authors considered a number of possible structures of dissociated bromine molecules adsorbed on the Si(100) surface. Their *ab initio* calculations of energetics were extended to determine the range of stability of various competing geometries with respect to bromine chemical potential, by calculating the surface free energy. In order to achieve patterning by a chemically reactive adsorbate such as bromine, one would like to obtain a stable adsorbate geometry that consists of a pattern, i.e., that does not simply consist of a uniform and full monolayer coverage of the substrate by adsorbate atoms. These previous authors found that over most of the range of bromine chemical potential considered by them, the most favored structure was either the clean surface without any adsorbed bromine, or a (3×2) pattern with full monolayer coverage. The unit cell of the (3×2) structure, which originates from an adsorbate-induced transformation of the surface, can be considered to consist of two single-monolayer steps, with all dangling bonds saturated with bromine atoms [see Fig. 6.2(j)]. More interesting, from the patterning point of view, is a $c(4 \times 2)$ structure at half coverage, where alternate dimers (in a staggered fashion on alternate dimer rows) are saturated with bromine atoms [see Fig. 6.2(f)]. However, the range of stability of this structure was found to be extremely narrow. Also, this structure is stable only at extremely low pressure. We should, however, note that such a structure has been observed in STM experiments on this system [135], though it has been reported that very careful experiments were needed to observe this [118]. We now wish to see whether the domain of stability for patterns of this sort can be extended, or new patterns can be formed, by co-adsorption of two gases.

Several authors have studied adsorption, diffusion and desorption of hydrogen on Si(100) [136–141]. Three stable phases have been observed in STM experiments when atomic hydrogen is present in the gas-phase [142–144]. While (1×1) and (2×1) [see Figs. 6.2(m) and 6.2(k)] structures can be obtained at double- and single-monolayer coverage, respectively, a (3×1) structure [see Fig. 6.2(l)] can only be observed on a specially prepared Si(100) surface. In a previous study [145], the author had calculated the free energy with respect to the atomic hydrogen chemical potential, and had reported that all three structures were

stable within the range of chemical potential considered.

Here, we want to address the following questions: (1) can we obtain new patterns by co-adsorbing Br_2 and H_2 at finite temperature and pressure? (2) can we extend the range of stability of patterns with Br_2 by co-adsorbing H_2? (3) what is the condition for extending the phase-stability to readily achievable experimental conditions by co-adsorption?

In this work, we are interested in equilibrium thermodynamics, and therefore restrict ourselves to computing the total energies of minimum-energy configurations, rather than energy barriers, which would be needed for a study that also included kinetics. However, one particular energy barrier is of interest to us: the activation barrier for atomic hydrogen and bromine, when adsorbed on Si(100), to combine to form hydrogen bromide. This has been shown to have a very high value, $\sim$ 3.0 - 3.5 eV [146]; we therefore believe we are justified in considering hydrogen and bromine to be co-adsorbed on the surface, rather than resulting in the formation of hydrogen bromide.

6.4 Computational Details

Our *ab initio* calculations have been performed using density functional theory (DFT) as implemented in the Quantum-ESPRESSO package [24]. A plane-wave basis set with a cutoff of 30 Ry was used to expand the electronic wave functions, and a cutoff of 300 Ry for the charge densities. The ion-electron interactions were treated by using an ultrasoft pseudopotential [**?**], while the exchange-correlation functional was approximated by a generalized gradient approximation of the Perdew-Burke-Ernzerhof form [20]. These parameters lead to a calculated bulk lattice constant for Si of 5.466 Å, which is in good agreement with the value of 5.47 Å reported earlier [118], as well as the experimental value of 5.43 Å. In order to obtain optimized geometries, the Broyden-Fletcher-Goldfarb-Shanno algorithm was used, until all components of the Hellmann-Feynman forces on the atoms being relaxed were less than 0.025 eV/Å.

The Si(100) surface was modeled by a slab geometry with eight atomic layers of silicon. A vacuum separation equivalent to 11 atomic layers was used, so as to minimize

the interaction between periodic images. In order to mimic the bulk, the atoms of the seventh and eighth Si layers were kept frozen at their bulk positions; all other atoms were allowed to relax. Each Si atom on the lower surface of the slab was passivated with two hydrogen atoms, which saturate the dangling bonds. To capture the c(4×2) surface reconstruction of Si(100), we have used a 4×2 surface supercell which includes four dimers on the upper surface. For this supercell a $2 \times 4 \times 1$ Monkhorst-Pack grid [27] was used to generate the k-point mesh for the Brillouin-zone sampling; the Marzari-Vanderbilt smearing technique [34] was used with the smearing width set equal to 0.005 Ry. We found that the dimers buckle on the clean Si(100) surface giving rise to a dimer bond-length and tilt-angle of 2.36 Å and 19°, respectively, which are comparable with the values of 2.28 Å and 17.4° reported earlier [137]. To take into account various configurations of the co-adsorbed surface, the supercell size in the x-y plane was varied up to 4×4. For the calculation of the chemical potential of an isolated molecule, the zero-point energy (ZPE) was calculated by taking into account the vibrational contribution at the Brillouin-zone centre. The vibrational frequencies were calculated by the density functional perturbation theory method [147, 148].

6.5 Results

6.5.1 Density functional theory calculations

In Fig. 6.2, we have shown all the thirteen configurations considered by us, for adsorption of one pure species alone. These configurations are labelled as P1, P2, ..., P13. In these, the coverage θ varies from 0.25 to 2.0. The adsorbate atoms are represented by large black spheres, while the silicon atoms of the first substrate layer are shown by small dark gray spheres and the remaining silicon atoms are represented by small light gray spheres. Notice that for $\theta < 1$, there are bare dimers present on the surface, while for $\theta \geq 1$, all dimers have atoms adsorbed on them. Due to steric effects, configurations P12 and P13 are not favored in the case of bromine, therefore these are only considered in the case of hydrogen adsorption. In previous studies, for adsorption of molecular bromine on Si(100),

configurations P6 and P10 were found to be the two minimum energy configurations that appeared in the phase diagram, with the former being energetically favorable for only a very narrow range of bromine chemical potential [118]. For the case of atomic hydrogen adsorption on Si(100), configurations P11, P12 and P13 were found to be the minimum energy configurations [145].

We have also studied co-adsorbed structures, labelled C1, C2, ..., C18 (see Figs. 6.3 and 6.4). Both bromine and hydrogen molecules generally dissociate upon adsorption on the Si(100) surface and usually saturate the dangling bonds on the same dimer. However, three kinds of exceptions can be imagined: one is where the two dangling bonds on a dimer are saturated by one H atom and one Br atom (see, e.g., configurations C3 and C6 in Fig. 6.3); another [149] is where only one Si atom of a dimer is saturated by an adsorbate atom, leaving the other Si atom unsaturated (see e.g., C6 and C7 in Fig. 6.3). A third exception is an adsorbate-induced modification of the surface, which results in some silicon atoms on the surface having two dangling bonds, to which adsorbate molecules can bind (see e.g., C8 to C10 in Fig. 6.4). Note that, except for full-monolayer coverages, we haven't considered any configurations where two neighboring (along x) dimers in two consecutive rows are occupied by Br atoms, since these are disfavored by steric interactions.

The adsorption energy (E_{ads}) and the co-adsorption energy ($E_{\text{co-ads}}$), per adsorbate atom, are defined as:

$$E_{\text{ads}} = \frac{1}{2N_{\text{A}}}(E_{\text{system}} - E_{\text{clean}} - N_{\text{A}}E_{\text{A}}), \tag{6.1a}$$

$$E_{\text{co-ads}} = \frac{1}{2N_{\text{tot}}}(E_{\text{system}} - E_{\text{clean}} - N_{\text{A}}E_{\text{A}} - N_{\text{B}}E_{\text{B}}), \tag{6.1b}$$

where E_{system} and E_{clean} are the total energy of the slab with and without the adsorbates, respectively. E_{A} (E_{B}) is the sum of the total energy and the zero-point energy of molecule A (B) in the gas phase. Here we are assuming that the contributions from the zero-point energies of the clean and adsorbate-covered surfaces mostly cancel out. Within a surface-supercell, the total number of A (B) molecules present on the upper surface of the

slab is denoted as N_A (N_B), and N_{tot} represents the total number of adsorbate molecules present on the upper surface, i.e., $N_{tot} = N_A + N_B$. E_{clean} is the total energy of the slab without the adsorbates present. Note that in calculating E_{clean}, the upper surface is taken as having a c(4×2) reconstruction. Therefore, appropriate modifications, e.g., incorporating the chemical potential of Si atoms, have to be made to Eq. (6.1) when considering configurations such as C8 to C13, where the unit cell size and the density of Si atoms on the upper surface differ from those in the configurations with the (4×2) unit cell. The factor of 2 in the denominator in Eq. (6.1) indicates that E_{ads} and $E_{co\text{-}ads}$ are defined as a quantity per atom, rather than per molecule. Note that a negative (positive) value of E_{ads} and $E_{co\text{-}ads}$ would refer to bound (unbound) states for the adsorbates.

In Table 6.1 we have listed our values for E_{ads}, obtained using Eq.(6.1a). In addition, we have also tabulated the relative stability (δE) of each configuration, with respect to the lowest energy configuration at that coverage. The co-adsorption energies are listed in Table 6.2, with corresponding values of δE.

We first consider our results for the pure phases. Let us examine the configurations P1 to P4, at a coverage $\theta_{Br} = 0.25$. These allow us to compare the relative importance of two effects: steric interactions, and having areas of the surface that are covered with patches of bare Si(100) with alternately buckled dimers, for convenience we will refer to these as ABD patches [150]. The configurations P1, P2 and P3 all have 3/4 of the surface covered with ABD patches, whereas P4 has only 1/2 of the surface covered with an ABD patch. However, the distances between bromine atoms (that are not on the same dimer) also vary between the different configurations, being least in P1, and increasing in the order P2, P4 and P3. Thus steric interactions are highest in P1 and lowest in P3. We find that P4 lies highest in energy, suggesting that having a relatively low proportion of the surface covered with an ABD patch carries a higher energetic cost than the steric repulsion between Br atoms on consecutive dimers in a row; note however that the energy differences between P1, P2, P3, and P4 are small. P1, P2 and P3 all have the same proportion of the surface covered with an ABD patch, and as expected, of these, P1, which has the largest steric repulsion, lies highest in energy. The situation is rather similar for hydrogen, in that P4,

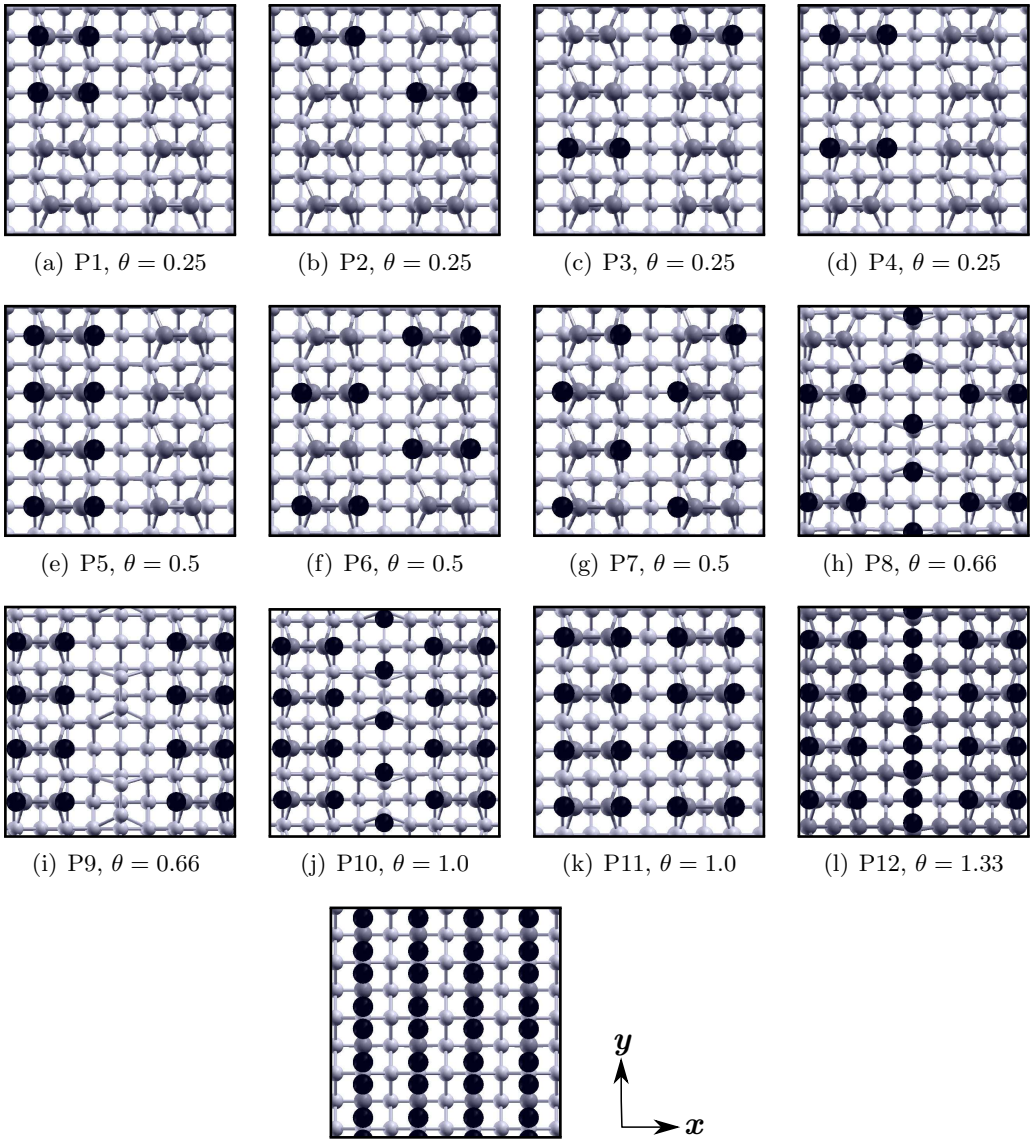

(a) P1, $\theta = 0.25$ (b) P2, $\theta = 0.25$ (c) P3, $\theta = 0.25$ (d) P4, $\theta = 0.25$

(e) P5, $\theta = 0.5$ (f) P6, $\theta = 0.5$ (g) P7, $\theta = 0.5$ (h) P8, $\theta = 0.66$

(i) P9, $\theta = 0.66$ (j) P10, $\theta = 1.0$ (k) P11, $\theta = 1.0$ (l) P12, $\theta = 1.33$

(m) P13, $\theta = 2.0$

Figure 6.2: *Top views of the atomic arrangement of Si(100) surfaces with pure (single component) adsorbates at different coverages θ. Only the first eleven configurations were considered for bromine adsorption, whereas all thirteen configurations were considered for hydrogen. The adsorbate atoms, Si atoms in the topmost layer, and the remaining Si atoms, are represented by large black, small dark gray, and small light gray spheres, respectively. Note that a non-integral number of unit cells is shown for P8, P9, P10 and P12.*

with the smallest ABD patch, lies highest in energy. However, for hydrogen, where the adsorbate atoms are small in size, steric effects are absent, and thus it is no longer true that P1 lies higher in energy than P2 and P3.

For both bromine and hydrogen, at $\theta = 0.5$, we find that P7, in which only one Si

Table 6.1: *Adsorption energies E_{ads} of Br_2 or H_2 on Si(100) for different configurations at various coverages θ. Relative energies δE are calculated with respect to the lowest energy configuration at that coverage. A blank in the last column indicates that only one configuration is considered at that coverage.*

Coverage	Config.	Unit cell	E_{ads} eV/atom	δE meV/(1×1)
Pure phases				
$\theta_{\mathrm{Br}} = 0.25$	P1	(4×4)	-2.13	2.2
$\theta_{\mathrm{Br}} = 0.25$	P2	(4×4)	-2.14	lowest
$\theta_{\mathrm{Br}} = 0.25$	P3	(4×4)	-2.13	0.5
$\theta_{\mathrm{Br}} = 0.25$	P4	(4×2)	-2.12	2.7
$\theta_{\mathrm{Br}} = 0.5$	P5	(4×2)	-2.10	9.8
$\theta_{\mathrm{Br}} = 0.5$	P6	(4×2)	-2.12	lowest
$\theta_{\mathrm{Br}} = 0.5$	P7	(2×2)	-1.93	95.7
$\theta_{\mathrm{Br}} = 0.66$	P8	(3×2)	-2.11	lowest
$\theta_{\mathrm{Br}} = 0.66$	P9	(3×2)	-2.07	28.0
$\theta_{\mathrm{Br}} = 1.0$	P10	(3×2)	-2.09	lowest
$\theta_{\mathrm{Br}} = 1.0$	P11	(2×1)	-2.07	21.0
$\theta_{\mathrm{H}} = 0.25$	P1	(4×4)	-1.06	lowest
$\theta_{\mathrm{H}} = 0.25$	P2	(4×4)	-1.05	3.5
$\theta_{\mathrm{H}} = 0.25$	P3	(4×4)	-1.04	4.3
$\theta_{\mathrm{H}} = 0.25$	P4	(4×2)	-1.04	4.8
$\theta_{\mathrm{H}} = 0.5$	P5	(4×2)	-1.07	lowest
$\theta_{\mathrm{H}} = 0.5$	P6	(4×2)	-1.04	14.2
$\theta_{\mathrm{H}} = 0.5$	P7	(4×2)	-0.84	115.0
$\theta_{\mathrm{H}} = 0.66$	P8	(3×2)	-1.04	lowest
$\theta_{\mathrm{H}} = 0.66$	P9	(3×2)	-1.04	0.1
$\theta_{\mathrm{H}} = 1.0$	P10	(3×2)	-1.06	10.9
$\theta_{\mathrm{H}} = 1.0$	P11	(2×1)	-1.07	lowest
$\theta_{\mathrm{H}} = 1.33$	P12	(3×1)	-0.82	
$\theta_{\mathrm{H}} = 2.0$	P13	(2×1)	0.98	unbound

atom on the dimers is saturated by an adsorbate atom, lies highest in energy of the three configurations considered by us. For bromine, the remaining two configurations, P5 and P6, once again allow us to see the competition between steric effects and the presence of ABD patches: if the former effect were dominant, one would expect P6 (where there are lower steric interactions but no ABD patch) to be lower in energy, whereas if the latter were dominant, P5 (where the ABD patch covers half the surface but there are large steric interactions) should be lower in energy. Note, however that compared to the configuration P1 at $\theta_{\mathrm{Br}} = 0.25$, steric interactions are higher in P5. In P1, every Br atom has one

nearest-neighbor (NN) Br atom on the same dimer, and one next-nearest-neighbor (NNN) Br atom on the neighboring dimer (along the y axis) in the dimer row. However, in P5, in addition to the NN Br atom, there are *two* NNN Br atoms along y; for this reason, steric interactions now prevail slightly over the effect of having ABD patches, and P6 is slightly favored over P5. Once again, for hydrogen, the steric effects are absent, and the ABD effect prevails, and thus P5 is favored over P6.

At $\theta = 0.66$, we find that P8 is favored over P9 for bromine, due to steric effects. In P8 each Br atom has a NN Br atom at a distance of 4.00 Å, a NNN Br atom at 4.43 Å, and a 3rd-NN Br atom at 4.52 Å. In contrast, in P9, each Br atom has a NN Br atom at 3.83 Å, and two NNN Br atoms at 4.08 Å. Thus, we see that the distances between Br atoms are shorter in P9 than in P8, the former therefore has greater steric repulsion, and lies higher in energy. However, in the case of hydrogen adsorption, these steric effects are not present, and P8 and P9 are almost degenerate in cornenergy.

At $\theta = 1.0$, as no bare Si(100) regions are exposed, the ABD effect is absent. This again allows us to examine the importance of steric effects for bromine but not hydrogen. In P11, a Br atom has four Br neighbors at distances of 3.8 – 3.9 Å, with steric repulsions between them. However, in P10, because of the corrugated nature of the surface, there are only three Br neighbors at a distance of 3.8 – 3.9 Å, and the next-nearest Br neighbors are at a distance > 4.3 Å. Thus, for bromine adsorption, P10 is lower in energy than P11. We find the difference in energy between P10 and P11 to be 21 meV per (1×1) cell, which is in agreement with the previously reported value of 15 meV/(1×1) [118]. For hydrogen adsorption, these steric interactions are absent; but P10 requires the additional energy of restructuring the Si surface from the c(4×2) to the (3×2) reconstruction. As a result, for hydrogen adsorption, P10 is higher in energy than P11.

The adsorption energy of hydrogen is found to vary from -1.06 eV/atom at $\theta = 0.25$, to -0.82 eV/atom at $\theta = 1.33$. This may be compared with a low-coverage value of -0.98 eV/atom reported by a previous author [141]. For $\theta = 2.0$, E_{ads} becomes positive (unbound); note that this is true with respect to molecular hydrogen in the gas phase, but not with respect to atomic hydrogen in the gas phase [145]. Bromine binds more strongly

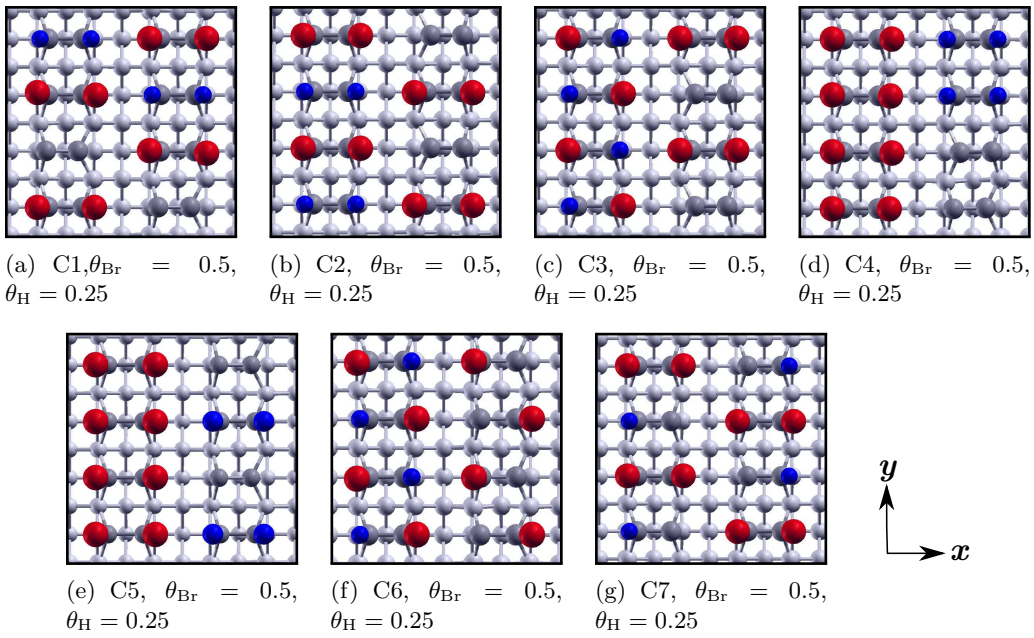

(a) C1,θ_{Br} = 0.5, θ_H = 0.25 (b) C2, θ_{Br} = 0.5, θ_H = 0.25 (c) C3, θ_{Br} = 0.5, θ_H = 0.25 (d) C4, θ_{Br} = 0.5, θ_H = 0.25

(e) C5, θ_{Br} = 0.5, θ_H = 0.25 (f) C6, θ_{Br} = 0.5, θ_H = 0.25 (g) C7, θ_{Br} = 0.5, θ_H = 0.25

Figure 6.3: *Top views of different configurations considered for co-adsorption of Br_2 and H_2 on Si(100) for Br-rich phases, with $\theta_{Br} + \theta_H < 1.0$. The Br, H, Si atoms in the topmost layer, and the remaining Si atoms, are represented by large red, small blue, small dark gray, and small light gray spheres, respectively. The H-rich configurations can be obtained by interchanging the large red and small blue atoms.*

to the Si(100) surface than hydrogen does. At $\theta = 1.0$, we find E_{ads} for bromine to be -2.09 eV/atom, which compares well with a previously reported value of -2.13 eV/atom [151].

For co-adsorbed surfaces with $\theta = \theta_{Br} + \theta_H < 1$, we have considered both (θ_{Br}=0.5, θ_H=0.25) and (θ_{Br}=0.25, θ_H=0.5); for each of these cases we have considered seven configurations (see configurations C1 to C7 in Fig. 6.3). For both the cases we found the C1 configuration to be the lowest in energy among all the configurations considered here. Let us first consider the Br-rich case, i.e., (θ_{Br}=0.5, θ_H=0.25). Out of seven Br-rich surfaces, C4 to C7 are higher in energy than C1, C2 and C3. This is due to steric repulsion between bromine atoms on consecutive dimers (along the y direction) in C4 and C5. C4 lies lower in energy than C5 because of the presence of an ABD patch in C4. Again, C6 and C7, where only one Si atom on the dimers is saturated by an adsorbate atom, lie highest in energy. The three lowest energy configurations lie close in energy. In C1 and C2, all Br atoms have only one Br NN, at a distance of 3.9 Å, however in C3, some Br atoms have two NN Br atoms at 3.8-3.9 Å. Thus there is increased steric repulsion in C3, leading to a

higher energy. For the H-rich phases, five configurations, C1 to C5, are almost degenerate. Note that C4 and C5 are closer in energy for the H-rich case than the Br-rich case. This is because in the H-rich case, the energy lowering effect of the ABD patch in C4 is offset by the increased steric repulsion between the Br atoms on neighboring dimers along the y direction. As before, C6 and C7, with single adsorbate atoms adsorbed on dimers, are the most disfavored configurations.

Table 6.2: *Co-adsorption energies $E_{\text{co-ads}}$ of Br_2 and H_2 on Si(100), for different configurations at various coverages θ. Relative energies δE are calculated with respect to the lowest energy configuration at a given coverage. A blank in the last column indicates that only one configuration is considered at that coverage.*

Coverage		Config.	Unit cell	$E_{\text{co-ads}}$	δE
θ_{Br}	θ_{H}			eV/atom	meV/(1×1)
$\theta < 1$					
0.5	0.25	C1	(4×4)	-1.79	lowest
0.5	0.25	C2	(4×2)	-1.79	1.7
0.5	0.25	C3	(4×2)	-1.78	8.3
0.5	0.25	C4	(4×4)	-1.76	20.2
0.5	0.25	C5	(4×2)	-1.75	26.8
0.5	0.25	C6	(4×2)	-1.72	50.6
0.5	0.25	C7	(4×2)	-1.70	75.0
0.25	0.5	C1	(4×4)	-1.43	lowest
0.25	0.5	C2	(4×2)	-1.43	1.4
0.25	0.5	C3	(4×2)	-1.43	0.1
0.25	0.5	C4	(4×4)	-1.43	2.0
0.25	0.5	C5	(4×2)	-1.43	3.7
0.25	0.5	C6	(4×2)	-1.36	53.8
0.25	0.5	C7	(4×2)	-1.33	75.4
$\theta \geq 1$					
0.33	1	C8	(3×2)	-1.09	
0.66	0.66	C9	(3×1)	-1.34	lowest
0.66	0.66	C10	(3×1)	-1.00	447.2
0.66	0.33	C11	(3×2)	-1.78	
0.33	0.66	C12	(3×2)	-1.43	lowest
0.33	0.66	C13	(3×2)	-1.42	4.9
0.5	0.5	C14	(4×2)	-1.62	lowest
0.5	0.5	C15	(2×2)	-1.62	0.8
0.5	0.5	C16	(2×1)	-1.59	24.8
0.5	0.5	C17	(4×2)	-1.59	25.6
0.25	0.75	C18	(4×4)	-1.35	

For co-adsorbed surfaces at $\theta \geq 1$, we have considered three configurations at $\theta = 1.33$

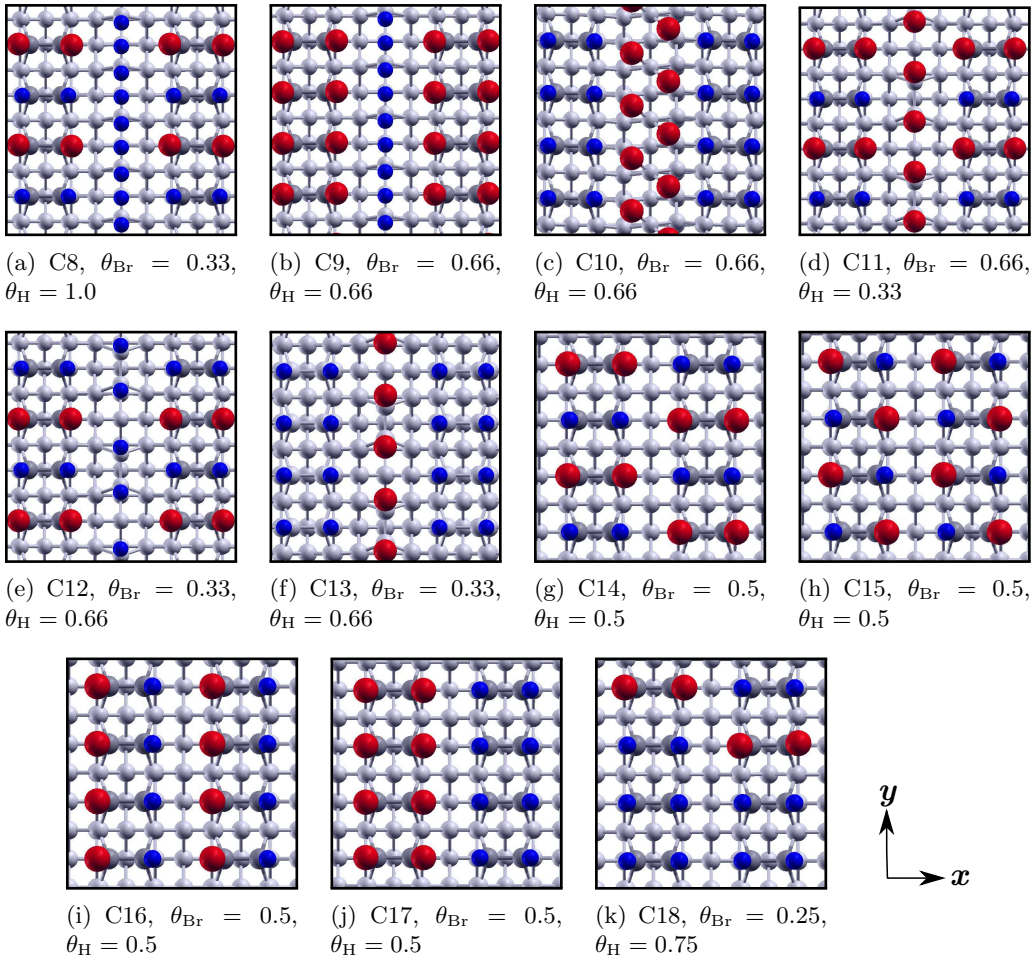

(a) C8, $\theta_{Br} = 0.33$, $\theta_H = 1.0$ (b) C9, $\theta_{Br} = 0.66$, $\theta_H = 0.66$ (c) C10, $\theta_{Br} = 0.66$, $\theta_H = 0.66$ (d) C11, $\theta_{Br} = 0.66$, $\theta_H = 0.33$

(e) C12, $\theta_{Br} = 0.33$, $\theta_H = 0.66$ (f) C13, $\theta_{Br} = 0.33$, $\theta_H = 0.66$ (g) C14, $\theta_{Br} = 0.5$, $\theta_H = 0.5$ (h) C15, $\theta_{Br} = 0.5$, $\theta_H = 0.5$

(i) C16, $\theta_{Br} = 0.5$, $\theta_H = 0.5$ (j) C17, $\theta_{Br} = 0.5$, $\theta_H = 0.5$ (k) C18, $\theta_{Br} = 0.25$, $\theta_H = 0.75$

Figure 6.4: *Top views of different configurations considered for co-adsorption of Br_2 and H_2 on Si(100), with $\theta_{Br}+\theta_H \geq 1.0$. The Br, H, Si atoms in the topmost layer, and the remaining Si atoms, are represented by large red, small blue, small dark gray, and small light gray spheres, respectively.*

and eight at $\theta = 1.0$ (see configurations C8 to C18 in Fig. 6.4). Of those combinations of θ_{Br} and θ_H for which we have considered more than one configuration, we first consider (θ_{Br}=0.66, θ_H=0.66). Here, in C9, Br atoms have one Br NN at a distance of 4.12 Å, while in C10, they have two Br NNs at distances of 3.23 Å and 3.39 Å. Thus, for steric reasons, C9 is favored over C10. Next, for (θ_{Br}=0.33, θ_H=0.66), we compare C12 and C13. In the former, the Br atoms have one Br NN at a distance of 3.97 Å, whereas in the latter, they have two Br NNs at distances of 3.82 Å and 3.91 Å. Therefore, C12 is lower in energy than C13. Finally, we consider (θ_{Br}=0.5, θ_H=0.5). C14, with atoms of the same type on every dimer, is the most favored. The higher cost of the heteropolarity of the adsorbates on

dimers in C15 is however offset by the lowering of electrostatic energy in the checkerboard arrangement here. C16 and C17 have higher steric interactions between Br atoms and therefore lie highest in energy.

The total energies obtained from *ab initio* DFT calculations are valid at zero temperature and pressure. Moreover, using them we can only compare configurations which contain the same number of adsorbate molecules of each type. If we want to go beyond this to obtain stable phases at finite temperature T and pressure p, allowing the number of adsorbate molecules to vary, we have to extend the work presented in this Section by using it as input into a treatment using *ab initio* atomistic thermodynamics.

6.5.2 *Ab initio* atomistic thermodynamics: construction of Gibbs free energy

Let us consider a system consisting of the clean Si(100) surface and two gas reservoirs, one each for hydrogen and bromine molecules, kept at temperature T. We restrict ourself to "constrained thermodynamics" of the system, where the bromine and hydrogen reservoirs are separately in thermal equilibrium with the Si(100) surface, but not with each other. This emphasizes the fact that the gas-phase reaction between the two reservoirs is prohibited. When the system achieves thermodynamic equilibrium, a stable co-adsorbed phase can be obtained. The surface Gibbs free energy γ, of a co-adsorbed phase with surface area S, can be defined as: [41, 42]

$$\gamma(T, \{p_i\}, \{N_i\}) = \frac{1}{S}[G_{\text{co-ads}}(T, \{p_i\}, \{N_i\}) - \sum_i \mu_i N_i], \tag{6.2}$$

where $G_{\text{co-ads}}$ is the total Gibbs free energy of the co-adsorbed system, which is the sum of the vibrational energy and the total electronic energy $E_{\text{co-ads}}$ of the co-adsorbed system. p_i is the partial pressure of species i. μ_i is the chemical potential of an atom (molecule) and N_i is the total number of atoms (molecules) of species i. (For pure phases, $G_{\text{co-ads}}$ will be replaced by the corresponding quantity for a one-component adsorbate, G_{ads}.) Further, we can define the stability of the co-adsorbed surface with respect to clean Si(100), and

write the relative surface free energy as:

$$\Delta\gamma(T,\{p_i\},\{N_i\}) = \gamma(T,\{p_i\},\{N_i\}) - \gamma_{\text{clean}}(T,\{p_i\},\{N_i\}), \tag{6.3}$$

where

$$\gamma_{\text{clean}}(T,\{p_i\},\{N_i\}) = \frac{1}{S}[G_{\text{clean}}(T,\{p_i\},\{N_i\}) - \mu_{\text{Si}}N_{\text{Si}} - \mu_{\text{H}_2}N_{\text{H}_2}^{\text{lower}}]. \tag{6.4}$$

G_{clean} and $N_{\text{H}_2}^{\text{lower}}$ in Eq. (6.4) denote the total Gibbs free energy of the slab without any adsorbates on the upper surface, and the total number of passivating hydrogen molecules present on the lower surface, respectively. For this study we have neglected the contribution to the free energy from atomic vibrations. As we take a difference of the free energies [see Eq. (6.3)], there will be a partial cancellation of the vibrational contributions from the co-adsorbed surface and the clean Si(100) surface [41, 152].

Before proceeding along these lines, one should however be aware of the limitations of this approach. Of course, the phase diagram cannot yield any configurations other than those considered in the DFT calculations. We are not including the vibrational contribution to the free energy of the surfaces; neglect of these may lead to slight shifts in transition pressures and temperatures, though qualitative features of the phase diagram should remain unchanged. In addition, we have not included the contributions from the configurational entropy, which may become important at low coverage. Finally, our treatment does not include any consideration of kinetic effects, which will however be present in actual experimental scenarios. In experimental situations the coverage of adsorbates is often determined by kinetics rather than thermodynamics. In such cases a formalism based on the grand canonical ensemble may not be appropriate.

6.5.3 Limits of chemical potential

The chemical potential of a molecule X_2 in the gas phase can be defined as the change of Gibbs free energy per molecule, and for a single molecule can be written as:

$$\mu_{X_2} = E^{gas}_{X_2} + E^{ZPE}_{X_2} + \Delta\mu_{X_2}(T,p), \tag{6.5}$$

where $E^{gas}_{X_2}$ and $E^{ZPE}_{X_2}$ are the total energy calculated by DFT, and the zero-point energy of the molecule in the gas phase, respectively. The last term in Eq. (6.5) is the contribution arising from all other degrees of freedom. Assuming that the ideal gas law holds for the molecules in the gas phase, one can write [41]:

$$\Delta\mu_{X_2}(T,p) = \mu_{X_2}(T,p^0) - \mu_{X_2}(T^0,p^0) + k_B T \ln(p/p^0), \tag{6.6}$$

where T^0 and p^0 denote the ambient temperature and pressure, and k_B is the Boltzmann constant. The difference between the first two terms on the right hand side of Eq. (6.6) can be obtained from the thermochemical tables [153]. As $\Delta\mu_{X_2}(T,p)$ contains all the effects of temperature and pressure, we can express the Gibbs free energy as a function of $\Delta\mu_{X_2}(T,p)$, instead of $\mu_{X_2}(T,p)$.

The adsorbate chemical potential cannot be varied indefinitely in an experiment. Theoretically, we can determine the allowed range of chemical potential of an adsorbate molecule at $T = 0$ [41, 42]. We assume that the limits do not change within the range of temperature and pressure considered here. The upper limit of the chemical potential is the limit beyond which the gas phase of the molecule starts to condense. At the upper limit, the chemical potential of a molecule becomes equal to the total energy in the gas phase, since $\Delta\mu_{X_2} = \mu_{X_2} - E^{gas}_{X_2} + E^{ZPE}_{X_2} = 0$. On the other hand, the lower limit sets the boundary beyond which the clean Si(100) surface becomes more stable than the co-adsorbed surface. This leads to a condition where $\Delta\mu_{X_2}$ overshoots the binding energy of the molecule on the surface. The upper and lower limits can also be called "adsorbate-rich" and "adsorbate-poor" gas-phase environments. Combining these two limits, we get the following criterion,

$$E^{X_2}_{bind} < \Delta\mu_{X_2} < 0, \tag{6.7}$$

where $E^{X_2}_{bind}$ is the binding energy of a single molecule on the surface. Below the lower

limit one should obtain the clean Si(100) surface to be the most stable phase.

6.5.4 Thermodynamic analysis: phase diagram

To obtain the range of stability (phase diagram) of the co-adsorbed phases, we have calculated $\Delta\gamma$ as a function of adsorbate chemical potentials $\Delta\mu_{Br_2}$ and $\Delta\mu_{H_2}$, using Eqs. 6.3 and 6.6, for the phases considered at $T = 0$. Note that only the lowest energy configuration at each coverage is included in the thermodynamic analysis.

The allowed range of chemical potentials per bromine and hydrogen molecule is obtained as follows: -4.28 eV $< \Delta\mu_{Br_2} < 0$, and -2.14 eV $< \Delta\mu_{H_2} < 0$. We have however varied $\Delta\mu_{Br_2}$ and $\Delta\mu_{H_2}$ slightly below the lower limit, in order to verify that we obtain the clean Si(100) surface in this region. In Fig. 6.5(a) we have plotted the surface Gibbs free energy $\Delta\gamma$, as a function of $\Delta\mu_{Br_2}$ and $\Delta\mu_{H_2}$. For each configuration, the plane given by Eqs. 6.3 and 6.6 is plotted using the numerical results from the DFT calculations. At each value of ($\Delta\mu_{Br_2}$, $\Delta\mu_{H_2}$) the lowest lying configuration is then determined to yield the phase diagram shown in Fig. 6.5(b). We find that there are five pure phases and six co-adsorbed phases present in the phase diagram; however three of these (C11, C18 and Br-rich C1) are present as only very narrow lines in the phase diagram. A fourth phase C9 appears in a tiny region at the top of the phase diagram.

Let us concentrate first on the $\Delta\mu_{Br_2}$-axis of Fig. 6.5(b), and compare with previous results on the adsorption of molecular bromine alone. Within the allowed range of $\Delta\mu_{Br_2}$, we observe three stable patterns: over a broad range, the lowest free-energy configuration is P10 (with θ_{Br}=1.0), and over a much narrower range, it is P6 (with θ_{Br}=0.5). While these two phases appear in the phase diagram of previous authors [118], we obtain an additional stable phase, viz., P2 (with θ_{Br}=0.25), also with only a narrow range of stability. This configuration was not considered by the previous authors. Note that the zero of the chemical potential of bromine is defined differently in our work and theirs. Note also that the ranges of stability of P2 and P6 could conceivably increase if contributions from configurational entropy were included.

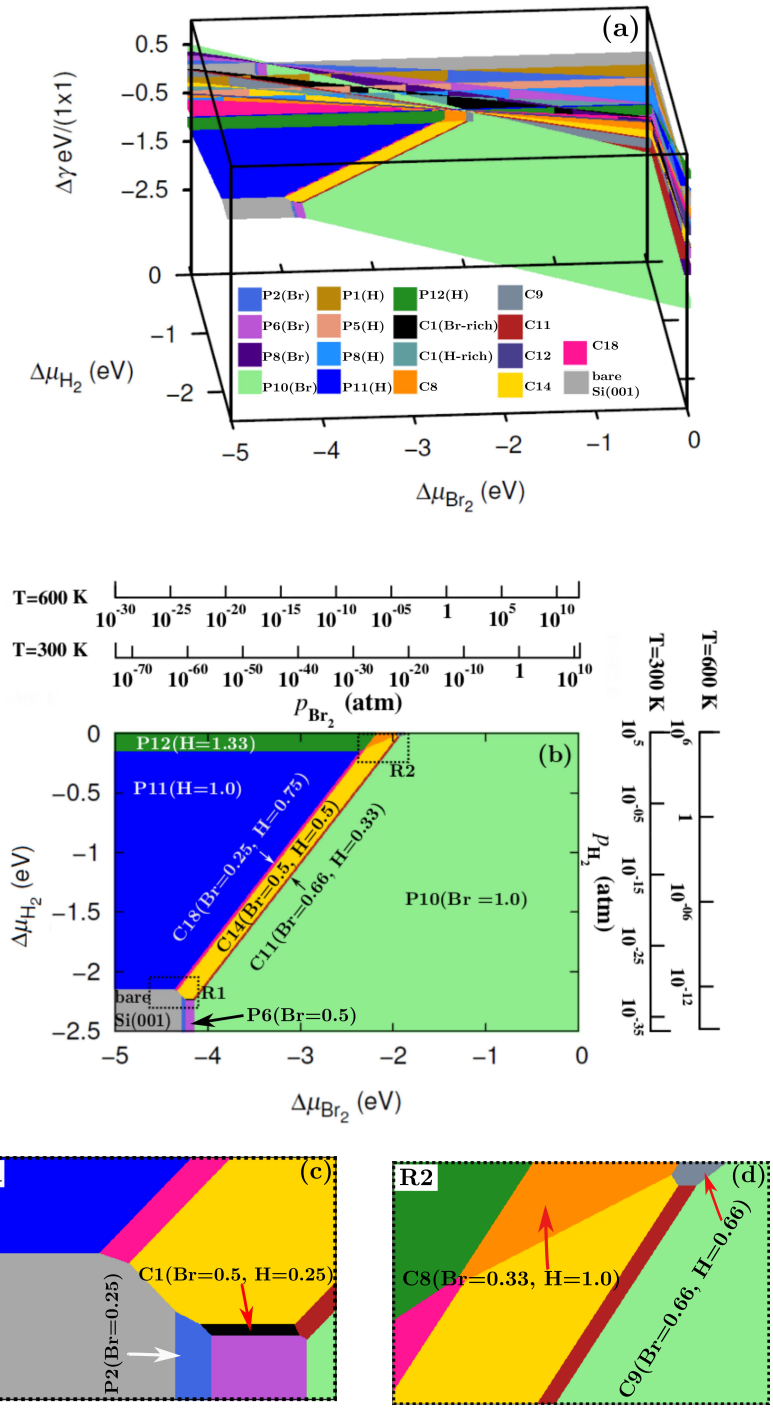

Figure 6.5: *Phase diagrams: (a) shows the surface Gibbs free energy $\Delta\gamma$ of different configurations as a function of adsorbate chemical potentials ($\Delta\mu_{Br_2}$, $\Delta\mu_{H_2}$) and (b) shows the two-dimensional surface phase diagram in the $\Delta\mu_{Br_2}$-$\Delta\mu_{H_2}$ plane. Different colors correspond to different configurations. Chemical potentials for each molecule are converted into a pressure scale at two different temperatures, 300 K and 600 K. (c) and (d) show a zoomed in view of the regions R1 and R2 indicated by the dotted black rectangles in (b).*

Next, we focus on the $\Delta\mu_{H_2}$-axis in order to determine the stable phases of the hydrogen-covered surface. We find that there are two stable phases, which are the P11 configuration, with $\theta_H = 1.0$, and the P12 configuration, with $\theta_H = 1.33$. Note that no phase with $\theta_H < 1.0$ appears to be stable. In a previously published study [145], the author had reported three stable phases, P11, P12 and P13 with $\theta_H = 1.0, 1.33$ and 2.0, respectively. However, we find that P13 has a positive adsorption energy, i.e., is not bound. There are two possible sources of the discrepancy between the results of Ref. [145] and ours: (i) the earlier results are referenced to atomic hydrogen, not molecular hydrogen, (ii) in this very early study, extremely low plane-wave cut-offs were used, which could possibly lead to numerical inaccuracies.

Over most of the range of $\Delta\mu_{Br_2}$ and $\Delta\mu_{H_2}$, we find that the stable phases are either P10(Br) [light green in Fig. 6.5(b)], which contains bromine alone, or P11(H) [blue in Fig. 6.5(b)], which contains hydrogen alone; these were obtained also in the adsorption of the one-component gases. There is a small range where the stable phase is P2(Br) [cornflower blue in Figs. 6.5(b) and 6.5(c)]; this is a patterned arrangement, consisting of zigzag lines of pairs of Br atoms running along the x direction, successive lines are separated by 15.47 Å. There is a narrow line of C18 (magenta), which is similar to P2(Br), except that the bare Si areas of P2(Br) are H-covered in C18. There is a small (purple) region where we find P6(Br), which is also a patterned configuration, with a checkerboard arrangement of Br atoms [see Fig. 6.2(f)]. There is also a fairly substantial (yellow) region of the phase diagram corresponding to the co-adsorbed structure C14, which is similar to P6(Br), except that there are also H atoms present [see Fig. 6.4(g)]. Thus, by co-adsorbing with hydrogen, we have managed to extend the range of chemical potentials of bromine over which one can get such a pattern. There are two very narrow lines (red and black) where one obtains C11 and C1(Br-rich), respectively. C1(Br-rich) is similar to C14 and P6(Br) in the arrangement of the Br atoms, and C11 is an interesting pattern, with a grid-like arrangement of Br atoms, though given its very narrow range of stability, it may be difficult to stabilize this configuration in experimental conditions. At the top of the phase diagram (i.e., $\Delta\mu_{H_2}$ close to 0) we find one pure phase, P12(H) (dark green) with $\theta_H = 1.33$, and

two co-adsorbed phases, C8 (orange) and C9 (dark gray). The C8 configuration consists of Br atoms arranged in a rectangular checked pattern and C9 has alternating Br and H stripes. We thus see that, by co-adsorbing hydrogen with bromine, we have not only increased the range of chemical potentials over which we can obtain certain patterns, we have also obtained a greater diversity of interesting patterned arrangements of the bromine atoms. However, we should note that several of the patterns of interest here lie only very slightly lower in energy than other competing configurations at the same coverage, and it may therefore be difficult to observe them experimentally. For example, P6(Br) lies only slightly lower in energy than P5(Br), C14 is close in energy to C15, and P2(Br) to P3(Br).

To shed more light on the phase diagram, we have plotted the pressure variations along with the adsorbate chemical potentials at two temperatures, 300 and 600 K. To obtain the pressure scale from a given chemical potential scale, we have used Eq. (6.6). The difference between the first two terms on the right hand side of Eq. (6.6), i.e., $\mu_{X_2}(T, p^0) - \mu_{X_2}(T^0, p^0)$, is obtained from the thermochemical table [153]. The value of this for bromine molecules is -0.66 eV and -1.47 eV at 300 K and 600 K, respectively, whereas for hydrogen molecules the value at 300 K is -0.31 eV, and the value at 600 K is -0.75 eV. From the pressure and temperature scale in Fig 6.5(b), one can see that at ambient pressure of both the molecules only the P10(Br) configuration is favored, with $\theta_{Br} = 1.0$. It is of interest to see under what conditions the patterned configurations P6(Br), which contains only bromine, and the very similar C14, which contains co-adsorbed bromine and hydrogen, can be obtained. When only bromine is adsorbed, in order to obtain P6(Br), one needs a pressure of about 10^{-60} atm at 300 K and 10^{-24} atm at 600 K. However, when bromine and hydrogen are co-adsorbed, it is possible to obtain the corresponding patterned configuration C14 over a range of higher partial pressures of bromine and hydrogen, e.g., at $p_{Br_2} \sim 10^{-40}$ atm and $p_{H_2} \sim 10^{-14}$ atm at 300 K, or at $p_{Br_2} \sim 10^{-18}$ atm and $p_{H_2} \sim 10^{-8}$ atm at 600 K; such conditions are much more accessible to experimental techniques. Similarly, the co-adsorbed configuration C18 is observable at higher pressures than the corresponding pure Br configuration P2(Br). Thus we see that by co-adsorbing bromine and hydrogen, not only have we extended the area of phase-space in which we can obtain patterned configurations

of interest to us, we have pushed up the pressures at which these can be achieved into a region that is much easier to attain experimentally.

6.5.5 Condition for extending the range of stability of pure bromine phases to higher pressure regime

We now attempt to understand why co-adsorption with hydrogen extends the region of phase stability to higher pressures than those at which the corresponding pure bromine configuration is stable. To do this, we examine why the slopes of the relevant co-existence boundaries in Fig. 6.5 (e.g., between C11 and C14, or between C14 and C18) are positive. Eq. (6.3) for a configuration Ci can be rewritten as:

$$\Delta\gamma^{Ci} = \frac{1}{S}(2N^{Ci}_{\text{tot}}E^{Ci}_{\text{co-ads}} - N^{Ci}_{\text{Br}_2}\Delta\mu_{\text{Br}_2} - N^{Ci}_{\text{H}_2}\Delta\mu_{\text{H}_2}), \tag{6.8}$$

where $N^{Ci}_{\text{Br}_2}$ and $N^{Ci}_{\text{H}_2}$ are the total number of adsorbed bromine and hydrogen molecules per area S in configuration Ci, respectively, and $N^{Ci}_{\text{tot}} = N^{Ci}_{\text{Br}_2} + N^{\text{Ci}}_{\text{H}_2}$. Along a co-existence boundary between two configurations Ca and Cb, $\Delta\gamma^{Ca} = \Delta\gamma^{Cb}$, and the equation of the co-existence boundary therefore becomes:

$$(N^{Ca}_{\text{Br}_2} - N^{Cb}_{\text{Br}_2})\Delta\mu_{\text{Br}_2} + (N^{Ca}_{\text{H}_2} - N^{Cb}_{\text{H}_2})\Delta\mu_{\text{H}_2} = 2(N^{Ca}_{\text{tot}}E^{Ca}_{\text{co-ads}} - N^{Cb}_{\text{tot}}E^{Cb}_{\text{co-ads}}). \tag{6.9}$$

The slope of the co-existence boundary between Ca and Cb in the $\Delta\mu_{\text{Br}_2}$-$\Delta\mu_{\text{H}_2}$ phase diagram is therefore given by:

$$m = \frac{N^{Cb}_{\text{Br}_2} - N^{Ca}_{\text{Br}_2}}{N^{Ca}_{\text{H}_2} - N^{Cb}_{\text{H}_2}} = \frac{\theta^{Cb}_{\text{Br}} - \theta^{Ca}_{\text{Br}}}{\theta^{Ca}_{\text{H}} - \theta^{Cb}_{\text{H}}}, \tag{6.10}$$

where θ^{Ci}_{Br} and θ^{Ci}_{H} are the coverages of Br and H, respectively, in configuration Ci. In any situation where the sum of the coverages of the two adsorbates is the same in the two co-existing phases, i.e., $\theta^{Ca}_{\text{Br}} + \theta^{Ca}_{\text{H}} = \theta^{Cb}_{\text{Br}} + \theta^{Cb}_{\text{H}}$ (=1 for {P10(Br),C11}, {C11,C14}, {C14,

C18}, {C18,P11(H)}), on substituting into Eq. (6.10), we get $m = +1$, i.e., the co-existence boundary has a positive slope, which is why the phase extends to higher pressures. Note, however, that such an analysis alone would not suffice to tell us that co-adsorption would allow us to extend patterns to higher pressures. We need our *ab initio* results in order to determine that these phases appear in the phase diagram at all.

In the phase diagram, there are several phase boundaries between the eleven configurations; at each phase-boundary the surface may undergo an order to disorder phase-transition till a new stable pattern with different adsorbate concentrations gets stabilized. If the surface becomes disordered near phase transitions, then the configurational entropy also contributes significantly to the surface Gibbs free energy; this leads to smearing of the phase boundaries. As a result, near phase-boundaries, the surface may not show any long-ranged order, while local ordering may be present. Several of the phases that appear in our phase diagram, e.g., C1(Br), C11 and C18 may not show long-ranged ordering as they exist over a very narrow range of adsorbate chemical potentials. Note that we find that the surface goes from the P6(Br) configuration (θ_{Br}=0.5, θ_{H}=0) to the C14 configuration (θ_{Br}=0.5, θ_{H}=0.5) via the intermediate configuration C1 (θ_{Br}=0.5, θ_{H}=0.25). Similarly, the transition between the P10 configuration (θ_{Br}=1.0) and C14 configuration (θ_{Br}=0.5, θ_{H}=0.5) proceeds via the intermediate configuration C11 (θ_{Br}=0.66, θ_{H}=0.33). Transitions such as these might occur in a continuous fashion.

6.6 Summary

In summary, we have studied the co-adsorption of Br_2 and H_2 on Si(100) and predicted the stability of the co-adsorbed phases by using density functional theory calculations in combination with *ab initio* atomistic thermodynamics. By considering different configurations with varying coverages of adsorbates on the surface, and comparing the surface Gibbs free energy as a function of adsorbate chemical potentials, we are able to predict the ranges of stability of various phases at different temperature and pressure.

When comparing the energies of different possible configurations at a given coverage,

we have seen clearly the importance of two dominant effects in determining the relative energetics of competing structures. One is steric interactions that always disfavor configurations where Br atoms are too near each other, except when they are on the same dimer. The other is a tendency to favor configurations which expose regions of the bare Si(100) surface that are large enough to feature areas where alternately buckled dimers (ABD) are present. These two effects seem to compete with each other, with the former prevailing at high Br coverage, and the latter at low Br coverage. It is also clearly seen that configurations in which an adsorbate atom is bound to only one of the two atoms of a dimer pair, lie very high in energy.

Over a large range of bromine and hydrogen chemical potentials, the favored configuration is found to be one with only bromine atoms adsorbed on the surface, at full coverage, in a (3×2) pattern. However, we also find regions of the phase diagram where there are configurations with either only bromine atoms, or bromine and hydrogen atoms, arranged in an interesting pattern with a (4×2) surface unit cell. In these the bromine atoms are arranged, in pairs, in a checkerboard fashion on the Si(100) dimers. Most interestingly, we find that by co-adsorbing with hydrogen, we manage to bring this pattern into a region of the phase diagram corresponding to pressures that are significantly higher than those where it is observed with bromine alone. This makes this pattern much easier to achieve in experimental conditions. Other interesting patterns occur in small areas of the phase diagram, such as zigzag lines of bromine atoms, alternating stripes of bromine and hydrogen, and a rectangular checked pattern. As halogen-covered Si(100) surfaces are known to undergo spontaneous etching, it would be interesting to find out what happens to the co-adsorbed surface, and whether etching occurs here.

Chapter 7

Ab initio modeling of etching: conventional and supersaturation etching of Si(100) by Br_2

7.1 Introduction

In the previous chapter, we have studied a way to tune the morphology of Si(100) by patterning using molecular self-assembly. Here, in this chapter, we focus our attention on obtaining a modified morphology of the Si(100) surface by etching with molecular bromine.

Dry plasma etching is a crucial process in semiconductor microfabrication [154, 155]. In this process, the target material is bombarded with a plasma containing an electrically neutral mixture of molecules, atoms, ions and electrons [156]. These remove some part of the target material, so as to create desired features. Halogen plasmas are known to yield a high etch rate [157, 158]. For various applications in very large scale integration (VLSI), as well as dynamic random access memories (dRAMs) and microelectromechanical systems, high aspect ratio trenches with straight edges are desirable [156]. In order to achieve such anisotropic features, chlorine and bromine plasmas are preferred over fluorine plasmas [159]. Another desirable property for an etchant is that it should remove the material being etched selectively over the mask or the underlying film; bromine displays

a higher etch rate and a greater selectivity for etching silicon over silicon dioxide, when compared to chlorine [9]. In order to be able to tune etching conditions so as to optimize yield while retaining control over fine features, it is desirable to have a theoretical atomistic understanding of the underlying processes.

Etching is said to be "spontaneous" if secondary ionization or bombardment with electron beams is not used during the etching process [117, 160]. While there have been a number of theoretical studies that investigate the spontaneous etching of Si(100) by chlorine [161–163], till date, no such theoretical study appears to exist for bromine. Due to the lack of theoretical studies on bromine, the barriers for etching by Br_2 were heretofore assumed to be the same as those for Cl_2 [164]. However, there are two main reasons that make this assumption possibly inaccurate: (1) chlorine binds more strongly to the Si(100) surface than bromine [151], so the energy required to break Si-Cl bonds is expected to be more than that needed for breaking Si-Br bonds (as we will see below, this bond breaking is a necessary step to commence etching), and (2) there are stronger steric interactions between bromine atoms on Si(100) than between chlorine atoms [118]; this might facilitate etching at high coverage. These two facts suggest that the etch barriers might be lower in the case of Br_2 than Cl_2. Therefore, in this study, using *ab initio* density functional theory, we have investigated the formation of $SiBr_2$ during spontaneous etching of Si(100) by Br_2 in the conventional ($\theta_{Br} \leq 1$) and supersaturation ($\theta_{Br} > 1$) etching regimes. For each of these cases, we have compared our results with the results obtained for Cl_2 in Refs. [161] and [162], and tried to obtain an atomistic understanding of the origins of the differing behaviors of Br_2 and Cl_2 as etchants.

7.2 Previous Studies

Although etching has been performed for many centuries, experimental insight into the detailed atomic-scale mechanism had been achieved only with the advent of powerful surface probes like scanning tunneling microscopy (STM). Together with thermal desorption spectroscopy (TDS) [also known as temperature programmed desorption (TPD)], STM

can provide information about the reaction mechanism of etching by capturing the change in surface morphology as a function of temperature and bias voltage, at different values of the adsorbate coverage θ. While STM provides information about the evolving surface morphology as well as the post-etching morphology of the surface, TPD allows one to determine etch products and overall etch rates. Intuitively, one might think that the etching process roughens the surface to a degree where a probe like STM cannot distinguish between different etching regimes. However, quite contrary to this, STM images exhibit definite shapes/structures on Si(100) produced by etching with halogens [158].

Previous experimental studies on etching by Br_2 have shown that both the surface morphology and the etch products vary as a function of temperature [117,165–167]. These studies showed that mainly two different types of surface structures can be present, irrespective of the temperature of the surface: (a) single-layer deep etch pits consisting of missing dimer atoms, or more extended vacancy islands produced due to the removal of surface Si atoms, and (b) one-dimensional chains and two-dimensional islands due to Si regrowth on the surface. Except at low temperatures, at all temperature ranges, an anisotropic surface morphology was observed due to etching; the shape anisotropy was shown to arise from the preferential etching by Br_2 along the dimer row direction (here "row" refers to the ladder-like structure made by the dimers) [167]. Once a missing atom or a dimer vacancy is created on the surface, it destabilizes the nearby Si atoms of the same row, and this leads to an extension of the vacancy lines and etch pits [158]. While $SiBr_2$ was observed to form at high temperatures ($\sim$ 750-1100 K) as a volatile etch product, $SiBr_3$ and $SiBr_4$ were shown to be the dominant etch products at low temperatures ($\sim$ 350-700 K). However, a higher etching yield was achieved at higher temperatures ($\sim$ 900 K) [166].

Similar experimental studies have also been performed for Cl_2 [168–170]. Moreover, significant insight into the intermediate stages of etching processes by chlorine have been provided by the theoretical studies of Wijs *et al.* [161,162], where the authors have shown that at low coverage, monochloride-dichloride isomerization occurs by breaking the dimer bond. In this process, one chlorine atom hops from one Si atom to the other Si atom of the same dimer, thus giving rise to a $SiCl_2(a)$ unit attached to one of the Si atoms of a dimer.

Next, the chlorine-free Si atom of the dimer, often called the "Si bystander", diffuses away on the surface, thus facilitating the stability of the $SiCl_2(a)$ unit on the surface by impeding the reverse reaction. These results agree well with experimental investigations which show that the maximum etch rate for this system can be obtained at $\theta_{Cl} = 0.8$ ML, and that the etch rate eventually decreases at higher coverage due to the lack of availability of vacant Si sites for diffusion [171, 172]. Nakayama *et al.* [173] showed that this decrease of etch rate is not as pronounced in the case of bromine due to an adsorbate-mediated transformation from the (2×1) to the (3×1) phase at high bromine coverage.

The above mechanism proposed by Wijs *et al.* [161, 162] can explain the occurrence of etching when $\theta_{Cl} \leq 1$ (this is called the conventional etching regime). However, recently [174, 175], a finite etch rate and novel etching pathway for the spontaneous supersaturation etching (SSE) of a fully chlorine-passivated surface were reported. Intuitively, one might think no etching could occur on a fully-saturated surface due to the absence of dangling bonds which can bind the etchant atoms. However, a dangling bond can be created on the surface due to the desorption of a Cl atom via a phonon-activated electron-stimulated desorption (PAESD) process [176,177]. This process is the key step to commence supersaturation etching on the Si(100) surface. The newly created dangling bond on the Si atom then mediates the dissociation of an impinging Cl_2 molecule, leading to the saturation of the dangling bond and insertion of the other chlorine atom on the same Si atom, or on the bridge site of the same dimer, or on the Si atoms of the second substrate layer. The authors suggested that etching occurs due to the diffusion of the inserted Cl atom on the surface, leading to the formation of $SiCl_2(a)$ precursors, which finally desorb. The advantage of SSE over the conventional etching ($\theta_{Cl} \leq 1$) is that the surface morphology is free of Si regrowth islands which generally roughen the surface uncontrollably. Till date, no such experiments have been done for Br_2; to the best of our knowledge.

Partly motivated by these studies, we here address the following questions: (1) Are etching barriers different for Br_2 compared to Cl_2? (2) If yes, why do Br_2 and Cl_2 behave differently? (3) Is supersaturation etching of Si(100) by Br_2 feasible?

7.3 Steps in Etching Reaction

The complex process of etching of Si(100) by halogen molecules consists of three main reaction steps [158]:

(i) The dissociative adsorption of the halogen molecules on the surface, where an etchant halogen molecule dissociates into two halogen atoms and gets adsorbed at chemically active dimer sites on the surface.

(ii) The formation of intermediate precursors, such as $SiX_n(a)$ (where X = Cl or Br; n= 1–4), on the surface by breaking one or more Si-Si and Si-X bonds.

(iii) The desorption of volatile SiX_n by breaking further Si-Si bonds.

Note that in some cases, the step (ii) might be comprised of several sub-steps.

7.4 Computational Details

All the calculations have been done using *ab initio* density functional theory (DFT) as implemented in the Quantum ESPRESSO package [24]. We have used the same values for all the parameters as in Chapter 6 (see Section 6.4).

To calculate the activation barriers for the complex (intermediate) steps in the etching process, the climbing image nudged elastic band (NEB) method [44] was employed, especially when the reaction coordinates are not known. We first geometrically optimized the "initial" (refers to the reactant) and "final" (refers to the product) configurations using DFT. Then, using the NEB method, the minimum energy path of a reaction going from the initial configuration to the final configuration was obtained, along with the transition state. The total number of configurations generated, including the initial and the final configurations was 12 for all the intermediate reaction steps. This number was chosen such that the generalized distance between two consecutive images in the configuration space is less than 1.5 a.u. For the calculations of the diffusion barrier, a constrained minimization (CM) scheme was employed; in this case the reaction coordinate was taken to be the distance traversed on the surface by the atom being diffused. We again used the CM method

to calculate the desorption barrier, and the distance between the volatile molecules and the surface was varied up to 3.5 Å above the surface, in order to ensure negligible interactions between the two in the final state.

7.5 Results

Etching of Si(100) by Br_2 is a thermally activated process; this indicates that the system mostly stays near the minima of the potential energy surface (PES) and occasionally explores configurations with higher energy with the help of the energy provided by thermal fluctuations. Thus, during a reaction, on going from reactants to products, the system has to overcome an activation barrier and the configuration corresponding to the top of this barrier is called the "transition state" of the reaction. For such a reaction, the (empirical) relation between the reaction rate constant (k) and the temperature is given by the Arrhenius expression:

$$k(T) = \nu \exp\left(-\frac{E^*}{k_B T}\right) \tag{7.1}$$

where ν is the prefactor (depends on temperature), E^* is the activation barrier, k_B is Boltzmann's constant, and T is the temperature at which the reaction takes place. If ν and E^* are known, one can calculate the rate constant of the reaction at a particular temperature. In order to obtain the rate (r) of a reaction, one has to invoke reaction kinetics. The rate laws connect the rate of a reaction to the concentration of the reactants (θ) through the rate constant (k). For a multistep reaction like etching, the rate of the overall reaction has to be obtained. In a multistep reaction, the "slowest" reaction (with the largest activation barrier) is called the "rate-limiting step", and the overall rate of the reaction becomes equal to the rate of this step. Below we calculate the energy barriers for conventional etching (in Section 7.5.1) and supersaturation etching (in Section 7.5.2). The reaction rates for the rate-limiting steps are also obtained.

7.5.1 Conventional etching

For the calculation of low and high coverage etching of Si(100) by bromine, we have taken a 4×4 and a 6×3 surface unit cell, respectively. The coverages for molecular bromine (θ_{Br}) are taken as 0.125 (low coverage) and 0.94 (high coverage). First, let us consider etching at low coverage.

The first step of the etching reaction is the adsorption of Br_2 on Si(100). Br_2 dissociatively absorbs on Si(100) and saturates the dangling bonds of the Si atoms. For this study, we have restricted ourselves to considering the c(4×2) reconstructed Si(100) surface. Herrmann and Boland [135] showed that at low temperature, the dissociation of Br_2 can lead to two types of geometries: (1) saturation of two nearby Si atoms of adjacent dimers of the same dimer row and (2) saturation of the Si atoms of the same dimer. However, the results obtained in Chapter 6 suggest that the latter geometry is likely to be more stable energetically than the former, due to having a larger proportion of alternating buckled dimer (ABD) patches of bare (Br-free) surface; the STM images obtained by Rioux *et al.* [165] are in agreement with this result. Therefore, we have calculated the adsorption energy (E_{ads}) of Br_2 upon saturating the Si atoms of a dimer [see Figs. 7.1(a) and 7.1(e)]. The adsorption reaction can be written as:

$$\mathrm{Si}(100) + \mathrm{Br}_2(g) \rightleftharpoons 2\mathrm{SiBr} - E_{\mathrm{ads}}, \tag{7.2}$$

where "(g)" represents the gaseous state. The adsorption energy is defined as the energy difference between the reactants and the product of the reaction presented in Eq. (7.2). The value of E_{ads} is calculated to be -2.12 eV per Br atom. A negative value of E_{ads} suggests that this reaction is exothermic.

The second step is the monobromide-dibromide isomerization (see Fig. 7.1), which is the crucial step for the etching reaction [161, 178]. During this process, one Br atom (shown as red spheres) jumps from one Si atom (shown as dark gray spheres) to the other Si atom of the same dimer by first breaking the Si-Si (dimer) bond and then breaking one of the Si-Br bonds. As a result a "dibromide" $SiBr_2(a)$ unit is formed [see Figs. 7.1(d) and

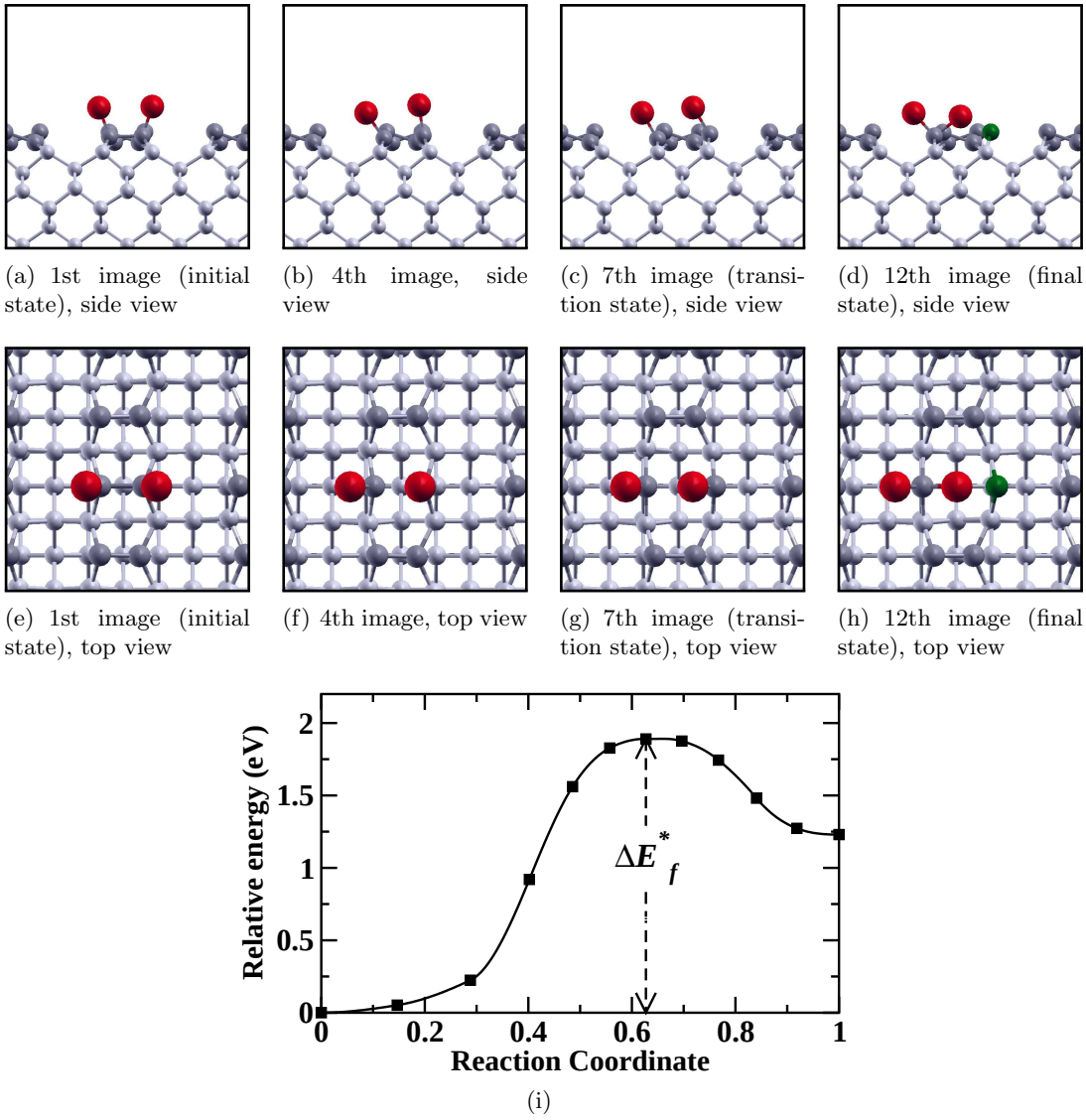

(a) 1st image (initial state), side view

(b) 4th image, side view

(c) 7th image (transition state), side view

(d) 12th image (final state), side view

(e) 1st image (initial state), top view

(f) 4th image, top view

(g) 7th image (transition state), top view

(h) 12th image (final state), top view

(i)

Figure 7.1: *Isomerization reaction for low coverage ($\theta_{\mathrm{Br}} = 0.125$) etching of Si(100) by Br_2. (a)-(d) show side views and (e)-(h) show top views of how the atomic positions change as the isomerization reaction proceeds. The red, dark green, dark gray and light gray spheres represent Br atoms, Si(s) atoms, Si atoms in the topmost layer and the remaining Si atoms, respectively. (i) shows the activation barrier (ΔE_f^*) for the reaction. See Appendix C for a video file depicting the isomerization reaction.*

7.1(h)]. "(*a*)" denotes the precursor state that is attached to the surface. This reaction can be written as:

$$2\mathrm{SiBr} \rightleftharpoons \mathrm{SiBr_2}(a) + \mathrm{Si}(s) - \Delta E_f^* \tag{7.3}$$

where Si(s) is the Si bystander atom that has been shown in Figs. 7.1(d) and 7.1(h) as a green sphere. Note that this newly created Si(s) atom has two dangling bonds. Fig. 7.1(i) shows the variation of relative energy as a function of reaction coordinate. This plot indicates that isomerization is an activated process and the activation barrier (ΔE^*_f) for isomerization is 1.89 eV. From this figure it is also clear that the formation energy [E_f, the energy difference between the reactants and products of the reaction given by Eq. (7.3)] of the $SiBr_2(a)$ is 1.22 eV and this reaction is endothermic. These values indicate that the barrier for the reverse isomerization reaction ($\Delta E^*_{-f} = \Delta E^*_f - E_f$) is 0.66 eV. As $\Delta E^*_{-f} < \Delta E^*_f$, it might seem that the formation of $SiBr_2(a)$ by isomerization is very unlikely, and as a result, no etching is likely to occur in this pathway. However, the formation of $SiBr_2(a)$ strongly depends on the third reaction step, which reduces the probability of the reverse isomerization reaction occurring.

As Si(s) is chemically active, it can act like an "adatom" on the surface and can diffuse on the surface to saturate the dangling bonds. Wijs *et al.* [161] showed that in the case of Cl_2, the diffusion barrier for Si(s) along the dimer row direction (through the channel between two consecutive dimer rows) is lower than the corresponding barrier along the direction perpendicular to the dimer row. For Br_2, we have plotted the relative energy as a function of the distance d_s between the original and the displaced position of Si(s) in Fig. 7.4(a), where d_s is taken to vary along the dimer row direction. We find that the diffusion barrier [$\Delta E_{\mathrm{diff}(1)}$] is 1.17 eV. As d_s increases further, the barrier for diffusion of Si(s) [$\Delta E_{\mathrm{diff}(2)}$] becomes 0.69 eV. Note that the latter barrier is similar in magnitude to the barrier for diffusion of a Si adatom on the clean Si(100) surface ($\sim$ 0.6 eV) [179]. The Si(s) atom can finally get attached to a step edge or can form Si regrowth islands on the surface. Based on statistical probability, one can rule out the chances of Si(s) coming back to its original position at low coverages. So, the stability of the $SiBr_2(a)$ increases due to the diffusion of Si(s); the reverse reaction gets inhibited by the absence of the Si(s) atom.

By comparing the values of $\Delta E_{\mathrm{diff}(1)}$ and E^*_{-f}, we find that the barrier for the reverse isomerization is 0.51 eV lower than the barrier for the diffusion process. However, the constrained minimization method, which was used to obtain $\Delta E_{\mathrm{diff}(1)}$, always gives an

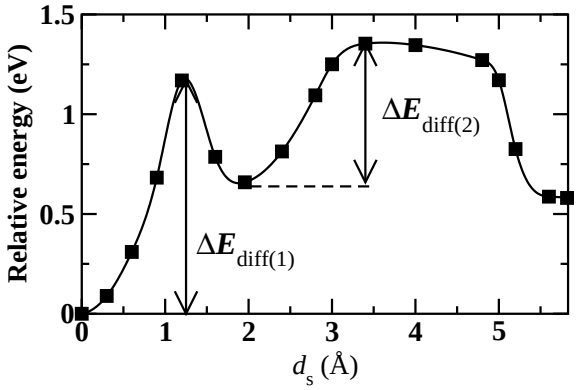

(a)

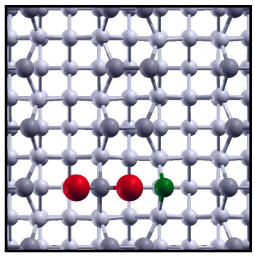

(b) 1st image (initial state)

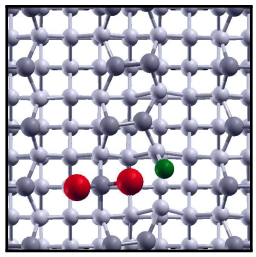

(c) 5th image

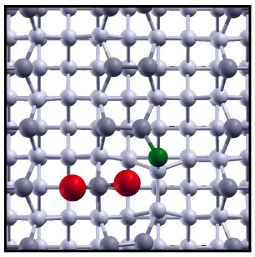

(d) 7th image (transition state)

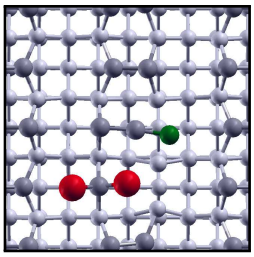

(e) 11th image (transition state)

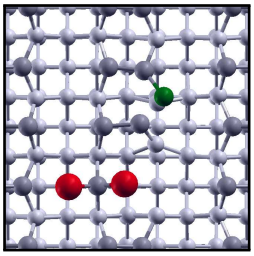

(f) 17th image (final state)

Figure 7.2: *Barriers for Si(s) diffusion for low coverage ($\theta_{Br} = 0.125$) etching of Si(100) by Br_2. (a) show the barriers for diffusion ($\Delta E_{diff(1)}$ and $\Delta E_{diff(2)}$). Top views of the atomic configurations corresponding to the initial, transition state (TS), and final states are shown in (b)-(f). The red, dark green, dark gray and light gray spheres represent Br atoms, Si(s) atom Si atoms in the topmost layer and the remaining Si atoms, respectively. See Appendix C for a video file depicting the diffusion process.*

upper-bound to the activation energies. At a high enough temperature ($\sim$ 750-1100 K), where $SiBr_2$ forms, the thermal fluctuations in the system may be expected to facilitate the diffusion reaction to occur.

Once the $SiBr_2(a)$ becomes stable, the final step involves the formation of the volatile $SiBr_2(g)$ by breaking the Si-Si backbonds, which are the bonds that connect the first and

second layer Si atoms. The desorption reaction can be written as:

$$\mathrm{SiBr_2}(a) \rightleftharpoons \mathrm{SiBr_2}(g) - \Delta E^*_{\mathrm{des}}. \tag{7.4}$$

Note that this is also an activated process. We have obtained the desorption barrier ($\Delta E^*_{\mathrm{des}}$) to be 2.63 eV per $SiBr_2$ molecule. This barrier is equal to the value of the energy difference between the reactant and the product of the reaction presented in Eq. (7.4). As soon as the $SiBr_2$ desorbs from the surface, a dimer vacancy gets created due to etching. This creates a defect on the surface and such defects can facilitate further etching of the surface.

Next, we will turn our focus toward conventional etching at high coverage. As θ_{Br} increases, the number of dangling bonds on the surface decreases. In such cases, the path (through the channel between two consecutive dimer row) for diffusion of Si(s) becomes no longer available. For Cl_2, Wijs *et al.* [161] proposed an alternative way to make the $SiCl_2(a)$ stable at full coverage ($\theta_{\mathrm{Cl}} = 1$). By considering the possibility of hopping of a Cl atom from a nearby Si atom to a Si(s) site, they had shown that the energy required for such hopping is 0.9 eV. Their calculation suggests that the desorption energy in that case becomes 3.5 eV. Here, we propose yet another alternative reaction pathway for etching at a high coverage ($\theta_{\mathrm{Br}} = 0.94$). Recently, it has been shown [176, 177] that Br atoms can desorb from the fully-saturated surface via a phonon-activated electron-stimulated desorption (PAESD) process. Such a process gives rise to single Br-free Si atoms on some dimers [see Fig. 7.3(a)] and can permit a possible reaction pathway for etching at high coverage. The Br atoms on one of the adjacent dimers (of the same dimer row) of this now Br-free Si atom can go through isomerization and form the $SiBr_2(a)$ and Si(s) [see Eq. (7.3)]. We find that the hopping of a Br atom from the Si atom which is nearer to the dangling bond created by PAESD is more favorable than hopping of the other Br atom [see Fig. 7.3(d)]. In this case, we find that the values of ΔE^*_f and E_f to be 2.04 eV and 1.51 eV, respectively [see Fig. 7.3(i)]. This leads to the value of ΔE^*_{-f} to be 0.53 eV. However, Si(s) can diffuse along the dimer row direction and get attached to the Br-free Si atom of

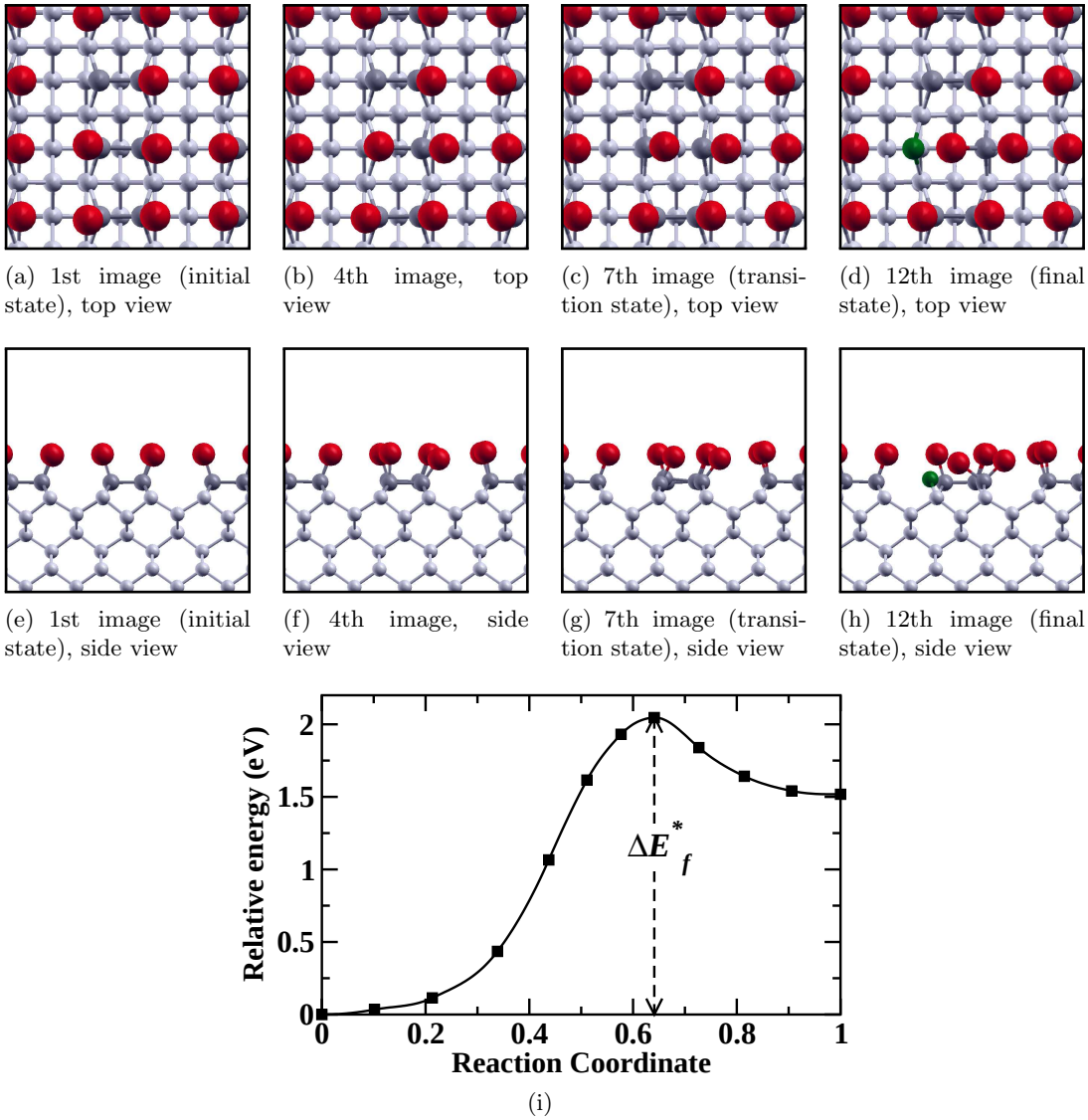

(a) 1st image (initial state), top view
(b) 4th image, top view
(c) 7th image (transition state), top view
(d) 12th image (final state), top view
(e) 1st image (initial state), side view
(f) 4th image, side view
(g) 7th image (transition state), side view
(h) 12th image (final state), side view
(i)

Figure 7.3: *Isomerization reaction for high coverage ($\theta_{\mathrm{Br}} = 0.94$) etching of Si(100) by Br_2. (a)-(d) show top views and (e)-(h) show side views of how the atomic positions change as the isomerization reaction proceeds. The red, dark green, dark gray and light gray spheres represent Br atoms, Si(s) atom, Si atoms in the topmost layer and the remaining Si atoms, respectively. (i) shows the activation barrier (ΔE_f^*) for the reaction. See Appendix C for a video file depicting the isomerization reaction.*

the next dimer [see Fig. 7.4(d)]. The diffusion barrier ΔE_{diff} is calculated to be 1.07 eV. Note that in this way Si(s) gets displaced by 1.3 Å away from its original position. This diffusion consequently increases the stability of $SiBr_2(a)$. We find the value of ΔE_{des} is 2.61 eV per $SiBr_2$ molecule. We observe that even in this case a dimer vacancy gets created on the surface due to etching at high coverage. There is a possibility that the Si(s) atom

eventually diffuses to the lower terrace, partially filling up the etch-pit.

Thus, we find that the conventional etching commences by creating either a dimer vacancy or a single atom vacancy on the surface [165]. Once these defects are created on the surface, they elongate with time and result in dimer vacancy lines or single-atom vacancy lines. However, due to the unrestrained diffusion of Si(s) atoms, the etch morphology can not be controlled during conventional etching.

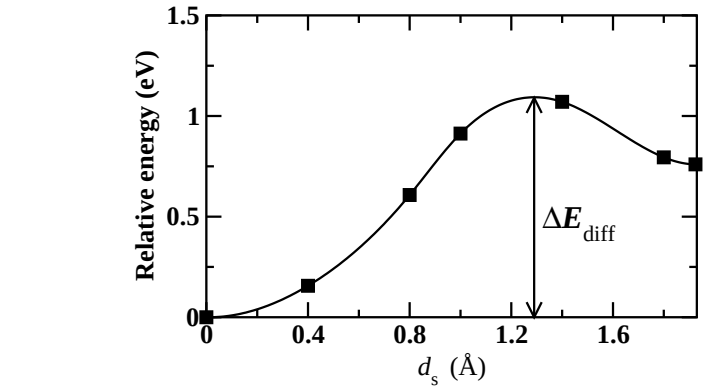

(a)

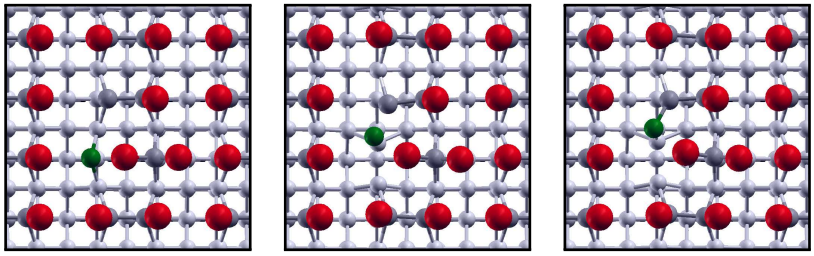

(b) 1st image (initial state)

(c) 5th image (transition state)

(d) 7th image (final state)

Figure 7.4: *Diffusion of Si(s) for low coverage (θ_{Br} = 0.94) etching of Si(100) by Br_2. (a) shows the barrier for diffusion (ΔE_{diff}). Top views of the atomic configurations corresponding to the initial, transition state (TS), and final states are shown in (b)-(d). The red, dark green, dark gray and light gray spheres represent Br atoms, Si(s) atom Si atoms in the topmost layer and the remaining Si atoms, respectively. See Appendix C for a video file depicting the diffusion process.*

In Table 7.1, we compare the results obtained by us for low and high coverage etching with Br_2. We also compare these values with the results obtained by Wijs *et al.* [161,162] for Cl_2. First, by examining the results obtained above, we find that the values of the activation energies do not differ significantly on going from low to high bromine coverages. A slight increase in E_f and ΔE_f^* on going from low to high coverage may originate from

Table 7.1: *Comparison of the calculated barriers for conventional etching of Si(100) [both at high and low adsorbate coverage] between Br_2 and Cl_2. Numbers for Cl_2 are taken from Refs. [161, 162]. All values are in eV.*

Quantity	low coverage		high coverage	
	Cl_2	Br_2	Cl_2	Br_2
E_f	1.4	1.22	1.3	1.51
ΔE_f^*	2.1	1.89	–	2.04
$\Delta E_{-f}^* = \Delta E_f^* - E_f$	0.7	0.66	–	0.53
ΔE_{diff}	0.6-1.0	0.69-1.17	0.9	1.07
ΔE_{des}	3.2	2.63	3.5	2.61

the stronger steric interaction at high coverage. Upon comparing the results for Br_2 and Cl_2, we find that at low coverage, the values of E_f, ΔE_f^* and ΔE_{des} are lower for Br_2 compared to Cl_2. The largest difference is found for ΔE_{des}, which is lower by ~ 0.6 eV and ~ 0.9 eV at low and high coverage, respectively, for Br_2 compared to Cl_2. For ΔE_{diff}, the value for Br_2 is observed to be larger than the value for Cl_2 by only 0.1–0.17 eV. These results suggest that the overall activation energy is lower in the case of Br_2 as compared to Cl_2. However, the rate of the reaction also depends strongly on the prefactor ν, reaction kinetics and the rate-limiting reaction. Below we try to deduce the rate of the reaction for conventional etching. Note that the coverages used in the calculations are slightly different for Cl_2 and Br_2 at high coverage; for Cl_2, $\theta_{\text{Cl}} = 1.0$ and for Br_2, $\theta_{\text{Br}} = 0.94$.

Flowers *et al.* [180] showed from their TPD data that the desorption of $SiBr_2$ for conventional etching ($\theta_{\text{Br}} \leq 1.0$) is consistent with first-order reaction kinetics. The reaction barrier was observed to be almost unchanged with respect to temperature and the value was found to be 2.64 eV per $SiBr_2$ desorption. The prefactor ν was found to be 2×10^{15} s^{-1}. From Table 7.1, one can clearly see that this value is in excellent agreement with the value of ΔE_{des}. Comparing all the values of activation barriers, we also see that the activation barrier is the largest for the desorption process. This implies that the desorption is the rate-limiting process. For Cl_2, the desorption barrier is 3.2 eV (at low coverage). Considering that the overall etching process by a halogen is a first-order reaction, it is easy to show that the rate of etching by Br_2 is at least 10^4 times faster than that by Cl_2 at low coverage. Note that due to the lack of availability of the value of ν for Cl_2, we have taken

it to be the same as that for Br_2 in calculating the rate of the reactions.

In order to confirm whether or not the reaction mechanism discussed above would be the most likely reaction pathway for etching in the conventional regime or not, we have considered another pathway where etching commences by breaking Si-Si backbonds. The activation barrier is found to be 4.2 eV in that case; this is almost twice as large as the required energy barrier for breaking the Si-Si dimer bond and the Si-Br bond. Hence, we conclude that etching is likely to follow the first pathway discussed above.

7.5.2 Supersaturation etching

Next we consider the possibility of supersaturation etching of Si(100) by Br_2. For this, we have chosen a 6×4 surface supercell. We first consider the adsorption of a Br_2 molecule on an almost fully-saturated surface with one Br-free Si atom per supercell that has been created by the PAESD process. For Cl_2, Weaver and co-workers [174, 175] suggested that the Cl-free Si atom (generated by PAESD) mediates the dissociation of any incoming Cl_2 molecule; one Cl atom of the molecule saturates the dangling bond, while the other Cl atom gets "inserted". Based on this, we have considered a similar mechanism for adsorption for Br_2. The inserted Br atom is denoted as Br(i) (shown as a black sphere in Fig. 7.5). In Fig. 7.5, we have shown the top view and the side view of the atomic arrangements of one such configuration, where the Br(i) gets inserted by breaking the Si dimer bond. The adsorption reaction can be written as:

$$2\mathrm{SiBr}^* + \mathrm{Br}_2(g) \rightleftharpoons \mathrm{Si}_2\mathrm{Br}_3 - E_{\mathrm{ads}}, \tag{7.5}$$

where 2SiBr* denotes a fully Br-saturated surface except for a few Br-free Si atoms. The value of E_{ads} is calculated to be -1.38 eV/ Br atom; this indicates that the reaction is exothermic.

The STM images obtained by Weaver and co-workers [174, 175] reveal that the post-etch morphology of the surface contains dimer-vacancy lines/pits. The authors argued that only an adsorption geometry like the one considered in this study can give rise to such a

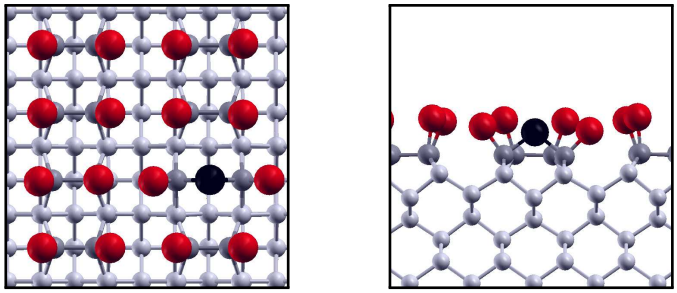

(a) Top view (b) Side view

Figure 7.5: *Adsorption geometry for supersaturation etching of Si(100) by Br_2: (a) and (b) show the top view and the side view, respectively. The red, black, dark gray and light gray spheres represent Br atoms, Br(i) atoms, Si atoms in the topmost layer and the remaining Si atoms, respectively. See the text for the description of the Br(i) atom.*

morphology. Here, etching is considered to commence by breaking the Si-Si dimer bond due to the diffusion of a Br(i) atom to the adjacent dimer of the same dimer row. In

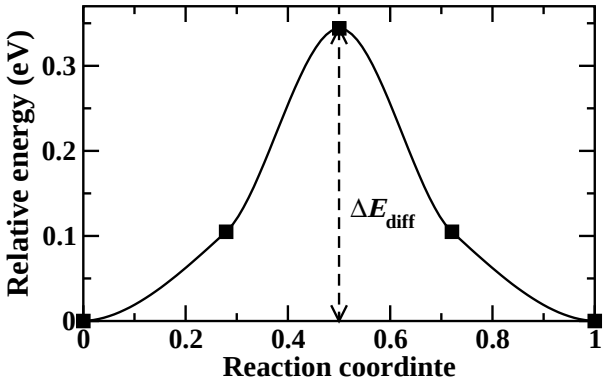

(a)

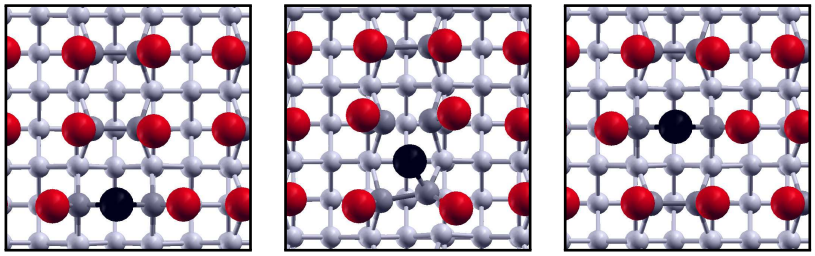

(b) Initial state (c) TS state (d) Final state

Figure 7.6: *Diffusion of Br(i) atom during supersaturation etching of Si(100) by Br_2. (a) shows the diffusion barrier (ΔE_{diff}). (b)-(d) show the atomic configurations corresponding to the initial, transition state (TS), and final configurations. The red, black, dark gray and light gray spheres represent Br atoms, Br(i) atoms, Si atoms in the topmost layer and the remaining Si atoms, respectively. See the text for the description of the Br(i) atom. See Appendix C for a video file depicting the diffusion process during supersaturation etching.*

Fig. 7.6(a), we have plotted the relative energy as a function of the generalized distance traversed by the Br(i) atom. We find that the diffusion barrier ($\Delta E_{\rm diff}$) for moving a Br(i) atom to the next dimer is 0.34 eV.

This type of diffusion can then lead to a configuration where two Br(i) atoms on two adjacent dimers of the same dimer row can pair up [see Fig 7.7(b)]. Next, one of the Br(i) atoms can hop to the adjacent dimer to give rise to $2SiBr_2(a)$ [see Figs. 7.7(e) and 7.8(b) for the top view and side view, respectively]. This reaction can be written as:

$$2Si_2Br_3 \rightleftharpoons 2SiBr_2(a) + 2SiBr - \Delta E^*_{\rm hop}. \tag{7.6}$$

From Fig. 7.7(a) we find that this reaction is a barrier-less reaction. This implies that diffusion and pairing of Br(i) leads to the (spontaneous) formation of two $SiBr_2(a)$ containing Si atoms of the same dimer.

The final step involves the desorption of the two $SiBr_2$ molecules one by one. The desorption reaction can be written as:

$$2SiBr_2(a) \rightleftharpoons SiBr_2(g) + SiBr_2(a) + \Delta E^*_{\rm des(1)} \rightleftharpoons 2SiBr_2(g) + \Delta E^*_{\rm des(2)}. \tag{7.7}$$

We find that the desorption barrier ($\Delta E^*_{\rm des(1)}$) for the first $SiBr_2$ molecule is 0.8 eV per molecule [see Fig. 7.8(a)]. However, the desorption energy for the second $SiBr_2$ molecule ($\Delta E^*_{\rm des(2)}$) is 2.25 eV. So, the final morphology of the surface is again the dimer vacancy pit [see Fig. 7.9(d)]. In contrast to conventional etching, we see that due to supersaturation etching the surface morphology remains clean, i.e., no Si regrowth islands are formed. Thus, the surface morphology can be controlled in this case.

We again compare the barriers for supersaturation etching of Si(100) by Br_2 (obtained in this study) with those for Cl_2 [162,175] in Table 7.2. We find that each of these barriers is smaller for Br_2 than Cl_2. Most significantly, we find that the formation of $2SiBr_2(a)$ on the same dimer (see the value of $\Delta E^*_{\rm hop}$ in Table 7.2) is a barrier-less process for Br_2, whereas for Cl_2 the barrier was reported to be 2.5 eV [175]. Again, the values of $\Delta E_{\rm des}$ are $\sim$0.6 eV lower in the case of Br_2 than Cl_2. The reason for the reduction of the barriers on going from

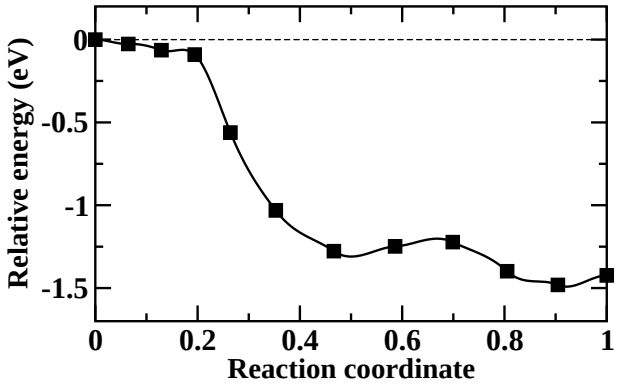

(a)

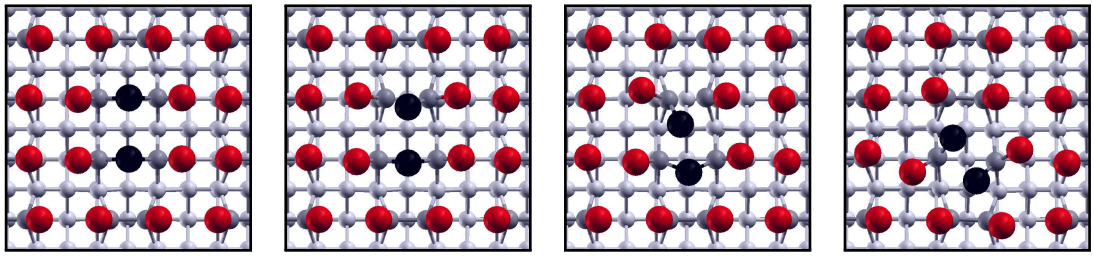

(b) 1st image (Initial state) (c) 5th image (d) 8th image (e) 12th image (Final state)

Figure 7.7: *Formation of $2SiBr_2(a)$ during supersaturation etching of Si(100) by Br_2. (a) shows the barrier (ΔE^*_{hop}) for the formation of $2SiBr_2(a)$. (b)-(f) show atomic configurations corresponding to the initial state, transition state (TS), and final state. The red, black, dark gray and light gray spheres represent Br atoms, Br(i) atom, Si atoms in the topmost layer and the remaining Si atoms, respectively. See the text for the description of the Br(i) atom. See Appendix C for a video file depicting this reaction.*

Cl_2 to Br_2 could be due to the stronger steric interaction in the case of Br_2. Examining the values of the barriers one can conclude that supersaturation etching is feasible for Br_2. Moreover, these values also suggest that the effective barrier for supersaturation etching by Br_2 is much less than for etching in the conventional regime by Br_2.

Table 7.2: *The comparison between barriers for Cl_2 and Br_2 during supersaturation etching of Si(100). All values are in eV. Numbers for Cl_2 are taken from Refs. [162, 175].*

Quantity	Halogen	
	Cl_2	Br_2
ΔE^*_{diff}	0.4	0.34
ΔE^*_{hop}	2.5	0.00
$\Delta E^*_{\text{des(1)}}$	1.4	0.80
$\Delta E^*_{\text{des(2)}}$	2.9	2.25

The above mentioned mechanism of supersaturation etching only commences when Br-free Si sites are created via the PAESD process. Thus, it seems that the etch rate would depend strongly on the rate of creation of Br-free Si sites. Trenhaile *et al.* [176,177] showed that the PAESD rate is different for Cl_2 and Br_2. If we compare these reaction rates for Br_2 and Cl_2 at 750 K, we find that the PAESD rate is 10 times faster in the case of Br_2. This, along with the results presented in Table 7.2, suggests that supersaturating etching by Br_2 is likely to occur at supersaturated surfaces.

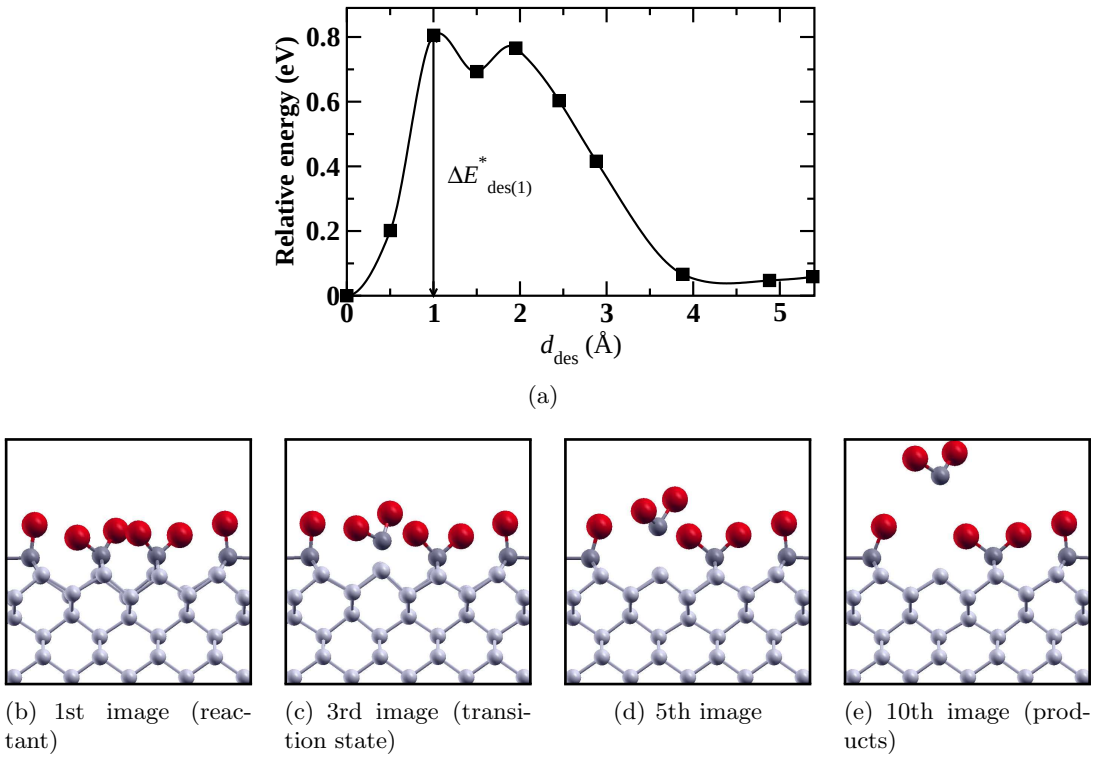

(a)

(b) 1st image (reactant)

(c) 3rd image (transition state)

(d) 5th image

(e) 10th image (products)

Figure 7.8: *Desorption of the first $SiBr_2$ during supersaturation etching of Si(100) by Br_2. (a) shows the variation of the relative energy as a function of the distance d_s between $SiBr_2$ and the surface. $\Delta E^*_{des(1)}$ indicates the barrier for desorption. The atomic configurations corresponding to the reactant, transition state (TS), and products are shown in (b)-(e). The red, dark gray and light gray spheres represent Br atoms, Si atoms in the topmost layer and the remaining Si atoms, respectively. See Appendix C for a video file depicting the desorption during supersaturation etching.*

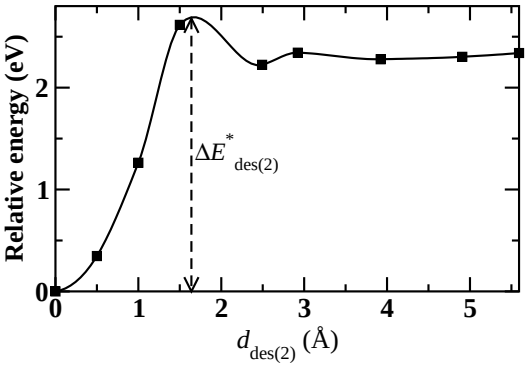

(a)

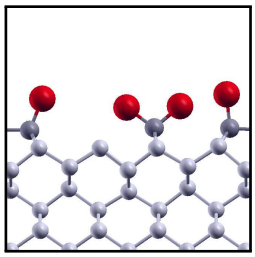

(b) 1st image (reactant)

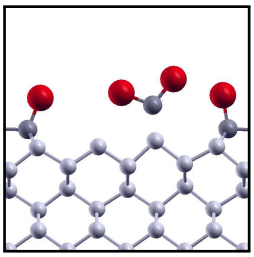

(c) 4th image

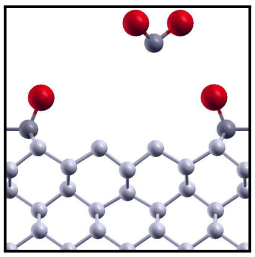

(d) 9th image (products)

Figure 7.9: *Desorption of the second $SiBr_2$ during supersaturation etching of Si(100) by Br_2. (a) shows the variation of the relative energy as a function of the distance d_s between $SiBr_2$ and the surface. $\Delta E^*_{\mathrm{des(1)}}$ indicates the barrier for desorption. The atomic configurations corresponding to the reactant, transition state (TS), and products are shown in (b)-(d). The red, dark gray and light gray spheres represent Br atoms, Si atoms in the topmost layer and the remaining Si atoms, respectively. See Appendix C for a video file depicting the desorption during supersaturation etching.*

7.6 Discussion

7.6.1 Why is Br_2 a better etchant than Cl_2?

From Tables 7.1 and 7.2, we find that the activation barriers for etching reactions are lower in the case of Br_2 than Cl_2. In order to obtain an understanding of the differing behavior of Br_2 and Cl_2, let us first examine the adsorption energies (E_{ads}) of both the molecules on the Si(100) surface. The values of E_{ads} for Br_2 and Cl_2 on clean Si(100) are -2.15 eV and -2.7 eV per molecule, respectively. These values indicate that chlorine atoms bind more strongly to the Si(100) surface compared to bromine atoms. Since we have found that the etching is likely to commence by breaking both the Si-Si dimer bond and Si-X bonds, with X being a halogen atom, breaking of Si-Cl bonds would require a

higher energy than breaking of Si-Br bonds. This suggests that the barrier for etching is likely to be higher for Cl_2 than Br_2. Another reason that may play a crucial role in making Br_2 a better etchant than Cl_2 is steric interactions. Being smaller in size, chlorine atoms do not show significant steric interactions on Si(100). However, the bromine atoms being larger in size exhibit strong steric interactions, especially at high coverages [118]. Such steric interactions are likely to play a significant role during etching at high coverages.

7.6.2 Change of surface morphology due to etching

We find that in both conventional and supersaturation etching a dimer vacancy is created. However, in the case of high coverage conventional etching, such vacancy pits may not be stable and the Si(s) atoms can diffuse to vacancy sites. In spite of this, the barriers for further similar reactions can decrease considerably for atoms lying near the dimer vacancy created at the initial stages of etching [161]. Thus, the vacancy will eventually grow to form an extended pit [171]. These types of vacancy pits are mobile at low temperatures and can get annihilated at step edges. However, at high temperature, vacancy dynamics are (kinetically) hindered, so it is possible to retain the etched morphology, especially in the case of supersaturation etching.

We have seen in Chapter 6 that the Br-covered surface transforms from a (2×1) phase to a (3×2) phase when $\theta_{\mathrm{Br}} \geq 0.66$ and the (2×1) phase lies only 21 meV per (1×1) higher in energy than the (3×2) phase at $\theta_{\mathrm{Br}} = 1.0$ [116]. Although, long-range ordering of the (2×1) phase was observed in STM experiments by Herrmann and Boland [135] at full coverage, both phases may be expected to coexist in an experimental scenario. Thus, etching mechanisms that consider adsorbate-mediated surface reconstructions also needed to be explored.

7.6.3 Etching vs. roughening

We have seen that etching occurs by the desorption of $SiBr_2$. Nakayama *et al.* [181] had shown that at a temperature below the desorption threshold, the Cl atom of $SiCl_2(a)$ can

hop to the Cl-free Si atoms of the surface. In that case, the surface morphology gets modified without any desorption and etching does not occur. Such modification of the surface is referred to as roughening. Both etching and roughening produce Si dimer vacancies (which grow into dimer vacancy lines and pits) and Si regrowth islands. However, from a technological point of view, etching is preferable over roughening. Thus, a careful experimental set up is required for etching, which can be obtained by tuning the temperature properly.

7.7 Summary

In this chapter, we have studied conventional and supersaturation etching of Si(100) by Br_2 using density functional theory. We find that etching always commences by breaking surface bonds, Si-Si dimer bonds and Si-Br bonds. For conventional etching, the calculated barriers are in excellent agreement with the experimental results. The results obtained here suggest that the activation barriers for supersaturation etching are significantly lower than the barriers for conventional etching. Moreover, by considering first-order reaction kinetics, we find that the rate of etching by Br_2 is faster by 10^4 times than the rate of etching by Cl_2 for low coverage conventional etching and by 10 times faster than the rate of etching by Cl_2 in the supersaturation regime. These observations can be explained in terms of stronger steric interactions and weaker binding to the surface of Br_2 compared to Cl_2.

Here we have mainly considered the Langmuir–Hinshelwood type of mechanism for spontaneous etching, where a gas molecule gets adsorbed on the surface and the product is formed due to interactions between the adsorbed species. In this type of reaction, the reactants and products are in thermal equilibrium. However, one cannot rule out the possibility of other kinds of reaction mechanisms for etching; e.g., an Eley-Rideal mechanism or a "precursor" mechanism involving hot electrons, where the incoming gas molecules directly interact with the surface atoms without getting adsorbed (in the case of an Eley-Rideal mechanism) or are thermally accommodated on the surface (for the "precursor" mechanism). Such reactions are "nonthermal" reactions and generally involve transfer of energy between the adsorbate and the surface. Such mechanisms would occur in

processes like reactive-ion etching (RIE) where high energy plasmas are bombarded toward the surface.

Chapter 8

Summary and outlook

In this chapter, the main findings and highlights of this thesis are summarized, and we also list open questions that could be addressed in the future work. In this thesis, we have tried to develop strategies to tailor the magnetic and chemical properties of surfaces. We have primarily used density functional theory calculations for these studies, along with the *ab initio* atomistic thermodynamics method and the nudged elastic band method.

In Part A of the thesis we have tried to develop strategies to control the magnetic properties of surfaces. The main highlights of this part of the thesis are described below.

First, the long-standing controversial problem of Cr/Ag(100) was revisited. We showed that a Cr monolayer on Ag(100) wants to go sub-surface and prefers an antiferromagnetic ordering. By considering different sub-surface positions of the Cr monolayer, we found that the lowest energy structure is the one where the Cr monolayer is buried below one monolayer of Ag. We also find that the deposition of Cr leads to several new surface states. Recently obtained low energy electron diffraction (LEED) images support these observations. Also, the angle-resolved photoemission spectroscopy (ARPES) data are in excellent agreement with the theoretically obtained band structure. Thus, in this work, we have seen satisfying synergy between theory and experiments.

Second, in this thesis we have predicted "new" stable surface alloys: Mn_xAu_{1-x}-/Ru(0001), with x being the concentration of Mn atoms. The driving force behind the

formation of this alloy system has been examined in terms of the band energy, the magnetic energy and the stress-relief mechanism. Showing that both band energy and magnetic energy are related to the effective coordination number, we demonstrated that the "effective coordination number" (ECN) is a good tool to understand the stability of surface alloys. In the absence of magnetism, the structure with the highest ECN is favored, while in the presence of ferromagnetism, the structure with the lowest ECN is favored. This finding should serve as a simple yet useful guiding principle when searching for stable structures in alloy phase diagrams. We found that Mn-Au/Ru(0001) surface alloys get stabilized by magnetism. The role of magnetism in determining the stability was found be two-fold: (1) magnetic interactions increase the magnetic moments in the alloy phases compared to the phase-segregated phases; thus magnetic energy helps lower the total energy of the alloys and (2) magnetism also helps to reduce the surface stress in the alloy phases via the magneto-volume effect.

Next, we have studied the ground state magnetic properties of one of these newly obtained surface alloys: $MnAu_2$/Ru(0001), along with another surface alloy system: $FeAu_2$-/Ru(0001). For both these systems, we find that the lowest-energy magnetic configuration corresponds to a left-rotating spin spiral, in which the sense of rotation is determined by the Dzyaloshinskii-Moriya interaction. These spirals are lower in energy than the ferromagnetic configuration by a rather small amount of 3–4 meV per nm^2. This demonstrates that magnetic surface alloys constitute a new class of systems in which one can search for the rare phenomenon of spin spirals. The primary reason for the stability of the spin spiral in $FeAu_2$/Ru(0001) is found to be the asymmetric exchange interaction (Dzyaloshinskii-Moriya interaction), whereas the spin spiral in $MnAu_2$/Ru(0001) is stabilized mostly by symmetric exchange interactions. We also find that $FeAu_2$/Ru(0001) has a significantly high magnetic anisotropy energy, of the order of 1 meV per Fe atom. By comparing with the corresponding freestanding alloy monolayers, we find that the presence of the Ru substrate plays a significant role in determining the magnetic properties of the surface alloy systems.

Part B of the thesis deals with developing strategies to tune the chemical properties of surfaces. The main findings of this part of the thesis are discussed below.

Here, we have first developed strategies to tune patterning conditions by co-adsorption of gases. Earlier work had shown that it is possible to pattern the Si(100) surface by depositing Br_2 alone; however, the patterns of interest can only be obtained at very low pressures and in a very narrow range of the phase diagram. We have shown that by co-adsorbing Br_2 and H_2, the stability of these kind of patterns can be brought into a region of the phase diagram corresponding to pressures that are significantly higher than those where they are observed with Br_2 alone. We have also shown that new kinds of patterns are obtained via co-adsorption. With the help of a simple equation, we are able to show why the patterns move to higher partial pressures upon co-adsorption. Thus, our finding can apply to co-adsorption in general.

Finally, an atomistic picture of etching has been obtained for Si(100) etching by Br_2. The reaction pathways and activation barriers for the etching reactions for the formation of $SiBr_2$ are obtained for both conventional etching (at $\theta_{Br} \leq 1$) and supersaturation etching (at $\theta_{Br} > 1$) regimes, θ_{Br} being the coverage of Br_2. For both these cases, etching of Si(100) is found to occur via a complex sequence of reactions, featuring one or more intermediate precursors. Comparing the effective activation barriers for Br_2 with the corresponding values for Cl_2 (obtained in an earlier study) at both etch conditions, we find that Br_2 should be a better etchant than Cl_2, i.e., most of the barriers are lower in the Br_2 case than in the Cl_2 case. This is primarily due to the fact that the Si–Br bond is much weaker than the Si–Cl bond. Most importantly, we observe that the effective etch barrier for supersaturation etching is lower compared to the effective barrier for conventional etching. This counter-intuitive result is explained by the large steric interactions between the Br atoms.

There are many open questions which can be addressed in the future. Below we describe them briefly.

For Cr deposition on Ag(100), it would be interesting to explore what effect, if any, the incorporation of spin-orbit interactions has on the electronic structure and geometry.

In the case of surface alloys of Mn_xAu_{1-x}/Ru(0001), one can extend the study of stability of the alloys by including the effect of antiferromagnetic interactions along with the

ferromagnetic interactions. It would be interesting to see how the relation between the effective coordination number and magnetic moments changes in the case of antiferromagnetic interactions.

For etching of Si(100) by Br_2 we have only considered the formation of $SiBr_2$ from the Si(100) surface. It would be interesting to study the reaction pathways where $SiBr_3$ and $SiBr_4$ are also formed. In future work, we hope to explore some of these issues.

Appendices

Appendix A

List of configurations of Mn_xAu_{1-x}/Ru(0001)

Here, we have depicted the optimized structures for all the configurations considered by us in Chapter 4. As the relaxation of the overlayer atoms is slightly different in the non-magnetic (NM) and the ferromagnetic (FM) configurations, we have shown the top views of the atomic arrangement in both the configurations for comparison. Note that all the structures are grouped according to their structural similarities (see Section 4.4). The blue and golden spheres represent the Mn and Au atoms, respectively.

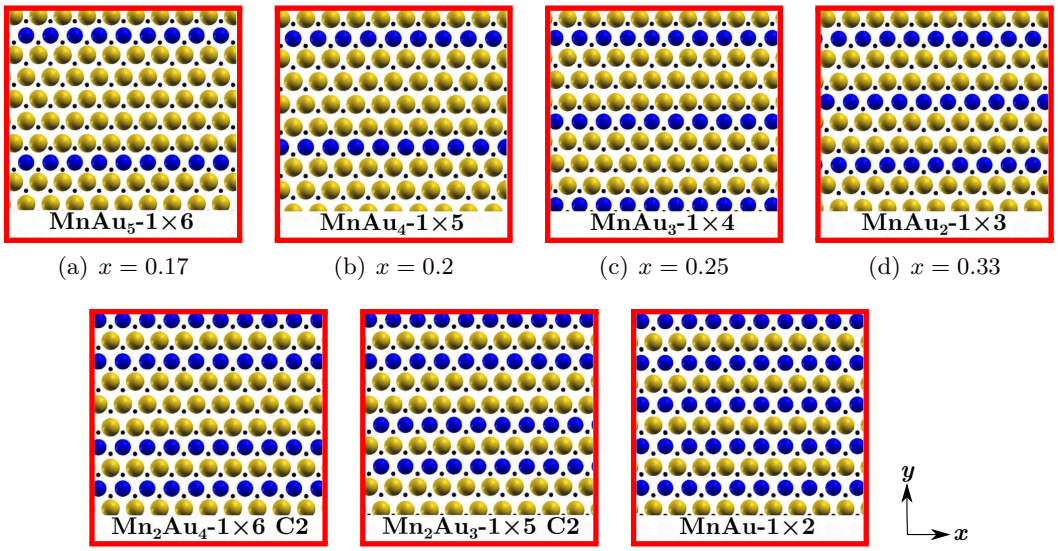

(a) $x = 0.17$ (b) $x = 0.2$ (c) $x = 0.25$ (d) $x = 0.33$

(e) $x = 0.33$ (f) $x = 0.4$ (g) $x = 0.5$

Figure A.1: *Group A, non-magnetic*

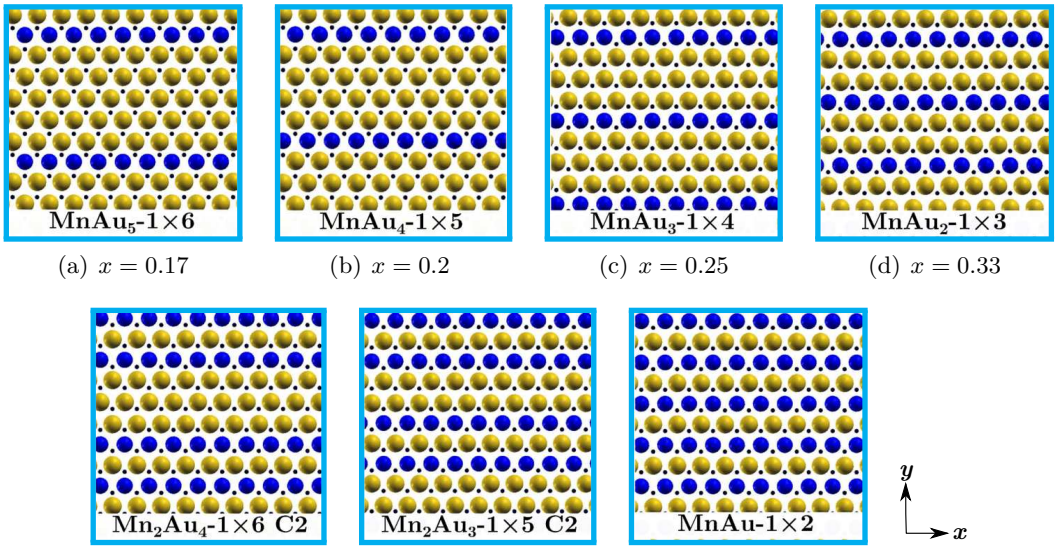

(a) $x = 0.17$ (b) $x = 0.2$ (c) $x = 0.25$ (d) $x = 0.33$

(e) $x = 0.33$ (f) $x = 0.4$ (g) $x = 0.5$

Figure A.2: *Group A, ferromagnetic*

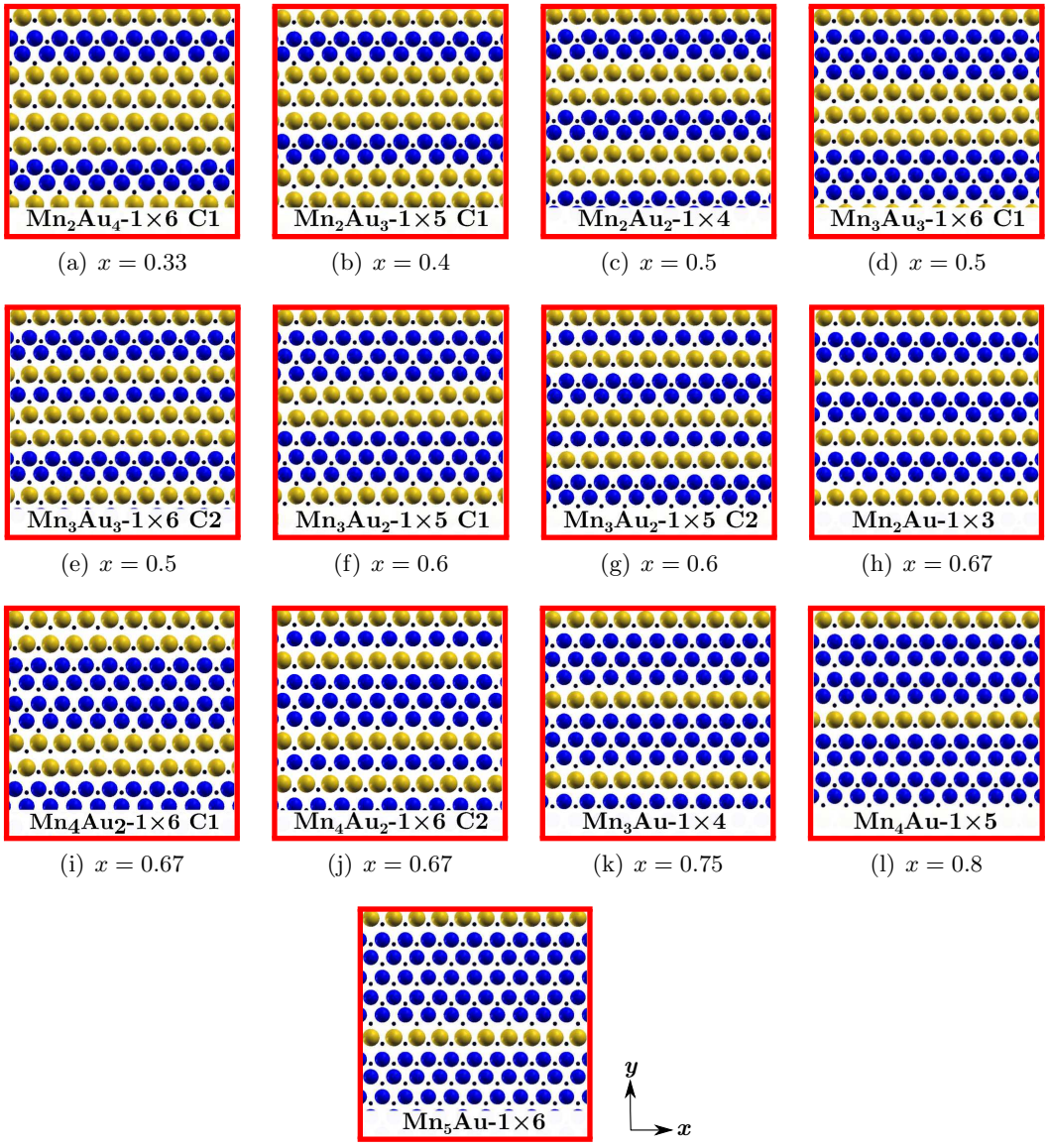

(a) $x = 0.33$ (b) $x = 0.4$ (c) $x = 0.5$ (d) $x = 0.5$

(e) $x = 0.5$ (f) $x = 0.6$ (g) $x = 0.6$ (h) $x = 0.67$

(i) $x = 0.67$ (j) $x = 0.67$ (k) $x = 0.75$ (l) $x = 0.8$

(m) $x = 0.83$

Figure A.3: *Group B, non-magnetic*

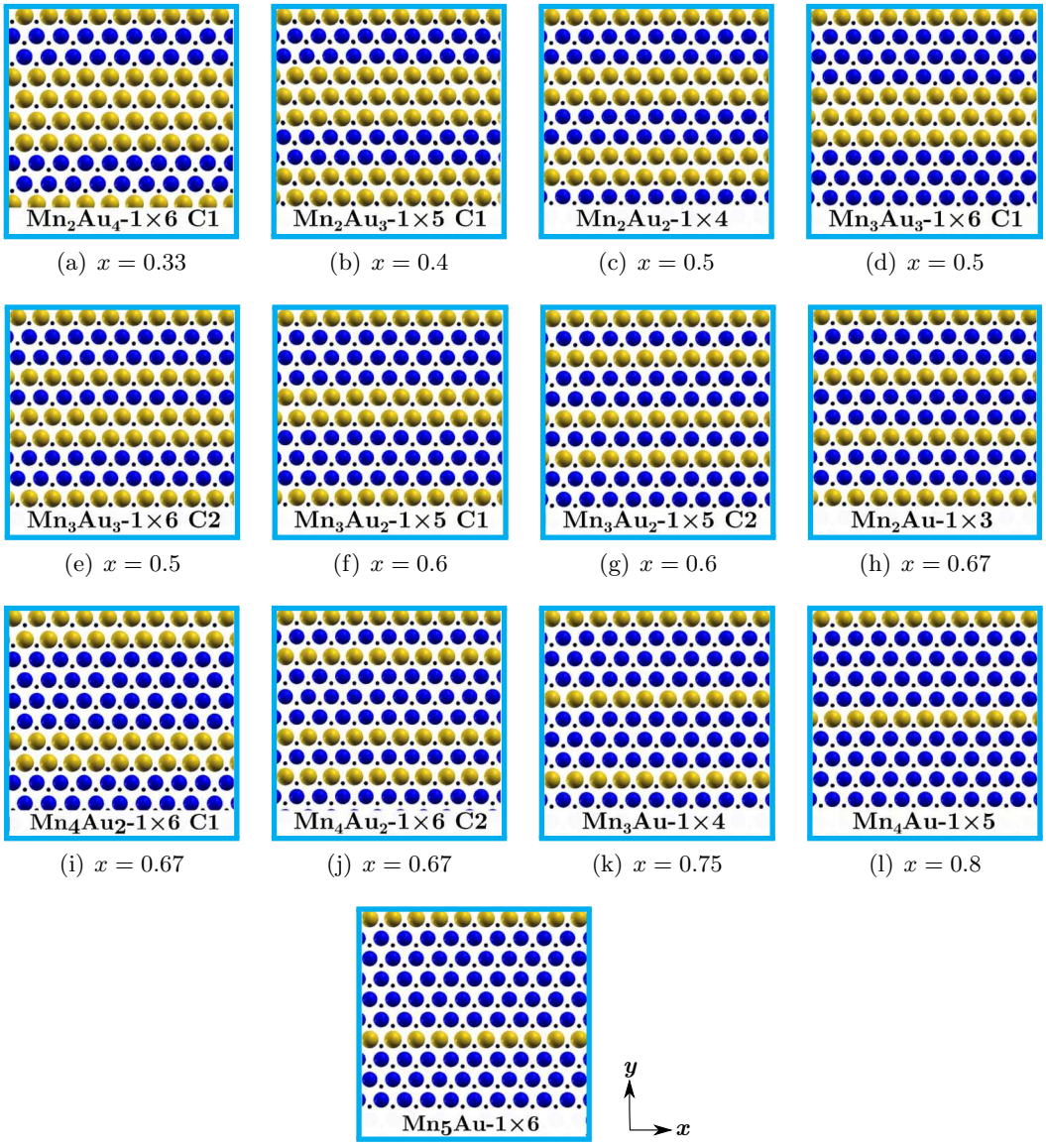

(a) $x = 0.33$ (b) $x = 0.4$ (c) $x = 0.5$ (d) $x = 0.5$

(e) $x = 0.5$ (f) $x = 0.6$ (g) $x = 0.6$ (h) $x = 0.67$

(i) $x = 0.67$ (j) $x = 0.67$ (k) $x = 0.75$ (l) $x = 0.8$

(m) $x = 0.83$

Figure A.4: *Group B, ferromagnetic*

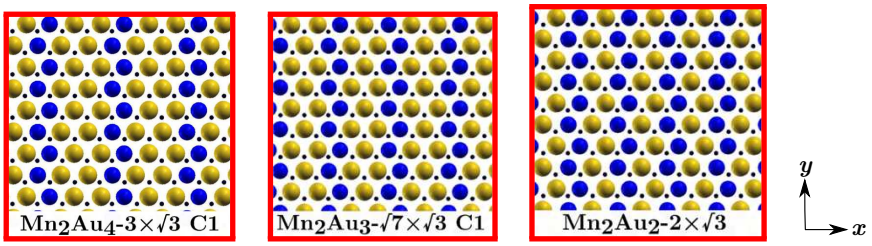

(a) $x = 0.33$ (b) $x = 0.4$ (c) $x = 0.5$

Figure A.5: *Group C, non-magnetic*

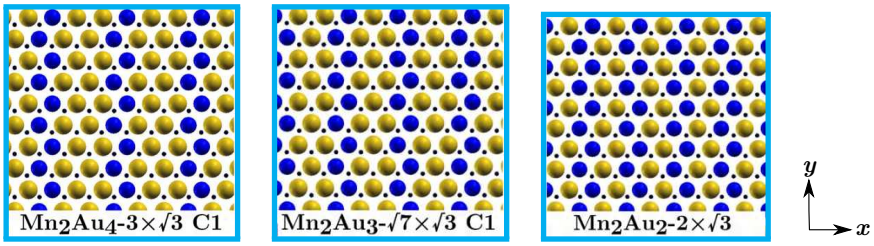

(a) $x = 0.33$ (b) $x = 0.4$ (c) $x = 0.5$

Figure A.6: *Group C, ferromagnetic*

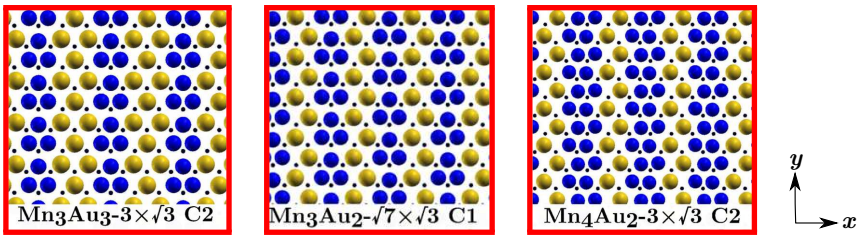

(a) $x = 0.5$ (b) $x = 0.6$ (c) $x = 0.67$

Figure A.7: *Group D, non-magnetic*

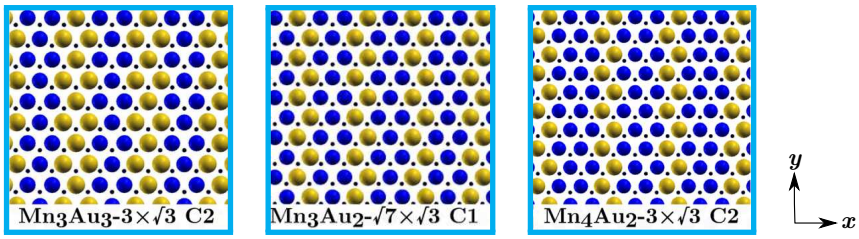

(a) $x = 0.5$ (b) $x = 0.6$ (c) $x = 0.67$

Figure A.8: *Group D, ferromagnetic*

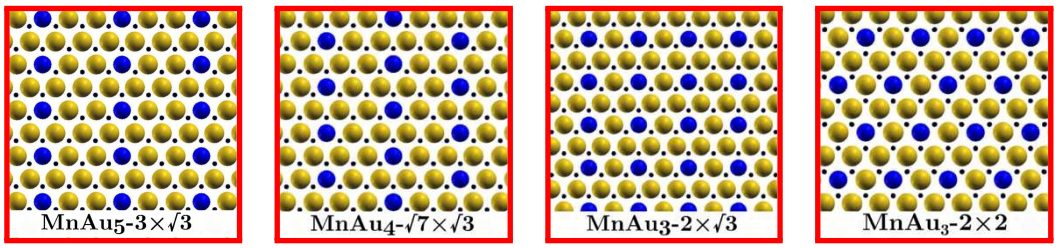

(a) $x = 0.17$ (b) $x = 0.2$ (c) $x = 0.25$ (d) $x = 0.25$

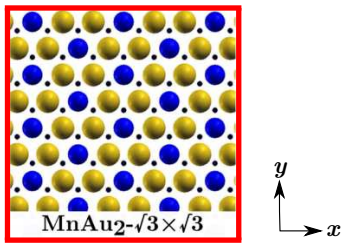

(e) $x = 0.33$

Figure A.9: *Group E, non-magnetic*

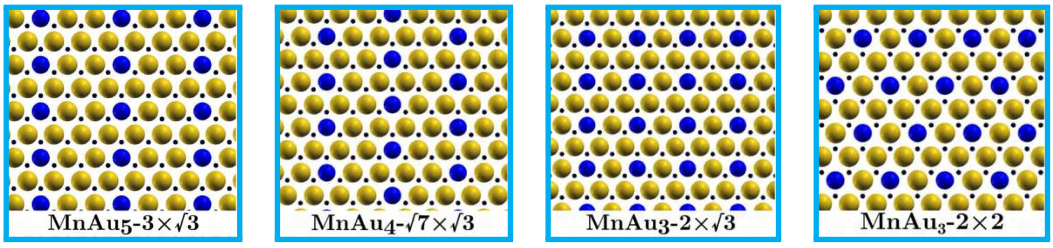

(a) $x = 0.17$ (b) $x = 0.2$ (c) $x = 0.25$ (d) $x = 0.25$

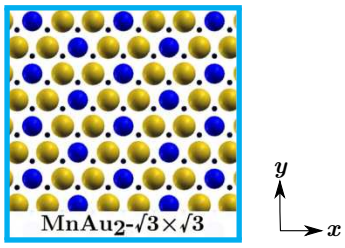

(e) $x = 0.33$

Figure A.10: *Group E, ferromagnetic*

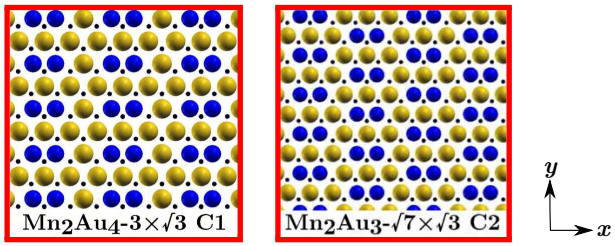

(a) $x = 0.33$ (b) $x = 0.4$

Figure A.11: *Group F, non-magnetic*

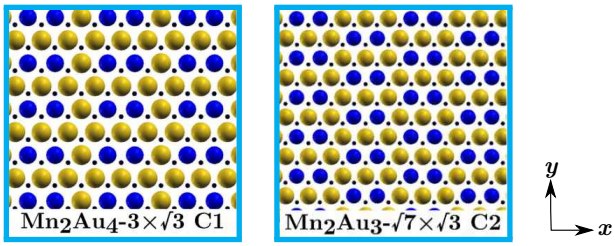

(a) $x = 0.33$ (b) $x = 0.4$

Figure A.12: *Group F, ferromagnetic*

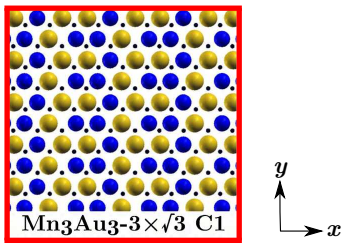

(a) $x = 0.5$

Figure A.13: *Group G, non-magnetic*

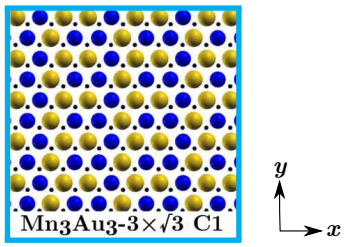

(a) $x = 0.5$

Figure A.14: *Group G, ferromagnetic*

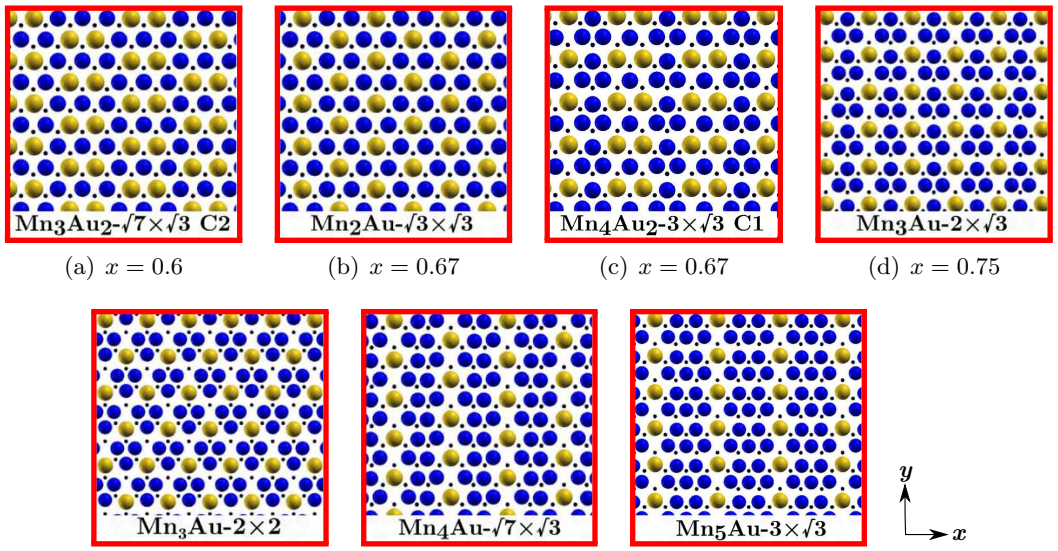

(a) $x = 0.6$ (b) $x = 0.67$ (c) $x = 0.67$ (d) $x = 0.75$

(e) $x = 0.75$ (f) $x = 0.8$ (g) $x = 0.83$

Figure A.15: *Group H, non-magnetic*

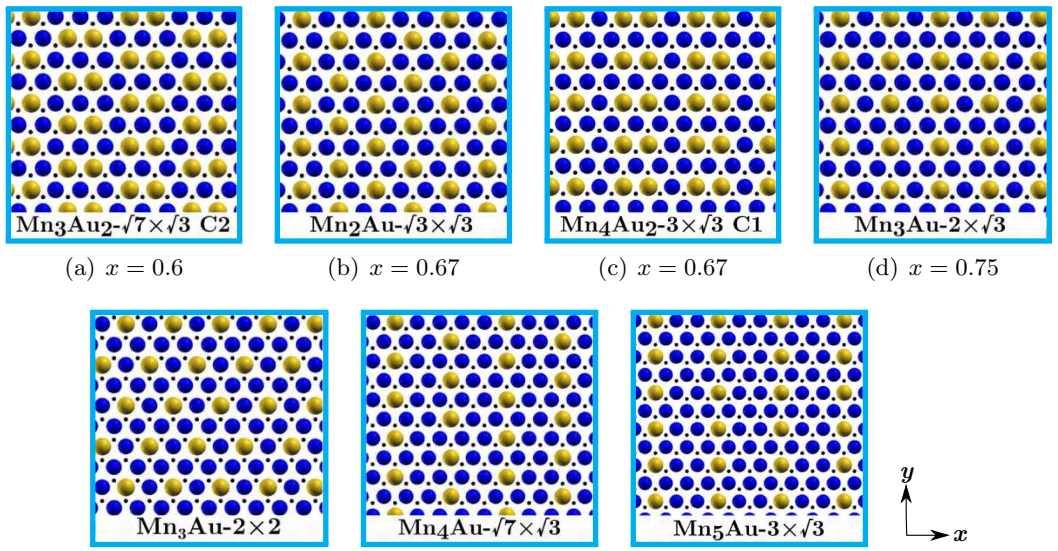

(a) $x = 0.6$ (b) $x = 0.67$ (c) $x = 0.67$ (d) $x = 0.75$

(e) $x = 0.75$ (f) $x = 0.8$ (g) $x = 0.83$

Figure A.16: *Group H, ferromagnetic*

Appendix B

Applicability of the Force Theorem

In section 5.6.3A, we showed that the force theorem (FT) failed to yield an accurate value for $\delta E_{\rm HE}$, the difference in energy from symmetric exchange interactions, between two spin spirals of slightly different wavelengths, especially for $MnAu_2$/Ru(0001). Here, we discuss this issue further.

We first consider conical spin spirals, where the magnetic moments are not constrained to lie in a plane, but precess around the axis of rotation, making an angle α with it. Note that for planar spin spirals, $\alpha = \frac{\pi}{2}$. The energy difference $\delta E_{\rm SE}(\alpha)$ between two spin spirals with wavevectors $\mathbf{q}_1$ and $\mathbf{q}_2$ can be written as: [182]

$$\begin{aligned} \delta E_{\rm SE}(\alpha) &= E_{\rm SE}^{\mathbf{q}_1}(\alpha) - E_{\rm SE}^{\mathbf{q}_2}(\alpha), & \text{(B.1)} \\ &\simeq \sin^2\alpha \, \left(E_{\rm SE}^{\mathbf{q}_1}(\frac{\pi}{2}) - E_{\rm SE}^{\mathbf{q}_2}(\frac{\pi}{2}) \right), \\ &\equiv \sin^2\alpha \, \delta E_{\rm SE}(\frac{\pi}{2}), & \text{(B.2)} \end{aligned}$$

where the approximation holds for a small difference between $\mathbf{q}_1$ and $\mathbf{q}_2$, and does not depend on the method of calculation [FT or self-consistent (SC)]. For our calculations we have taken $|\mathbf{q}_1|$ and $|\mathbf{q}_2|$ to be 0 and 3.3 $\rm nm^{-1}$, respectively, for $MnAu_2$/Ru(0001), and 8.8 and 11 $\rm nm^{-1}$, respectively, for freestanding $MnAu_2$, along the [110] direction.

First, we checked whether the approximation holds in our case. In order to do this, we have obtained $\delta E_{\rm SE}(\alpha)$ from Eqs. (B.1) and (B.2) by using the FT for different values of α. We have used 5041 $\mathbf{k}_{\parallel}$-points in the irreducible Brillouin zone of $MnAu_2$/Ru(0001), while for the freestanding monolayer of $MnAu_2$, 2304 $\mathbf{k}_{\parallel}$-points are used. The results thus obtained are shown in Fig. B.1, where we have plotted $\delta E_{\rm SE}(\alpha)$ as a function of α for both $MnAu_2$/Ru(0001) and a freestanding $MnAu_2$ monolayer. The values obtained from Eqs. (B.1) and (B.2) are shown by dots and dashed lines, respectively. For both the systems, we see that the values obtained from Eq. (B.1) deviate slightly from sinusoidal

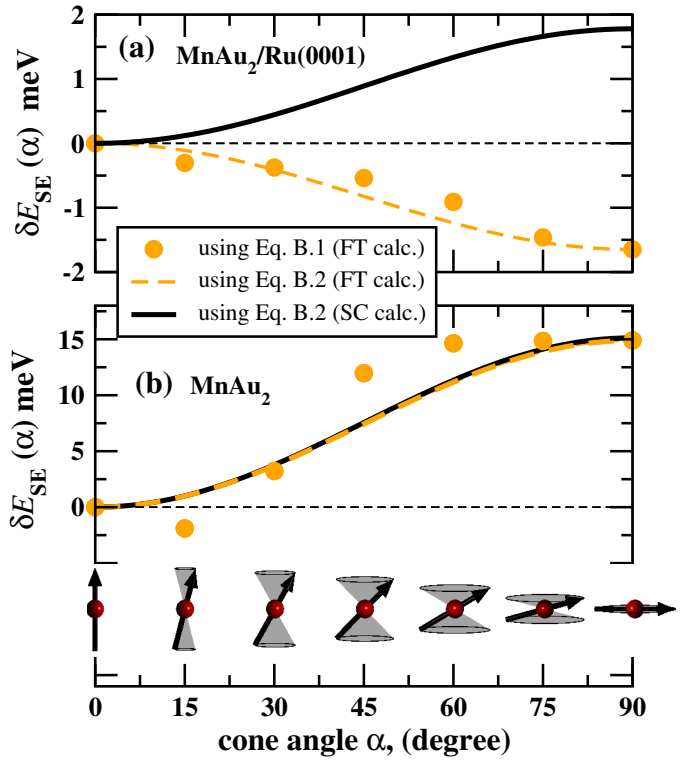

Figure B.1: *The variation of $\delta E_{\mathrm{SE}}(\alpha)$ as a function of the cone angle α for (a) $MnAu_2$/Ru(0001) and (b) $MnAu_2$ freestanding monolayers. The gray (orange online) dots and dashed lines are obtained from FT calculations, while the black line is obtained from SC calculations. The bottommost row of figures show how the spin precesses around the axis of rotation as the cone angle α is varied.*

behavior, but agree qualitatively with the values obtained from Eq. (B.2).

Having shown that values of δE_{SE} can be calculated approximately by the FT method from Eq. (B.2), we proceed to calculate the values self-consistently (SC) using only Eq. (B.2). The number of k-points used for these calculations is 800 and 400 for $MnAu_2$/Ru(0001) and freestanding $MnAu_2$, respectively. By comparing the energies obtained for $MnAu_2$/Ru(0001) from SC (black solid line in Fig. B.1) and FT (dots and dashed line) methods, we see that the values of $\delta E_{\mathrm{SE}}(\alpha)$ do not agree with each other, in fact, they even have opposite sign. On the other hand, for the freestanding monolayer of $MnAu_2$, the values match quite well. This suggests that the FT is applicable for the calculation of δE_{SE} between two spin spirals (both conical and planar) of the freestanding $MnAu_2$ monolayer, at least when the difference in wavevectors is small. However, the FT breaks down for $MnAu_2$/Ru(0001) even when α is very small. We conclude that the applicability of the force theorem has to be tested for all cases individually, since the breakdown of the FT for $MnAu_2$/Ru(0001) could not have been anticipated, either from the comparison to the freestanding layers, or to the $FeAu_2$/Ru(0001) case.

Appendix C

Video files showing the etching reaction step by step

Here, we show the reaction pathway for both conventional and supersaturation etching discussed in Chapter 7 by showing the step by step changes in the atomic arrangement as the reaction progresses. This has been done by making a set of video files. Please see the attached CD-ROM for these video files. Fig. C.1 shows the contents of the CD-ROM.

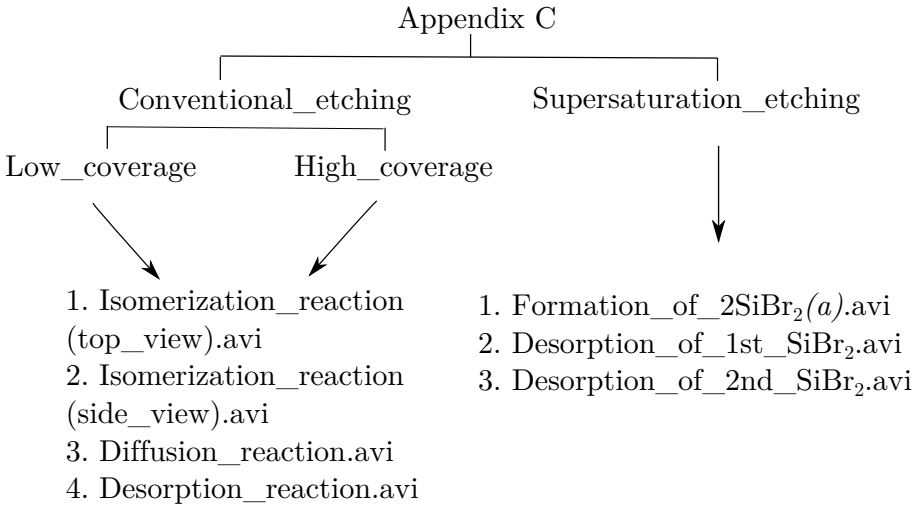

Figure C.1: *The arrangement of the video files in CD-ROM.*

Bibliography

[1] M. N. Baibich, J M. Broto, A. Fert, F. van dau Nguyen, F. Petroff, P. Etienne, G. Creuzet, A. Friederich, and J. Chazeles, Phys. Rev. Lett. **61**, 2472 (1988).

[2] G. Binash, P. Grnberg, F. Saurenbach, and W. Zinn, Phys. Rev. B **39**, 4828 (1989).

[3] M. Julliere, Physics Letters A **54**, 225–226 (1975).

[4] E. C. Stoner, Proc. Roy. Soc. London A **165**, 372 (1938).

[5] I. E. Dzialoshinskii, Sov. Phys. JETP **5**, 1259 (1957).

[6] T. Moriya, Phys. Rev. **120**, 91 (1960).

[7] S. I. Kiselev, J. C. Sankey, I. N. Krivorotov, N. C. Emley, R. J. Schoelkopf, R. A. Buhrman and D. C. Ralph, Nature (London) **425**, 380 (2003).

[8] I. N. Krivorotov, N. C. Emley, J. C. Sankey, S. I. Kiselev, D. C. Ralph, and R. A. Buhrman, Science **307**, 228 (2005).

[9] S. Pearton and D. P. Norton, Plasma Process. Polym. **2**, 16 (2005).

[10] B. Wu, J. Vac. Sci. Technol. B **24**, 1 (2006).

[11] T. R. Eaton, D .M .Torres, M. Buck, and M. Mayor, CHIMIA International Journal for Chemistry **67**, 222-226 (2013).

[12] M. Born and J. R. Oppenheimer, Ann. Physik **84**, 457 (1927).

[13] P. Hohenberg and W. Kohn, Phys. Rev. **136**, B864 (1964).

[14] R. M. Martin, *Electronic Structure Basic Theory and Practical Methods*, Cambridge University Press, Cambridge (2004).

[15] W. Kohn and L. J. Sham, Phys. Rev. **140**, A1133 (1965).

[16] U. von Barth and L. Hedin, J. Phys. C **5**, 1629 (1972).

[17] A. K. Rajagopal and J. Callaway, Phys. Rev. B **7**, 1912 (1973).

[18] R. O. Jones and O. Gunnarsson, Rev. Mod. Phys. **61**, 689 (1989).

[19] J. P. Perdew and Y. Wang, Phys. Rev. B **46**, 12947 (1992).

[20] J. P. Perdew, K. Burke, and M. Ernzerhof, Phys. Rev. Lett. **77**, 3865 (1996).

[21] H. Krakauer, M. Posternak, and A. J. Freeman, Phys. Rev. B **19**, 1706 (1979).

[22] D. Vanderbilt, Phys. Rev. B **41**, 7892 (1990).

[23] S. G. Louie, S. Froyen, and M. L. Cohen, Phys. Rev. B **26**, 1738 (1982).

[24] see http://www.quantum-espresso.org for Quantum-ESPRESSO package; P. Giannozzi *et al.*, J. Phys.: Condens. Matter **21**, 395502 (2009).

[25] M. Weinert, J. Math. Phys. **22**, 2433 (1981).

[26] For more information see http://www.flapw.de.

[27] H. Monkhorst and J. Pack, Phys. Rev. B **13**, 5188 (1976).

[28] D. J. Chadi and M. L. Cohen, Phys. Rev. B **8**, 5747 (1973).

[29] A. Baldereschi, Phys. Rev. B **7**, 5212 (1973).

[30] O. Jepsen and O. K. Andersen, Solid State Commum. **9**, 1763 (1971).

[31] G. Lehmann and M. Taut, Phys. Status Solidi B **54**, 469 (1972).

[32] C. L. Fu and K. M. Ho, Phys. Rev. B **28**, 5480 (1983).

[33] M. Methfessel and A. T. Paxton, Phys. Rev. B **40**, 3616 (1989).

[34] N. Marzari, D. Vanderbilt, A. De Vita, and M. C. Payne, Phys. Rev. Lett. **82**, 3296 (1999).

[35] R. P. Feynman, Phys. Rev. **56**, 340 (1939).

[36] P. Pulay, Mod. Phys. **17**, 197 (1969).

[37] O. H. Nielsen and R. Martin, Phys. Rev. Lett. **50**, 697 (1983).

[38] L. Sandratskii, Phys. Status Solidi B **136**, 167 (1986).

[39] A. R. Mackintosh and O. K. Andersen, *Electrons at the Fermi Surface*, ed. M. Springford (1980).

[40] A. I. Liechtenstein, M. I. Katnelson, V. P. Antropov, and V. A. Gubavov, J. Magn. Magn. Mater. **67**, 65 (1987).

[41] K. Reuter and M. Scheffler, Phys. Rev. B **65**, 035406 (2001).

[42] K. Reuter and M. Scheffler, Phys. Rev. B **68**, 045407 (2003).

[43] H. Jónsson, G. Mills, K. W. Jacobsen, *Nudged Elastic Band Method for Finding Minimum Energy Paths of Transitions, in Classical and Quantum Dynamics in Condensed Phase Simulations*, ed. B. J. Berne, G. Ciccotti and D. F. Coker, 385 (World Scientific, 1998).

[44] G. Henkelman, B. P. Uberuaga, and H. Jónsson, J. Chem. Phys. **113**, 9901 (2000).

[45] Ph. Kurz, G. Bihlmayer, K. Hirai, and S. Blügel, Phys. Rev. Lett. **86**, 1106 (2001).

[46] D. Wortmann, S. Heinze, Ph. Kurz, G. Bihlmayer, and S. Bl"ugel Phys. Rev. Lett. **86**, 4132 (2001).

[47] A. J. Freeman and C. L. Fu, J. Appl. Phys. **61**, 3356 (1987).

[48] M. C. Hanf, L. Haderbache, P. Wetzel, C. Pirri, J. C. Peruchetti, D. Bolmont, and G. Gewinner, Solid State Commun. **68**, 113 (1988).

[49] D. A. Newstead, C. Norris, C. Binns, and P. C. Stephenson, J. Phys. C: Solid State Phys. **20**, 6245 (1987).

[50] A. D. Johnson, J. A. C. Bland, C. Norris, and H. Lauter, J. Phys. C **21**, L899 (1988).

[51] J. W. Evans, Phys. Rev. B **39**, 5655 (1989).

[52] C. Krembel, M. C. Hanf, J. C. Peruchetti, D. Bolmont, and G. Gewinner, J. Magn. Magn. Mater. **93**, 529 (1991).

[53] C. Krembel, M. C. Hanf, J. C. Peruchetti, D. Bolmont, and G. Gewinner, Phys. Rev. B **44**, 11472 (1991).

[54] C. Krembel, M. C. Hanf, J. C. Peruchetti, D. Bolmont, and G. Gewinner, Phys. Rev. B **44**, 8407 (1991).

[55] E. Tamura, S. Blügel, and R. Feder, Solid State Commun. **65**, 1255 (1988).

[56] S. Blügel, M. Weinert, and P. H. Dederichs, Phys. Rev. Lett. **60**, 1077 (1988).

[57] S. Blügel, B. Drittler, R. Zeller, and P. H. Dederichs, Appl. Phys. A **49**, 547-562 (1989).

[58] G. Allan, Phys. Rev. B **44**, 13641 (1991).

[59] A. J. Quinn, J. F. Lawler, R. Schad, and H. van Kempen, Surf. Sci. **385**, 395 (1997).

[60] J. F. Lawler, R. G. P. van der Kraan, H. van Kempen, and A. J. Quinn, J. Magn. Magn. Mat. **165**, 195 (1997).

[61] P. Steadman, C. Norris, C. L. Nicklin, N. Jones, J. S. G. Taylor, S. A. de Vries, and S. L. Bennett, Phys. Rev. B **64**, 245412 (2001).

[62] M. C. Hanf, C. Krembel, and G. Gewinner, Surf. Sci. **519**, 1–14, (2002).

[63] J. Das, S. Biswas, A. K. Kundu, S. Narasimhan, and K. S. R. Menon, unpublished.

[64] D. M. Kolb, W. Boeck, K.-M. Ho, and S. H. Liu, Phys. Rev. Lett. **47**, 1921 (1981).

[65] B. Reihl, K. H. Frank and R. R. Schlittler, Phys. Rev. B. **30**, 7328 (1984).

[66] T.G. Dargam, R. .B. Capaz, and B. Koiller Phys. Rev. B. **56**, 9625 (2010).

[67] T. B. Boykin and G. Klimeck, Phys. Rev. B. **71**, 115215 (2005)

[68] W. Ku, T. Berlijin, and C.-C. Lee, Phys. Rev. Lett. **104**, 216401 (2010).

[69] V. Popescu and A. Zunger, Phys. Rev. B. **85**, 085201 (2012).

[70] P. V. Medeiros, S. Stafström, and J. Björk, Phys. Rev. B. **89**, 085201 (2014).

[71] S. Blügel, D. Pescia, and P. H. Dederichs, Phys. Rev. B **39**, 1392 (1989).

[72] P. W. Palmberg, R. E. DeWames, and L. A. Vredevoe, Phys. Rev. Lett. **21**, 682 (1968).

[73] K. S. R. Menon, S. Mandal, J. Das, T. O. Menteş, M. A. Niño, Andrea Locatelli, and Rachid Belkhou, Phys. Rev. B. **84**, 132402 (2011)

[74] J. Tersoff, Phys. Rev. Lett. **74**, 434, (1995).

[75] M. Schick, J. Schäfer, K. Kalki, G. Ceballos, P. Reinhardt, H. Hoffschulz, and K. Wandelt, Surf. Sci. **287–288**, 960 (1993).

[76] B. Sadigh, M. Asta, V. Ozoliš, A. K. Schmid, N. C. Bartelt, A. A. Quong, and R. Q. Hwang, Phys. Rev. B **83**, 1379 (1999).

[77] J. L. Stevens and R. Q. Hwang, Phys. Rev. Lett. **74**, 2078, (1995).

[78] J. Yuhara, M. Schmid, and P. Varga, Phys. Rev. B **67**, 195407 (2003).

[79] M. Wuttig, Y. Gauthie, and S. Blügel, Phys. Rev. Lett. **70**, 3619 (1993).

[80] S. Blügel, Appl. Phys. A **63**, 595 (1996).

[81] T. Yamada, N. Kunitomi, and Y. Nakai, J. Phys. Soc. Jpn. **28**, 615, (1970).

[82] P. A. Herpin and P. Meriel, J. Phys. Radium **22**, 337 (1961).

[83] K. Sato, T. Hirone, H. Watanabe, S. Maeda and K. Adachi, J. Phys. Soc. Jpn. **17** (Suppl. B-I) 160 (1962).

[84] M. Matsumoto, S. Abe, H. Yoshida, S. Mori, T. Kanomata and T. Kaneko, J. Magn. Magn. Mater. **104-107**, 2061 (1992).

[85] M. Matsumoto, T. Kaneko and K. Kamigaki, J. Phys. Soc. Jpn. **25**, 631 (1968).

[86] S. Abe, M. Matsumoto, H. Yoshida, S. Mori, T. Kanomata and T. Kaneko, J. Magn. Magn. Mater. **104-107** 2059 (1992).

[87] S. Abe, M. Matsumoto, T. Kanekoa, H. Yoshida, H. Morita, and T. Kanomata, J. Magn. Magn. Mater. **140-144** 103-104 (1995).

[88] S. Khmelevskyi and P. Mohn, Appl. Phys. Lett. **93**, 162503 (2008).

[89] L. Udvardi, S. Khmelevskyi, L. Szunyogh, P. Mohn, and P. Weinberger, Phys. Rev. B **73**, 104446 (2006).

[90] S. Mehendale, Y. Girard, V. Repain, C. Chacon, J. Lagoute, S. Rousset, M. Marathe, and S. Narasimhan, Phys. Rev. Lett. **105**, 056101, (2010) and supplementary information therein.

[91] M. Marathe, A. D´iaz-Ortiz, and S. Narasimhan, Phys. Rev. B **88**, 245442 (2013).

[92] M. Marathe, M. Imam, and S. Narasimhan, Phys. Rev. B **79**, 085413 (2009).

[93] N. W. Ashcroft and N. D. Mermin, *Solid State Physics* (Thomson Asia Pte. Ltd., Bangalore, 2004)

[94] A. J. Bradley and J. Thewlis, Proc. R. Soc. London Ser.A **115**, 456 (1927).

[95] A. Crépieux and C. Lacroix, J. Magn. Magn. Mater. **182**, 341 (1998).

[96] A. Baraldi, L. Bianchettin, E. Vesselli, S. de Gironcoli, S. Lizzit, L. Petaccia, G. Zampieri, G. Comelli, and R. Rosei, New J. Phys. **9**, 143 (2007)

[97] M. S. Daw and M. I. Baskes, Phys. Rev. Lett. **50**, 1285 (1983).

[98] M. S. Daw, Phys. Rev. B **39**, 7441 (1989).

[99] K. W. Jacobsen, J. K. Nørskov, and M. J. Puska, Phys. Rev. B **35**, 7423 (1987).

[100] S. Narasimhan and D. Vanderbilt, Phys. Rev. Lett. **69**, 1564 (1992).

[101] J. H. Van Vleck, Phys. Rev. **52**, 1178, (1937).

[102] P. Ferriani, K. von Bergmann, E. Y. Vedmedenko, S. Heinze, M. Bode, M. Heide, G. Bihlmayer, S. Blügel, and R. Wiesendanger, Phys. Rev. Lett. **101**, 027201 (2008).

[103] Y. A. Izyumov, Soviet Phys. Uspekhi **27**, 845 (1984).

[104] M. Bode, M. Heide, K. von Bergmann, P. Ferriani, S. Heinze, G. Bihlmayer, A. Kubetzka, O. Pietzsch, S. Blügel, and R. Wiesendanger, Nature (London) **447**, 190 (2007).

[105] Y. Yoshida, S. Schröder, P. Ferriani, D. Serrate, A. Kubetzka, K. von Bergmann, S. Heinze, and R. Wiesendanger, Phys. Rev. Lett. **108**, 087205 (2012).

[106] S. Meckler, N. Mikuszeit, A. Preßler, E. Y. Vedmedenko, O. Pietzsch, and R. Wiesendanger, Phys. Rev. Lett. **103**, 157201 (2009).

[107] N. Romming, C. Hanneken, M. Menzel, J. E. Bickel, B. Wolter, K. von Bergmann, A. Kubetzka, and R. Wiesendanger, Science **341**, 636 (2013).

[108] B. Hardrat, A. Al-Zubi, P. Ferriani, S. Blügel, G. Bihlmayer, and S. Heinze, Phys. Rev. B **79**, 094411 (2009).

[109] V. Dupuis, M. Maurer, M. Piecuch, M. F. Ravet, J. Dekoster, S. Andrieu, J. F. Bobo, F. Baudelet, P. Bauer, and A. Fontaine, Phys. Rev. B **48**, 5585 (1993).

[110] N. W. Ashcroft and N. D. Marmin, *Solid State Physics* (Thomson Asia Pte. Ltd. Bangalore 2004).

[111] L. M. Sandratskii, Phys. Status Solidi B **135**, 167 (1986).

[112] A. R. Mackintosh and O. K. Andersen, *Electrons at the Fermi Surface* edited by M. Springford (Cambridge University Press, Cambridge, 1980).

[113] M. Heide, G. Bihlmayer, and S. Blügel, Physica B **404**, 2678, (2009).

[114] A. Fert and P. M. Levy, Phys. Rev. Lett. **44**, 1538 (1980).

[115] P. Bruno, Phys. Rev. B **39**, 865 (1989).

[116] S. Biswas, S. V. Deshpande, D. N. Dunn, and S. Narasimhan, J. Chem. Phys. **139**, 184713 (2013).

[117] M. Chander, Y. Z. Li, D. Rioux, and J. H. Weaver, Phys. Rev. Lett. **71**, 4154 (1993).

[118] G. A. de Wijs and A. Selloni, Phys. Rev. B **64**, 041402(R) (2001).

[119] G. J. Xu, E. Graugnard, B. R. Trenhaile, K. S. Nakayama, and J. H. Weaver, Phys. Rev. B **68**, 075301 (2003).

[120] G. J. Xu, N. A. Zarkevich, A. Agrawal, A. W. Signor, B. R. Trenhaile, D. D. Johnson, and J. H. Weaver, Phys. Rev. B **71**, 115332 (2005).

[121] A. Sgarlata, A. Balzarotti, I. Berbezier, P. Szkutnik, F. N. Motta, *International Conference on Nanoscience and Nanotechnology (ICONN '06)*, (2006).

[122] M. Kammler, R. Hull, M. C. Reuter, and F. M. Ross, Appl. Phys. Lett. **82**, 1093 (2003).

[123] J. Erlebacher, M. J. Aziz, E. Chason, M. B. Sinclair, and J. A. Floro, Phys. Rev. Lett. **82**, 2330 (1999).

[124] V. Gianneta, A. Olziersky, and A. G. Nassiopoulou, Nanoscale Research Letters **8**, 71 (2013).

[125] R. Martel, Ph. Avouris, and I. W. Lyo, Science **272**, 385 (1996).

[126] F. J. Ruess, L. Oberbeck, M. Y. Simmons, K. E. J. Goh, A. R. Hamilton, T. Hallam, S. R. Schofield, N. J. Curson, and R. G. Clark, Nano Lett. **4**, 1969 (2004).

[127] R. M. Tromp, R. J. Hamers, and J. E. Demuth, Phys. Rev. Lett. **55**, 1303 (1985). C. Manzano, W. -H. Soe, H. Kawai, M. Saeys, and C. Joachim, Phys. Rev. B **83**, 201302(R) (2011).

[128] Y. Yamamoto, Phys. Rev. B **50**, 8534 (1994).

[129] G. Binnig, H. Rohrer, Ch. Gerber, and E. Weibel, Phys. Rev. Lett **50**, 120 (1983).

[130] T. Yokoyama and K. Takayanagi, Phys. Rev. B **61**, 5078 (2000).

[131] W. Cai, Z. Lin, T. Strother, L. M. Smith, and R. J. Hamers, J. Phys. Chem. B **106**, 2656 (2002).

[132] N. A. Zarkevich and D. D. Johnson, Surf. Sci. **591**, L292 (2005).

[133] N. D. Shinn, J. F. Morar, and F. R. McFeely, J. Vac. Sci. Technol. A **2**, 1593 (1984).

[134] C. J. Wu and E. A. Carter, Phys. Rev. B **45**, 9065 (1992).

[135] C. F. Herrmann and J. J. Boland, Surf. Sci. **460**, 223 (2000).

[136] Z. H. Lu, K. Griffiths, P. R. Norton, and T. K. Sham, Phys. Rev. Lett. **68**, 1343 (1992).

[137] P. Kratzer, B. Hammer, and J. K. Nørskov, Phys. Rev. B **51**, 13432 (1995).

[138] M. R. Radeke and E. A. Carter, Phys. Rev. B **54**, 11803 (1996).

[139] D. R. Bowler, J. H. G. Owen, K. Miki, and G. A. D. Briggs, Phys. Rev. B **57**, 8790 (1998).

[140] J. H. G. Owen, D. R. Bowler, C. M. Goringe, K. Miki, and G. A. D. Briggs, Phys. Rev. B **54**, 14153 (1996).

[141] E. Pehlke, Phys. Rev. B **62**, 12932 (2000).

[142] Y. J. Chabal and K. Raghavachari, Phys. Rev. Lett. **52**, 1055 (1985).

[143] J. J. Boland, Phys. Rev. Lett. **65**, 3325 (1990).

[144] Y. J. Chabal and K. Raghavachari, Phys. Rev. Lett. **54**, 1055 (1985).

[145] J. E. Northrup, Phys. Rev. B **44**, 1419 (1991).

[146] D. D. Koleske and S. M. Gates, J. Chem. Phys. **99**, 8218 (1993).

[147] X. Gonze and C. Lee, Phys. Rev. B **55**, 10355 (1997).

[148] S. Baroni, S. de Gironcoli, A. Dal Corso, and P. Giannozzi, Rev. Mod. Phys. **73**, 515 (2001).

[149] C. F. Herrmann and J. J. Boland, J. Phys. Chem. B **103**, 4207 (1999).

[150] D. Chen and J. J. Boland, Phys. Rev. Lett. **92**, 096103 (2004).

[151] J. Y. Lee and M. -H Kang, Phys. Rev. B **69**, 113307 (2004).

[152] P. Frondelius, H. Häkkinen, and K. Honkala, Angew. Chem. Int. Ed. **49**, 7913 (2010).

[153] D. R. Stull and H. Prophet, *JANAF Thermochemical Tables*, 2nd ed., U.S. National Bureau of Standards (U.S. EPO, Washington, D.C., 1971).

[154] M. J. Madou, *Fundamentals of Microfabrication: The Science of Miniaturization, 2nd ed.* (CRC Press LLC, 2002).

[155] V. M. Donnelly and A. Kornblit, J. Vac. Sci. Technol. A **31**, 050825 (2013).

[156] B. Wu, A. Kumar, and S. Pamarthy, J. Appl. Phys. **108**, 051101 (2010).

[157] R. B. Jackman, R. J. Price, and J. S. Foord, Appl. Surf. Sci., **36**, 296 (1989).

[158] C. M. Aldao and J. H. Weaver, Prog. Surf. Sci. **68**, 189-230 (2001).

[159] H. Jansen, H. Gardeniers, M. de Boer, M. Elwenspoek, and J. Fluitman, J. Micromech. Microeng. **6**, 14 (1996).

[160] H. F. Winters and J. W. Coburn, Surf. Sci. Rep. **14**, 161 (1992).

[161] G. A. de Wijs, A. De Vita, and A. Selloni, Phys. Rev. Lett. **78**, 4877 (1997).

[162] G. A. de Wijs, A. De Vita, and A. Selloni, Phys. Rev. B **57**, 10021 (1998).

[163] S. P. Chan, Z. F. Liu, W. M. Lau, J. S. Tse, Surf. Sci. **432**, 125 (1999).

[164] C. F. Herrmann and J. J. Boland, Phys. Rev. Lett. **87**, 115503 (2001).

[165] D. Rioux, R. J. Pechman, M. Chander, and J. H. Weaver, Phys. Rev. B **50**, 4430 (1994).

[166] D. Rioux, M. Chander, Y. Z. Li, and J. H. Weaver, Phys. Rev. B **49**, 11071 (1994).

[167] M. Chander, Y. Z. Li, J. C. Patrin, and J. H. Weaver, Phys. Rev. B **47**, 13035 (1993).

[168] M. Chander, D. A. Goetsch, C. M. Aldao, and J. H. Weaver, Phys. Rev. Lett. **74** , 2014 (1995).

[169] M. Chander, D. A. Cxoetsch, C. M. Aldao, and J. H. Weaver, Phys. Rev. B **52**, 8288 (1995).

[170] R. B. Jackman, H. Ebert, and J. S. Foord, Surf. Sci. **176**, 183 (1986). Q. Gao, C. C. Cheng, P. J. Chen, W. J. Choyke, and J. T. Yates, J. Chem. Phys. **98**, 8308 (1993). A. Szabo, P. D. Farrall, and T. Engel, Surf. Sci. **312**, 284 (1994).

[171] K. Nakayama, C. M. Aldao, and J. H. Weaver, Phys. Rev. Lett. **82**, 568 (1999).

[172] Z. Dohnálek, H. Nishino, N. Kamoshida, and J. T. Yates, J. Chem. Phys. **110**, 4009 (1999).

[173] K. Nakayama, C. M. Aldao, and J. H. Weaver, Phys. Rev. B **59**, 1593 (1999).

[174] A. Agrawal, R. E. Butera and J. H. Weaver, Phys. Rev. Lett. **98**, 136104 (2007).

[175] C. M. Aldao, A. Agrawal, R. E. Butera, and J. H. Weaver, Phys. Rev. B **79**, 125303, (2009).

[176] B. R. Trenhaile, V. N. Antonov, G. J. Xu, K. S. Nakayama, J. H. Weaver, Surf. Sci. **583**, L135 (2005).

[177] B. R. Trenhaile, V. N. Antonov, G. J. Xu, A. Agrawal, A. W. Signor, R. E. Butera, K. S. Nakayama and J. H. Weaver, Phys. Rev. B **73**, 125318 (2006).

[178] J. J. Boland, Science **262**, 1703 (1993).

[179] G. Brocks, P. J. . Kelly, and R. Car, Phys. Rev. Lett. **66**, 1729 (1991).

[180] M. C. Flowers, N. B. H. Jonathan, Y. Liu, and A. Morris, Surf. Sci. **343**, 133 (1995)

[181] K. S. Nakayama, E. Graugnard, and J. H. Weaver, Phys. Rev. Lett. **88**, 125508 (2002).

[182] M. Ležaić, Ph. Mavropoulos, G. Bihlmayer, and S. Blügel, Phys. Rev. B **88**, 134403 (2013).